

AD-767 287

FUNDAMENTAL STUDIES OF SEMICONDUCTOR HETEROEPITAXY

ROCKWELL INTERNATIONAL CORP.

PREPARED FOR
ARMY MISSILE COMMAND
ADVANCED RESEARCH PROJECTS AGENCY

AUGUST 1973

DISTRIBUTED BY:

NTIS

**National Technical Information Service
U. S. DEPARTMENT OF COMMERCE**

AD

AD 767287

FUNDAMENTAL STUDIES OF SEMICONDUCTOR HETEROEPITAXY

FINAL REPORT PART I

DDC
RECEIVED
OCT 1 1973
RECEIVED
C

ARPA Support Office
Research, Development, Engineering and Missile Systems Laboratory
United States Army Missile Command AMSMI RND
Redstone Arsenal
Huntsville, Alabama
Contract No. DAAH01-70-C-1311

Distribution of this document
is unlimited.

Sponsored by:
Advanced Research Projects Agency
ARPA Order No. 1585

DISTRIBUTION STATEMENT
Approved for public release

Reproduced by
NATIONAL TECHNICAL
INFORMATION SERVICE
US Department of Commerce
Springfield, VA. 22151

FUNDAMENTAL STUDIES OF SEMICONDUCTOR HETEROEPITAXY

FINAL REPORT

PART I

**R. P. Ruth, A. J. Hughes, J. L. Kenty, H. M. Manasevit,
D. Medellin, A. C. Thorsen, Y. T. Chan, C. R. Viswanathan, and M. A. Ring**

**Research and Technology Division
Electronics Group
Rockwell International**

August 1973

**ARPA Support Office
Research, Development, Engineering and Missile Systems Laboratory
United States Army Missile Command AMSMI RND**

**Redstone Arsenal
Huntsville, Alabama
Contract No. DAAH01-70-C-1311**

**Distribution of this document
is unlimited.**

**Sponsored by:
Advanced Research Projects Agency
ARPA Order No. 1585**

DOCUMENT CONTROL DATA - R & D

(Security classification of title, body of abstract and indexing annotation must be entered when the overall report is classified)

1. ORIGINATING ACTIVITY (Corporate author) Rockwell International Corp., Electronics Group Electronics Research Division Anaheim, California		2a. REPORT SECURITY CLASSIFICATION Unclassified	
		2b. GROUP	
3. REPORT TITLE Fundamental Studies of Semiconductor Heteroepitaxy, Part I			
4. DESCRIPTIVE NOTES (Type of report and inclusive dates) Final Report, June 1970 through June 1973			
5. AUTHOR(S) (First name, middle initial, last name) Ralph P. Ruth, A. James Hughes, Joseph L. Kenty, Harold M. Manasevit, Arthur C. Thorsen, Y. T. Chan, C. R. Viswanathan, Morey A. Ring			
6. REPORT DATE August 1973	7a. TOTAL NO. OF PAGES 275	7b. NO. OF REFS 67	
8a. CONTRACT OR GRANT NO. DAAH01-70-C-1311	8b. ORIGINATOR'S REPORT NUMBER(S) C71-86/501		
8c. PROJECT NO.	8d. OTHER REPORT NO(S) (Any other numbers that may be assigned this report)		
10. DISTRIBUTION STATEMENT Distribution of this document is unlimited.			
11. SUPPLEMENTARY NOTES		12. SPONSORING MILITARY ACTIVITY Advanced Research Projects Agency ARPA Order No. 1585 Washington, D.C.	
13. ABSTRACT The results of a three-year research program are described. The overall objective of the program was to carry out a fundamental study of nucleation and film growth mechanisms in heteroepitaxial semiconductor thin films. The specific technical objectives were 1) investigation of various aspects of the mechanisms of heteroepitaxial film growth, to establish technical guidelines for the preparation of better films; 2) preparation of improved, high-quality, device-grade heteroepitaxial films of Si and GaAs on insulating substrates by chemical vapor deposition (CVD) methods; 3) development of new or improved methods of characterizing heteroepitaxial semiconductor films; and 4) design and fabrication of selected thin-film devices taking advantage of the unique properties of heteroepitaxial films. The program involved both theoretical and experimental investigations of nucleation and growth mechanisms and development of improved techniques for film and substrate preparation and characterization. The CVD method of growing semiconductor films was emphasized because of its importance in the semiconductor device industry. Main emphasis was on the Si-on-Al ₂ O ₃ system, with attention also given to the Si-on-MgAl ₂ O ₄ and GaAs-on-Al ₂ O ₃ systems. The work was divided among seven subtasks: 1) theory of epitaxy and heteroepitaxial interfaces; 2) deposition studies and film growth; 3) analysis and purification of CVD reactants; 4) preparation and characterization of substrates; 5) studies of <u>in situ</u> CVD film growth in the electron microscope; 6) evaluation of film properties; and 7) design and fabrication of special devices.			

KEY WORDS	LINK A		LINK B		LINK C	
	ROLE	WT	ROLE	WT	ROLE	WT
Epitaxy GaAs Si Al ₂ O ₃ (sapphire) MgAl ₂ O ₄ (spinel) Chemical vapor deposition (CVD) <u>In situ</u> film growth Electron microscopy Epitaxy theory Heteroepitaxy Thin-film devices Semiconductors Film nucleation Transport properties Metalorganic compounds Physical vapor deposition (PVD) Substrate Polishing Gas-phase etching Anisotropy Thermally induced stress Piezoresistance						
<p>Principal technical accomplishments include 1) experimental discovery and empirical characterization of significant anisotropy in the electrical properties of Si/Al₂O₃ films of several crystallographic orientations, and theoretical explanation of the effects in terms of a model that combines thermally-induced stresses due to expansion coefficient differences with the piezoresistance effect in Si; 2) delineation of preferred substrate orientations, deposition temperatures, film growth rates, and carrier gas atmosphere for optimized film properties in the Si/Al₂O₃ and Si/MgAl₂O₄ systems; 3) identification of the influence of surface-state conduction on measured electrical properties in Si films with carrier concentrations $<10^{16} \text{ cm}^{-3}$; 4) identification of the role of the Al₂O₃ surface as a catalyst for the pyrolytic decomposition of SiH₄ in the formation of Si films by CVD; 5) development of gas-phase etching and improved mechanical polishing techniques for preparing surfaces of Al₂O₃ and MgAl₂O₄ substrates for the heteroepitaxial growth of semiconductor films; 6) development of an ion-beam sputtering technique for preparing ultrathin ($<500\text{\AA}$) regions in Al₂O₃ substrates for transmission electron microscopy; 7) observation of the <u>in situ</u> growth of Si by physical vapor deposition (PVD) and CVD on Al₂O₃ and amorphous carbon substrates in the electron microscope; 8) observation and characterization of the transport of photoinjected electrons through single-crystal Al₂O₃; 9) measurement of carrier lifetimes in Si heteroepitaxial films on Al₂O₃ and correlation of lifetimes with various experimental parameters; 10) determination of surface-state density distributions in Si heteroepitaxial films on Al₂O₃; and 11) the successful fabrication in Si/Al₂O₃ of charge-coupled devices exhibiting good charge-transfer efficiency at high frequencies. Details of these and other results and investigations are given by means of data tabulations, graphs, photographs, and narrative. An extensive bibliography of electron microscope <u>in situ</u> film nucleation and growth studies is also included. The report is bound in three separate parts.</p>						

ABSTRACT

The results of a three-year research program are described. The overall objective of the program was to carry out a fundamental study of nucleation and film growth mechanisms in heteroepitaxial semiconductor thin films. The specific technical objectives were 1) investigation of various aspects of the mechanisms of heteroepitaxial film growth, to establish technical guidelines for the preparation of better films; 2) preparation of improved, high-quality, device-grade heteroepitaxial films of Si and GaAs on insulating substrates by chemical vapor deposition (CVD) methods; 3) development of new or improved methods of characterizing heteroepitaxial semiconductor films; and 4) design and fabrication of selected thin-film devices taking advantage of the unique properties of heteroepitaxial films.

The program involved both theoretical and experimental investigations of nucleation and growth mechanisms and development of improved techniques for film and substrate preparation and characterization. The CVD method of growing semiconductor films was emphasized because of its importance in the semiconductor device industry. Main emphasis was on the Si-on- Al_2O_3 system, with attention also given to the Si-on- MgAl_2O_4 and GaAs-on- Al_2O_3 systems. The work was divided among seven subtasks: 1) theory of epitaxy and heteroepitaxial interfaces; 2) deposition studies and film growth; 3) analysis and purification of CVD reactants; 4) preparation and characterization of substrates; 5) studies of *in situ* CVD film growth in the electron microscope; 6) evaluation of film properties; and 7) design and fabrication of special devices.

Principal technical accomplishments include 1) experimental discovery and empirical characterization of significant anisotropy in the electrical properties of Si/ Al_2O_3 films of several crystallographic orientations, and theoretical explanation of the effects in terms of a model that combines thermally-induced stresses due to expansion coefficient differences with the piezoresistance effect in Si; 2) delineation of preferred substrate orientations, deposition temperatures, film growth rates, and carrier gas atmosphere for optimized film properties in the Si/ Al_2O_3 and Si/ MgAl_2O_4 systems; 3) identification of the influence of surface-state conduction on measured electrical properties in Si films with carrier concentrations $<10^{16}\text{cm}^{-3}$; 4) identification of the role of the Al_2O_3 surface as a catalyst for the pyrolytic decomposition of SiH_4 in the formation of Si films by CVD; 5) development of gas-phase etching and improved mechanical polishing techniques for preparing surfaces of Al_2O_3 and MgAl_2O_4 substrates for the heteroepitaxial growth of semiconductor films; 6) development of an ion-beam sputtering technique for preparing ultrathin ($<500\text{\AA}$) regions in Al_2O_3 substrates for transmission electron microscopy; 7) observation of the *in situ* growth of Si by physical vapor deposition (PVD) and CVD on Al_2O_3 and amorphous carbon substrates in the electron microscope; 8) observation and characterization of the transport of photoinjected electrons through single-crystal Al_2O_3 ; 9) measurement of carrier lifetimes in Si heteroepitaxial films on Al_2O_3 and

correlation of lifetimes with various experimental parameters; 10) determination of surface-state density distributions in Si heteroepitaxial films on Al_2O_3 ; and 11) the successful fabrication in Si/ Al_2O_3 of charge-coupled devices exhibiting good charge-transfer efficiency at high frequencies.

Details of these and other results and investigations are given by means of data tabulations, graphs, photographs, and narrative. An extensive bibliography of electron microscope in situ film nucleation and growth studies is also included. The report is bound in three separate parts.

PROGRAM SUMMARY

The overall objective of this three-year program was to carry out a fundamental study of nucleation and film growth mechanisms in heteroepitaxial semiconductor thin-film systems which would lead to new knowledge and understanding of these processes, and then to apply the results to the preparation of improved semiconductor thin films and thin-film devices on insulating substrates.

The specific technical objectives were the following: 1) investigation of various aspects of the mechanisms of heteroepitaxial film growth, to establish technical guidelines for the preparation of better films which could be applied to real situations; 2) preparation of improved, high-quality, device-grade heteroepitaxial films of Si and GaAs on insulating substrates by chemical vapor deposition (CVD) methods; 3) development of methods of characterizing heteroepitaxial films as to their suitability for subsequent device fabrication; and 4) design and fabrication of selected thin-film devices which take advantage of the unique properties of such films.

The plan for accomplishing these objectives involved the study of the fundamentals of heteroepitaxial semiconductor film growth on insulating substrates as the primary activity, with specialized device fabrication used as a means both of evaluating film properties and of exploiting certain unique properties of heteroepitaxial semiconductor-insulator systems. Both theoretical and experimental investigations were involved. The theoretical studies consisted of two types: 1) direct interaction with the experimental program, involving data analyses, suggestion of definitive experiments, and postulation of specific models to explain experimental observations; 2) development of original contributions to the theory of heteroepitaxial growth. The experimental investigations were also of two types: 1) fundamental explorations to delineate mechanisms and general empirical principles of the heteroepitaxial growth process; 2) practical device studies accompanying the fundamental investigations, so that new developments could be applied to the improvement of films and thin-film devices.

The chemical vapor deposition (CVD) method of growing semiconductor films was emphasized because of its importance in the semiconductor device industry. Main emphasis was on the Si-on- Al_2O_3 system, with attention also given to the Si-on- MgAl_2O_4 and GaAs-on- Al_2O_3 systems. The work was divided among seven subtasks: 1) theory of epitaxy and heteroepitaxial interfaces; 2) deposition studies and film growth; 3) analysis and purification of CVD reactants; 4) preparation and characterization of substrates; 5) studies of *in situ* CVD film growth in the electron microscope; 6) evaluation of film properties; and 7) design and fabrication of special devices.

The program was carried out primarily at facilities of the Electronics Group of the Rockwell International Corporation, by Rockwell personnel. Parts of three of the specific subtasks were performed by personnel of the University of California at Los Angeles (UCLA), in the Department of Electrical Sciences and Engineering and the Chemistry Department. Work on another subtask was done in part in the Department of Chemistry of California State University, San Diego (CSUSD). Both the UCLA and the CSUSD programs were supported by subcontracts from Rockwell.

The principal technical accomplishments of the program include the following: 1) experimental discovery and extensive characterization of significant anisotropy in the electrical properties of Si/Al₂O₃ films, and theoretical explanation of the effect in terms of a model that combines thermally-induced stresses with the piezoresistance effect in Si; 2) delineation of preferred substrate orientations, deposition temperatures, film growth rates, and carrier gas atmospheres for optimized film properties in the Si/Al₂O₃ and Si/MgAl₂O₄ systems; 3) identification of the influence of surface-state conduction on measured electrical properties in Si films with carrier concentrations $<10^{16} \text{ cm}^{-3}$; 4) identification of the catalytic role of the Al₂O₃ surface in the heterogeneous pyrolytic decomposition of SiH₄ to form Si films by CVD; 5) development of gas-phase etching and improved mechanical polishing techniques for preparing surfaces of Al₂O₃ and MgAl₂O₄ for the heteroepitaxial growth of semiconductor films; 6) development of an ion-beam sputtering technique for preparing ultrathin ($<500\text{\AA}$) regions in Al₂O₃ substrates for transmission electron microscopy; 7) observation of the in situ growth of Si by physical vapor deposition (PVD) and by CVD on Al₂O₃ and amorphous carbon substrates in the electron microscope; 8) observation and characterization of the transport of photoinjected electrons through single-crystal Al₂O₃; 9) measurement of carrier lifetimes in Si heteroepitaxial films on Al₂O₃; 10) determination of surface-state density distributions in Si heteroepitaxial films on Al₂O₃; and 11) the successful fabrication in Si/Al₂O₃ of charge-coupled devices exhibiting good charge-transfer efficiency at high frequencies.

A summary of the work of the contract program by subtask follows:

Subtask 1: Theory of Epitaxy and Heteroepitaxial Interfaces. Several separate investigations were carried out in attempts to model heteroepitaxial systems. An extension of the island alignment model using a Gaussian-atom Fourier-transform technique, the Frank-van der Merwe model, a Green's-function/Wannier-function approach, a contrived potential-energy model, and a molecular-orbital method for developing the heteroepitaxial interface were all critically reviewed for the purpose, and all were found inadequate for application to the real systems of interest. A two-body interatomic potential method, although also initially rejected, was finally adopted for modeling the Al₂O₃ lattice with Morse potentials and a suitable computer program; mechanical stability and surface reconstruction phenomena in Al₂O₃ were treated successfully by this method, involving relaxation of the several atomic planes nearest the Al₂O₃ surface. An electron-on-network method was also considered for determination of surface atom configurations and interfacial binding energies in situations where the surface structure is allowed to relax, but was also eventually found inadequate for realistic calculations in heteroepitaxial systems.

Extension of the modeling to the Si/Al₂O₃ composite was interrupted by the theoretical investigation of the effects on electrical properties of stresses in the Si films resulting from differential thermal contraction of substrate and film, prompted by the experimental observation of ~10% anisotropy in the carrier mobility in (001)Si/Al₂O₃ and ~40% anisotropy in (221)Si/Al₂O₃. A model combining thermal expansion stress and the piezoresistance effect, incorporating the anisotropies in substrate thermal expansion, Si elastic constants, and Si piezoresistance coefficients, was developed and applied to (001), (221) and (111)Si

films on Al_2O_3 . Excellent agreement was obtained between theory and experiment in the first two cases; the amount of anisotropy and the directions (in the plane of the film) of maximum and minimum carrier mobility were correctly predicted. In (111)Si (on two different Al_2O_3 substrate orientations), however, the theoretically predicted effects were too small to account for the experimental observations, indicating that other (not yet identified) phenomena are more important in determining anisotropy in the (111)Si/ Al_2O_3 system.

Extensive calculations were made for the general (xx1)Si orientation ($0 \leq x \leq \infty$), which defines all Si orientations along the zone that includes (001), (111), (221), and (110)Si and thus all of the Si/ Al_2O_3 epitaxy modes of major interest. For n-type Si/ Al_2O_3 , the predicted stress effects ranged from a ~30% reduction for (001)Si to a ~25% enhancement in maximum mobility near (110)Si. For p-type Si films, the predicted stress effect is always a mobility enhancement, with the maximum mobility ranging from $\sim 1.07\mu_0$ for (001)Si to $\sim 2.4\mu_0$ for (110)Si, where μ_0 is the zero-stress mobility. It is significant that the Si film orientation most used in commercial devices - (001) - is the one showing the lowest mobilities of all those investigated. Thus, considerable improvement in performance of certain types of devices could be realized by exploiting these predicted effects, which have major significance for heteroepitaxial device technology.

Subtask 2: Deposition Studies and Film Preparation. A major part of the work of this subtask consisted of preparing a variety of Si and GaAs heteroepitaxial film samples for use in other parts of the program. Experimental investigations of the effects of various deposition parameters upon the properties of Si and GaAs films continued throughout the program, including examination of the following: 1) dependence of electrical properties on growth temperature, growth rate, and crystallographic orientation of substrate (including the (11 $\bar{2}$ 0) orientation, not previously used for heteroepitaxy studies); 2) variations in Si film properties with thickness; 3) formation and properties of p-type Si/ Al_2O_3 films; 4) effects of autodoping (at temperatures above $\sim 1050\text{C}$) in Si films on Al_2O_3 and MgAl_2O_4 ; 5) effects of reactor configuration on film properties; 6) characteristics of early-stage growth of Si films on Al_2O_3 ; 7) growth of Si films by SiH_4 pyrolysis at reduced pressures (1 to 10 torr); 8) growth of Si films in gaseous atmospheres other than pure H_2 ; 9) effects of annealing during growth on properties of Si films (no significant improvement in film properties observed); and 10) growth of GaAs films on Al_2O_3 and MgAl_2O_4 . These studies revealed the strong interrelationships that exist among the various parameters involved in optimizing Si growth on insulators. Evaluation of the electrical properties of Si films on Al_2O_3 demonstrated that growth conditions (1) must be optimized for the particular substrate orientation chosen; (2) differ for those Al_2O_3 orientations which produce the same Si orientation; (3) are dependent upon reactor geometry and gaseous atmosphere; and (4) must be optimized for the particular film thickness desired.

Based on electrical properties of the films grown, the preferred substrate for Si heteroepitaxy was identified as one that produces (111)Si growth rather than (100)Si growth, namely $\sim(11\bar{2}0)\text{Al}_2\text{O}_3$ or (111) MgAl_2O_4 , the highest mobilities being obtained on (111) MgAl_2O_4 . Optimum growth temperatures varied with substrate orientation: (100)Si on (0112) Al_2O_3 , 1050-1075C; (111)Si on (10 $\bar{1}$ 4) Al_2O_3 , 1075-1100C; (111)Si on $\sim(11\bar{2}0)\text{Al}_2\text{O}_3$, 1075-1100C; and (111)Si on (111) MgAl_2O_4 , $\sim 1025\text{C}$. The preferred growth atmosphere appeared to be either H_2 or a He-H_2

mixture for growth on $(01\bar{1}2)Al_2O_3$ or $\sim(11\bar{2}0)Al_2O_3$, but both $(10\bar{1}4)Al_2O_3$ and $(111)MgAl_2O_4$ apparently need a He-rich atmosphere ($\sim 90\% He-10\% H_2$) for obtaining high quality films. For essentially every orientation studied, growth rates from $\sim 2\mu m/min$ to $\sim 4\mu m/min$ were found sufficient, although good growth was also achieved on $(01\bar{1}2)Al_2O_3$ at lower rates. These growth conditions are optimum for the reactor system used, but should be useful guides for CVD film growth in systems with other reactor geometries. These observations should lead to definite improvements in Si/Al_2O_3 film properties and thus to improved performance and reliability in Si/Al_2O_3 devices and circuits.

Subtask 3: Analysis and Purification of CVD Reactants. Since the impurity content of the various reactants used for CVD of Si and GaAs heteroepitaxial films probably provides the real limitation on the achievable impurity levels in the films themselves, a study was undertaken to attempt to identify and establish the concentrations of the principal impurities in the reactants that might influence the film properties if they were to become incorporated into the films during growth. During the first year, techniques of gas chromatography were developed for analysis of the reactants used for Si and GaAs heteroepitaxy by CVD, with silicone oil and polymer columns used for the chromatography. Several extraneous impurity peaks were observed in the chromatograms of SiH_4 samples, and diborane (B_2H_6) was tentatively identified as a significant impurity (~ 10 ppm), although not confirmed by mass spectrometer techniques. Small quantities of purified SiH_4 , free of diborane, were prepared by successive injections in the chromatograph, but the quantities were too small for use in laboratory CVD experiments. Beginning in the second year of the program, samples of SiH_4 and of trimethylgallium (TMG) used for Si and GaAs CVD experiments were analyzed for impurity content by sensitive mass spectrometric techniques. Disilane and trimethylsilane, together with several other impurities of less concern, were found in the SiH_4 samples.

Significant impurity concentrations in some of the reactants (especially SiH_4) at times limited the accuracy of the study of the effects of deposition parameters on Si film properties. Cooperative efforts with vendors for preparation of improved-purity reactants continued throughout the program, as did analyses of reactants by mass spectrometer techniques. It was made clear that significant differences occurred in the purity of reactant materials; not only did they vary from supplier to supplier but also different tanks of the same material from the same supplier were not consistent in purity. Another problem was the lack of agreement in the analyses supplied by different analytical laboratories for the same tank of reactant and the differences in detection limits for the same element or compound that different laboratories possessed, making it difficult to determine which results were the most reliable and which supplier of gases was best. A "use test" still appears to be the most reasonable way of evaluating materials for the intended application. The analyses demonstrated the ultimate lack of understanding of the role of impurities in epitaxial film growth and the minimum requirements for the analytical methods that should be used in detecting these impurities. An extensive collaborative study involving the reactant supplier, the analytical laboratory, and the ultimate user is needed.

To examine some of the fundamentals of the chemistry and reaction kinetics of the CVD processes used for growing heteroepitaxial films of Si and GaAs, investigations of the reactions involved in the formation of Si by SiH_4 pyrolysis and of GaAs by the trimethylgallium (TMG)- AsH_3 reaction were undertaken. The influence of the Al_2O_3 surface on the mechanism of decomposition of SiH_4 as a function of temperature, and the decomposition modes and reaction products of TMG and

AsH₃ as functions of temperature, concentration ratio, and H₂ partial pressure (to attempt to determine the requirements for formation of optimum-quality GaAs) were examined. It was found that the surface of single-crystal Al₂O₃ does catalyze the thermal decomposition of SiH₄, whereas the pyrolysis is homogeneous over a Si surface. No effect of preheating the Al₂O₃ to temperatures as high as 1200C was found. A variety of observations made on the TMG-AsH₃ system included the following, among others: 1) GaAs does result from the reaction of TMG with AsH₃, and an excess of AsH₃ should be used in any application of the process; and 2) both CH₄ (methane) and H₂ are produced in the series of step-wise reactions leading to the final product. Further study of the reaction at high temperatures is recommended.

Subtask 4: Preparation and Characterization of Substrates. It was demonstrated that Al₂O₃ surfaces prepared by mechanical polishing techniques and used routinely for semiconductor heteroepitaxy typically had severe surface and subsurface damage, with many scratches often several microns deep yet often rendered invisible to close inspection because of amorphous or fine-grained debris embedded in the scratches in the final polishing stages. Early in the second year a much improved technique for mechanical polishing of (1014)Al₂O₃ was developed, and very good surfaces in this previously troublesome orientation were then obtained. Gas-phase etching/polishing procedures using SF₆ and various fluorinated halocarbons in the 1350 to 1500C temperature range were found to produce essentially scratch-free surfaces on (0112) and near-(1120)Al₂O₃ substrates. Extensive gas-phase etch-rate data were obtained as a function of crystallographic orientation in this temperature range. The technique was further developed for (1) thinning Al₂O₃ substrates; (2) evaluating the effects of prolonged etching on (0112), (0001), and ~-(1120)Al₂O₃; and (3) assessing the subsurface damage caused by various mechanical polishing procedures. Evaluation of mechanical polishing methods for MgAl₂O₄ surfaces indicated that surface fill-in occurs for this material, just as for Al₂O₃. Some exploratory gas-phase etching experiments with MgAl₂O₄ surfaces were also carried out during the second year of the program.

Ion-beam sputtering techniques were developed for preparing ultra-thin (~200Å)Al₂O₃ wafers for use as substrates in the in situ CVD experiments with Si. Wafers successfully thinned to ~50µm or less by mechanical polishing techniques were subsequently thinned by ion etching to the point of perforation in some areas, resulting in adjoining regions of thicknesses suitable for transmission electron microscopy as applied in the in situ experiments. Three different Al₂O₃ orientations were successfully thinned by this method - (0001), (1014), and (0112). Considerable study of properties of the resulting thinned substrates was carried out, and improvements in the ion-thinning process were realized during the final year of the program, when the thinned substrates were used in the in situ CVD experiments (Subtask 5).

Mechanical lapping and polishing methods that produce good quality surfaces suitable for use as substrates for epitaxy were developed during the contract for several orientations of Al₂O₃ - (0001), (0112), (1014), (1120), ~6 deg off (1120) and (1122). By means of etch-rate techniques developed for this

material it was possible to determine the apparent depth of damage in Al_2O_3 substrate wafers at various stages of preparation. At a given stage in the processing, the damage depth was found to increase for various orientations in the following order: $(10\bar{1}4)$, $(11\bar{2}0)$, $(01\bar{1}2)$, and (0001) .

A technique utilizing the photoelectric process in a metal-insulator-semiconductor structure, consisting of an Al_2O_3 substrate with a Si or GaAs film grown on one surface and a semitransparent Al film on the other, demonstrated that photoexcited electrons from either the semiconductor or the metal film can be transported through single-crystal Al_2O_3 of several mils thickness. Further study of the charge transport process also established that (1) the Al_2O_3 used for substrates for growth of heteroepitaxial semiconductor films has trap levels approximately 0.18 eV below the conduction band; (2) the transport of photoinjected electrons occurs through the Poole-Frenkel conduction mechanism; and (3) the quantum efficiency for the photoelectric process is quite low, approximately 10^{-5} .

Routine characterization of substrate surfaces at various stages of preparation continued throughout the program, utilizing various standard techniques of x-ray and electron diffraction analysis and optical and electron (including scanning) microscopy.

Subtask 5: Studies of in situ Film Growth in the Electron Microscope.

In the first year of the program many of the modifications required in the transmission electron microscope for in situ observation of the nucleation and early-stage growth of CVD semiconductor films on insulating substrates were completed. Early in the second year a series of electron microscope modifications and tests was finished, culminating in the first series of successful PVD experiments inside the electron microscope. Al was deposited onto a heated carbon substrate and a sequence of micrographs was taken during the growth process, demonstrating the feasibility of performing in situ nucleation and growth studies in the equipment. Additional in situ PVD experiments were carried out in the second year, with both Al and Au deposited onto amorphous carbon substrates to delineate further the required techniques and experimental problems to be encountered in the later CVD experiments. Calculations and design for the CVD microchamber were also completed during the second year, and the fabrication of the microchamber and associated hardware was begun.

During the final year of the program the fabrication of the CVD microchamber and its mounting flange was completed, and a gas-handling manifold was installed on the electron microscope. Gas flow experiments were performed to determine the flow rate of gas through the microchamber as a function of pressure and to determine the maximum pressure attainable in the microchamber.

In addition, a number of in situ Si CVD experiments were performed resulting in the successful growth of Si films in the electron microscope by the pyrolysis of SiH_4 . The nucleation and early growth of Si on both amorphous carbon and single-crystal Al_2O_3 substrates was observed, leading to the following conclusions: 1) the pyrolysis of SiH_4 to form Si films by CVD inside the electron microscope is feasible; 2) the in situ study by trans-

mission electron microscopy of the post-nucleation and early growth stages of a semiconductor film grown by CVD is feasible; 3) the nucleation and early growth processes for CVD Si are fundamentally similar to those of metal films grown by PVD, although some specific differences exist; 4) single-crystal Si growth on $(01\bar{1}2)Al_2O_3$ results primarily from the growth of nuclei of a preferred orientation at the expense of randomly oriented nuclei, and not from the large nucleation rate of these favorably oriented nuclei; 5) the ion-beam sputtering process can produce electron-transparent Al_2O_3 suitable for use as substrates for in situ CVD film growth experiments.

Subtask 6: Evaluation of Film Properties. From the beginning of the program, routine evaluation of film properties was carried out by established methods of x-ray and electron diffraction analysis, metallographic analysis, and electrical measurements of transport properties. A new technique for evaluating the characteristics of the interfacial region of heteroepitaxial films was developed, involving measurements of photoelectron emission from monochromatically-illuminated films in the MIS configuration on insulating substrates (see Subtask 4). Photocurrents due to electron transport through the single-crystal Al_2O_3 substrates were measured as a function of photon energy, permitting determination of various parameters in the Si/ Al_2O_3 and GaAs/ Al_2O_3 systems. These measurements gave values of 1.0eV for the electron affinity of Al_2O_3 , 3.15eV for the barrier height at an Al_2O_3 -Al interface, 4.50eV for the Si_2 - Al_2O_3 interface barrier height, $\sim 0.37eV$ for the band-bending in Si near the Si_2 - Al_2O_3 interface, $\sim 0.10eV$ for the band-bending in GaAs films near the Al_2O_3 interface, and electron escape lengths of at least $12\mu m$ in Si and $23\mu m$ in GaAs. Values for the work function of various metals were also determined by these measurements.

Determination of the energy spectrum of back-scattered proton or alpha-particle beams injected in channeling directions in heteroepitaxial semiconductor films was investigated as a means of measuring the density and the location of structural defects in the films. Experiments indicated that Si/insulator films have less imperfect interfacial regions than do GaAs/insulator films. The best structures of those examined were found in $(100)Si$ films on $(01\bar{1}2)Al_2O_3$ substrates and in $(111)Si$ films grown on near- $(11\bar{2}0)Al_2O_3$ substrates. Information on the early growth stages of Si on Al_2O_3 was also obtained by conventional transmission electron microscopy of very thin Si films grown on ion-thinned Al_2O_3 substrates in a conventional (atmospheric-pressure) vertical-flow CVD reactor. These experiments showed that the growth of a single-crystal Si film by CVD is the result of coalescence processes in the early growth stages and not of nucleation phenomena alone, producing films with a relatively higher incidence of defects and relatively lower carrier mobilities.

Rapid acquisition of data on electrical properties of the films was very important to the conduct of film growth experiments, especially in the second and third years; measurements of film conductivity type, resistivity, carrier concentration, and carrier mobility were made routinely on a majority of the epitaxial samples prepared on the program, utilizing either the van der Pauw method or the more accurate and conventional Hall-effect bridge method. These data were essential for the study of the effects of changes in deposition parameters on Si/ Al_2O_3 and Si/ $MgAl_2O_4$ film properties, and provided

considerable insight into the factors which most strongly influence film quality so that identification of the conditions for optimized film growth could be made.

It was determined that the electrical properties of undoped n-type hetero-epitaxial Si films grown on various orientations of Al_2O_3 (and also MgAl_2O_4) by the pyrolysis of SiH_4 are dominated by surface-state conduction for carrier concentrations of $\sim 10^{16} \text{cm}^{-3}$ or below. It was found that there were inhomogeneities in the donor concentration of typical CVD Si/ Al_2O_3 films over the film area, and that a concentration gradient existed from the center of the susceptor radially outward; films reflected this variation depending upon the placement of the substrate on the susceptor during CVD growth. Gas flow characteristics or a non-uniform temperature of the rf-heated pedestal (susceptor) were thought to account for the effect. Measurements were made of the variation of electrical properties of Si/ Al_2O_3 with temperature, and some of the observed effects were attributed to high defect densities (e.g., deep-lying donor levels) or inhomogeneous strains in the films.

The most significant development to come from the film evaluation procedures was the observation of the anisotropy in electrical properties in Si/ Al_2O_3 films. Mobility measurements as a function of azimuthal direction (every 18 deg) in the film plane indicated a maximum mobility in two directions and a minimum mobility in two directions, the latter displaced by 90 deg from the former. The mobility anisotropy factor A, defined as the ratio of the difference between the maximum and minimum values of mobility in the plane of the film to the average value of the mobility in that plane, was found to be about 40% for (221)Si/(11 $\bar{2}$ 2) Al_2O_3 and about 9% for (001)Si/(01 $\bar{1}$ 2) Al_2O_3 . Results of theoretical calculations (Subtask 1) agreed well with the experimental data. The calculations and the experimental results indicated that (221)Si exhibits higher electron mobilities than other more commonly used orientations. Measurements of anisotropy at 77K were also consistent with the corresponding increases in piezoresistance coefficients at that temperature. Data analyses predicted zero-stress mobilities significantly below bulk crystal values, however, indicating mechanisms other than thermally-induced stresses were dominant in reducing carrier mobilities in hetero-epitaxial films. Extensive studies of (111)Si on (11 $\bar{2}$ 0) Al_2O_3 and on (10 $\bar{1}$ 4) Al_2O_3 gave experimental anisotropies averaging 16% and 30%, respectively, much larger than theoretical predictions, again indicating the presence of other major influencing factors. There appeared to be an inverse relationship between anisotropy in (111)Si and the minimum or the average mobility, higher anisotropy corresponding to lower mobility. Attempts were made to correlate these results with reactor configuration (i.e., horizontal or vertical) and various deposition conditions. Measurements were also begun to examine the possibility of mobility anisotropy being present in the Si/ MgAl_2O_4 system.

The surface-state density of thermally oxidized Si films on Al_2O_3 was determined late in the program using the MOS C-V technique. Evidence of both donor- and acceptor-type surface states was found; a peak in the acceptor-state density appeared at $\sim 0.16 \text{eV}$ below the conduction band, but the exact

location of the donor-state density peak could not be determined. Measurements of high-field transport properties of Si and GaAs heteroepitaxial films on Al_2O_3 were also undertaken, early in the program, to obtain drift mobility data for some of the films.

Subtask 7: Design and Fabrication of Devices. In the first year of the contract apparatus for determining minority carrier lifetime by pulsed C-V measurements in MOS structures was designed and constructed and tests were begun. A special MOS structure was designed for measurement of channel conductance, high- and low-field transport properties, and various interface characteristics of heteroepitaxial films. Initial attempts to fabricate Schottky-barrier diodes in Si/ Al_2O_3 films as a means of evaluating their electrical properties were not successful and were not pursued further. In the second year the design of a Schottky-barrier type of FET was completed for use in fabricating experimental FET structures in GaAs/insulator films for operation at 1 GHz. Most of the device-oriented effort centered about the determination of carrier lifetimes using the MOS pulsed C-V technique (work which extended to the end of the program) and attempts to fabricate Schottky-barrier FET's in GaAs/ Al_2O_3 .

Recent device efforts produced Schottky-barrier diodes (in n-type Si/ Al_2O_3 samples) having good reverse but unsatisfactory forward characteristics. The Schottky-barrier FET structures were still not satisfactory. Preliminary work on fabricating and evaluating Schottky-barrier photovoltaic cells using illumination from the back side was begun, and charge-coupled devices (CCD's) in Si/ Al_2O_3 composites were successfully designed, fabricated, and tested.

The lifetime measurement method used has the important advantage that the actual carrier lifetime is magnified by the factor N/n_i , where N is the impurity concentration in the semiconductor and n_i is the intrinsic concentration, so that very short lifetimes typical of heteroepitaxial systems (10^{-10} - 10^{-9} sec) could be measured. Carrier lifetimes and values of surface recombination velocity were obtained for As-doped n-type Si/ Al_2O_3 samples and for As-doped n/ n^+ -type Si/ Al_2O_3 samples grown by CVD on this contract, as well as for some commercially-obtained Si/ Al_2O_3 samples that were P-doped. Lifetimes for As-doped (100)-oriented Si varied from $\sim 10^{-10}$ sec for films 1-3 μm thick to $\sim 5 \times 10^{-9}$ sec for films $\sim 10\mu\text{m}$ thick; the particular P-doped films measured exhibited lifetimes nearly an order of magnitude longer. No clear dependence of lifetime on As doping concentration or on Si orientation ((100) and (111) were studied) was detected. It was found that an underlying n^+ layer ($\sim 3 \times 10^{18}\text{cm}^{-3}$) significantly enhanced the lifetime in a 3 μm top layer of As-doped ($\sim 10^{16}\text{cm}^{-3}$) Si for a given total film thickness, the enhancement being greater the greater the n^+ layer thickness ($\tau \sim 1\mu\text{sec}$ for 18 μm total thickness); the n^+ sublayer evidently acts as a "getter" for the trapping centers that tend to lower the lifetime in the n-type material.

Since CCD's had previously been fabricated in Si and showed good charge transfer and since other Si/ Al_2O_3 devices had exhibited good high-frequency and radiation-resistant characteristics it was determined that fabrication of CCD's should be undertaken in Si/ Al_2O_3 . The devices were successful, with good transfer

efficiency at high frequencies; four-phase 8-mil-per-cell CCD's were operated at 2MHz with 0.99 efficiency. Low-frequency operation, however, was found to be limited by the short carrier lifetime which allowed charge-up of the potential well.

CONTENTS

	<u>Page</u>
ABSTRACT	iii
PROGRAM SUMMARY	v
<u>PART I</u>	
SECTION 1. INTRODUCTION	1
1. Contract Objectives	1
2. Program Scope	2
3. Program Description by Subtask	3
SECTION 2. THEORY OF EPITAXY AND HETEROEPITAXIAL INTERFACES	6
1. Gaussian Atom Extension of the Island Alignment Model	10
2. Application of Electron-on-network Techniques to Heteroepitaxy	18
3. Other Theoretical Approaches to Modeling Heteroepitaxial Systems	22
4. Studies of the Si/Al ₂ O ₃ System Using Interatomic Potentials	30
5. Stress Effects on Electrical Properties of Si/Al ₂ O ₃	39
SECTION 3. DEPOSITION STUDIES AND FILM PREPARATION	49
1. Electrical Properties of Si Films as Functions of Growth Parameters	52
2. Variations in Si Film Properties with Thickness	62
3. Properties of P-type Si/Al ₂ O ₃ Films	70
4. Study of Autodoping in Si Films on Al ₂ O ₃ and MgAl ₂ O ₄	75
5. Effects of Reactor Configuration on Deposition Process and Film Properties	82
6. Studies of Early-stage Growth of Si Films on Al ₂ O ₃	87
7. CVD Growth of Si Films at Reduced Pressures	92
8. Growth of Si by CVD in Atmospheres other than H ₂	96
9. Effect of Annealing during Growth on Si Film Properties	107
10. GaAs Growth Studies	115
11. Conclusions	119
SECTION 4. ANALYSIS AND PURIFICATION OF CVD REACTANTS	123
1. Reactant Analysis by Gas Chromatography	124
2. Reactant Analysis by Routine Mass Spectrometry	133
SECTION 5. CHEMISTRY AND REACTION KINETICS OF CVD PROCESSES	141
1. Pyrolysis of SiH ₄	142
2. Reaction of TMG and AsH ₃	146

	<u>Page</u>
SECTION 6. PREPARATION AND CHARACTERIZATION OF SUBSTRATES	152
1. Preparation of Insulator Substrate Surfaces for Use in Heteroepitaxy Experiments	153
a. Mechanical Polishing Methods for Al_2O_3 and $MgAl_2O_4$	154
b. Gas-phase Etching/Polishing Techniques	166
c. Ion-beam Etching/Sputtering	183
2. Determination of Depth of Damage in Al_2O_3 Substrates	185
3. Preparation of Ultrathin Electron-transparent Al_2O_3 Substrates	191
a. Mechanical Lapping/Polishing Techniques	191
b. Gas-phase Etching and Chemical Etching Methods	192
c. Ion-beam Sputtering Techniques	196
SECTION 7. Al_2O_3 CHARACTERIZATION BY CARRIER INJECTION AND TRANSPORT MEASUREMENTS	218
1. Theory of Transport of Electrons in Insulators	220
2. Measurement of Quantum Efficiency of Photoinjection	226
3. Photocurrent Variation with Sample Temperature	230
REFERENCES FOR PART I	R-1
 <u>PART II</u>	
SECTION 8. STUDIES OF <u>IN SITU</u> FILM GROWTH IN THE ELECTRON MICROSCOPE	236
1. Electron Microscope Modifications for <u>In Situ</u> Experiments	238
2. <u>In Situ</u> PVD Experiments	242
a. Al Deposition Experiments	243
b. PVD Experiments with other Materials	245
3. <u>In Situ</u> CVD Experiments	247
a. CVD Microchamber Design, Construction and Test	251
b. Si Film Growth on Amorphous Carbon Substrates	262
c. Si Film Growth on Thinned Single-crystal Al_2O_3 Substrates	267
4. Discussion and Recommendations	280
a. Substrate Alignment	280
b. Temperature Calibration	281
c. Recommendations for Further Work	283

	<u>Page</u>
SECTION 9. ELECTRICAL PROPERTIES OF HETEROEPITAXIAL FILMS	235
1. Homogeneity of Electrical Properties of Heteroepitaxial Films	287
2. Variation of Electrical Properties of Si/Al ₂ O ₃ with Temperature	291
3. Anisotropy in Electrical Properties of Heteroepitaxial Si Films	297
4. Measurement of Carrier Lifetimes in Heteroepitaxial Semiconductor Films	300
a. Theoretical Considerations	301
b. Preliminary Results	309
c. Recent Experimental Results	311
5. Determination of Surface-state Density in Si/Al ₂ O ₃	322
a. Experimental Procedure	323
b. Results and Discussion	324
6. Measurement of High-field Transport Properties of Heteroepitaxial Films	329
SECTION 10. ANISOTROPY IN ELECTRICAL PROPERTIES OF Si FILMS ON Al ₂ O ₃	335
1. Anisotropy in (221)Si/(11 $\bar{2}$ 2)Al ₂ O ₃	338
2. Anisotropy in (001)Si/(01 $\bar{1}$ 2)Al ₂ O ₃	346
3. Anisotropy in (111)Si on Al ₂ O ₃	351
a. (111)Si/(11 $\bar{2}$ 0)Al ₂ O ₃	351
b. (111)Si/(10 $\bar{1}$ 4)Al ₂ O ₃	363
c. Summary	370
SECTION 11. MISCELLANEOUS STRUCTURAL EVALUATIONS OF HETEROEPITAXIAL SEMICONDUCTOR FILMS	372
1. Post-growth Electron Microscopy of Si Films on Al ₂ O ₃	374
2. Rutherford Backscattering and Channeling Analyses of Heteroepitaxial Semiconductor Films on Al ₂ O ₃	381
3. Measurement of Photoelectric Effects at the Si/Al ₂ O ₃ Interface	388
SECTION 12. DESIGN AND FABRICATION OF SPECIAL DEVICES	400
1. Charge-coupled Devices in Si/Al ₂ O ₃	400
2. Schottky-barrier Solar Cell in Si/Al ₂ O ₃	407
REFERENCES FOR PARTS I AND II	R-1

<u>PART III</u>	<u>Page</u>
APPENDIX 1. WORK FUNCTIONS AND SURFACE DOUBLE LAYER POTENTIALS OF MONOVALENT METALS FROM A NETWORK MODEL	A-1
APPENDIX 2. ANISOTROPY IN ELECTRICAL PROPERTIES OF $\{001\}$ Si $\{0112\}$ Al ₂ O ₃	B-1
APPENDIX 3. ANISOTROPY IN THE ELECTRICAL PROPERTIES OF N-TYPE (221)Si/(11 $\bar{2}$ 2)Al ₂ O ₃	C-1
APPENDIX 4. STRESS INDUCED ANISOTROPY IN THE ELECTRICAL PROPERTIES OF Si/Al ₂ O ₃	D-1
APPENDIX 5. BIBLIOGRAPHY - ELECTRON MICROSCOPE <u>IN SITU</u> NUCLEATION AND GROWTH STUDIES	E-1
APPENDIX 6. ELECTRON SCATTERING BY GASEOUS ATOMS	F-1
APPENDIX 7. PRELIMINARY EM6 MODIFICATIONS FOR <u>IN SITU</u> CHEMICAL VAPOR DEPOSITION	G-1

ILLUSTRATIONS

<u>Figure</u>	<u>Page</u>
PART I	
1. Theoretical Carrier Mobility Ratios μ_{\max}/μ_0 and μ_{\min}/μ_0 for N-type Si/Al ₂ O ₃ along (xxl)Si Zone.	45
2. Theoretical Carrier Mobility Ratios μ_{\max}^e/μ_0 and μ_{\min}^e/μ_0 for P-type Si/Al ₂ O ₃ along (xxl)Si Zone.	47
3. Schematic Diagram of Chemical Vapor Deposition Apparatus	54
4. Variation of Hall Mobility with Growth Temperature for Si/Al ₂ O ₃ Films Having Net Donor Carrier Concentration of $1-5 \times 10^{16} \text{ cm}^{-3}$.	58
5. Variation of Net Donor Carrier Concentration with Growth Temperature for Si/Al ₂ O ₃ Films Grown at $\sim 2 \mu\text{m}/\text{min}$ with Constant Dopant-gas Flow Rate.	58
6. Variation of Hall Mobility with Growth Rate for N-type Si/Al ₂ O ₃ Films Grown at 1075C.	60
7. Variation of Net Donor Carrier Concentration with Growth Rate for Si/Al ₂ O ₃ Films Grown at 1075C with Constant Dopant-gas Flow Rate.	60
8. Variation of Net Donor Carrier Concentration with AsH ₃ Flow Rate for Si/Al ₂ O ₃ Films.	61
9. Carrier Mobility as Function of Distance from Interface for CVD Si Films on Three Orientations of Al ₂ O ₃ .	63
10. Net Donor Carrier Concentration as Function of Distance from Interface for CVD Si Films on Three Orientations of Al ₂ O ₃	63
11. Variation of Film Properties with Film Thickness for Thin N-type Si/Al ₂ O ₃ Films.	65
12. Variation of Hall Mobility with Film Thickness for Intentionally Undoped P-type Si/Al ₂ O ₃ Films.	66
13. Variation of Net Acceptor Concentration with Film Thickness for Intentionally Undoped Si/Al ₂ O ₃ Films.	66
14. Hall Mobility as Function of Film Thickness for N-type (111)Si/(111)MgAl ₂ O ₄ . (Sample initially $5.4 \mu\text{m}$ thick.)	69
15. Hall Mobility as Function of Film Thickness for N-type (111)Si/(111)MgAl ₂ O ₄ . (Sample initially $1.4 \mu\text{m}$ thick.)	69

<u>Figure</u>	<u>Page</u>
16. Calibration Curve for Growth of P-type Si/Al ₂ O ₃ Films Using B ₂ H ₆ Dopant Source	71
17. Electrical Properties of P-type Si/Al ₂ O ₃ Films Doped with Boron	71
18. Variation of Net Acceptor Carrier Concentration Due to Al Autodoping as Function of Growth Temperature for Intentionally Undoped Si/Al ₂ O ₃ Films	76
19. Evidence of Contamination of Si by Al ₂ O ₃ in H ₂ Atmosphere. a) Overall Appearance (3.7X). b) Etched Region (406X)	78
20. Subsurface Doping in Si Caused by Contamination from Al ₂ O ₃ . a) Region below and adjoining Al ₂ O ₃ Wafer (etched area on right.) b) Si Region below Al ₂ O ₃ after Annealing 1/2 hr in O ₂ and 2 hr in N ₂	80
21. Variation of Hall Mobility with Growth Temperature for N-type Si/Al ₂ O ₃ Films Grown in Horizontal Reactor	83
22. Net Carrier Concentration in Si Film on Al ₂ O ₃ as Function of Position on Susceptor in Vertical Reactor	86
23. Surfaces of Neighboring Pieces of (011̄2)Al ₂ O ₃ after 1 sec Si Nucleation on (a) H ₂ -etched Substrate; (b) and (c) Freon-etched Substrate.	88
24. Nature of Si Islands on (a), (b) H ₂ - and (c), (d) Freon-etched (011̄2)Al ₂ O ₃ after 1 sec Si Growth	89
25. Nature of Si Islands on (a) H ₂ -etched and (b) Freon-etched (011̄2)Al ₂ O ₃ after approximately 1/4 sec Si Growth	91
26. (a) Surface Structure and (b) RED Pattern for 9-sec Si Growth (~1200 Å) on Freon-etched (011̄2)Al ₂ O ₃	91
27. Changes in Si Growth Rate at 1025C Caused by H ₂ Additions to He Carrier Gas	98
28. Effect of Growth Temperature on Si Growth Rate for SiH ₄ Flow Rate of 150 ccpm and H ₂ /He = 0.8%	98
29. Variation in Hall Mobility with Growth Rate for (111)Si/(111)MgAl ₂ O ₄	100
30. Variation in Hall Mobility with (high) Growth Rate for (111)Si/(111)MgAl ₂ O ₄	100
31. Schematic of Gas Sample Handling System for GC	126

<u>Figure</u>	<u>Page</u>
32. SiH ₄ Chromatogram on DC-200 Silicone Column Packing	126
33. Chromatogram for SiH ₄ and other Compounds on Chromosorb 102 Column at Ambient Temperature	129
34. Chromatogram of Mixture of SiH ₄ and B ₂ H ₆ on Chromosorb 102 Column at 60C.	129
35. Photomicrographs of Same Region of Surface of (10 $\bar{1}$ 4)Al ₂ O ₃ Substrate at Various Stages of Polishing; (a) as Received from Vendor; (b) after ~2 min Polishing with Cab-O-Sil (0.05 μ m SiO ₂) on Nylon Cloth; (c) after Additional 5 min Polishing	156
36. Scanning Electron Micrographs of Surface of (10 $\bar{1}$ 4)Al ₂ O ₃ Substrate, Showing Detail of Polishing Scratch (Arrows) ² at a) 200X, b) 10,000X, c) 20,000X	158
37. Typical Surface Finish Obtained on (10 $\bar{1}$ 4)Al ₂ O ₃ Substrate with Special Cast Iron Laps with Slurry of 1 μ m Synthetic Diamond on Optical Polisher	161
38. a) Surface Finish on (10 $\bar{1}$ 4)Al ₂ O ₃ Substrate after Using Special Brass Lap with Slurry of 0.5 μ m Synthetic Diamond on Optical Polisher. b) Same Area after 66 hr Polishing on Vibratory Polisher Using 0.25 μ m Synthetic Diamond on Nylon Cloth	162
39. (111) Czochralski MgAl ₂ O ₄ (a) before Etching; (b) after Etching in Hot HF for 30 min	165
40. Photomicrograph of Surface of (01 $\bar{1}$ 2)Al ₂ O ₃ Substrate a) as Received from Vendor; b) after Gas-phase Etching in Freon at 1450C for 5 min (~3 μ m of material removed); c) after 15 min (total) Etching (~8 μ m of material removed)	167
41. Rate of Etching of Al ₂ O ₃ by Freon at 1400C	169
42. Rate of Etching of Al ₂ O ₃ by Freon at 1450C	169
43. Rate of Etching of Al ₂ O ₃ by Freon at 1500C	169
44. (01 $\bar{1}$ 2)Al ₂ O ₃ Surface after Etch-polishing with Freon at Flow Rate of 13 ml/min at Three Temperatures.	170
45. Effect of Progressive Etching of (01 $\bar{1}$ 2)Al ₂ O ₃ at 1500C with Freon Flow Rate of 13 ml/min. Surface (a) as Received, (b) after 5 μ m of Surface Removed, (c) after 9 μ m of Surface Removed.	172

<u>Figure</u>	<u>Page</u>
46. (10 $\bar{1}$ 4)Al ₂ O ₃ Surface after Etch-polish with Freon at Flow Rate of 13 ml/min at Various Temperatures	173
47. (10 $\bar{1}$ 4)Al ₂ O ₃ Surface after Etch-polishing with Freon at Flow Rate of 60ml /min at (2) 1450C and (b) 1500C.	174
48. Surface of Czochralski-grown (01 $\bar{1}$ 2)Al ₂ O ₃ after Etching at 1500C with Freon at Flow Rate of 13 cc/pm for (a) 25 min, (b) 50 min, (c) 75 min, and (d) 100 min.	176
49. Surfaces of Different Substrates of Verneuil-grown (11 $\bar{2}$ 0)Al ₂ O ₃ after Etching at 1500C with Freon at Flow Rate of 13 cc/pm for (a) 25 min, (b) 50 min, (c) 75 min, (d) 100 min	177
50. Surface of (0001)Al ₂ O ₃ after Etching at 1500C with Freon at Flow Rate of 13 cc/pm for (a) 25 min, (b) 50 min, (c) 75 min and (d) 100 min	178
51. Surface of (10 $\bar{1}$ 4)Al ₂ O ₃ (a) after Mechanical Polishing; (b) after 10-min Etch with Freon at 1400C; (c) after 30-min Etch with Freon at 1400C	180
52. (10 $\bar{1}$ 4)Al ₂ O ₃ Wafer Ion-beam Etched at Low Angle to Remove (a) <0.1 μ m, (b) 9.6 μ m	184
53. Variation in Al ₂ O ₃ Etching Rate with Depth into Wafer for As-sawed Surfaces of Several Orientations	187
54. Variation in Al ₂ O ₃ Etching Rate with Depth into Wafer for Surfaces of Several Orientations Lapped with 40 μ m Boron Carbide	187
55. Variation in Al ₂ O ₃ Etching Rate with Depth into Wafer for Surfaces of Several Orientations Lapped with 12 μ m Silicon Carbide	189
56. Variation in Al ₂ O ₃ Etching Rate with Depth into Wafer for Surfaces of Several Orientations Polished with 0.25 μ m "Top" Diamond	189
57. Surface Structure of (10 $\bar{1}$ 4)Al ₂ O ₃ after Removal of ~7 μ m of Al ₂ O ₃ by Freon Etch at 1550C	194
58. Surface of Verneuil-grown (10 $\bar{1}$ 4)Al ₂ O ₃ after Etching with Freon at 1500C for ~3 hr at Nominal Rate of 0.6 μ m/min	195
59. Configuration of IBMA Working Chamber	195

<u>Figure</u>	<u>Page</u>
60. Optical Micrograph of Ion-thinned (0001)Al ₂ O ₃ Substrate (a) 25X, (b) 450X	199
61. Ion-thinned Al ₂ O ₃ (0.030 in dia) prior to Perforation	200
62. Optical Photomicrograph of Thinned (10 $\bar{1}$ 4)Al ₂ O ₃ Substrate	204
63. Electron Diffraction (a) Spot and (b) Kikuchi Pattern from (0001)Al ₂ O ₃ Substrate	209
64. Electron Diffraction Spot and Kikuchi Pattern from (10 $\bar{1}$ 4)Al ₂ O ₃ Substrate	210
65. Electron Diffraction (a) Spot and (b) Kikuchi Pattern from (01 $\bar{1}$ 2)Al ₂ O ₃ Substrate	210
66. Electron Micrograph of (0001)Al ₂ O ₃ Substrate	212
67. Electron Micrograph of (0001)Al ₂ O ₃ Substrate	212
68. Electron Micrograph of (10 $\bar{1}$ 4)Al ₂ O ₃ Substrate	213
69. Electron Micrograph of (10 $\bar{1}$ 4)Al ₂ O ₃ Substrate	214
70. Electron Micrograph of (10 $\bar{1}$ 4)Al ₂ O ₃ Substrate	214
71. Electron Micrograph of (01 $\bar{1}$ 2)Al ₂ O ₃ Substrate	215
72. Electron Micrograph of (01 $\bar{1}$ 2)Al ₂ O ₃ Substrate	215
73. Schematic of Experimental Arrangement for Measuring Properties of Photoinjected Carriers in Al ₂ O ₃	221
74. Schematic Diagram of Experimental Setup for Calibrating Light Source	221
75. Quantum Efficiency as Function of Photon Energy for Various Bias Voltages for Carrier Photoinjection into Al ₂ O ₃ from Al Film 400Å Thick	228
76. Quantum Efficiency of Carrier Photoinjection into Al ₂ O ₃ from 400Å Al Film as Function of Bias Voltage, for Various Photon Energies	228
77. Quantum Efficiency of Carrier Photoinjection into Al ₂ O ₃ as Function of Al Electrode Thickness for 4.8 eV Photon, for Various Bias Voltages	229

<u>Figure</u>	<u>Page</u>
78. Quantum Efficiency of Carrier Photoinjection into Al_2O_3 as Function of Al Electrode Thickness for 5.2 eV Photon, for Various Bias Voltages	229
79. Quantum Efficiency of Carrier Photoinjection into Al_2O_3 as Function of Al Electrode Thickness for 5.5 eV Photon, for Various Bias Voltages	231
80. Calibrated Photocurrent in Al_2O_3 as Function of Al Electrode Thickness for 5.2 eV Photon Energy, at Several Bias Voltages	231
81. Photoinjected Current in Al_2O_3 as Function of Bias Voltage at Various Temperatures, for 5.0 eV Photon Energy	232
82. Plot of $\log(I/T^2)$ as Function of $1/T$ to Test Equation (57), for Various Bias Voltages	234
PART II	
83. Electron Microscope and Gas Handling Manifold for <u>In Situ</u> CVD Experiments	239
84. Sequence of Electron Micrographs Recorded during Al PVD at Times of (a) 0 sec, (b) 110 sec, (c) 130 sec, (d) 150 sec, (e) 190 sec, (f) 10 min	244
85. Au Film Grown in Electron Microscope by PVD. (a) Region Observed during Growth; (b) Adjoining Region not Irradiated by Electron Beam; (c) Lower Magnification View of Regions (a) and (b)	246
86. <u>In Situ</u> Nucleation and Growth of Cr on $(01\bar{1}2)Al_2O_3$ after (a) 0 min, (b) 8 min, (c) 14 min, (d) 16 min, (e) 18 min	248
87. <u>In Situ</u> Chemical Vapor Deposition Microchamber.	254
88. CVD Microchamber, Disassembled	255
89. CVD Flange for Electron Microscope, with Assembled Microchamber Mounted in Place	255
90. Schematic Diagram of Gas-handling Manifold for <u>In Situ</u> Studies	258
91. Measured Pressure in Electron Microscope as Function of Microchamber Pressure	258
92. Measured Gas Flow through Microchamber as Function of Pressure	260

<u>Figure</u>	<u>Page</u>
93. Electron Micrographs Showing Image Quality in CVD Microchamber at (a) 1×10^{-4} torr (normal microscope vacuum) and (b) 3.5 torr (50% SiH_4 and 50% H_2).	261
94. <u>In Situ</u> Nucleation on Amorphous Carbon Substrate at (a) zero time, (b) 4 min, (c) 10 min, (d) 37 min, (e) 44 min, (f) 45 min	264
95. <u>In Situ</u> Growth of Si on Amorphous Carbon Substrate	266
96. CVD Microchamber Heating Grid (a) before and (b) after Loading Al_2O_3 Substrate	269
97. <u>In Situ</u> Nucleation of Si on Al_2O_3 (Sample #19)	272
98. <u>In Situ</u> Nucleation of Si on Al_2O_3 (Sample #16)	274
99. Nucleation of Si on Al_2O_3 after <u>In Situ</u> Growth (a) Micrograph, (b) Diffraction Pattern (Sample #22)	275
100. Diffraction Pattern of Si Film on $(01\bar{1}2)\text{Al}_2\text{O}_3$ Substrate, Showing Strong (111) Spots on Polycrystalline Rings	276
101. Contamination Observed during <u>In Situ</u> Experiment with Sample #18	276
102. Reaction of Ti Heating Grid with Al_2O_3	277
103. Reaction of Si with Al_2O_3 during <u>In Situ</u> Growth	277
104. Normalized Carrier Concentration as Function of Distance from Center of Susceptor for Pairs of Si/ Al_2O_3 Samples Grown Simultaneously	289
105. Electron Mobility as Function of Temperature for Two Samples of Arsenic-doped N-type Si/ Al_2O_3 Grown under Identical Conditions	295
106. Net Carrier Concentration as Function of Temperature for 3.9 μm -thick Si/ Al_2O_3 Film and for Bulk Single-crystal Si	295
107. MOS Geometry for Carrier Lifetime Measurements	302
108. Characteristics of MOS Capacitor in Si/ Al_2O_3 . (a) Gate Voltage Pulse $V_G(t)$; (b) Resulting MOS Capacitance Transient Response; (c) Zerbst Plot for Capacitor	302
109. $\frac{N_S}{N_B}$ vs x_1 (in μm) for Phosphorus- and Boron-doped Si under Various Oxidation Conditions	306

<u>Figure</u>	<u>Page</u>
110. Impurity Redistribution Function $B(C)$ vs Normalized MOS Capacitance C/C_0 for Phosphorus- and Boron-doped Si under Various Oxidation Conditions	306
111. Schematic Diagram of Apparatus for Measuring Carrier Lifetime by Pulsed C-V Technique in MOS Structures. a) Full Apparatus; b) Flip-flop Circuit; c) Typical $C(t)$ Response	312
112. Mask Set Used for Fabricating MOS Capacitor for Carrier Lifetime Measurements	314
113. Carrier Lifetime in N-type Si/ Al_2O_3 as Function of Film Thickness for As-doped and P-doped Films	316
114. Carrier Lifetime in N-type As-doped Si/ Al_2O_3 as Function of Doping Concentration	316
115. Carrier Lifetime in N-type As-doped Si Film on N^+ Layer on Al_2O_3 Substrate, as Function of Total Si Thickness	318
116. Carrier Lifetime in N-type (100)Si/(01 $\bar{1}$ 2) Al_2O_3 as Function of Temperature	321
117. Surface Recombination Velocities as Function of Temperature for Si/ Al_2O_3 Samples of Figure 116	322
118. C-V Characteristics for N-type (100)Si/(01 $\bar{1}$ 2) Al_2O_3 at Various Frequencies	325
119. Surface Potentials for Si/ Al_2O_3 as Function of Applied Voltage, Obtained from Low-frequency C-V Data	325
120. Density Distribution of Donor- and Acceptor-type Surface States in Si Film on Al_2O_3 Substrate; Distribution of States with Time Constant <6 msec Included	327
121. C-V Characteristics at Two Frequencies for N-type Si/ Al_2O_3 Sample Obtained from Commercial Supplier	328
122. Experimental Arrangement for Film Mobility Measurements at High Fields	330
123. Current Density as Function of Electric Field for N-type Si/ Al_2O_3 Film	330
124. Current Density as Function of Electric Field for P-type Si/ Al_2O_3 Film	331

<u>Figure</u>	<u>Page</u>
125. High-field i - \mathcal{E} Characteristic of N-type (111)GaAs/(0001)Al ₂ O ₃	333
126. High-field i - \mathcal{E} Characteristic of N-type (100)Si/(01 $\bar{1}$ 2)Al ₂ O ₃	333
127. High-field i - \mathcal{E} Characteristic of Si/Al ₂ O ₃ Sample of Figure 126 at Several Temperatures	334
128. Double Hall-bridge Pattern for Measuring Anisotropic Electrical Parameters	339
129. Variation in Hall Mobility as Function of Direction in (221)Si/(11 $\bar{2}$ 2)Al ₂ O ₃	340
130. Transverse Electric Field Associated with Piezoresistance Effect and Thermally Induced Stress in (221)Si/(11 $\bar{2}$ 2)Al ₂ O ₃	343
131. Anisotropy and Transverse-effect Coefficient for Various Film Thicknesses for (221)Si/(11 $\bar{2}$ 2)Al ₂ O ₃ Samples	345
132. Variation of Hall Mobility with Direction in (001)Si/(01 $\bar{1}$ 2)Al ₂ O ₃	347
133. Variation in Hall Mobility with Direction at 77K in (001)Si/(01 $\bar{1}$ 2)Al ₂ O ₃	350
134. Transverse Electric Field Associated with Thermally Induced Stress and Piezoresistance Effect in (001)Si/(01 $\bar{1}$ 2)Al ₂ O ₃	350
135. Plot of Anisotropy Factor A vs μ_{\min} for 13 N-type (111)Si/(10 $\bar{1}$ 4)Al ₂ O ₃ Films	366
136. Electron Micrograph of Si Grown on (01 $\bar{1}$ 2)Al ₂ O ₃ at 1030C for 1 sec; (a) Bright Field, (b) Dark Field, (c) Diffraction Pattern	376
137. Electron Micrograph of Si Grown on (01 $\bar{1}$ 2)Al ₂ O ₃ at 1030C for 3 sec; (a) Bright Field, (b) Diffraction Pattern	377
138. Electron Micrograph of Si Grown on (01 $\bar{1}$ 2)Al ₂ O ₃ at 1200C for 3 sec; (a) Bright Field, (b) Diffraction Pattern	380
139. Backscattered Proton Energy Spectra for Randomly Oriented and Aligned (111) Single-crystal GaAs	383
140. Backscattered Proton Energy Spectra for Heteroepitaxial (111)Si Film on (10 $\bar{1}$ 4)Al ₂ O ₃ for both Randomly Oriented and [111] Injections	385
141. Calculated Disorder Density as Function of Depth below Surface of (111)Si Film on (10 $\bar{1}$ 4)Al ₂ O ₃ Substrate	385

<u>Figure</u>	<u>Page</u>
142. Calculated Disorder Density as Function of Depth below Surface of (111)Si Film on $\sim(11\bar{2}0)\text{Al}_2\text{O}_3$ Substrate	386
143. Calculated Disorder Density as Function of Depth below Surface of Sample of Figure 142, but in Twinned Region of Film	386
144. Calculated Disorder Density as Function of Depth below Surface of (100)Si Film on $(01\bar{1}2)\text{Al}_2\text{O}_3$ Substrate	387
145. Calculated Disorder Density as Function of Depth below Surface of (111)GaAs Film on $(0001)\text{Al}_2\text{O}_3$ Substrate.	387
146. Schematic of Experimental Arrangement for Photoelectric Current Measurement in MIS Structures	389
147. Configuration of Semitransparent Al Stripes Deposited on Al_2O_3 Substrates	392
148. Photocurrent as Function of Position of Scanning Light Beam, with Al Biased Negative	394
149. Photocurrent as Function of Position of Light Beam, with Al Biased Positive	394
150. Fowler Plot of Room-temperature Photocurrent as Function of Photon Energy for Al- Al_2O_3 Interface	396
151. Energy-band Diagram for Al- Al_2O_3 Interface	397
152. Plot of Cube Root of Room-temperature Photoelectric Current Due to Emission of Electrons from Si and from GaAs into Al_2O_3 , as Function of Photon Energy.	399
153. Exploratory C-V Measurements on Si/ Al_2O_3 Sample to Determine Charge-up Times	402
154. Schematic Diagram of CCD Structure in Si/ Al_2O_3	404
155. Typical Processed 2-bit CCD Structure in Si/ Al_2O_3	405
156. Characteristics of CCD in Si/ Al_2O_3 at 5 KHz and 2 MHz. Top Trace: CCD Output. Middle Trace: Input Diode Voltage. Bottom Trace: 0 Deg Phase Gate Voltage	406
157. Characteristics of CCD in Si/ Al_2O_3 at Several Operating Frequencies. Top Trace: CCD Output. Middle Trace: CCD Input Pulse. Bottom Trace: 0 Deg Phase Gate Voltage	408

<u>Figure</u>		<u>Page</u>
158.	Characteristics of CCD in Si/Al ₂ O ₃ at Higher Operating Frequencies. Top Trace: CCD Output. Middle Output: CCD Input Pulse. Bottom Trace: 0 Deg Phase Gate Voltage	409
159.	Diagram of Schottky-barrier Photovoltaic Cell Structure in Si/Al ₂ O ₃	411
160.	Dark-current Characteristics of Schottky-barrier Diode in Si/Al ₂ O ₃	411

TABLES

<u>Table</u> <u>PART I</u>	<u>Page</u>
1. Interatomic Distances for Al_2O_3 Lattice (\AA)	33
2. Hexagonal Half-cell Data for Al_2O_3	37
3. Properties of $2\mu\text{m}$ -thick P-type (100)Si Films on $(01\bar{1}2)\text{Al}_2\text{O}_3$	72
4. Properties of $2\mu\text{m}$ -thick P-type (111)Si Films on $\sim(11\bar{2}0)$ and $(10\bar{1}4)\text{Al}_2\text{O}_3$ at 1075C	73
5. Autodoping in Si/(111)Mg Al_2O_4 Using 0.8 Percent H_2 -in-He as Carrier Gas	77
6. Properties of Si Films Grown in Jacketed Reactor	84
7. Properties of Si Films Grown on Al_2O_3 by Pyrolysis of SiH_4 at Low Pressures	93
8. Properties of Si Films Grown on Al_2O_3 by Pyrolysis of SiH_4 at Medium Pressures	94
9. Effect of Growth Rate on Doping Level for Si Films Grown on (111)Spinel at 1025C in He- H_2 Atmospheres (constant dopant gas flow rate)	99
10. Comparison of Properties of Si/ Al_2O_3 and Si/Mg Al_2O_4 Grown at Two Different Temperatures	103
11. Effect of Growth Atmosphere on the Properties of $2\mu\text{m}$ -thick Si Films on Al_2O_3	104
12. Electrical Properties of Si Films Annealed in H_2 for 20 min after Growth of $\sim 1000\text{\AA}$ Thickness on Al_2O_3 Substrates (growth rate $\sim 2\mu\text{m}/\text{min}$)	108
13. Electrical Properties of Si Films Annealed in H_2 for 20 min after Growth of $\sim 2000\text{\AA}$ Thickness on Al_2O_3 Substrates (growth rate $\sim 4\mu\text{m}/\text{min}$)	109
14. Effects of Extended O_2 and N_2 Anneals on Electrical Properties of Three As-Doped, $\sim 2\mu\text{m}$ -thick Si/ Al_2O_3 Films (growth temperature 1100C)	110
15. Effects on Film Properties of Order of Sequential Annealing Steps in O_2 and N_2 for $\sim 2\mu\text{m}$ -thick As-doped Si Films Grown at Various Temperatures on $\sim(11\bar{2}0)\text{Al}_2\text{O}_3$ at Rate of $\sim 2\mu\text{m}/\text{min}$	111

<u>Table</u>	<u>Page</u>
16. Properties of Si Films Grown at 1100C at a Nominal Growth Rate of 2 μ m/min (annealed and unannealed samples)	114
17. Evaluation of Source Materials by GaAs Growth on (0001)Al ₂ O ₃	116
18. Retention Index and Concentration of Impurities in SiH ₄ Samples	128
19. Comparison of Retention Data and Boiling Points of Solutes Eluted According to Figure 33	131
20. Mass Spectrometric Data for CH ₄	131
21. Mass Spectrometric Analyses of SiH ₄	134
22. Mass Spectrometer Analyses of SiH ₄	137
23. Mass Spectrometric Analyses of AsH ₃ in Carrier Gas from Three Vendors	139
24. SiH ₄ Pyrolysis Experiments	144
25. Decompositions of 10 cc of SiH ₄ over Al ₂ O ₃	145
26. Reactions of TMG with AsH ₃	149
27. Effect of Gas-phase Etching of (01 $\bar{1}$ 2)Al ₂ O ₃ on Si Film Properties	182
28. Depth of Surface Damage in Al ₂ O ₃ Wafers by Etch-rate Method	190
29. Size of Completely Unshadowed Area for Various Beam Incidence Angles in IBMA	207
30. Values of β_p for Al ₂ O ₃ at Several Temperatures	233

Part II

31. Maximum Permissible Pressure-time (Pt) Product for SiH ₄ and O ₂ for Various Electron Beam Intensity Losses	252
32. Electrical Characteristics of Two As-doped Si/(01 $\bar{1}$ 2)Al ₂ O ₃ Films Used for Low-Temperature Measurements	293

<u>Table</u>	<u>Page</u>
33. Mobility Anisotropy Parameters for (111)Si/(111)MgAl ₂ O ₄ at Room Temperature	299
34. Thermal Generation Carrier Lifetimes τ_g for Two Orientations of Si/Al ₂ O ₃	321
35. Anisotropy Parameters of Several (221)Si/(11 $\bar{2}$ 2)Al ₂ O ₃ Films	341
36. Anisotropy Data for (001)Si/(01 $\bar{1}$ 2)Al ₂ O ₃	348
37. Room Temperature Anisotropy Parameters for N-type (111)Si/(11 $\bar{2}$ 0)Al ₂ O ₃	352
38. Room Temperature Anisotropy Parameters for N-type (111)Si/(1014)Al ₂ O ₃	364
39. Anisotropy Parameters for N-type (111)Si/(1014)Al ₂ O ₃ at Liquid Nitrogen Temperature	369
40. Deposition Conditions for CVD Si Grown on Ion-thinned (01 $\bar{1}$ 2)Al ₂ O ₃	375
41. Relationship between Relative Polarity of Bias Voltage and Illuminated Metal Layer	391
42. Properties of Si/Al ₂ O ₃ Composites Used for Fabrication of Charge-coupled Devices	401
43. Photocurrent and Quantum Efficiency as Function of Reverse Bias Voltage in Schottky-barrier Photovoltaic Cell	412

SECTION 1

INTRODUCTION

This is the Final Technical Report for this contract. It describes work carried out during the period 25 June 1970 - 30 June 1973. Semiannual reports (Refs 1-5) have described work done in the first 30 months of the program; this report summarizes the work of the entire program.

1. CONTRACT OBJECTIVES

The overall objective of the program, as originally proposed, was to carry out a fundamental study of nucleation and film growth mechanisms in heteroepitaxial semiconductor thin films which would lead to new knowledge and understanding of these processes, and then to apply these results to the preparation of improved semiconductor thin films and thin-film devices on insulating substrates.

The specific technical objectives of the three-year program were the following:

1. Investigation of various aspects of the mechanisms of heteroepitaxial film growth, to establish technical guidelines for the preparation of better films which could be applied to real situations.
2. Preparation of improved, high-quality, device-grade heteroepitaxial films of Si and GaAs on insulating substrates by chemical vapor deposition (CVD) methods.
3. Development of methods of characterizing heteroepitaxial films as to their suitability for subsequent device fabrication.
4. Design and fabrication of selected thin-film devices which take advantage of the unique properties of such films.

The general plan for accomplishing these objectives involved as the primary effort a study of the fundamentals of heteroepitaxial semiconductor film growth on insulating substrates. Specialized device fabrication was used both as a means of evaluating certain properties of the films (and thus as a measure of film quality as the program progressed) and as a means of exploiting certain unique properties of heteroepitaxial semiconductor-insulator systems.

The identification of the mechanisms, properties, and processes to be investigated was based on previous knowledge of epitaxy and its problems and on experience with thin-film device difficulties encountered over a period of several years. The problems studied were not restricted to those identified a priori; experimental (and theoretical) attention was shifted as needed as the program progressed, to help achieve the goal of a better understanding of heteroepitaxial processes and the corollary improvements in thin-film active semiconductor devices.

2. PROGRAM SCOPE

The program involved both theoretical and experimental investigations of nucleation and growth mechanisms of heteroepitaxial films in semiconductor-insulator systems, the development of improved techniques for preparation of heteroepitaxial semiconductor films, and the fabrication of some devices utilizing these films.

The theoretical studies consisted of two types. First, there was direct interaction with the experimental program involving data analyses, suggestion of definitive experiments, and postulation of specific models to explain experimental observations. Second, there was development of original contributions to the theory of heteroepitaxial growth. The experimental investigations were also of two types. Fundamental explorations were carried out to delineate mechanisms and general empirical principles of the heteroepitaxial growth process. Also, practical studies accompanied the fundamental investigations so that new developments could be applied to the improvement of

semiconductor films and thin-film devices.

The work emphasized the CVD method of growing semiconductor thin films because of its importance in the semiconductor industry. This emphasis on the fundamental mechanisms of CVD growth distinguished this program from most previous fundamental studies of epitaxy, which concentrated upon physical vapor deposition (PVD) methods.

The program emphasis was on films of Si and GaAs and substrates of sapphire (Al_2O_3) and spinel (MgAl_2O_4). The main emphasis was on the Si-on- Al_2O_3 system, with increasing attention being given to the Si-on- MgAl_2O_4 and GaAs-on- Al_2O_3 systems as the program progressed. Si and GaAs were chosen because of the preeminence of the former in the semiconductor industry and the high-frequency and high-temperature attributes of the latter; in addition, they represent the elemental and compound semiconductors for which most comparative information has existed.

The program was carried out primarily at facilities of the Electronics Group of the Rockwell International Corporation by Rockwell personnel. Parts of three of the specific subtasks were performed by personnel of the University of California at Los Angeles (UCLA), in the Department of Electrical Sciences and Engineering and the Chemistry Department. Work on another of the subtasks was done in part in the Department of Chemistry of California State University, San Diego (CSUSD). Both the UCLA and the CSUSD programs were supported by subcontracts from Rockwell.

3. PROGRAM DESCRIPTION BY SUBTASK

The three-year program was originally divided into nine subtasks - two theoretical and seven experimental (Refs 1, 2). However, at the start of the second year it was decided, on the basis of the way in which the work of the first year had developed, that the contract work would be more accurately described in terms of seven main subtasks. The seven subtasks, which were modified as needed as the program progressed, were as follows:

Subtask 1: Theory of Epitaxy and Heteroepitaxial Interfaces. Theoretical examination of CVD kinetics and the processes of nucleation, surface migration, and film growth with emphasis on crystallographic relationships between overgrowth and substrate to attempt to identify mechanisms and establish general principles of heteroepitaxial growth; theoretical modeling of the heteroepitaxial interface using appropriate potentials to determine surface configurations and interfacial binding energies in real and/or simplified systems.

Subtask 2: Deposition Studies and Film Preparation: Investigation of the effects of various experimental parameters upon the properties of deposited semiconductor films; preparation of films for use in other parts of the program.

Subtask 3: Analysis and Purification of CVD Reactants. Analysis of the impurity content of reactant materials used in metalorganic-hydride and other CVD processes; preparation of research-sample quantities of improved-purity reactants for use in film growth experiments; investigation of the chemistry and reaction kinetics of CVD processes to improve the detailed understanding and control of the chemical reactions involved in the preparation of heteroepitaxial semiconductor films by CVD.

Subtask 4: Preparation and Characterization of Substrates. Preparation of substrate wafers and characterization of surfaces and impurity content of substrates used for semiconductor heteroepitaxy; development of reproducible new and/or improved substrate polishing, cleaning, and handling methods.

Subtask 5: Studies of *in situ* Film Growth in the Electron Microscope. *In situ* observation and study of the early stages of growth of CVD films in the electron microscope, to develop additional fundamental knowledge of the epitaxy process; results of experimental observations to be incorporated into theoretical studies wherever possible.

Subtask 6: Evaluation of Film Properties. Measurement of the electrical, optical, crystallographic, and thermal properties of heteroepitaxial semiconductor films on insulators, by a variety of measurement techniques; standard techniques employed and new methods developed where required for measurement of film properties which best characterize ultimate device performance.

Subtask 7: Design and Fabrication of Devices. Design and experimental fabrication of certain types of devices, using heteroepitaxial films produced in the above studies; some devices used to evaluate material properties and others to exploit semiconductor film characteristics unique to heteroepitaxial systems.

The principal results and activities of this three-year program are described herein. The report has been organized along subject-matter, rather than subtask, lines to provide a more logical presentation. The reader is referred to the Program Summary for a brief overview of the entire contract program, but specific details can be found by reference to the Table of Contents.

results of direct experimental significance in the Si/Al₂O₃ system.

Adoption of the above criteria for relevance of theory to Si/Al₂O₃ epitaxy is in no way indicative of any attempt to demean the model calculations which have appeared in the literature in recent years. These calculations may someday form the "building blocks" of a unified theory of epitaxy and then be highly significant. However, the theoretical goals adopted here are more specific and--to the extent possible--focus on the basic phenomena important to film quality and on physical parameters, such as carrier mobility, which are directly relevant in device applications of Si/Al₂O₃ films.

The basic theoretical studies consisted of several short-to-medium term investigations which were eventually terminated in favor of a long-term theoretical investigation of Si charge carrier mobility and mobility anisotropy in terms of thermal stress effects arising at the heteroepitaxial interface and caused by the differential thermal contraction of film and substrate. The latter study originated as an on-line response to the experimental discovery (in this program) of an anisotropy of carrier mobility in heteroepitaxial Si films. The results appear to have major practical significance in determining useful film/substrate orientations to investigate experimentally and in improving device performance in some applications. This work has emerged as the most significant theoretical contribution to epitaxy developed on this contract.

During the first year of the contract a formal theoretical method of replacing overgrowth atoms on a substrate with Gaussian mass distributions was further developed for those cases where the effective interatomic potential is known. The technique, applicable to irregular-shaped islands or films of finite extent, was applied to a simplified model to determine preferred orientation relationships from calculated film-substrate interaction energies. The method was not pursued further, however, because it was not sufficiently adaptable to real systems. Several other possible approaches to the theoretical modeling of heteroepitaxial systems were critically reviewed, including the Frank-Van der Merwe model, a Green's-function/Wannier-function approach,

a contrived potential-energy model, and the two-body interatomic potential method. It was concluded at the time that most existing theories are inadequate for application to real systems.

The feasibility of a molecular orbital development of the heteroepitaxial interface was then investigated. However, early in the second year it was determined infeasible to apply this technique in a manner directly relevant to heteroepitaxy, so this effort was terminated. The interatomic potential approach to heteroepitaxy was then reinstigated, with the goal being the computer simulation of growth of Si on Al_2O_3 . Mechanical stability conditions for an Al_2O_3 lattice modeled with two-body potentials were investigated and determined to the depth required for these applications. Computer programming of the Al_2O_3 lattice energy and elastic constants was carried out for use in determining appropriate empirical potentials required for modeling this lattice.

The empirical interatomic potentials determined for the Al_2O_3 lattice were then employed in a theoretical treatment of the surface of the Al_2O_3 substrate in which the O and Al atomic planes are allowed to relax to new interplanar separations determined by minimizing the lattice energy. Following the successful completion of this phase of the study, the modeling of Si and Al_2O_3 lattices using interatomic potentials was terminated in favor of the theoretical investigation of carrier mobility in Si films mentioned above.

In addition, during the first half of the second year the application of the electron-on-network theory to the problem of determining surface configurations and interfacial binding energies in heteroepitaxial systems where the surface structure is allowed to relax was investigated, and initially it appeared promising for real systems. Normalized eigenvectors were developed as a basis for a secular equation the solution of which is fundamental to the solution of the total problem. The electron-on-network technique was then employed to calculate work functions and surface double-layer potentials of monovalent metals. Extension of the technique to materials such as Al_2O_3 was investigated, but it was concluded that such an extension to heteroepitaxial systems

was not feasible because of limitations in the method encountered in the preliminary studies.

The second type of theoretical study is represented by the analysis of the measured anisotropy of electrical properties in the Si/Al₂O₃ heteroepitaxial system. It has historically been tacitly assumed that for a given film/substrate orientation the electrical properties, such as the carrier mobility, are isotropic in the plane of the film and do not depend upon current direction or the orientation of devices fabricated in the film.

In the last half of the second contract year, extensive measurements of carrier mobility as a function of angular orientation within the plane of the film demonstrated that the mobility was in fact anisotropic for (001)Si and (221)Si film orientations. The measurements further suggested that some degree of anisotropy would probably occur for all Si/Al₂O₃ orientations and appeared to be a general feature of Si/Al₂O₃ epitaxy.

Initial theoretical attempts to explain the ~10% mobility anisotropy in (001)Si films and the ~40% mobility anisotropy in (221)Si films as a stress phenomenon acting through the piezoresistance effect and induced by the differential thermal expansion between the Si film and the Al₂O₃ substrate were successful. This result and its potential significance to the preparation of heteroepitaxial semiconductor films for device use argued that an extensive theoretical investigation should be carried out. This has been done and represents the major theoretical effort on this contract program.

The theoretical model that has been developed allows the effect of thermal stress on mobility to be calculated for arbitrary Si/Al₂O₃ orientations and for the four principal modes of epitaxy. Initially emphasis was placed on calculation of the amount of anisotropy in mobility for a given Si film growth and the directions within the Si plane that yield the maximum and minimum mobilities; this was done because the theoretical anisotropy and maximum mobility directions could be compared directly with experimental data for these quantities.

Since both theoretical and experimental considerations indicated that thermal stress effects on mobility are large for Si/Al₂O₃, it was felt that mobilities calculated on the basis of thermal stress for various film/substrate orientations might offer a means of determining new orientations of Si/Al₂O₃ worthy of experimental growth and characterization.

To pursue this possibility, calculations were performed for a general (xxl) zone of Si. Values of the Miller indices x ranging from zero to infinity were employed, and relative mobilities for Si film orientations along the crystallographic zone defined by (001), (111), (221) and (110)Si orientations were obtained. A substantial dependence of mobility upon the film orientation along this zone was found for both n- and p-type Si. In both cases, the mobility is a minimum for (001)Si and then increases significantly (by a factor of 1.6 to 2.4) proceeding along the zone.

This work is believed to represent the first means for theoretically predicting mobilities as a function of orientation in Si/Al₂O₃ films, and should be of practical significance in directing experimental attention to new orientations offering potentially higher carrier mobilities. The higher mobilities potentially achievable should be important in applications in which device speed or frequency of operation is dependent upon and limited by the carrier mobility.

A more detailed discussion of these theoretical studies is given in the following sections.

1. GAUSSIAN ATOM EXTENSION OF THE ISLAND ALIGNMENT MODEL*

Many epitaxial films are found experimentally to be formed by the nucleation, growth and coalescence of three-dimensional islands. One feature of films

*This work carried out by H. Reiss of the Chemistry Department at the University of California at Los Angeles.

which grow in this manner is that a substantial fraction of the islands are initially misaligned by rotation about the normal to the film plane. Experimentally, it is known that some misaligned nuclei are able to maintain their misalignment for long periods of time. Simple models dealing with this misalignment stability question are now well known in the literature. Most of the models are extensions of the well-known coincidence model for high-angle grain boundaries. The island model of Reiss (Ref 6) is somewhat different and predicts low-energy interfaces (e.g., stable orientational positions) in addition to those obtained in the earlier coincidence model calculations.

During the first year of the contract, a formal theoretical method of replacing overgrowth atoms on a substrate with Gaussian mass distributions for those cases where the effective interatomic potential is known was further developed, as a means of extending the Reiss model to irregular-shaped islands or films of finite extent. The basic physical assumptions of the Reiss model remained unchanged. The replacement of overgrowth atoms by Gaussian mass distributions is simply a calculational technique which makes it possible to work in Fourier transform space in which various irregular or non-simple island configurations can be handled analytically.

If an individual free overgrowth atom migrates on the exposed substrate surface, it will experience a potential (usually periodic, except for perturbations due to defects) which will be denoted by $U_p(\bar{r})$, where \bar{r} is the position vector on the substrate surface. For reasons of achieving convergence in an analytical representation of the interface potential for a film of such atoms, it is convenient to replace the usual "point" atom with a two-dimensional Gaussian distribution of mass which has the same total interaction with the substrate as does the real or "point" atom. The mass in such a "Gaussian" atom is distributed about a center located at $\bar{r} = \bar{r}_0$ as follows:

$$\rho_g(\bar{r}-\bar{r}_0) = \frac{1}{\pi n^2} e^{- (\bar{r}-\bar{r}_0)^2/n^2}, \quad (1)$$

where ρ_g is the mass density and n measures the "width" of the Gaussian atom.

Thus, the Gaussian atom becomes a point atom of unit mass when $n \rightarrow 0$.

An interaction potential ϕ per unit mass is chosen such that

$$U_g(\bar{r}) = \int \phi(\bar{r}_o) \rho_g(\bar{r}-\bar{r}_o) d\bar{r}_o, \quad (2)$$

where $U_g(\bar{r})$ is the total potential experienced by the Gaussian atom. For example, consider that $U_p(\bar{r})$ is given by

$$U_p(\bar{r}) = A \left(1 - \cos \frac{2\pi x}{b} \cos \frac{2\pi y}{b} \right), \quad (3)$$

in which A and b are constants and x and y are the components of \bar{r} , i.e., $\bar{r} = \bar{i}x + \bar{j}y$.

The potential corresponds to a substrate having a primitive square lattice of parameter $b/\sqrt{2}$ rotated at an angle of 45 degrees to the x -direction. Potential minima occur over substrate atoms. In terms of a nonprimitive unit cell, the lattice is a face-centered square lattice of parameter b parallel to the x -direction. Either of these descriptions is satisfactory. If $\phi(\bar{r}_o)$ is chosen as

$$\phi(\bar{r}_o) = \alpha - \beta \cos \frac{2\pi x_o}{b} \cos \frac{2\pi y_o}{b}, \quad (4)$$

then Equations (1) and (2) require that

$$U_g(\bar{r}) = \alpha - \beta e^{-\pi^2 n^2 / b^2} \cos \frac{2\pi x}{b} \cos \frac{2\pi y}{b}. \quad (5)$$

To ensure that the point atom potential $U_p(\bar{r})$ and the Gaussian atom potential $U_g(\bar{r})$ are equivalent it is necessary that

$$\alpha = A$$

and

$$\beta = A e^{\pi^2 n^2 / b^2}. \quad (6)$$

The potential of the entire film is next considered. In order to obtain an analytical expression for the film potential it is first necessary to find an expression for the distributed mass density in a periodic film constructed of Gaussian atoms. This density may be written as

$$\rho_f(\vec{r}) = \sum_i \rho_g^{(i)}(\vec{r} - \vec{r}_i), \quad (7)$$

where $\rho_g^{(i)}$ refers to the i^{th} Gaussian atom centered at \vec{r}_i in the film. Because of the periodic nature of the extended film it is possible to expand ρ_f in a Fourier series whose coefficients are indexed in the reciprocal lattice of the film.

First, however, an internal coordinate system rigidly fixed in the film must be introduced. The position vector in this system is $\vec{s} = \vec{i}'u + \vec{j}'v$, where \vec{i}' and \vec{j}' are unit vectors fixed in the film, and u and v are the corresponding components of \vec{s} . The transformation between \vec{s} and \vec{r} is

$$x = u \cos \theta - v \sin \theta,$$

and

$$y = u \sin \theta + v \cos \theta, \quad (8)$$

where θ is the angle of rotation of the film coordinate system with respect to that of the substrate.

It now follows that

$$\rho_f(\vec{s}) = \sum_{\vec{h}} \rho_{\vec{h}} e^{-i2\pi\vec{h}\cdot\vec{s}}, \quad (9)$$

where \vec{h} is a reciprocal vector and $\rho_{\vec{h}}$ are the Fourier coefficients. Since $\rho_f(\vec{s})$ can be expressed as

$$\rho_f(\vec{s}) = \sum_i \rho_g^{(i)}(\vec{s} - \vec{s}_i), \quad (10)$$

it follows that $\rho_{\bar{h}}$ can be calculated in a straightforward manner. For example, if the film consists of a simple square lattice of parameter a with a Gaussian atom centered at each node point, it can be shown that

$$\rho_f(\bar{s}) = \frac{1}{a^2} \left\{ 1 + \sum_{\ell=-\infty}^{\infty} ' e^{-\frac{\pi^2 n^2 \ell^2}{a^2}} \cos \frac{2\pi \ell u}{a} + \sum_{m=-\infty}^{\infty} ' e^{-\frac{\pi^2 n^2 m^2}{a^2}} \cos \frac{2\pi m v}{a} + \sum_{\ell=-\infty}^{\infty} ' \sum_{m=-\infty}^{\infty} ' e^{-\frac{\pi^2 n^2 (\ell^2 + m^2)}{a^2}} \cos \frac{2\pi \ell u}{a} \cos \frac{2\pi m v}{a} \right\}. \quad (11)$$

In this equation ℓ and m are integers, and the primes on the summation signs indicate that the terms $\ell = 0$ and $m = 0$ are omitted. As given above, $\rho_f(\bar{s})$ is strictly correct only for a film of infinite extent since it involves an expansion in terms of reciprocal lattice vectors. The application of Equation (11) to finite films will therefore be an approximation. First, the mass distributions of individual Gaussian atoms are required to be sensibly non-overlapping; therefore, the Gaussian width parameter n is chosen to be $\leq a/8$. Second, $\rho_f(\bar{s})$ is set equal to zero whenever the position vector \bar{s} lies outside of the finite film being treated. For example, for a square island of film having $(2p+1)$ atoms on a side and length $2L = a(2p+1)$, $\rho_f(\bar{s})$ is zero whenever

$$|u| \geq L + \frac{a}{2}$$

and

$$|v| \geq L + \frac{a}{2}. \quad (12)$$

When this is done, Equation (11) can be used to approximately describe finite films. Thus, for a finite film the density can be expressed as

$$\rho'_f(\bar{s}) = H(u,L)H(v,L)\rho_f(\bar{s}), \quad (13)$$

where the H functions are zero whenever the conditions of Equation (12) hold.

The various series in Equation (11) converge fairly rapidly for finite $n = a/8$; this indicates one reason for using Gaussian atoms. However, caution must be exercised and the convergence determined only after the convolution of ρ'_f with ϕ , since there are constructive interferences between the periodic density distribution and the periodic potential which persist to very high orders. The total finite film potential U_f may now be expressed solely in terms of the lattice parameter a and the angle of rotation θ by

$$U_f(a,\theta) = \int \phi(\bar{r})\rho'_f(\bar{s}) d\bar{s}. \quad (14)$$

Equation (8) must be used to express the position vector \bar{r} , in $\phi(\bar{r})$ above, in terms of \bar{s} before the integration in Equation (14) is performed.

It is assumed in all of the above that the central atom of the island lies directly over a substrate atom. Translational effects can, however, be treated by removing this limiting assumption.

For small islands, and even for some extended films, there is experimental evidence that pseudomorphic deformation rather than dislocation generation is the mechanism for minimizing the combined elastic and interface energies. When this is the case, the increased negative binding energy associated with the pseudomorphic deformation more than compensates for the positive elastic energy due to the deformation, and thus a lower total energy is obtained.

If the natural lattice parameter of the film is a_0 , the strain energy in the equilibrium configuration can be approximated by

$$V(a) = \Gamma(a-a_0)^2, \quad (15)$$

where Γ is a modulus depending on the elastic coefficients. The total energy will then be

$$E(a, \theta) = V(a) + U_f(a, \theta). \quad (16)$$

Experimentally observed crystallographic orientations of film and substrate will correspond to configurations of minimum total energy. Within the framework of the present model, these configurations can be determined by minimizing $E(a, \theta)$ in the above equation with respect to a and θ .

The validity of this model and the above analysis has been established for the limiting case of an extended film, where $L \rightarrow \infty$ and $E(a, \theta)/N$ is the energy per atom. For simplicity, it was further assumed that $\Gamma \rightarrow 0$, i.e., no elastic energy. Non-zero values of the binding energy per atom $U_f(a, \theta)/N$ are obtained only when the geometrical conditions of either Equation (17a) or Equation (17b) are satisfied:

$$\cos \theta = \sin \theta = \frac{1}{\sqrt{2}} \quad \text{and} \quad a = b/\sqrt{2}. \quad (17a)$$

$$\left(\frac{m+l}{2}\right) \frac{b}{a} = -\sin \theta \quad \text{and} \quad \left(\frac{m-l}{2}\right) \frac{b}{a} = \cos \theta. \quad (17b)$$

Equation (17a) represents the simplest case, that of autoepitaxy, while Equation (17b) identifies all of the crystallographic relationships involving commensurability between overgrowth and substrate for the more general case. Thus, physically correct results have been obtained from the Gaussian atom model for these cases.

For films of finite extent the appropriate expressions can be made to converge rapidly by choosing the Gaussian width parameter n as large as $a/8$. In this way, the finite film case becomes tractable; the accuracy of the method has been checked for the simple case of small angles of rotation θ . It thus

appeared that the Gaussian atom formalism in principle would make the treatment of finite extent islands and islands of irregular geometry feasible, provided some information about the effective atomic interaction potential is either known or can be parameterized simply.

The question of the atomic interaction potential most appropriate for application to the Si/Al₂O₃ system was then explored. The island alignment model is essentially a two-dimensional model, and in formally examining the effective interface potential for Si/Al₂O₃ problems associated with the non-two-dimensionality of the true interface potential were encountered. The difficulty is particularly severe for high-index surfaces of unconventional topography. The symmetry and periodicity of the effective interface potential for use in the island model could, in principle, be determined by and result from a superposition of Morse potentials for several atomic layers on either side of the Si/Al₂O₃ interface. Thus, the symmetry of the effective potential might bear little relationship to the distribution of atoms at the interface surface.

Such potentially complicated interface potentials could be constructed ad hoc by incorporating additional parameters and periodicities into the potential. Model calculations could then be performed. However, the connection to reality and the significance of the result for real systems would remain quite unclear. Because of these problems, further work with the technique was deemed inappropriate for the more practical goals of the contract, and the studies were terminated.

2. APPLICATION OF ELECTRON-ON-NETWORK TECHNIQUES TO HETEROEPITAXY*

A second investigation of existing theoretical approaches for possible application to heteroepitaxy centered upon the electron-on-network technique and represented an attempt to develop a parameterized theory for the electronic properties of crystal surface states and for the interface states associated with the binding of one crystal to another, as in heteroepitaxial systems.

The work was directed toward development of a relative theory. The latter term implies that the theory is quasi-empirical in the following sense. If the properties of some standard exposed surface on a crystal are measured, the theory should make it possible to predict the properties of any other surface (interface). In other words, a theory was sought which would allow the approximate calculation of surface properties on any surface and which contained, at the most, a few parameters which could be determined through the measurement of properties on a standard surface.

Such theories are well known in the quantum mechanics of molecules. An example is the Hückel theory (Ref 7), in which molecular wave functions (molecular orbitals) are approximated by linear combinations of atomic wave functions (orbitals), each centered at a known position of an atom in a molecule. In the Hückel theory, which has achieved considerable practical success in the treatment of conjugated aromatic molecules containing π electrons, there are two parameters which correspond to so-called overlap integrals. These are treated as empirical quantities which are determined, for example, by measuring the properties of one molecule. Thereafter, they are used to predict the properties of other molecules.

An alternative to the Hückel theory is the so-called "free-electron molecular orbital" (FEMO) theory. This method, which was pioneered by Kuhn, Rudenberg, and Scherr (Ref 8), assumes that the π electrons in a molecule are constrained to travel along the bonds (one-dimensional lines) connecting atoms. On these lines, however, the π electrons behave like free electrons in a box. The

*This work carried out by H. Reiss of the Chemistry Department, University of California at Los Angeles.

molecular problem is then reduced to a series of one-dimensional problems which, with proper consideration of boundary conditions and symmetry, allow the development of another parameterized theory (this time the only parameter is the bond length) which agrees very well with experiment. It appears that the FEMO method may also be used for metallic crystals like Na in which there is one valence electron per atom, sufficiently delocalized.

In these studies the theory was applied to crystals of finite dimensions so that the Bloch theorem does not apply. The theory, however, was modified so that the depth of the potential box within which the electrons move is not infinite, as in the π -electron case, but finite and determined by the cohesive energy of the crystal (which becomes another parameter). In this way, the natural development of localized surface states has already been observed, and simple application of point-group theory isolates those wave functions which transform under irreducible representations which correspond to various kinds of surface states, e.g., corners and edges.

Recently, Montroll and coworkers (Ref 9) extended the FEMO theory making it possible to locate potential wells at the site of every atom in the crystal (or in a molecule, for that matter). For infinite crystals in which translational symmetry exists the Bloch theorem is applicable, and Montroll and coworkers combined the Bloch theorem with the FEMO theory to develop analytical solutions for the electronic theory of metals. This becomes possible in view of the fact that again the entire problem reduces to a collection of one-dimensional problems. Montroll also treated defects and surface states in this manner by using a Green's-function technique (the Green's functions are involved in the solution of difference equations), which he developed in connection with certain lattice dynamics problems. The Montroll technique by itself is not immediately applicable to the problem of heteroepitaxial interfaces because it assigns to atoms on and near surfaces the same potential well as is assigned to bulk atoms.

The procedure for adapting the Montroll technique to cases where lattice parameters near the surface are allowed to vary was developed and applied to calculations for the metal Na;* the plan was to then apply the procedure to the Si/Al₂O₃ system.

Although the method is simple in principle, it became clear that significant difficulties would be encountered in applying it to heteroepitaxial systems. For example, in the Na case the evaluation of electron density using network wave functions was found extremely difficult in view of the transcendental distribution of parameters indexing the wave functions, although the computation was completed in spite of this. This cast considerable doubt on the feasibility of using the method for an accurate assessment of interfacial binding. However, the technique has been used for computing variations in work function and surface double-layer potentials for single-crystal monovalent metals, and this work has been described in the literature (Ref 10 and Appendix 1). The model uses an electronic wave function which is defined to be nonzero only along the lines connecting first nearest neighbors in the metallic lattice. The electrons are summed to move freely along the lines between nearest neighbors. No electron-electron or electron-nucleus force is included in the model calculations (except for forces arising from the Pauli exclusion principle).

The work function is defined as the amount of energy required to move an electron from a point slightly inside the crystal to a point slightly outside. The contribution of the electronic double layer is included in the calculation of the work function as well as the dependence of the double-layer potential on the surface geometry. Surface states, where the electron is localized in the neighborhood of the face of the crystal, are found to have energies sufficiently above the Fermi level to eliminate the possibility that they make any contribution to the double-layer potential for the case of the (100) crystal plane. Consequently, surface states were ignored in all the calculations.

* The calculations for Na were carried out at UCLA on a separately-funded study not related to this contract.

The surface double layer is assumed to be caused by the presence of a finite potential barrier at the surface of the crystal. Bulk electronic wave functions can penetrate this barrier and decay exponentially outside the crystal. The only parameters required by the model are the nearest-neighbor distance for the lattice and the height of the potential barrier at the surface. The former quantity is fixed by the lattice structure (body-centered cubic for the alkali metals) and by the density, while the latter quantity can be adjusted to give the best agreement between the model calculations and experiment.

For the alkali metals, Li through Na, the best value of the barrier height is about 50 percent of the sum of the ionization potential energy, the heat of vaporization, and the calculated Fermi level for the corresponding metal. In addition, the value of the double-layer potential found for Na agrees very well with a more sophisticated calculation in the literature and is reasonably close to the experimental measurement. Further details are given in Appendix 1.

Summarizing, the electron-on-network procedure was extended theoretically and shown to be useful in calculating certain surface properties of simple metals. Difficulties were encountered in attempting to extend the technique to more complicated systems, and no further applications were made to either Si surface states or to the interface states between Si and Al_2O_3 . In principle, the technique should be applicable to interface states but the interface would have to be drastically idealized mathematically. It was believed that the results obtained thereby would bear little relation to the role of the interface in heteroepitaxy for real systems such as Si/ Al_2O_3 , so the technique was not further pursued for that purpose.

3. OTHER THEORETICAL APPROACHES TO MODELING HETEROEPITAXIAL SYSTEMS

Several possible approaches to the theoretical modeling of heteroepitaxial systems have been investigated under this contract. The general criteria originally adopted for determining suitability of a given technique were that the theoretical treatment and associated calculations should 1) relate explicitly to heteroepitaxy; 2) be as nearly as possible a "first-principles" approach; 3) relate as closely as possible to an actual system such as Si/Al₂O₃; and 4) represent an original contribution to the theory of heteroepitaxy.

Meeting these criteria is difficult, if not almost impossible. Nonetheless, the criteria are important in providing a framework and goals for the theoretical studies. The theoretical goals of these studies have been specific, directed toward the real Si/Al₂O₃ system. While a number of idealized "model" epitaxy problems can indeed be formulated and solved, such efforts are relatively useless in that they do not relate to the real and complicated Si/Al₂O₃ system.

In establishing a reference point for the studies of heteroepitaxial semiconductor/insulator systems, evaluation of the understanding of heteroepitaxy as supplied by earlier theoretical studies developed some important conclusions regarding those investigations.

It is well known that the results obtained experimentally in any heteroepitaxial system are dependent upon a variety of experimental conditions, including source material impurities, substrate preparation methods and surface perfection (including both intrinsic defects and extrinsic defects such as surface impurity atom complexes), and substrate crystallographic orientation* (Ref 11).

* The term "crystallographic orientation" is used here to include substrate surface reconstruction, where appropriate.

As suggested by Lewis (Ref 12), heteroepitaxy can be considered to involve the following topics: 1) saturation and critical nucleus size; 2) nucleation densities on the surface; 3) orientation-dependent nucleation rate; 4) nucleus reorientation during growth; 5) growth morphology; 6) coalescence of nuclei and clusters or islands; 7) growth of continuous films; and 8) epitaxial interfacial energy. In these theoretical studies the last of the above topics - the interfacial energy - has been emphasized.

It is clear that the film-substrate binding energy plays a role in determining the characteristics of the deposited heteroepitaxial film. The relative importance of this energy in comparison with those of other processes will vary from one film-substrate materials combination to another. For example, Sato and Shinozaki (Ref 13) discussed the influence of interfacial energy on the morphology and structure of epitaxial deposits. They presented evidence that the strength of the interaction between metal deposits and ionic crystal substrates, compared in relative magnitude with the film surface energy, is an important factor which determines the apparent characteristics of epitaxial behavior. Sato and Shinozaki indicated that the interfacial interaction energy of most metals on ionic crystals is very small - that is, the coupling is weak.

Reiss (Ref 6) also calculated the rotational energy of weakly coupled nuclei on a substrate, based on a simple sinusoidal potential model with a simplified model of lattice registry. A phenomenological but more general treatment of the interfacial energy was developed by Bettman (Ref 14). The importance of interfacial interactions has been emphasized by other workers over many years (Refs 15, 16). However, these efforts have generally not been adequate to reveal in detail the role of the interfacial interaction as related to the general characteristics of epitaxy.

The initial goal of the theoretical study on this contract was the development of a suitable theoretical treatment and model for the interfacial energy. Emphasis was on the development of an approach sufficiently realistic and related to the actual film and substrate materials (principally Si on Al_2O_3) to allow interfacial energy calculations to be employed as an important tool in understanding and exploiting heteroepitaxy. Unlike metals on ionic substrates,

semiconductor films on insulating substrates were tentatively considered as examples of strong interfacial interactions in these studies.

The conceptual reference points for these investigations of the strong interfacial interaction problem are the so-called Frank-Van der Merwe model (Refs 17, 18) and the models developed by Fletcher and Adamson (Refs 19, 20). The approaches employed in these references have much in common; they all attempt to determine the dependence of the equilibrium configurations of a thin single-crystal epitaxial film on the strengths of the interactions between film and substrate and the strength of the cohesive bonds in the film. Generally, the interfacial potential is assumed to be a simple sinusoidal "energy band" type of potential. The bonds between atoms in the film are usually brought into the problem through continuum elastic theory. In many cases substrate deformations are neglected, although the work of Fletcher and Adamson (Ref 20) is a variational method which, in principle, allows displacements of atoms near the interface to be included.

A number of interesting qualitative features emerged from these studies, and they represent forceful attacks on a very difficult problem. However, they suffer from a few important defects which make any application to actual film-substrate combinations impossible. For example, the potentials assumed are contrived interfacial potentials in the plane of the interface; they neglect the perpendicular direction entirely, and they are not the more fundamental three-dimensional two-body interatomic potentials. Second, the crystal lattices employed are simple cubic nets and are far removed from reality for materials such as Si on Al_2O_3 , which have multiple atoms per unit cell and a more complicated space group. Third, the elastic energy cannot be treated separately from the interfacial energy since, from the point of view of interatomic two-body potentials or bonds, both arise from the same physical source.

It was thus concluded that the above approaches are wholly inadequate for application to real systems and/or to different relative crystallographic orientations of film and substrate in real systems such as Si on Al_2O_3 . Further, it has been concluded that all existing theories are inadequate for the purpose

and cannot be extended to treat real systems such as Si/Al₂O₃. This conclusion has been reached as a result of essentially geometrical considerations of the atomic topography of ideal bulk Si and ideal bulk Al₂O₃ lattices. These ideal bulk lattices are sufficiently complicated to preclude any incorporation into existing theoretical approaches.

In reality the picture for existing theories is even more negative than stated above, since one important and experimentally significant physical phenomenon - that of substrate surface reconstruction - has not yet been included in the discussion. Recent investigation of Si-on-Al₂O₃ epitaxy by Chang (Ref 21) is of particular importance in this regard because it utilized low-energy electron diffraction (LEED) and Auger electron spectroscopy techniques, both of which are now capable of providing significant data for epitaxy investigations. It appears that a theoretical approach capable of incorporating LEED and Auger data, where appropriate, would be highly desirable.

The Si films prepared in Chang's studies were formed by high-temperature vacuum sublimation. Although other growth techniques and growth rates might not necessarily yield identical results, Chang's principal conclusions and relationships are probably general and widely applicable. Chang found that the epitaxial relationships and the electrical properties of the films depend on film-substrate interactions, substrate temperatures, and substrate surface structures.

Chang observed that Al₂O₃ substrates often exhibited surface superstructures whose periodicity - and sometimes even the symmetry - was different from that of the ideal bulk structure. Departures from the ideal configuration were especially large for the (0001)- and (11 $\bar{2}$ 0)-oriented faces. Chang also was able to show why both (111)//(11 $\bar{2}$ 0) and (110)//(11 $\bar{2}$ 0) epitaxial configurations have been obtained. He determined that (111)//(11 $\bar{2}$ 0) is the correct relationship, with the other being a result of faceting.

Chang's work is important in any theoretical study in that it provides some experimental relationships which can be employed as test cases by attempting to incorporate the substrate superstructure (before growth, but after high-temperature preparation to achieve equilibrium LEED patterns) into the calcu-

lation. However, there is still some uncertainty, in that it is possible that the substrate surface may be further reconstructed during the film deposition process at elevated temperature. Despite this, Chang's work implies that the interfacial energy is a sensitive function of the epitaxial relationship and is basic to theoretical epitaxy calculations.

Early in these studies attention was directed toward more basic and fundamental theoretical approaches. The feasibility of performing a Green's-function/Wannier-basis calculation of the interfacial redistribution energy was investigated. This technique is firmly grounded in principle, although practical problems have rarely been approached by this means. The investigation of this quasi-first-principles approach led, unfortunately, to the conclusion that the procedure was actually not feasible. The procedure would be feasible for certain types of problems dealing strictly with Si, since pseudopotentials and Wannier functions have been developed and employed for the ideal bulk Si lattice (Ref 22). A substantial difficulty for Si/Al₂O₃ is encountered in attempting to construct atomic pseudopotentials for Al₂O₃ and for the Si-Al₂O₃ adatom interaction within the delocalized electron-energy band picture. Successful application of this or any other quasi-first-principles approach thus appears to be many years in the future.

A less quantum-mechanical and more phenomenological approach - the modeling of the film and substrate by means of atoms interacting via pairwise two-body potentials - was then investigated. In this approach the total energy of a given static atomic configuration can be obtained by computer summation over all atoms. By allowing some atoms to relax near the surface or the interface, a minimum energy configuration can be determined.

The crucial requirement in such a "bond-counting" determination of interfacial or configurational energy is that realistic potentials between all atoms must be known. This question was examined in detail in these studies.

Interatomic potentials have been employed extensively in bulk-material solid-state physics for point-defect calculations and for lattice dynamics calcula-

tions. Most of the investigations reported in the literature have been concerned with migration and formation energies for point defects in metals. Examples include the work of Feit and Huntington (Ref 23), Johnson (Ref 24), Wynblatt (Ref 25), and Tick and Witt (Ref 26). These authors employed Morse potentials, Born-Mayer potentials, and combinations of Morse and Born-Mayer potentials. The various methods of determining potential parameters included the matching of elastic constants, compressibility, or cohesive energy.

Less work has been done with interatomic potentials in semiconductors. Point-defect calculations, such as for vacancies and interstitials, have been reported by Swalin (Ref 27) and Scholz and Seegar (Ref 28). Swalin assumed a Morse potential determined from covalent-bond dissociation energy and enthalpy data. Scholz and Seegar used a combination of the Born-Mayer and Morse potentials.

The use of interatomic potentials in the above calculations and in the interfacial energy calculations is viewed as having questionable validity and lacking in theoretical basis or foundation. Within the theoretical program of this contract considerable effort has been devoted to an investigation of interatomic potentials and to attempts to resolve problems connected with the use of these potentials.

First, there is a lack of uniqueness in the interatomic potential. Different forms of the potential can be, and have been, employed by various investigators. The detailed parameters of the particular potential are determined by matching various selected physical properties of the bulk material. Unfortunately, the numerical potential parameters appear to depend upon which of the various bulk physical properties are actually employed. This suggests that, rigorously speaking, interatomic potentials do not exist and that a crystal can not be modeled in this manner. Thus, the modeling of a crystal problem with interatomic potentials is viewed as a rough phenomenological approach. However, if the labor involved in determining the effective potentials and in carrying out the subject calculation is not excessive, the qualitative information to be obtained may be of enough interest to warrant the effort.

For Si/Al₂O₃ an additional point must be considered in assessing the practicality and desirability of modeling this system with interatomic potentials. In this case a general treatment would require six different potentials. The interaction between Si and Al₂O₃ is particularly troublesome. This interaction is explicitly interfacial in nature and cannot be derived from bulk properties; any determination in this instance would be difficult and very tenuous. As a result of such considerations it was concluded that such potentials probably cannot be realistically determined.

Consequently, the investigation and application of interatomic potentials to the Si/Al₂O₃ system was temporarily set aside in favor of an investigation of molecular orbital methods.* The possible application of the LCAO-MO (linear combination of atomic orbital-molecular orbital) technique for interfacial binding energy calculations was first considered. Since a large number of atoms are involved in the heteroepitaxial case, the simplest such technique - the extended Hückel theory (EHT), which is a semiempirical molecular-orbital approach (Ref 29) - was employed. In this approach, the interface, including nearby film and substrate atoms, is treated as an extended molecule and calculations performed for the total energy of the cluster of atoms.

The defect molecule consisting of a cluster of atoms in the solid near the interface is not in free space but is instead in a crystalline environment. Thus, the molecular orbital calculations encompasses conceptual problems not present in ordinary molecular orbital calculations. The major features are clear, however. The boundary between atoms in the defect molecule and in the rest of the crystal is merely a consequence of the model chosen. Thus, it would appear that external constraints imposed on the molecule at its surface must be consistent with the crystalline environment. Some of these questions are rather subtle and had not been either investigated or resolved satisfactorily by the end of the first year of the program.

*The modeling of the Al₂O₃ lattice with interatomic potentials was later reinstigated and the problem of relaxation of Al and O planes near the Al₂O₃ surface was successfully treated for one type of relaxation. See Section 2-4.

Theoretical efforts in the second year began with a more detailed investigation of the EHT for the Si/Al₂O₃ application. Because of the crystalline environment, questions of molecular charge distribution and fluctuations, overall charge neutrality, and boundary conditions at the surface of the molecule arise. Treating the interface as an extended molecule introduces an artifact, the surface of the molecule. The associated dangling bonds or surface states must be saturated or otherwise constrained by boundary conditions.

The study showed that the EHT for such a defect crystalline molecule apparently yields spurious charge gradients and fluctuations. It was originally hoped that these charge fluctuations were due to the boundary conditions at the surface of the molecule and thus subject to useful modification. However, it now appears that the charge fluctuations are fundamental results of the theoretical approach itself.

The charge fluctuations can be substantially reduced or eliminated by a more involved molecular orbital technique, the so-called CNDO (complete neglect of differential overlap) approach. Unfortunately, the attendant increase in labor required is quite large. This circumstance cast some doubt on the feasibility of the molecular orbital technique for the heteroepitaxial interface. The CNDO approach is, however, feasible and proper for a chemisorption calculation (Ref 30). Such a calculation for Si atoms adsorbed on Al₂O₃ would be of general interest but falls short in terms of the criterion for direct relevance to heteroepitaxy.

Partly because of these negative conclusions concerning the feasibility of molecular orbital methods for the heteroepitaxial problem, the exigencies of the program suggested that the interatomic potential approach should be reinstigated. It was recognized, however, that simplifying assumptions would be mandatory.

The subsequent theoretical work with interatomic potentials is described in the next section in some detail.

4. STUDIES OF THE Si/Al₂O₃ SYSTEM USING INTERATOMIC POTENTIALS

It now appears that a general solution to the heteroepitaxial Si/Al₂O₃ problem cannot be hoped for at this time and may indeed be several years in the future. It is possible to incorporate the geometrical and structural features of the Si and Al₂O₃ crystal lattices into a simplified model based on interatomic potential modeling of Si and of Al₂O₃. This should represent a reasonable way of incorporating those structural features of Si growth on Al₂O₃ which are caused by the Al₂O₃ lattice.

In using interatomic potentials to represent the interaction between atoms in the Si/Al₂O₃ system, the cohesive energy of a given configuration is obtained by summing over all interaction atom pairs. The concept of an interatomic potential in the present context is best regarded as a phenomenological construct. While there are quantum mechanical foundations which provide a basis for interatomic potentials at the philosophical or qualitative level, there do not appear to be any quantitative and rigorous calculations of interatomic potentials, with the possible exception of the case of Na. Even if rigorous atomic potentials existed and were available for the bulk "perfect-crystal" materials of interest, these potentials would be specific to the bulk crystal and would have to be altered in the presence of defects or at a heteroepitaxial interface.

For interatomic potentials to be useful in practice it is necessary to assume that the basic interatomic interaction is unaffected by atomic rearrangement. This assumption is therefore fundamental in these studies. A second consideration lies in the particular type of potential to be employed. These investigations assumed a simple two-body central-force interaction between atoms. More complicated non-central potentials could have been employed, in principle, but in practice they are out of the question for the complicated Al₂O₃ lattice. In this work the atomic potential modeling of Si and Al₂O₃ was regarded simply as a phenomenological treatment.

There are two attractive features which argue for application of atomic potentials to the Si/Al₂O₃ system: (1) Computer modeling with interatomic potentials has apparently been successful in the past for structural problems in simple metals. (2) There is at present no theory of epitaxy which makes it possible to predict the orientation of the overgrowth on the substrate in the Si/Al₂O₃ system. The orientation aspects of heteroepitaxy can be treated fairly directly in terms of interatomic potentials.

The theoretical modeling of the Si/Al₂O₃ system with interatomic potentials can be divided into five parts: (1) the modeling of the Al₂O₃ lattice by determination of phenomenological potentials meeting appropriate criteria or constraints; (2) the investigation of Al₂O₃ surface reconstruction on the basis of the determined potentials; (3) modeling of the Si lattice with an interatomic potential; (4) the parameterization, in lieu of useful empirical data, of the Si/Al₂O₃ adatom interaction; and (5) the simulation of Si growth on Al₂O₃ by computer computation of energy for small clusters of Si atoms.

The modeling of the Al₂O₃ lattice was carried out in terms of Morse potentials. This choice was suggested by the following factors: (1) The Si was to be modeled by means of a Morse potential available in the literature (Ref 27). (2) The Si/Al₂O₃ adatom potential, which was to be treated essentially as a parameter, could be conveniently expressed with Morse potentials. (3) Analytical expressions for the atomic force could be easily obtained for Morse potentials.

Al₂O₃, which has two types of atoms, would in general require three Morse potentials:

1. $D_{CC} \{ \exp (-2 \alpha_{CC} (R-R_{CC})) - 2 \exp (-\alpha_{CC} (R-R_{CC})) \}$
2. $D_{AC} \{ \exp (-2 \alpha_{AC} (R-R_{AC})) - 2 \exp (-\alpha_{AC} (R-R_{AC})) \}$
3. $D_{AA} \{ \exp (-2 \alpha_{AA} (R-R_{AA})) - 2 \exp (-\alpha_{AA} (R-R_{AA})) \}$

The subscripts CC, AC, and AA denote cation-cation, anion-cation and anion-anion interactions, respectively. A general determination of these three

interatomic potentials would require treatment of a nine-parameter system. A straightforward determination was therefore impractical, so it was important to incorporate as much physical and empirical data as possible in order to simplify the problem.

The appropriate cohesive energy (energy of formation), elastic constants, and lattice parameters are known experimentally. Gieske and Barsch (Ref 31), considering the elastic constants, have noted that Al_2O_3 is somewhat unusual compared with other oxides such as MgO in that the Cauchy relations $C_{12}=C_{16}$ and $C_{23}=C_{44}$ are approximately fulfilled. In addition, although Al_2O_3 is trigonal (rhombohedral), the second-order elastic constant data indicate that the deviation from pure hexagonal symmetry ($C_{14}=0$) is small. (C_{14} is about an order of magnitude smaller than the other elastic constants.) This suggests that the elastic properties are related primarily to the nearly-hcp oxygen framework.

Anderson (Ref 32) earlier expressed this same point of view - that the oxygen framework is dominant in determining elastic properties of this oxide. Since the Al atom sites in Al_2O_3 are believed to play an important role in hetero-epitaxial film-substrate orientation, a model based solely on anion-anion interactions would not be reasonable. Intuitively, the deviation from hcp symmetry would be exhibited most strongly through the cation-cation interaction, which relates explicitly to a non-hexagonal lattice with defects. It was therefore concluded that the cation-cation interactions do not play an important role in the lattice and that the exclusion of cation-cation interactions was a reasonable and important simplification. Consequently, only anion-anion and anion-cation potentials were employed throughout the modeling.

The phenomenological potentials were determined by requiring that the modeled lattice provide (1) the correct cohesive energy of about 34.54 eV per rhombohedral unit cell; (2) that the lattice energy be a local maximum and the derivative vanish at the observed lattice spacing; (3) that the forces on each of the cations in the unit cell vanish; and (4) that the forces on each of the anions in the unit cell also vanish.

Potentials meeting these four constraints were determined. To facilitate more detailed discussion of the procedure used in establishing these potentials, the first few interatomic distances in the Al_2O_3 lattice (anion-anion, cation-anion, and cation-cation distances) are given in Table 1. The first four anion-anion distances and the first two cation-anion distances relate to what would be first-neighbor interactions in an idealized Al_2O_3 lattice.

Table 1. Interatomic Distances for Al_2O_3 Lattice (Å)

<u>Anion- Anion</u>	<u>Cation- Anion</u>	<u>Cation- Cation</u>
2.524	1.857	2.649
2.619	1.969	2.792
2.725		3.222
2.869	3.223	3.499
	3.430	3.843
3.790	3.560	4.762
3.957	3.862	5.148
4.334	4.162	5.449
	4.325	
4.616	4.380	
4.762	4.429	
4.813	4.675	
4.945	5.064	
5.072	----	
----	5.244	
5.128	5.366	
5.252		

As a first attempt, only the four first-neighbor anion-anion and two first-neighbor cation-anion interactions were included in the analytical expression for cation and anion forces. Potentials were determined which gave the required zero forces. However, examination of the derivative of the cell energy showed that a maximum could never be obtained with only first neighbors. All subsequent discussion therefore relates to a model including 13 different anion-anion separations (up to 5.072Å) and 12 different cation-anion separations (up to 5.064Å). This cutoff point in the model is arbitrary but is believed to be reasonable for present purposes.

Potentials meeting the four constraints and including the interactions listed above were then determined for a range of values of the potential parameters R_{AC} and R_{AA} . It was originally planned that the remaining parameters R_{AC} and R_{AA} would be further restricted by calculation of elastic constants. The Al_2O_3 lattice, viewed as rhombohedral, contains 10 atoms per unit cell and involves internal (unequal) displacements or strains of the various atoms in the unit cell. The accurate calculation of elastic constants is an extremely involved task in the case of internal displacements. A calculation could be made in the approximation which neglects internal strain, and this was begun. Subsequent considerations indicated that such a procedure provided only an order-of-magnitude estimate. Therefore, elastic constant calculations were not pursued further, since they would have diverted the effort from the main task as related to heteroepitaxy.

One aspect of the use of elastic constant data should, however, be discussed. In interatomic potential calculations for simple cubic metals, as found in the literature, the calculation of elastic constants and the requirement that the strain energy be positive-definite is usually imposed for lattice stability. In such cases this is an important constraint, because the force on an atom vanishes identically due to lattice symmetry, and therefore imposes no constraint at all in determining an appropriate potential. The Al_2O_3 lattice is, perforce, unstable unless the potentials are determined such that the required forces are zero.

As mentioned above, potentials for Al_2O_3 were determined for a range of values of the parameters R_{AC} and R_{AA} . On general grounds and from examination of the constraint analytical expressions, it appeared that R_{AA} and R_{AC} both would lie in the range of $1.969\text{\AA} \leq R_{AA}$ and $R_{AC} \leq 2.524\text{\AA}$. The plan was to carry through subsequent investigations with perhaps two different potentials. For example, two different acceptable potentials can be distinguished from one another on the basis of the relative amounts of anion-anion and anion-cation energy represented in the energy per unit rhombohedral cell. The lattice potentials employed for the surface reconstruction investigations to be discussed below are for $D_{AC} = 0.77352 \text{ eV}$, $\alpha_{AC} = 1.31819\text{\AA}^{-1}$, $R_{AC} = 2.32\text{\AA}$ for the anion-cation

interaction and $D_{AA} = 0.14484$ eV, $\alpha_{AA} = 1.99225\text{\AA}^{-1}$, $R_{AA} = 2.32\text{\AA}$ for the anion-anion interaction.

It is interesting to note that early work in heteroepitaxy, rather naturally but without other foundation, made extensive use of the concept of minimum mismatch as a determining factor in establishing relative film-substrate orientations. However, LEED studies of a number of film and/or substrate materials have already established that some sort of surface reconstruction sufficient to yield modified LEED patterns is the rule rather than the exception. Thus, the surface periodicity and/or symmetry can be altered from that of the bulk crystal.

An investigation of surface reconstruction in basal-plane Al_2O_3 was initiated, using the potentials just discussed. Although basal-plane Al_2O_3 is not the substrate orientation of greatest practical importance, it was particularly convenient for beginning studies of reconstruction. The eventual goal of these studies was to predict or calculate the relative energies of the various (1×1) , $\sqrt{3}$, $3\sqrt{3}$, and $\sqrt{3}1 + 9$ deg LEED patterns described by Chang (Ref 21). However, it is not clear if all of these patterns can fit within the framework of the present model. Also, there is some evidence that impurities and/or surface stoichiometry may be determining factors producing the various LEED patterns. Thus, additional experimental information would be helpful in establishing which atomic surface configuration should be examined theoretically and in identifying the necessary theoretical ingredients.

Somewhat more basic but still related to surface stoichiometry is the question of the composition of the Al_2O_3 substrate at Si deposition temperatures. Early workers, in applying mismatch concepts at the interface, generally considered the deposited Si atoms to bond onto a bare plane of O atoms, with the Si atoms occupying the missing Al atom sites. On the other hand, since each O plane in Al_2O_3 is separated by two Al planes with long and short bonds to the O planes, Chang (Ref 21) suggests that mathematical cleavage could most easily take place between two Al planes, leaving one Al plane at the surface of each of the cleaved half-crystals. Intuitively, it appears that there would be consider-

able rearrangement of Al surface atoms if this is the case. Thus, one goal of the present work was to examine both simple alternatives for the surface configuration and determine what conclusions could be reached.

Studies of surface reconstruction of basal-plane Al_2O_3 were carried out by considering the relaxation of the four planes nearest to the surface. Table 2 lists the planes, atom type, and hexagonal coordinates of the 15 atoms which can be considered to represent the upper half of a 30-atom hexagonal unit cell. For this half-cell the origin of coordinates is at an Al atom hole (i.e., the site of a missing atom). The upper boundary of the half-cell then also contains an Al hole and defines a hexagonal network of holes.

In treating surface reconstruction it was assumed for definiteness that the surface is an O plane, labeled plane 2 in Table 2. Plane 1 is therefore excluded and planes 2, 3, 4, and 5 are included in the relaxation treatment.

For a mathematically-cleaved ideal (0001) Al_2O_3 crystal, since this half-crystal still possesses three-fold symmetry normal to the surface and along the z (c-axis) direction and in addition still retains translational periodicity in directions lying in the surface, it is clear that there must be appreciable relaxation taking place which possesses this rotational and translational symmetry. There will also probably be relaxation which is not symmetric, but its origin is somewhat obscure and may relate to impurities or surface stoichiometry.

Consider relaxations of atoms in planes 2-5 which are consistent with symmetry; two such relaxations are possible. The first type is associated with the parameter x in Table 2, which defines the positions of O atoms in the unit cell and is equal to 0.306 for bulk Al_2O_3 . With the absence of translational symmetry in the \bar{a}_4 or z direction, an allowable change would be for each O plane to relax toward a new value of x differing from the bulk value. Intuitively, it appears that the O plane at the surface would show the largest change. The magnitude of this type of relaxation was not numerically determined, but preliminary indications were that it is small.

Table 2. Hexagonal Half-cell Data for Al_2O_3

Plane No.	Atom Type	Hexagonal Coordinates a_1, a_2	\bar{a}_4	\bar{a}_4
			Initial Coordinate	Relaxed Coordinate
-	Al hole	(0,0)	0.5000	-
1	Al	(2/3, 1/3)	0.48133	-
2	O	(1/3-x, 2/3); (1/3, 2/3-x); (x+1/3, x+2/3)	0.41666	0.43853
3	Al	(0,0)	0.3520	0.34913
4	Al	(1/3, 2/3)	0.31466	0.31629
5	O	(x,0); (0,x); (1-x, 1-x)	0.250	0.24300
6	Al	(2/3, 1/3)	0.18533	-
7	Al	(0,0)	0.1480	-
8	O	(2/3-x, 1/3); (2/3, 1/3-x); (2/3+x, 1/3+x)	0.0833	-
9	Al	(1/3, 2/3)	0.01866	-
-	Al hole	(0,0)	0.0000	-

The second type of relaxation is that in which each of the various planes considered is allowed to move individually in the \bar{a}_4 or z direction. This type of relaxation appears significant for (0001) Al_2O_3 , and numerical results were obtained. The relaxed-plane positions were determined by an iterative procedure which relaxed planes 2, 3, 4 and 5 in turn toward the position of minimum energy until convergence was obtained. The results obtained are nearly as expected and are shown in the last column of Table 2. Plane 2, the surface plane of O atoms in this case, shows the greatest (outward) displacement. Planes 3 and 4 are displaced only slightly and tend to move somewhat closer together. Plane 5 is seen to move inward and away from the surface a moderate amount. This negative displacement could have been expected on general grounds from the work of Tick and Witt (Ref 26), who found a similar displacement for Ni-like metal systems.

At the time the above planar displacement problem was treated, it was intended that the interaction between Si and Al_2O_3 be parameterized and the growth of Si on Al_2O_3 be simulated for a small cluster of perhaps six Si atoms. It was recognized that parameterizing the interaction between Si and Al_2O_3 in essence defined a model problem which was probably oversimplified compared with the real lattices. However, this approach seemed reasonable as the most practical alternative.

Coincident in time with the above Al_2O_3 lattice relaxation study, theoretical investigation of the effect of thermally-induced stress on the carrier mobility in the Si/ Al_2O_3 system was begun as an on-line response to the electrical measurements program. The initial success achieved in theoretically explaining the ~10% mobility anisotropy in (001)Si/ Al_2O_3 and ~40% mobility anisotropy in (221)Si/ Al_2O_3 , and the potential significance of such an investigation to the preparation of heteroepitaxial semiconductor films for device use, dictated that this should become the principal theoretical task of the remainder of the contract program.

5. STRESS EFFECTS ON ELECTRICAL PROPERTIES OF Si/Al₂O₃

The theoretical analysis of stress effects on the mobility in Si/Al₂O₃ films began as an on-line response to the important experimental discovery, in the last half of the second contract year, that an anisotropy was present in the carrier mobility in (001)Si, (221)Si and (111)Si heteroepitaxial films grown on Al₂O₃ and would probably occur in all orientations of Si/Al₂O₃.

It was recognized that different physical mechanisms which could produce some form of mobility anisotropy would, in general, be expected to lead to different magnitudes of anisotropy and to different orientations for the mobility maxima and minima in the plane of the film. Thus, detailed studies of the mobility anisotropy could, in principle, provide a more powerful means than had previously been available for determining the role of various phenomena in establishing the carrier mobility in the Si/Al₂O₃ films. The anisotropy studies are thus considered to be of major importance to this contract program and to semiconductor heteroepitaxial film technology in general.

Physical phenomena which could lead to a mobility anisotropy in these heteroepitaxial systems include 1) surface scattering, 2) hot electron phenomena, 3) surface quantization, 4) dislocation scattering, and 5) both surface and bulk piezoresistance effects. All of these phenomena are inadequately understood at the present time, and - with the exception of the piezoresistance studies done on this program - all previous work that has been carried out has related to thin bulk crystals rather than to epitaxial films.

Since stresses in Si/Al₂O₃ are known experimentally to be on the order of 10^9 - 10^{10} dyn/cm² and since Si is a strongly piezoresistive material, it appeared that a piezoresistance-effect mobility-anisotropy model would be a useful tool and should relate substantially to experimental mobility anisotropies.

The idea that Si film stress acting through the piezoresistance effect can modify the film resistivity and hence the carrier mobility is not new, and

estimates of the change in mobility due to stress associated with thermal expansion mismatch between Si film and Al_2O_3 substrate are available in the literature (Ref 33). However, all previous investigations have assumed that the thermal expansion stress is isotropic in the plane of the film and thus for (001)Si and (111)Si leads to an isotropic mobility which is independent of the direction of measurement in the plane of the film.

However, thermal expansion in Al_2O_3 is known experimentally to be anisotropic (Ref 34) and would thus lead to an anisotropic stress in the Si film. It thus followed that a theoretical investigation in terms of an anisotropic model combining thermal expansion stresses and piezoresistance effects might yield an explanation for the observed anisotropies in the experimentally determined carrier mobilities.

A theoretical model was subsequently developed which explicitly incorporated the anisotropy in thermal expansion of the Al_2O_3 substrate, the anisotropy in the Si film elastic constants, and the anisotropy in the Si film piezoresistance coefficients. The model was then applied to n-type (001)Si// $(01\bar{1}2)\text{Al}_2\text{O}_3$ and (221)Si// $(11\bar{2}2)\text{Al}_2\text{O}_3$ film/substrate orientations which had been extensively investigated experimentally.

Theoretical and experimental data for n-type (001)Si/ $(01\bar{1}2)\text{Al}_2\text{O}_3$ films (Ref 35) and for n-type (221)Si/ $(11\bar{2}2)\text{Al}_2\text{O}_3$ (Ref 36) were published during the course of the program; these papers are included as Appendices 2 and 3 of this report and therefore will be discussed only briefly here.

The theory for (001)Si/ $(01\bar{1}2)\text{Al}_2\text{O}_3$ films predicts a maximum mobility direction along the [100]Si direction which is parallel to the $[2\bar{1}\bar{1}0]\text{Al}_2\text{O}_3$ direction. The minimum mobility direction is displaced 90 deg from the maximum mobility direction. The theoretical anisotropy in mobility, defined as

$$A = 200 \left(\frac{\mu_{\max} - \mu_{\min}}{\mu_{\max} + \mu_{\min}} \right), \quad (18)$$

is 9.3%. The maximum mobility direction is found experimentally to lie along the $[2\bar{1}\bar{1}0]Al_2O_3$ direction. A least-squares fit to the experimental mobility data on eight different samples yielded room-temperature experimental anisotropies ranging from 7.6 to 11.7%, with an average of 9.5%.

For the case of $(221)Si / (11\bar{2}2)Al_2O_3$ films, the theoretical maximum mobility direction is along the $[1\bar{1}0]Si$ direction parallel to the $[1\bar{1}00]Al_2O_3$ direction. The theoretical anisotropy A is 41%. Experimentally the maximum mobility direction is found to be as given by the theory. Least-squares fits to the mobility data on seven different samples yielded room-temperature experimental anisotropies ranging from 30.4 to 48.6%, with an average of 39%.

Analysis of the theoretical and experimental data for $(001)Si / (01\bar{1}2)Al_2O_3$ and $(221)Si / (11\bar{2}2)Al_2O_3$ has thus shown that the model and thermal stresses do indeed largely account for the anisotropy in the mobility and the angular location of mobility maxima and minima. Thus, the anisotropy in mobility can be substantially described in terms of thermal stresses without recourse to other physical phenomena such as residual growth stresses or dislocation scattering. However, the magnitude of the overall average mobility in these films is found to be significantly lower than bulk-crystal values. This indicates that some other phenomenon, such as defect or dislocation scattering, is quite important in determining the properties of these (001) and (221) Si films.

Attention was next directed to the $(111)Si$ case on two different Al_2O_3 substrate orientations: 5 deg off of the $(11\bar{2}0)$ plane and $(10\bar{1}4)$. For the $(11\bar{2}0)$ orientation, the theoretical anisotropy is too small by a factor of about 4. For the $(10\bar{1}4)$ orientation, the theoretical anisotropy is a factor of about 8 times smaller than the experimental average anisotropy. In both cases the predicted directions of mobility maxima and minima are rotated 90 to 100 deg away from those determined experimentally.

Extensive attempts, both theoretically and experimentally, have been made in efforts to explain the experimental $(111)Si$ results. The experimental results

show substantial data scatter, and attempts have been made both to determine the origin of the scatter and to reduce its magnitude. Inhomogeneity in film properties is one potential source of both scatter and ambiguity in the experimental data. The results of experimental studies of Si film inhomogeneity are discussed later in this report. While Si film inhomogeneity must be taken into account in accurately measuring mobility anisotropies, the film inhomogeneity does not itself appear to explain the large anisotropy or location of mobility maxima and minima, nor does surface-state conduction.

A second physical mechanism--hot electron phenomena--has been ruled out as a likely cause of the experimental results on (111)Si since the mobility of anisotropy is found to be independent of the magnitude of the electric field. Surface scattering and surface quantization are two other physical phenomena which could play a role in determining the experimentally measured anisotropy. For bulk thin films (i.e., no substrate) both these effects should lead to isotropic carrier mobilities on the basis of general symmetry arguments (Ref 35). The stress applied by the substrate is anisotropic and would thus be expected to lead to some anisotropy. However, intuitively this anisotropy would be expected to be of the same order as the (001)Si results--an anisotropy of 6 to 9%. These phenomena appear implausible as mechanisms for producing the rather large (16 to 30% average) (111)Si anisotropy that has been observed. It appears that a definitive explanation of the (111)Si mobility anisotropy results cannot be made at this time.

It is of interest to explore other potential origins for the anisotropy within the framework of a piezoresistance model. Calculations thus far have employed stresses calculated from the thermal expansion mismatch of film and substrate; it has long been recognized that lattice-constant mismatch between dissimilar materials can, in principle, lead to residual growth stresses. It is unlikely that residual growth stresses would modify the average stress $(T_1+T_2)/2$ substantially.* The anisotropy in the stress (T_1-T_2) calculated from the thermal

*See Reference 35 (Appendix 2) for identification and discussion of these stresses.

expansion model is typically 5 to 7% of the average stress. Thus, it is not impossible for small changes in T_1 and T_2 caused by residual strains to modify $(T_1 - T_2)$ appreciably, and in this way also affect the experimental mobility anisotropy.

At present there is apparently no way to determine if such growth stresses do in fact exist in Si films in the (111) orientation or why such stresses do not appear to be required in the theoretical explanation for the (001)Si and (221) Si anisotropy cases. However, a residual growth stress explanation does appear plausible; this explanation would, if found to be correct, represent a major step forward in understanding some of the basic physics of heteroepitaxial Si films.

Comparison between theory and experiment was made for three Si orientations, as indicated above. In two of the three cases substantial agreement was found both for the magnitude of the anisotropy and for the location of mobility maxima and minima. This agreement provided considerable confidence in the basic model and suggested that more extensive theoretical development of the model valid for other orientations would be useful.

The mathematical framework of the theoretical model was then extended in several regards. Calculations for a number of new Si orientations were performed, and a comprehensive theoretical paper was prepared which summarized the entire theoretical effort (Ref 37). This paper in preprint form is included as Appendix 4 of this report.

The significant new material developed in the paper includes a mathematical description of heteroepitaxial relations which allows arbitrary "off-orientation" Si/ Al_2O_3 films to be treated theoretically for the four major modes* of Si/ Al_2O_3 epitaxy. One mode of Si/ $MgAl_2O_4$ epitaxy was also treated.

A linear piezoresistance formalism had been employed in all previous calculations on this model. However, the extension to p-type Si indicated that the predicted change in resistivity due to stress was substantial and would result

* For a discussion of this topic see Appendix 4.

in anomalously large mobilities as an artifact of the linear formalism. A non-linear correction factor was developed which approximately takes into account the higher-order stress terms. Although both the linear and the non-linear models yield approximately identical results for n-type Si, the differences are marked for p-type Si. The non-linear model in this case is believed to be the most accurate, and all subsequent discussion is based upon data obtained using the non-linear correction factor.

The Si/Al₂O₃ orientations treated thus far have all been the subject of experimental investigation, and extensive growth studies have been performed in all these cases. The recent theoretical studies, however, have directed attention to the general (xxl)Si orientation, and the model was employed in a predictive sense to determine the effect of thermal stress on the mobility for other Si orientations not yet grown or researched experimentally.

In the calculations for the (xxl) Si orientation, x was varied from zero to infinity to map out all orientations of the form (xxl) lying along the zone defined by (001)Si, (111)Si, (221)Si, and (110)Si. These calculations were performed for four different modes of Si/Al₂O₃ epitaxy and one mode of Si/MgAl₂O₄ epitaxy, for both n-type and p-type Si. A substantial amount of data has been generated by the computer calculations. This collection of data is described in detail in the paper (Ref 37) given in Appendix 4 and will not be repeated here.

The theoretical mobility data obtained for the (xxl)Si zone and the four modes of Si/Al₂O₃ epitaxy are all rather similar and do not display a strong dependence upon the particular mode of epitaxy. Mobility data for n-type Si are shown in Figure 1, and curves for the maximum mobility ratio (μ_{\max}/μ_0) and the minimum mobility ratio (μ_{\min}/μ_0) are both presented as a function of orientation in the (xxl)Si zone*.

*The symbol μ_0 denotes the carrier mobility in the absence of stress.

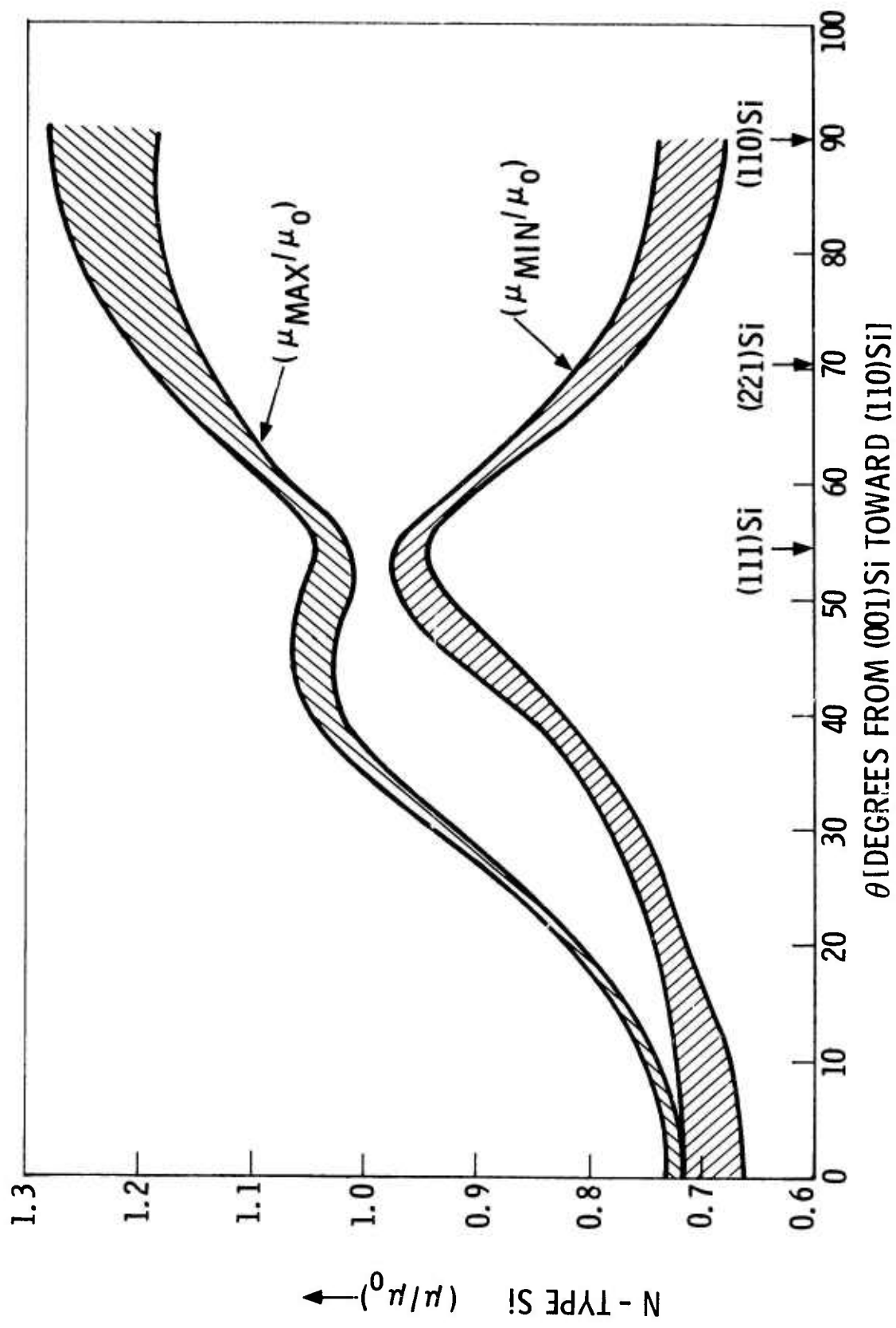


Figure 1. Theoretical Carrier Mobility Ratios μ_{max}/μ_0 and μ_{min}/μ_0 for N-type Si/Al₂O₃ along (xx1)Si Zone.

Mobility data for p-type Si are shown in Figure 2, and curves for the maximum mobility ratio (μ_{\max}^e/μ_0) and the minimum mobility ratio (μ_{\min}^e/μ_0) are both presented as a function of orientation. The superscript e denotes that the p-type data is derived from use of the non-linear piezoresistance model.

In Figures 1 and 2 the collective range of mobilities for all four modes of Si/Al₂O₃ epitaxy is plotted. The mobility ratios μ_{\max}/μ_0 or μ_{\min}/μ_0 for any particular mode of epitaxy will therefore be somewhere in the shaded regions of the graphs. Data for the individual modes are presented in tables in Appendix 4.

For n-type Si, the effect of thermal stress on the maximum mobility ranges from a reduction of ~30% in mobility for (001)Si up to an enhancement of ~25% in mobility near (110)Si. The range of the mobility ratio μ_{\max}/μ_{\min} for (110)Si and (001)Si is 1.7-1.9 and represents a significant increase in theoretical mobilities. The minimum mobility μ_{\min} is always less than μ_0 , the zero-stress mobility, by 30-40% near (001)Si and about 5% near (111)Si.

For p-type Si films, the effect of stress is always to increase the mobility, and both μ_{\max}^e and μ_{\min}^e are greater than μ_0 across the entire zone. The stress enhancement of the maximum mobility is minimal for (001)Si and increases rapidly in progressing across the zone. Values of the maximum mobility ratio μ_{\max}^e/μ_0 are in the range of 1.06-1.09 for (001)Si, 1.80-1.96 for (111)Si, 2.10-2.27 for (221)Si, and 2.32-2.44 for (110)Si.

It is interesting to note that the (001)Si orientation most commonly employed in Si-on-Al₂O₃ device fabrication is predicted to have the lowest mobility of all of the orientations studied. This holds for both n- and p-type Si, although the effect is somewhat more marked for p-type Si. These results indicate that the effect of thermal stress on mobility has a strong orientation dependence and that substantially larger mobilities may be achieved by prudent choice of film/substrate orientation.

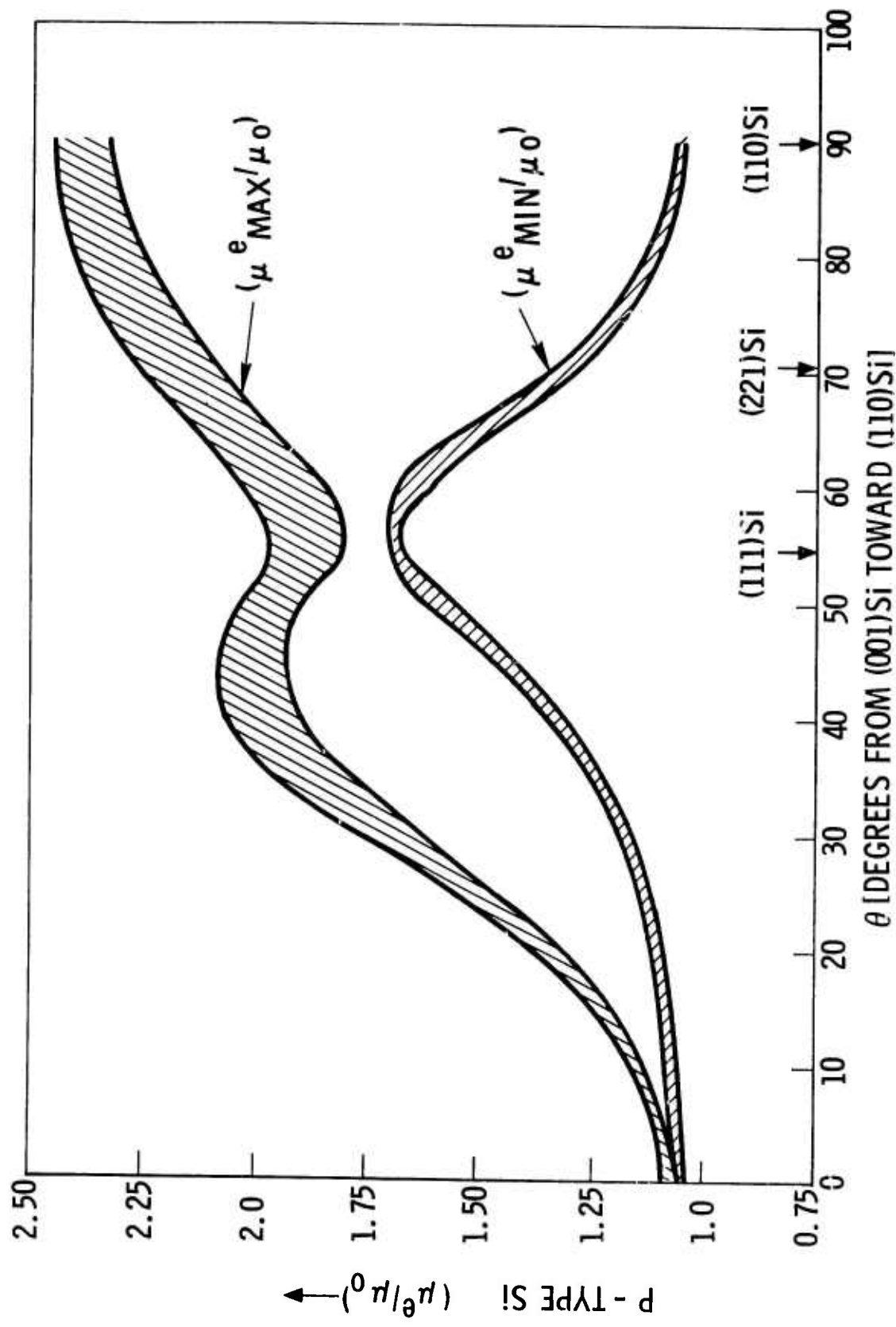


Figure 2. Theoretical Carrier Mobility Ratios $\mu_{\text{max}}^e / \mu_o$ and $\mu_{\text{min}}^e / \mu_o$ for P-type Si/ Al_2O_3 along (xx1)Si Zone.

The calculations for the (xxl)Si zone have assumed mathematically that each mode of epitaxy holds across the entire 90 deg zone from (001)Si to (110)Si. Experimentally it is well known that each mode of epitaxy holds over a more limited range. The theoretical thermal stress mobility data for n- and p-type Si/Al₂O₃ taken in conjunction with experimental growth data indicate that it would be worthwhile to explore experimentally Mode I epitaxial film growth in the approximate range from zero to 25 deg from (001)Si and Modes II, III and IV epitaxial film growth in the range +25 deg about (111)Si. (The mode definitions used here are as follows: Mode I: (001)Si//(01 $\bar{1}$ 2)Al₂O₃; Mode II: (111)Si//(11 $\bar{2}$ 4)Al₂O₃ and (221)Si//(11 $\bar{2}$ 2)Al₂O₃; Mode III: (111)Si//(11 $\bar{2}$ 0)Al₂O₃; and Mode IV: (111)Si//(10 $\bar{1}$ 4)Al₂O₃).

It is known that Si/Al₂O₃ film growth quality depends upon a variety of factors including intrinsic growth stresses, dislocation generation and carrier scattering, and impurity or heavy metal complexes, in addition to the thermal stress effect treated in this investigation. Although a formidable task, additional theoretical and experimental work directed toward understanding these phenomena should be undertaken.

This study of thermal stress effects represents the first systematic theoretical investigation of mobility as a function of orientation. The model provides a useful theoretical tool and, in conjunction with additional experimental investigations and selected-orientation growth studies, will lead to a better understanding of the Si/Al₂O₃ heteroepitaxial system and to means of optimizing Si/Al₂O₃ films for certain device applications.

SECTION 3

DEPOSITION STUDIES AND FILM PREPARATION

Throughout the program a continuing experimental study of the effects of various parameters upon the properties of deposited semiconductor films was carried out. In addition, a wide variety of film samples on various substrates was prepared for use in other parts of the contract program.

During these investigations the emphasis was placed on determining the effect of experimental parameters on the quality of Si epitaxial films grown by the SiH_4 pyrolysis CVD method on substrates of various orientations of Al_2O_3 and MgAl_2O_4 . In the early part of the program it was established for the growth system used that autodoping occurs in Si on Al_2O_3 at temperatures greater than about 1050C, so a concerted study was made which considered the effects of such factors as growth temperature, growth rate, and nucleation phenomena at or below this temperature.

It was determined that the electrical properties of undoped n-type heteroepitaxial Si films grown on various orientations of Al_2O_3 (and also MgAl_2O_4) by this method are dominated by surface-state conduction for carrier concentrations of $\sim 10^{16} \text{ cm}^{-3}$ or below. By adding AsH_3 to the SiH_4 n-type films of controllable carrier concentration could be prepared. Essentially equivalent (100)- and (111)-oriented Si films were grown on (01 $\bar{1}$ 2) and (10 $\bar{1}$ 4) Al_2O_3 substrates at deposition temperatures below the autodoping range ($\sim 1050\text{C}$).

Al_2O_3 orientations near the (11 $\bar{2}$ 0) plane, not previously used in heteroepitaxy studies, were also utilized as substrates for (111) Si heteroepitaxy. This resulted in electron mobilities of 600 to 700 $\text{cm}^2/\text{V-sec}$ for carrier concentrations of $10^{15} - 10^{17} \text{ cm}^{-3}$, exceeding mobilities obtained on either (01 $\bar{1}$ 2) or (10 $\bar{1}$ 4) Al_2O_3 substrates; however, good Si growth was achieved on (11 $\bar{2}$ 0) Al_2O_3 only at temperatures above the autodoping range. By increasing the Si growth rate and the deposition temperature T_g good quality films ($\mu \sim 500-600 \text{ cm}^2/\text{V-sec}$) were also formed on (01 $\bar{1}$ 2) Al_2O_3 ($1040\text{C} \leq T_g \leq 1100\text{C}$) and on (10 $\bar{1}$ 4) Al_2O_3 ($T_g \sim 1100\text{C}$).

Si films grown on $\sim(11\bar{2}0)\text{Al}_2\text{O}_3$ were still superior, however. At the high growth temperatures, autodoping took place during film growth, and annealing was found necessary to "homogenize" the electrical properties of the film. It was found that films $\sim 2\mu\text{m}$ thick seemed to stabilize after about 4 hr of total anneal; $5\mu\text{m}$ -thick films needed in many cases ~ 10 hr of total annealing time.

These studies revealed the strong interrelationships that exist among the various parameters involved in optimizing Si growth on insulators. Evaluation of the electrical properties of Si films on those orientations that produce the best Si overgrowths demonstrated that growth conditions (1) must be optimized for the particular substrate orientation chosen; (2) differ for those orientations which lead to the same Si orientation; (3) are dependent upon reactor geometry and gaseous atmosphere; and (4) must be optimized for the particular film thickness desired.

Studies of Si growth by SiH_4 pyrolysis at reduced pressures (1 to 10 torr) indicated that single-crystal growth can be obtained over a fairly wide temperature range, when conditions are optimized, on both Al_2O_3 and MgAl_2O_4 substrates; these results provided necessary confirmation of the feasibility of Si film growth in the pressure range to be used in the in situ CVD experiments in the electron microscope. Investigation of the growth of Si films on Al_2O_3 and MgAl_2O_4 using He as the growth atmosphere and the carrier gas showed that epitaxial growth could be achieved, although the conditions for best growth were not established at that time.

The effort in the final half of the second year was concentrated on continuing attempts to optimize the Si deposition process for growth on $\sim(11\bar{2}0)$ and $(01\bar{1}2)$ Al_2O_3 surfaces. In the course of this work the effects of post-nucleation annealing during the deposition process on ultimate film properties were examined, but no significant improvement in overall quality of Si films resulted from these procedures. The effects on film growth of gas-phase etching of Al_2O_3 surfaces prior to deposition were also evaluated further; there is some indication that surface damage may not be the primary factor in determining the quality of Si overgrowths, but this question must be examined in more detail.

The effects of cooled reactor chamber walls and various pedestal configurations on the Si growth process were also investigated, but no significant advantage of cooled walls in the vertical reactor systems used in this work was observed nor was a pedestal configuration found that improved the temperature uniformity across the pedestal surface.

Considerable additional study was made of the growth and properties of Si films deposited on Al_2O_3 and Czocharalski-grown stoichiometric spinel (MgAl_2O_4) in both He and He- H_2 atmospheres. This work indicated that Si films with electrical properties at least as good as those grown in H_2 atmosphere can be obtained on (01 $\bar{1}$ 2) and $\sim(11\bar{2}0)\text{Al}_2\text{O}_3$ when He- H_2 gas mixtures are used for the growth environment. It was also determined that autodoping is operative in the Si/ MgAl_2O_4 and Si/ Al_2O_3 systems in He- H_2 atmospheres at approximately the same temperatures as for Si/ Al_2O_3 grown in H_2 .

Toward the end of the contract program this work was concentrated on studies relating to the growth of Si on MgAl_2O_4 and GaAs on Al_2O_3 and GaAs, and to the support of other phases of the program by preparation of Si/ Al_2O_3 and GaAs/ Al_2O_3 films. These were prepared for further studies in anisotropy, lifetime measurements, fabrication of Schottky-barrier FET structures, high-field transport measurements, and for the evaluation of new tanks and sources of SiH_4 and AsH_3 .

These studies led to the formation of good quality n-type Si films on (111) MgAl_2O_4 with carrier mobilities higher than those achieved in the Si/ Al_2O_3 system. Mobilities as high as $925 \text{ cm}^2/\text{V-sec}$ were measured in films $\sim 2\mu\text{m}$ thick, but the mobilities were found to be influenced by the source tank of SiH_4 . It was also found to be more difficult to prepare a good quality film reproducibly on MgAl_2O_4 than on Al_2O_3 , presumably due to the relatively poorer MgAl_2O_4 surfaces.

P-type Si films were also grown using B_2H_6 as the dopant source. As in the case of the n-type films, better films were obtained on $\sim(11\bar{2}0)\text{Al}_2\text{O}_3$ ((111)Si growth) than on (01 $\bar{1}$ 2) Al_2O_3 ((100)Si growth), Hall mobilities being ~ 2 -3 times larger.

The GaAs studies, using the metalorganic growth process for both homoepitaxial and heteroepitaxial growth, were also found to be informative. It was demonstrated that the properties of films grown on Al_2O_3 and on GaAs substrates were almost equivalent for both thick and thin films; based on the properties obtained in these films it is expected that FET's can be successfully fabricated in thin films and Gunn devices in the thicker films grown on GaAs and on Al_2O_3 substrates.

Details of these investigations are given in the following sections.

1. ELECTRICAL PROPERTIES OF SI FILMS AS FUNCTIONS OF GROWTH PARAMETERS

Studies of the effects of various growth parameters and other variables on the quality of Si films grown on Al_2O_3 and MgAl_2O_4 substrates were undertaken early in the program, with attention directed toward identifying (1) the preferred substrate; (2) optimum growth temperatures; (3) preferred film orientations; (4) the preferred growth atmosphere; (5) preferred substrate orientations; and (6) the optimized overall growth process.

Particular attention was given initially to growth on Al_2O_3 , for this substrate has a rhombohedral crystal structure (Si is diamond-cubic) and could, therefore, provide epitaxial growth data potentially valuable to the theoretician's attempts to model heteroepitaxy. Since MgAl_2O_4 is a cubic material, like Si, it was considered initially as being less attractive as a host for Si in basic theoretical studies of heteroepitaxy because completely parallel orientation relationships (e.g., (111) Si// (111) MgAl_2O_4) have been observed in the Si- MgAl_2O_4 system.

On the other hand, considerable interest had been generated in MgAl_2O_4 as a possible preferred substrate for Si growth, based primarily on a comparison of the electrical properties of (100) Si growth on (01 $\bar{1}$ 2) Al_2O_3 with those of (111) Si growth on (111) MgAl_2O_4 . One of the criteria advanced for favoring MgAl_2O_4 over Al_2O_3 as a substrate for Si heteroepitaxy is that the thermal expansion coefficient for MgAl_2O_4 is less than that of (01 $\bar{1}$ 2) Al_2O_3 . However, the published data for this characteristic of the two materials vary, depending upon the reference source. Another criterion is the existence of a smaller lattice mismatch between Si and MgAl_2O_4 than between Si and Al_2O_3 .

Since one of the specific objectives of this program was the preparation of high-quality Si films on insulating substrates, comparative Si growth data on Al_2O_3 and MgAl_2O_4 were accumulated and evaluated. These studies were planned so as to lead to a realistic determination of the preferred substrate for hetero-epitaxial Si, based on such criteria as are listed above. There are several different orientations of Al_2O_3 that promote (111)Si growth; differences that are observed in the growth parameters which promote high quality (111)Si growth in these several cases should, therefore, be related to the condition of the substrate surface, its orientation, and its chemical behavior in the CVD environment. Such differences could be of considerable importance to the theoretician.

The Si growth studies in this program involved the formation of films by the pyrolysis of SiH_4 in the apparatus depicted in Figure 3. It consisted principally of a single vertical 60 mm-OD quartz (standard grade) tube 38 cm long, containing a SiC-covered carbon pedestal ("Ti-Kote", Texas Instruments) which could be inductively heated and rotated; a manifold made from 1/4-in stainless steel (type 316) tubing; appropriate flowmeters (Brooks Instruments) for monitoring the gas flows; a teflon connector (Beckman Instruments) to facilitate reactor exchange; and provision for separate evacuation of the flow lines and the reactor. During the working day a continual flow was maintained in the gas lines; only the reactor portion and connections were evacuated between experiments.

The H_2 carrier gas was Pd-purified, and the He was grade 6TM from Airco. The dopant sources used contained 200 ppm AsH_3 in H_2 and He carrier gases (Airco) and 195 ppm B_2H_6 in H_2 carrier gas (Scientific Gas).

Temperatures of the SiC-coated carbon pedestal were measured with an optical pyrometer and were not corrected for any apparent emissivity changes caused by the intervening quartz chamber wall. Because the composition of the gaseous atmosphere was found to affect the Si growth rate, during studies involving He- H_2 mixtures an infrared-sensing temperature monitor in combination with a recorder was used to determine when the desired film thickness was reached. This apparatus recorded the interference pattern caused by reflections in the double-layer Si and substrate system; the number of fringes displayed could

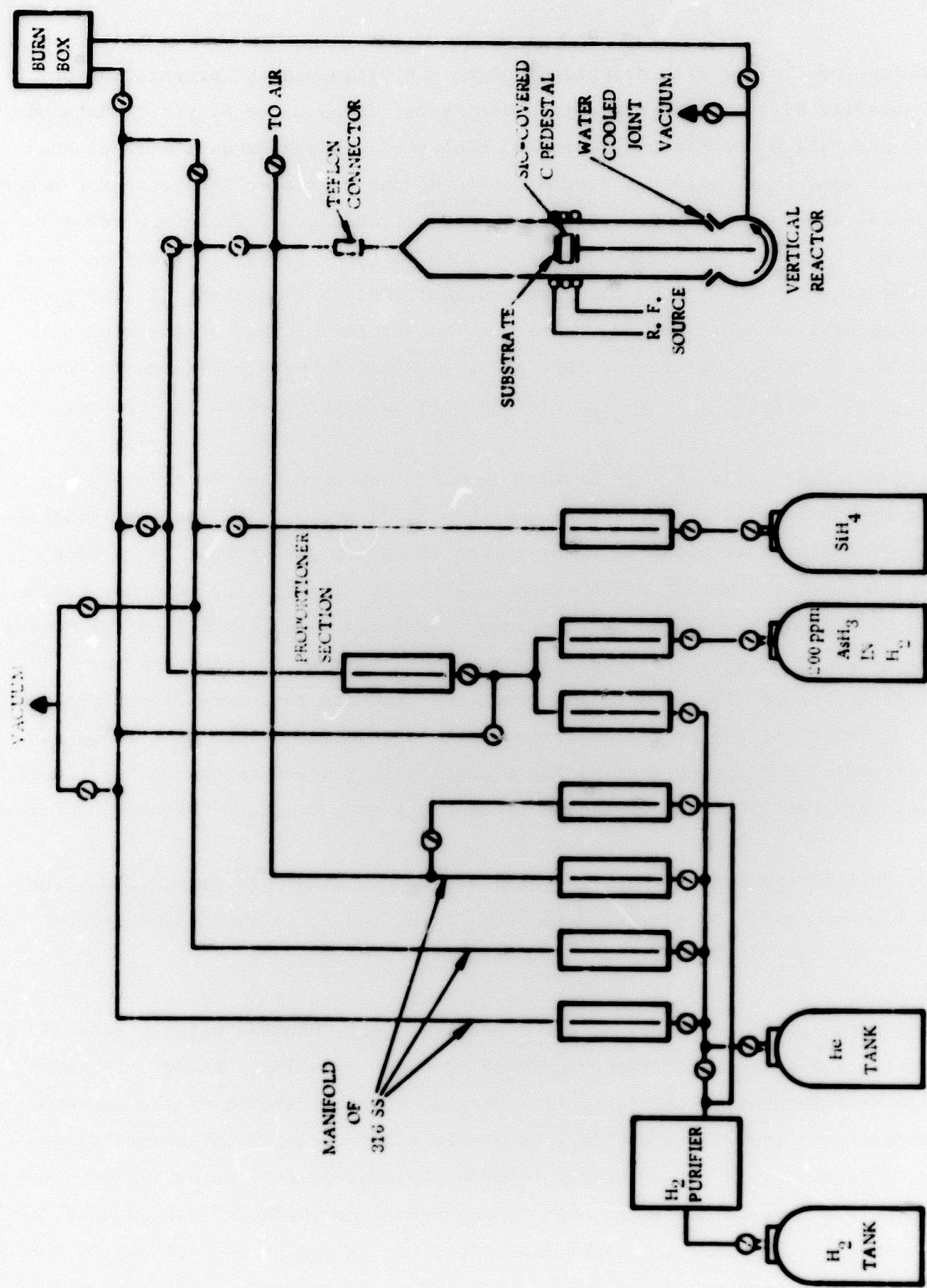


Figure 3. Schematic Diagram of Chemical Vapor Deposition Apparatus

be related to the film thickness. (It was observed that even after the SiH_4 and dopant sources were shut off, Si growth still continued in the CVD reactor for an additional $\sim 2000\text{\AA}$ of thickness when the SiH_4 concentration before the shut-off was relatively high and growth rates of $\sim 3\mu\text{m}/\text{min}$ were used.)

Based on previous studies of Si growth on Al_2O_3 (Ref 38) it is known that the orientation of the Si film can be controlled by selecting the orientation of the Al_2O_3 substrate. Major interest has been generated in the semiconductor industry in the growth of (100)Si which is obtained on $(01\bar{1}2)\text{Al}_2\text{O}_3$, but there have been reports of better electrical properties in (111)Si films grown on $(0001)\text{Al}_2\text{O}_3$ (Ref 39). This orientation appears to require relatively high temperatures ($\sim 1200\text{C}$) in the growth process for obtaining good quality films.

There are several orientations of Al_2O_3 that promote (111)Si growth, as indicated earlier, and some of these were examined along with $(01\bar{1}2)\text{Al}_2\text{O}_3$ in the process of determining preferred substrate orientations. Most studies of (111)Si growth on Al_2O_3 during this program were performed on $(10\bar{1}4)\text{Al}_2\text{O}_3$ and $\sim(11\bar{2}0)\text{Al}_2\text{O}_3$, with simultaneous growth being obtained on $(01\bar{1}2)\text{Al}_2\text{O}_3$ in many instances in order to compare (111)Si and (100)Si film properties. Some studies were also performed on $(11\bar{2}3)\text{Al}_2\text{O}_3$, which also promotes (111)Si growth, and on $(11\bar{2}2)\text{Al}_2\text{O}_3$, which promotes (221)Si growth. (See Section 10.)

Undoped thin Si films were prepared in the first part of the study in the expectation that the electrical properties of such films would be more sensitive to changes in CVD deposition parameters, substrate conditions, and other controllable factors. It was soon determined that undoped Si films which were n-type when grown below 1050C varied in donor carrier concentrations from $\sim 10^{12}$ to $\sim 7 \times 10^{15}\text{cm}^{-3}$, and some electron mobilities as high as $700\text{-}850\text{ cm}^2/\text{V-sec}$ were obtained; however, these electrical characteristics were found to be dominated by surface-state conduction, a very important effect which had not previously been reported in technical literature dealing with the properties of heteroepitaxial semiconductor films. (After those observations were first made, and possibly as a consequence of this situation being described in the early semiannual reports of this contract Refs 1, 2), a publication appeared which examined these surface effects (Ref 40).

It appeared expedient to add an n-type dopant, in this case As, to the growing film and to establish conditions for the growth of films with donor carrier concentrations from 10^{16} to $\sim 10^{18} \text{ cm}^{-3}$, so that the effects of the Si surface conduction might be minimized. It was found that the introduction of 0.03 to 0.3 ccpm of a mixture of 200 ppm AsH_3 in H_2 produced n-type films with $n = 10^{16}$ - 10^{17} cm^{-3} for a growth rate of $\sim 2 \mu\text{m}/\text{min}$. At lower growth rates, brought about by the introduction of less SiH_4 , a smaller quantity of AsH_3 was required to produce the same net donor doping level.

The electrical properties of n-type As-doped films grown in the early part of the program indicated essentially equivalent good quality (111)Si on $(10\bar{1}4)\text{Al}_2\text{O}_3$ and (100)Si on $(01\bar{1}2)\text{Al}_2\text{O}_3$ at growth temperatures as low as 950C. At temperatures $>1050\text{C}$ nominally undoped Si films grown in H_2 were invariably p-type (as determined with a thermoelectric hot probe), n-type when grown at 1000C, and sometimes both n-and p-type in adjoining areas when grown at $\sim 1050\text{C}$. It was also observed that hot-probe typing led to the same results for films grown in a He atmosphere, a rather surprising result which might be explained if the reaction of Equation (20) were more important than that of Equation (19) in an autodoping process.



The above considerations indicated that the preferred growth temperature range for further work with Si heteroepitaxy on Al_2O_3 was 950-1050C to provide (100)- and (111)-oriented Si films essentially uncompensated by Al. However, the films grown in H_2 on $(10\bar{1}4)\text{Al}_2\text{O}_3$ were not superior to those grown on $(01\bar{1}2)\text{Al}_2\text{O}_3$. When $\sim(11\bar{2}0)\text{Al}_2\text{O}_3$ was examined as a substrate for (111)Si growth - as a means for improving Si film quality - it was found necessary to use temperatures in excess of 1050C to obtain reflective n-type films. These were electrically superior to those grown on $(01\bar{1}2)\text{Al}_2\text{O}_3$ and on $(10\bar{1}4)\text{Al}_2\text{O}_3$, a mobility increase of about 20% being realized.

At the higher temperatures (e.g., ~1060C), determination of the correct carrier concentration was complicated by the presence of Al coming from the Al_2O_3 substrate and becoming incorporated into the film during growth. This impurity served to compensate the As already present and had to be removed before the As concentration could be estimated. For this reason, an 1100C anneal in an O_2 atmosphere for at least one hour was employed in the early studies before measurement in order to remove the Al impurity. The higher growth temperatures (up to 1100C) and subsequent anneal did not appear to degrade the electrical properties of (100)Si films grown on $(01\bar{1}2)\text{Al}_2\text{O}_3$, as indicated below.

A summary of the electrical properties of n-type Si/ Al_2O_3 films ~2 μm thick grown in H_2 is shown in Figures 4 and 5. Most of the data were obtained on films grown at ~2 $\mu\text{m}/\text{min}$. Lower growth rates tended to produce poorer films over most of the temperature range examined, except for films on $(01\bar{1}2)\text{Al}_2\text{O}_3$ which exhibited equivalent mobilities at growth rates of ~0.8 $\mu\text{m}/\text{min}$.

It was found that for a growth rate of 2 $\mu\text{m}/\text{min}$ the electron mobility in (100)Si/ $(01\bar{1}2)\text{Al}_2\text{O}_3$ was nearly independent of growth temperature for $1040\text{C} \leq T_g \leq 1100\text{C}$. At both higher and lower growth temperatures the data suggested that the mobility decreased. This is shown in Figure 4, where the mobilities of films grown on $(01\bar{1}2)$ and $(11\bar{2}0)\text{Al}_2\text{O}_3$ substrates are plotted as a function of growth temperature. At each temperature data for a number of films with net donor concentrations between 1 and $5 \times 10^{16} \text{cm}^{-3}$ are averaged; the error bars indicate the range of mobilities over which the points are averaged (not the error in the data point itself), and the number next to the point indicates how many samples contributed to the average value plotted. All films were annealed at least one hour in O_2 at 1100C to stabilize film properties.

Contrary to the case for the (100)Si growth on $(01\bar{1}2)\text{Al}_2\text{O}_3$, the data for (111)Si growth on the Al_2O_3 orientation near the $(11\bar{2}0)$ plane show that a 2 $\mu\text{m}/\text{min}$ growth rate yielded films which appeared to improve with increasing growth temperature and showed a mobility maximum around 1075-1100C.

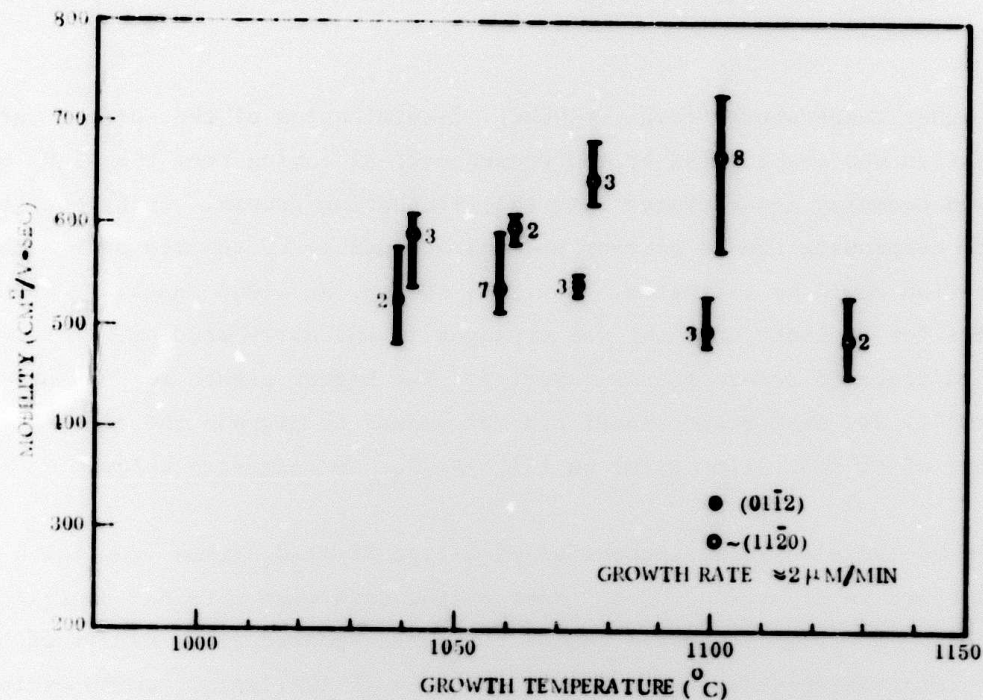


Figure 4. Variation of Hall Mobility with Growth Temperature for Si/Al₂O₃ Films Having Net Donor Carrier Concentration of $1-5 \times 10^{16} \text{cm}^{-3}$.

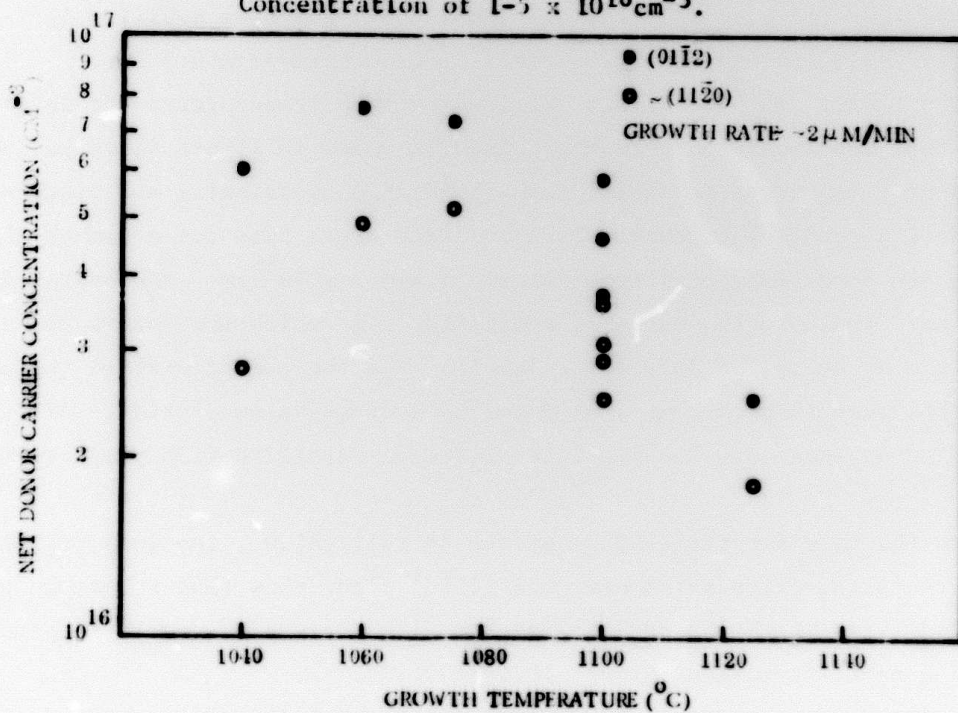


Figure 5. Variation of Net Donor Carrier Concentration with Growth Temperature for Si/Al₂O₃ Films Grown at $\sim 2 \mu\text{m}/\text{min}$ with Constant Dopant-gas Flow Rate.

The variations of carrier concentration with growth temperature for a constant dopant gas flow rate (0.22 ccpm $\text{AsH}_3\text{-H}_2$ mixture) and constant growth rate ($\sim 2\mu\text{m}/\text{min}$) are plotted in Figure 5 and indicate no definite trend except for the slight decrease in carrier concentration at the highest growth temperatures.

It was found that higher growth rates can improve mobilities for Si films grown on the $(01\bar{1}2)\text{Al}_2\text{O}_3$ orientation at higher temperatures. The effects of growth rate on the mobility of films on $(01\bar{1}2)$ and also on $\sim(11\bar{2}0)\text{Al}_2\text{O}_3$ are plotted in Figure 6 (for growth at 1075C). The mobility data indicate that high growth rates are necessary to produce optimized film properties at this (and presumably higher) temperature on $(01\bar{1}2)\text{Al}_2\text{O}_3$; for 1075C the mobility maximum seems to occur at a growth rate of about $4\mu\text{m}/\text{min}$ for the $(01\bar{1}2)$ orientation and about $2\mu\text{m}/\text{min}$ for the orientation near the $(11\bar{2}0)$.

These films were grown under conditions of constant dopant gas flow. However, the measured carrier concentration was found to vary with growth rate as shown in Figure 7. The observed behavior shown in Figure 7 suggests an exponential relationship between growth rate and carrier concentration. These data point out the importance of growth rate as well as growth temperature in determining the quality of Si films grown on Al_2O_3 substrates.

At constant growth rate the carrier concentration is related to the dopant gas flow as shown in Figure 8. The data are seen to agree with the dashed curve, representing a linear relationship between the two parameters, as would be expected. It is interesting to note that the carrier concentrations found in films on $\sim(11\bar{2}0)\text{Al}_2\text{O}_3$ were consistently lower than those grown simultaneously on $(01\bar{1}2)\text{Al}_2\text{O}_3$. This fact suggests that the dopant is incorporated less easily into the (111) -oriented Si lattice.

Growth of Si on various other Al_2O_3 orientations at high growth temperatures was also examined. This study was stimulated by the observation that the quality of $(111)\text{Si}$ appeared to be quite high at 1100C, and that some other orientations produced very reflective films at high temperatures. The $(10\bar{1}4)$, $(11\bar{2}2)$, and $(11\bar{2}3)\text{Al}_2\text{O}_3$ orientations were used as substrates for Si growth

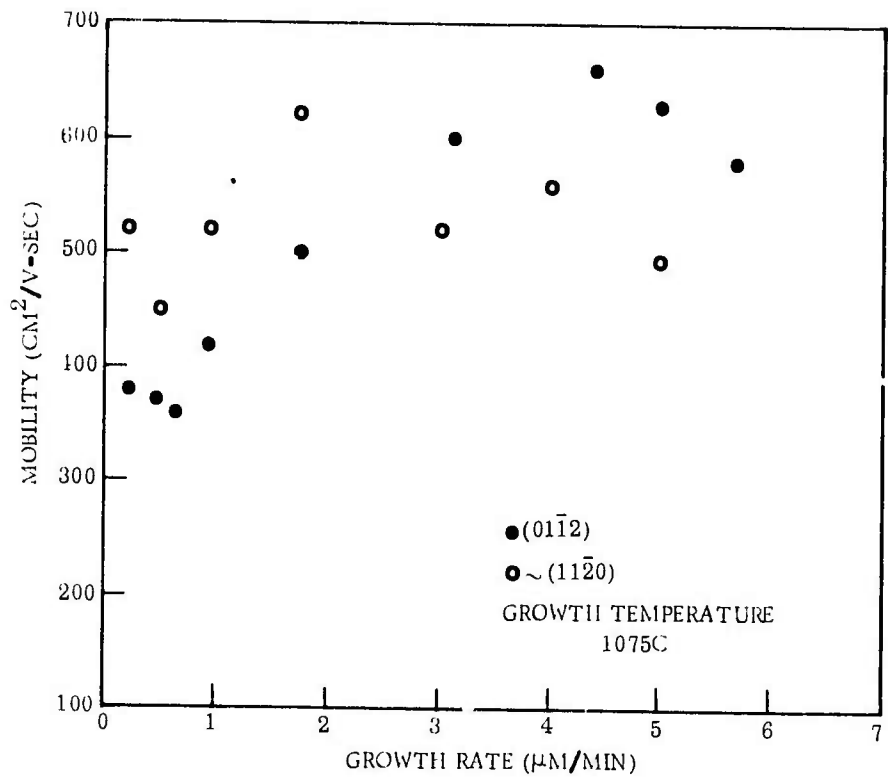


Figure 6. Variation of Hall Mobility with Growth Rate for N-type Si/Al₂O₃ Films Grown at 1075C.

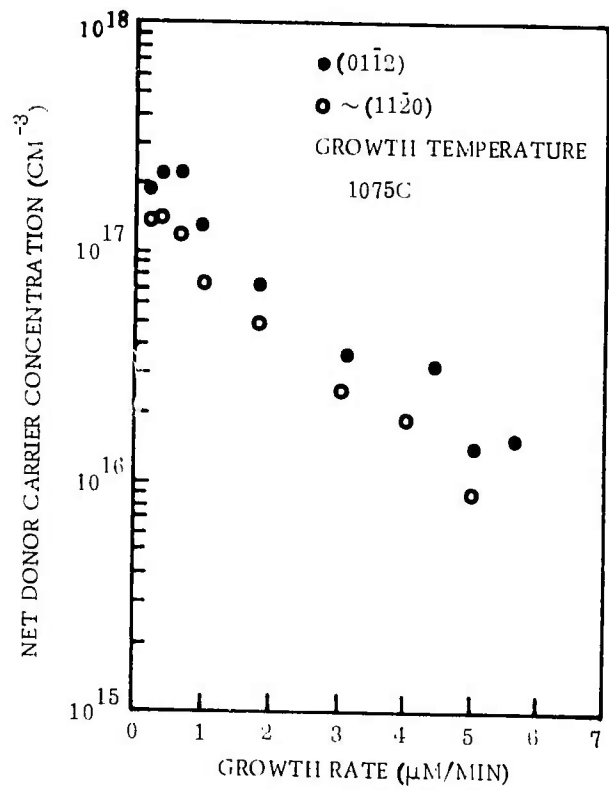


Figure 7. Variation of Net Donor Carrier Concentration with Growth Rate for Si/Al₂O₃ Films Grown at 1075C with Constant Dopant-gas Flow Rate.

at temperatures from 1075 to 1150C. For film thicknesses of 1.5 to 1.9 μ m and carrier concentrations of $1-2 \times 10^{16} \text{cm}^{-3}$, the (10 $\bar{1}$ 4) and (11 $\bar{2}$ 3) orientations yielded films with mobilities of 400 - 500 $\text{cm}^2/\text{V}\text{-sec}$ over the whole temperature range. The (11 $\bar{2}$ 2) orientation gave (221)-oriented Si films with surprisingly high mobilities - up to 770 $\text{cm}^2/\text{V}\text{-sec}$ in a 1.5 μ m thick film - suggesting that this orientation may be superior to those previously examined. The properties of films grown on (11 $\bar{2}$ 2)Al₂O₃ are further discussed later in the report in the section dealing with anisotropy/orientation correlations.

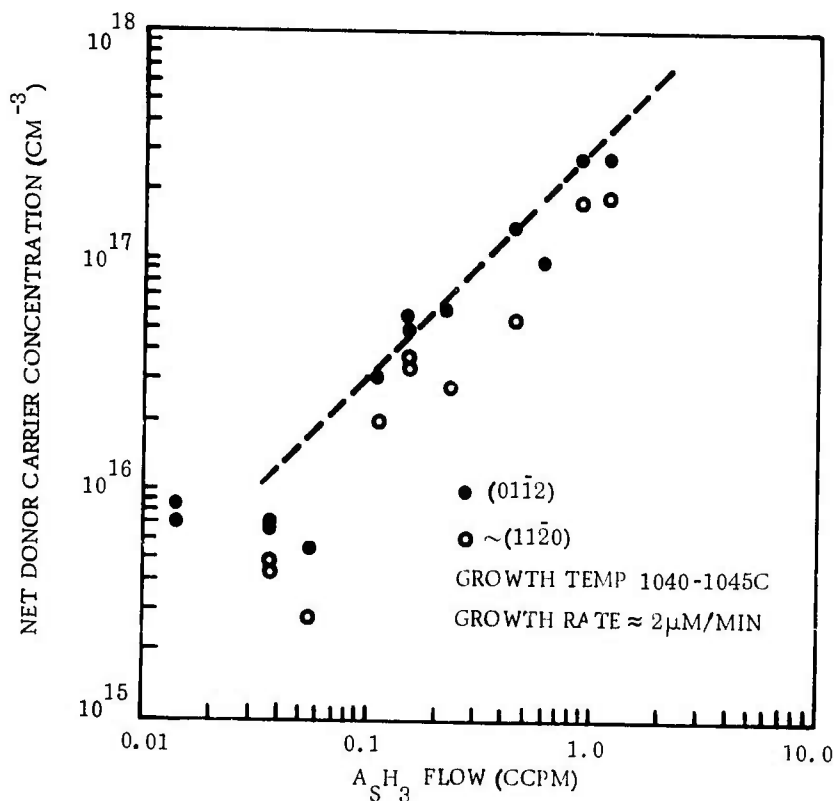


Figure 8. Variation of Net Donor Carrier Concentration with AsH₃ Flow Rate for Si/Al₂O₃ Films.

2. VARIATIONS IN Si FILM PROPERTIES WITH THICKNESS

Measurements of the variation of electrical properties with film thickness were also undertaken. It had been well established previously that the electrical properties of heteroepitaxial semiconductor films tend to be inferior close to the substrate on which growth occurs. An important task of this program was to determine the variation of electrical properties with distance from the substrate and deduce what steps might be taken to improve the properties of the interface layer, thereby reducing film inhomogeneity.

As a first step in this study, three $\sim 1.8\mu\text{m}$ -thick n-type Sb-doped Si/ Al_2O_3 films were examined by resistivity and Hall-effect measurements as the films were thinned in successive steps by metallographic polishing techniques. The films were grown simultaneously at 1065C on $(01\bar{1}2)$, $\sim(11\bar{2}0)$, and $(10\bar{1}4)\text{Al}_2\text{O}_3$ substrates. (The samples were not annealed to remove Al impurities and so might be considered to have greater variation in properties than corresponding annealed films.)

Electrical measurements were made after each polishing step and are recorded in Figures 9 and 10. The small variation in properties during the first several steps tends to rule out work damage introduced during polishing as the source of the observed behavior. In all cases the mobility (Figure 9) decreases and reaches approximately one-half the thick-film value at a thickness of about $0.5\text{-}0.7\mu\text{m}$. Below this thickness the mobility falls off more rapidly, suggesting an extremely low mobility at the interface.

The variation in carrier concentration (Figure 10) also decreases with decreasing film thickness except for the film grown on the $(10\bar{1}4)$ orientation, which appears to have an increase in donor concentration. The latter may be anomalous, however, due to the way in which the carrier concentrations were calculated. Such behavior could be the result of an underlying p-type layer (possibly due to enhanced Al concentration near the interface) resulting in an overestimate of the film thickness used in the calculation.

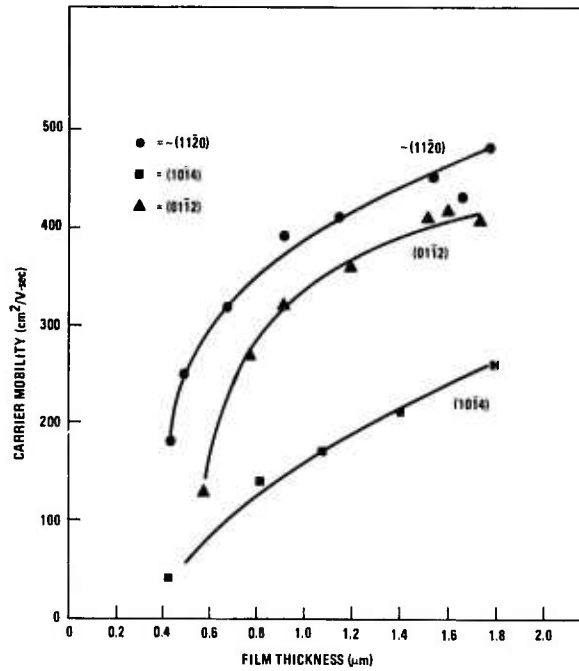


Figure 9. Carrier Mobility as Function of Distance from Interface for CVD Si Films on Three Orientations of Al_2O_3

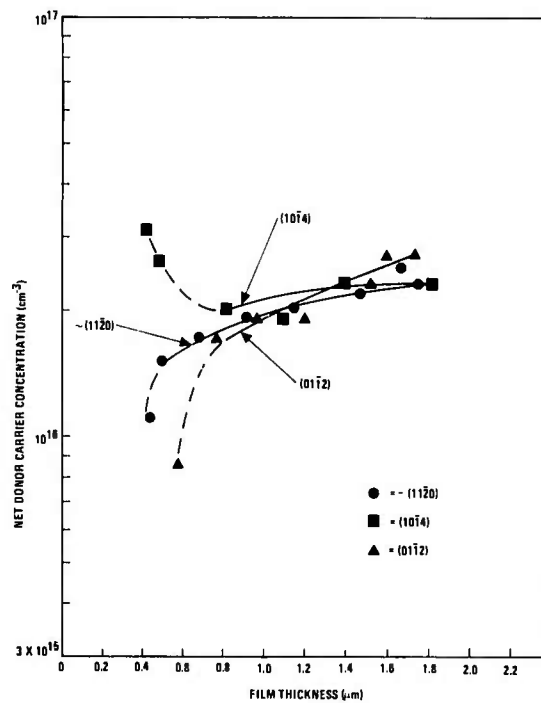


Figure 10. Net Donor Carrier Concentration as Function of Distance from Interface for CVD Si Films on Three Orientations of Al_2O_3

The electrical properties of As-doped n-type (100)Si/(01 $\bar{1}$ 2)Al₂O₃ films grown at 1100C were also examined as a function of film thickness. Measurements of as-grown films with thicknesses from 0.2 to 1.2 μ m indicated that a considerably higher acceptor concentration exists near the interface than farther away, as evidenced by a net donor concentration which increases with film thickness.

After a one-hour anneal in O₂ considerably less variation of film properties with thickness was apparent, as illustrated in Figure 11 for films grown on (01 $\bar{1}$ 2)Al₂O₃ and \sim (11 $\bar{2}$ 0)Al₂O₃ to the indicated thickness. The carrier concentrations remained relatively constant, decreasing only slightly for thinner films, but the mobilities showed a steady decrease with decreasing film thickness for both orientations.

When the films on (01 $\bar{1}$ 2)Al₂O₃ were reduced stepwise in thickness by polishing and then remeasured electrically, the average mobility showed the same general thickness dependence as that exhibited in Figure 11. The carrier concentrations, however, appeared to vary even less with thickness than the slight change indicated in the plot in Figure 11.

Although these results suggested that Al autodoping appears to be much heavier near the Si-Al₂O₃ interface, particularly in the first 1 μ m of growth, profiling studies of intentionally undoped p-type films \sim 5 μ m thick indicated a nearly uniform concentration of Al at thicknesses greater than 1 μ m. For these measurements, films were grown on (01 $\bar{1}$ 2), \sim (11 $\bar{2}$ 0), and (10 $\bar{1}$ 4)Al₂O₃ substrates at 1100C, and then reduced stepwise in thickness.

The results of electrical measurements made after each step are shown in Figures 12 and 13. Although the Al concentration appears to be relatively constant over the range of thicknesses investigated, it is interesting to note that the hole mobility appears to be steadily increasing with film thickness. The mobilities found in the films on (10 $\bar{1}$ 4) and \sim (11 $\bar{2}$ 0) substrates are nearly equivalent to that of bulk Si.

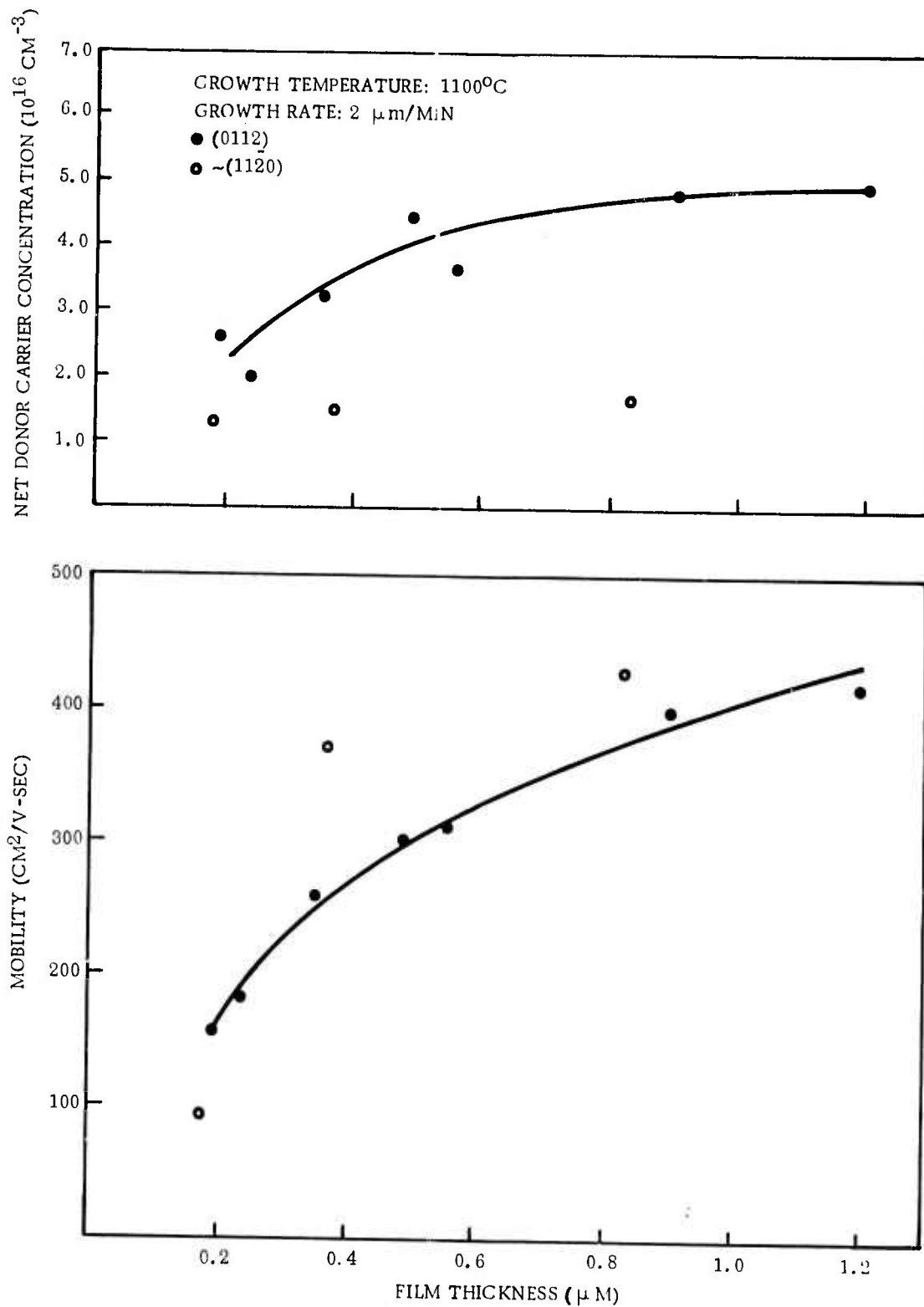


Figure 11. Variation of Film Properties with Film Thickness for Thin N-type $\text{Si}/\text{Al}_2\text{O}_3$ Films. (All films annealed after growth for 1-hr in O_2 at 1100C.)

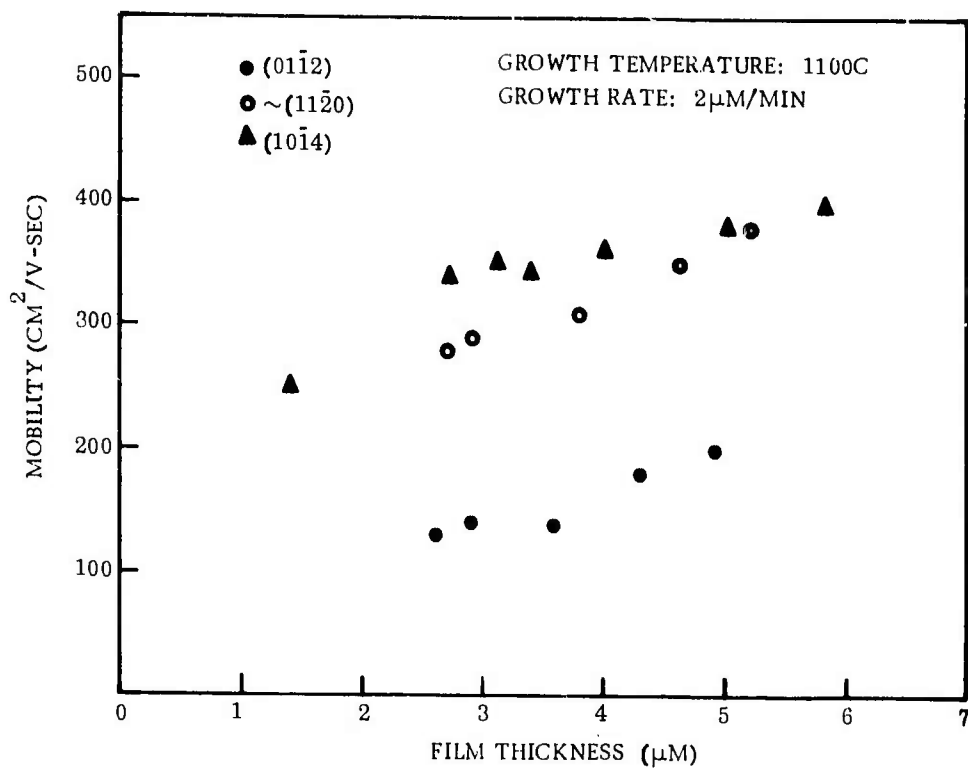


Figure 12. Variation of Hall Mobility with Film Thickness for Intentionally Undoped P-type Si/Al₂O₃ Films

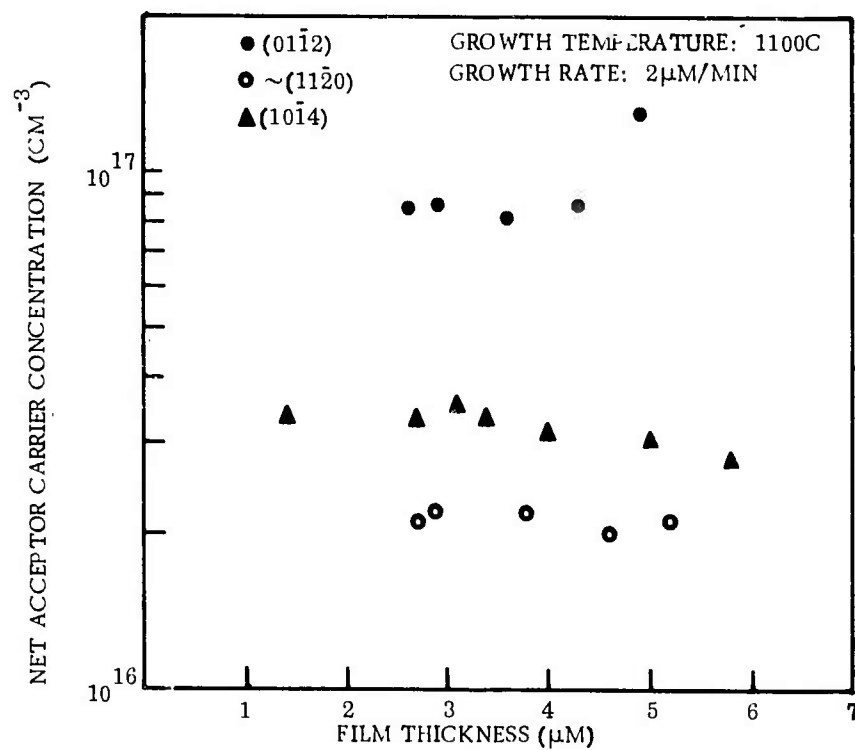


Figure 13. Variation of Net Acceptor Concentration with Film Thickness for Intentionally Undoped Si/Al₂O₃ Films

The uniformity in properties of Si films was also recently investigated by examining the variation in electrical properties over the surface of a typical n-type Si/Al₂O₃ film. Three Hall bridges were etched at various positions on each of several films, and results of measurements on these bridges were compared after annealing at 1100C in O₂ for one hour. Differences in electrical properties between bridges of ~20% or less were not considered to be significant, since the error in determination of bridge width and film thickness can easily lead to errors of $\pm 10\%$. Out of 10 samples examined (with three bridges on each), two samples showed differences in resistivity among bridges of nearly a factor of two, while one showed a difference of 50% and another a difference of 25%. The remaining films all showed a resistivity spread of 20% or less.

The degree of uniformity of film properties does not appear to be completely or exclusively related to film growth conditions and is probably strongly dependent upon details of substrate surface preparation. This study does clearly indicate that conclusions regarding such things as optimum growth conditions and optimum substrate species or orientation based on electrical data for only a few samples may be erroneous, and that a sufficiently large group of samples must be used in order to draw meaningful conclusions.

An apparent nonreproducibility of the electrical properties of Si films grown on MgAl₂O₄ substrates over a considerable period of time suggested that substrate crystal origin and surface preparation may have more significant influence on film quality than in the Si/Al₂O₃ system. Accordingly, some experiments were undertaken to evaluate the growth of Si/MgAl₂O₄ using substrates of various origins with growth surfaces prepared and treated in a variety of ways.

The Si films were grown under nominally the same growth conditions which had previously yielded good quality Si on Al₂O₃ substrates. The results indicated that no firm conclusions could be drawn; Hall mobility variations from approximately 400 to about 750 cm²/V-sec showed no definite trends relating to substrate origin and/or preparation. This suggests that an additional factor or factors may be controlling the Si film quality on MgAl₂O₄ substrates.

The electrical properties as a function of film thickness were examined in two n-type Si/(111)MgAl₂O₄ films. Data were obtained by successively thinning the films and remeasuring the electrical properties. The mobilities of the as-grown films were greater than those obtained for Si/Al₂O₃ films of approximately the same thickness and studied in the same way (Ref 3).

Data on a 5.4μm-thick sample are shown in Figure 14, and similar data on a 1.4μm-thick sample are shown in Figure 15. The mobilities were found to decrease much more rapidly with film thickness for thicknesses less than 0.5μm than was the case for the Si/Al₂O₃ films. This result is rather surprising and suggests that additional comparisons between the early stages of growth of (111)Si on Al₂O₃ and on MgAl₂O₄ substrates should be undertaken. If consistent results were to be obtained verifying the behavior described above, it could be a significant factor in the choice of substrate for device applications using films ~1μm thick.

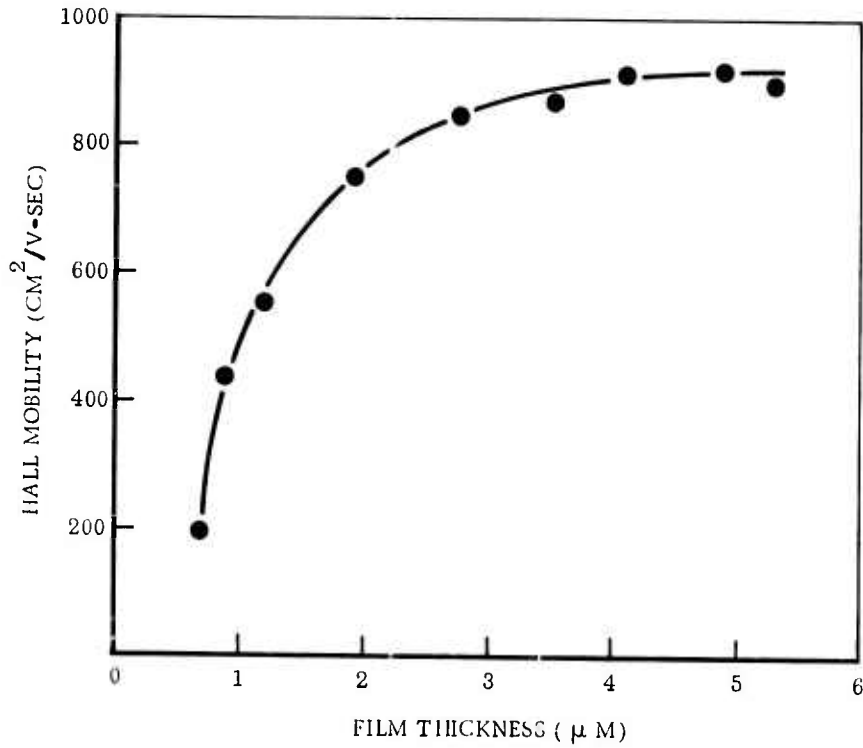


Figure 14. Hall Mobility as Function of Film Thickness for N-type (111)Si/(111)MgAl₂O₄. (Sample initially 5.4μm thick.)

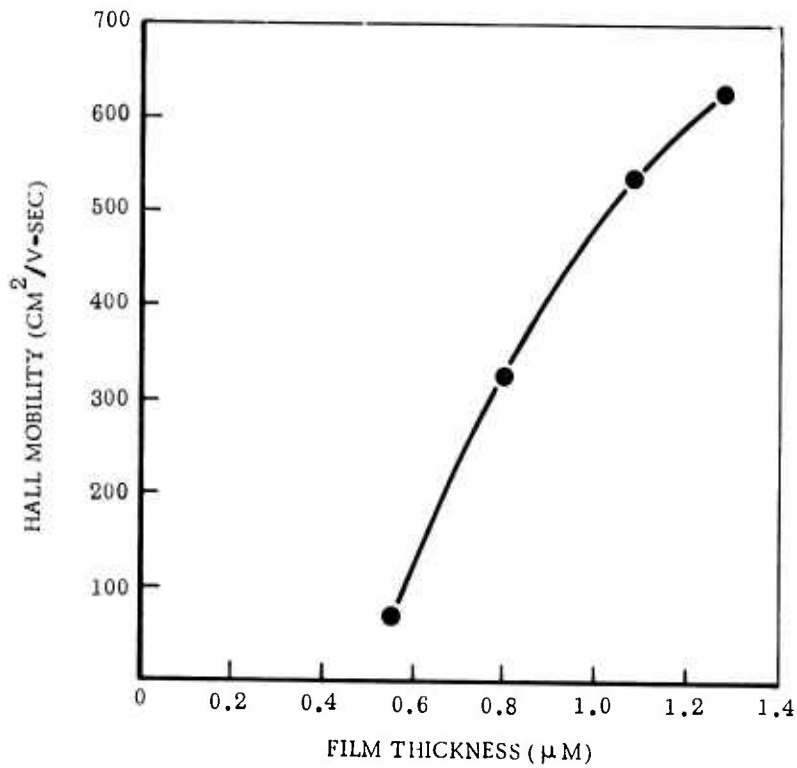


Figure 15. Hall Mobility as Function of Film Thickness for N-type (111)Si/(111)MgAl₂O₄. (Sample initially 1.4μm thick.)

3. PROPERTIES OF P-TYPE Si/Al₂O₃ FILMS

Doping experiments with Si films on Al₂O₃ for the purpose of achieving p-type films were undertaken with diborane (B₂H₆) as the source of B. A calibration curve for a range of carrier concentrations from $\sim 3 \times 10^{16}$ to $\sim 2 \times 10^{20} \text{ cm}^{-3}$ was established for p-type Si films grown on (01 $\bar{1}$ 2)Al₂O₃ at 1025C and on (01 $\bar{1}$ 2), $\sim(11\bar{2}0)$, and (10 $\bar{1}$ 4)Al₂O₃ at $\sim 1075\text{C}$; the curve is shown in Figure 16.

The electrical properties of the p-type Si-on-Al₂O₃ films prepared in these experiments are reported in Tables 3 and 4. The electrical properties of unannealed and annealed films were measured using the van der Pauw technique (Ref 41) and are therefore only approximate. The anneals consisted of 1/2 hr oxidation at 1100C followed by 2 hrs in N₂ at the same temperature.

The data for the films, most of them annealed, are shown graphically in Figure 17. The electrical properties of the p-type (100)Si on (01 $\bar{1}$ 2)Al₂O₃ are similar to those reported in the literature (Ref 42). These results indicate that annealing only slightly affects the properties of p-type (100)Si films grown at 1025C. However, for (100)Si films grown at 1075C (where autodoping phenomena can be important) annealing is definitely required for those films exhibiting hole concentrations in the range 10^{16} - 10^{17} cm^{-3} .

From Table 3 it can be seen that annealing changes the properties of as-grown (100) p-type films more severely at the higher growth temperature (1075C) than at the lower (1025C), as expected, presumably due to the removal of Al "autodoping" impurities. Since the electrical properties of the annealed films seem equivalent at both growth temperatures for films of the same carrier concentration, either growth temperature appears to be adequate for p-type (100) Si growth. The data in Tables 3 and 4, based on changes in properties upon annealing, suggest that autodoping is more severe in films grown at 1075C on (10 $\bar{1}$ 4)Al₂O₃ and (01 $\bar{1}$ 2)Al₂O₃ than on (11 $\bar{2}$ 0)Al₂O₃. This is consistent with the data in Figure 18 in the next section, which show the same trend.

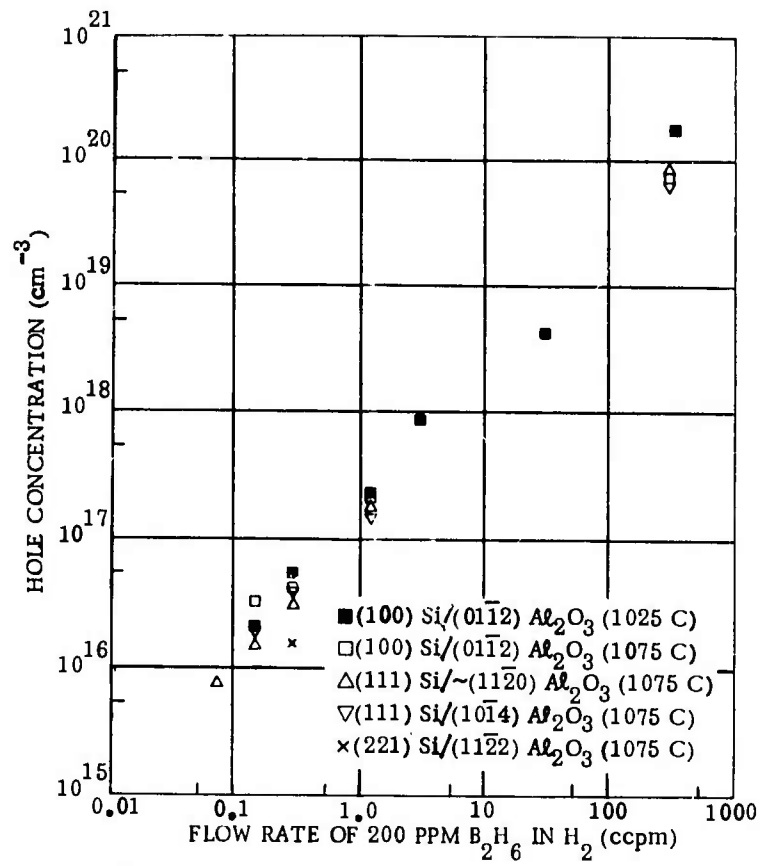


Figure 16. Calibration Curve for Growth of P-type Si/Al₂O₃ Films Using B₂H₆ Dopant Source

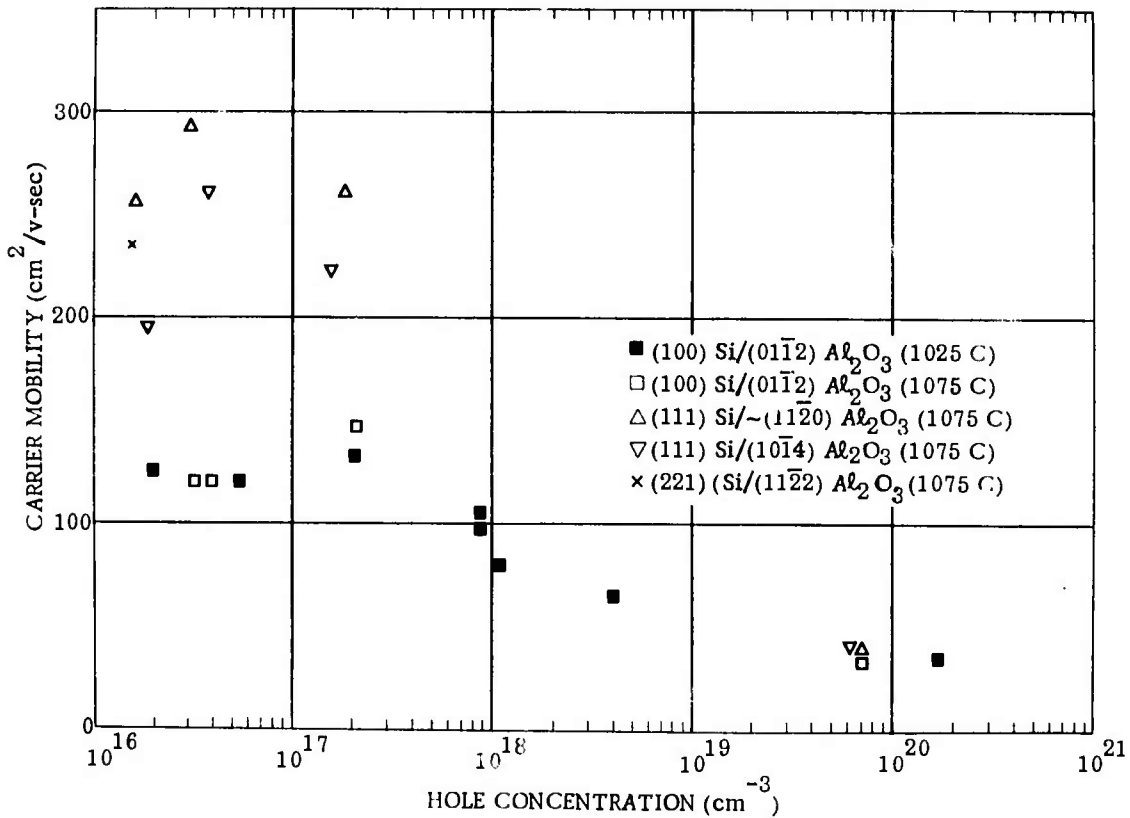


Figure 17. Electrical Properties of P-type Si/Al₂O₃ Films Doped with Boron

Table 3. Properties of 2 μ m-thick P-type (100)Si Films on (0112)Al₂O₃

Growth Temp. (C)	Flow Rate of Doping Mixture (200 ppm B ₂ H ₆ in H ₂) (ccpm)	Electrical Properties*			Annealing Step†
		Resistivity (ohm-cm)	Hole Concentration (cm ⁻³)	Hole Mobility (cm ² /V-sec)	
1025	0.15	3.0	1.8 x 10 ¹⁶	119	As Grown 1st
		2.5	2.0 x 10 ¹⁶	126	
1025	0.3	0.84	6.2 x 10 ¹⁶	120	As Grown 1st 2nd
		0.90	5.1 x 10 ¹⁶	136	
		0.95	5.4 x 10 ¹⁶	121	
1025	1.2	0.21	2.6 x 10 ¹⁷	113	As Grown 1st 2nd
		0.22	2.3 x 10 ¹⁷	121	
		0.22	2.1 x 10 ¹⁷	135	
1025	3.0	0.07	8.7 x 10 ¹⁷	106	As Grown
1025	30	0.024	3.9 x 10 ¹⁸	67	As Grown 1st
		0.024	4.0 x 10 ¹⁸	65	
1025	340	8.5 x 10 ⁻⁴	2.1 x 10 ²⁰	35	As Grown 1st
		1.0 x 10 ⁻³	1.7 x 10 ²⁰	36	
1075	0.15	1.0	5.6 x 10 ¹⁶	108	As Grown 1st
		1.6	3.3 x 10 ¹⁶	121	
~1075	0.3	0.45	1.2 x 10 ¹⁷	116	As Grown 1st 2nd
		1.0	5.0 x 10 ¹⁶	120	
		1.2	4.0 x 10 ¹⁶	120	
1075	1.2	0.17	3.3 x 10 ¹⁷	111	As Grown 1st 2nd
		0.19	1.8 x 10 ¹⁷	118	
		0.20	2.1 x 10 ¹⁷	147	
1075	300	2.7 x 10 ⁻³	6.9 x 10 ¹⁹	34	As Grown

* Obtained by van der Pauw measurements.

† Each anneal consisted of 1/2 hour in O₂ and 2 hours in N₂, at 1100C.

Table 4. Properties of 2 μ m-thick P-type (111)Si Films on $\sim(11\bar{2}0)$ and $(10\bar{1}4)Al_2O_3$ at 1075C

Al ₂ O ₃ Orientation	Flow Rate of Doping Mixture (200 ppm B ₂ H ₆ in H ₂)(ccpm)	Electrical Properties*			Annealing Step†
		Resistivity (ohm-cm)	Hole Concentration (cm ⁻³)	Hole Mobility (cm ² /V-sec)	
$\sim(11\bar{2}0)$	0.075	4.0	8.1 x 10 ¹⁵	192	As Grown** 1st
		3.5	7.4 x 10 ¹⁵	241	
$\sim(11\bar{2}0)$	0.15	1.0	2.6 x 10 ¹⁶	243	As Grown 1st
		1.6	1.6 x 10 ¹⁶	255	
$\sim(11\bar{2}0)$	0.3	0.44	6.1 x 10 ¹⁶	234	As Grown 1st 2nd
		0.68	3.5 x 10 ¹⁶	260	
		0.66	3.2 x 10 ¹⁶	294	
$\sim(11\bar{2}0)$	1.2	0.12	2.2 x 10 ¹⁷	236	As Grown 1st 2nd
		0.13	2.0 x 10 ¹⁷	242	
		0.13	1.9 x 10 ¹⁷	258	
$\sim(11\bar{2}0)$	300	2.1 x 10 ⁻³	7.8 x 10 ¹⁹	38	As Grown
$(10\bar{1}4)$	0.15	1.0	3.2 x 10 ¹⁶	203	As Grown 1st
		1.8	1.9 x 10 ¹⁶	191	
$(10\bar{1}4)$	0.3	0.31	9.6 x 10 ¹⁶	211	As Grown 1st 2nd
		0.58	4.2 x 10 ¹⁶	257	
		0.62	3.9 x 10 ¹⁶	258	
$(10\bar{1}4)$	1.2	0.15	2.2 x 10 ¹⁷	189	As Grown 1st 2nd
		0.17	1.8 x 10 ¹⁷	205	
		0.17	1.6 x 10 ¹⁷	224	
$(10\bar{1}4)$	300	2.3 x 10 ⁻³	6.6 x 10 ¹⁹	41	As Grown

* Obtained by van der Pauw measurements

† Each anneal consisted of 1/2 hr in O₂ and 2 hrs in N₂, at 1100C.

**3.7 μ m thick

As compared for n-type films, the doping levels in p-type (100)Si appear to be higher than in (111)Si films grown on Al_2O_3 at the same temperature, for a given amount of dopant added. The differences, however, are not as great in the p-type films.

The electrical data for the p-type films grown on $\sim(11\bar{2}0)$ and $(10\bar{1}4)\text{Al}_2\text{O}_3$ are most encouraging, with properties exceeding those measured on $(01\bar{1}2)\text{Al}_2\text{O}_3$ twofold or more for hole concentrations at least in the $10^{16} - 10^{18} \text{ cm}^{-3}$ range (see Figure 17). The results are essentially equivalent to values for bulk Si, and appear to be the largest yet recorded for Si films only $2\mu\text{m}$ thick on Al_2O_3 . Further comparisons of Tables 3 and 4 indicate a lower hole concentration in (111)Si films than in (100)Si films for the same amount of dopant added, and almost equivalent properties for p-type (111) films grown on $(10\bar{1}4)$ and $\sim(11\bar{2}0)\text{Al}_2\text{O}_3$. (For n-type films grown in H_2 it was found the films grown on $\sim(11\bar{2}0)\text{Al}_2\text{O}_3$ were superior to those on $(10\bar{1}4)$ substrates.)

4. STUDY OF AUTODOPING IN Si FILMS ON Al_2O_3 AND MgAl_2O_4

As discussed earlier, Al autodoping from the Al_2O_3 substrates has been shown to cause appreciable doping of epitaxial Si films at temperatures greater than ~ 1050 C. In order to determine more precisely the extent of this doping, a number of films not intentionally doped were grown in H_2 as a function of temperature from 1050 to 1150 C. The average acceptor concentrations measured in these films are shown plotted versus growth temperature in Figure 18 for ~ 2 μm -thick films grown at a rate of approximately 2 $\mu\text{m}/\text{min}$. Each data point represents an average value for data obtained from 1 to 3 samples. It is clear that slight changes in growth temperature can appreciably alter the extent of Al doping, since the acceptor concentration varies by over two orders of magnitude for growth temperature changes of just 100 deg C.

These experiments raise the question of the extent to which autodoping affects the quality of Si films and any devices formed in such films. As will be discussed in the next section, annealing sequences can apparently deactivate, i.e., electrically neutralize, the Si films in such a way as to minimize the effects of autodoping on electrical properties. From the data presented earlier, it is apparent that some of the best films, in terms of electron mobility, have been grown at temperatures where autodoping is most severe. The extent to which autodoping affects device performance, however, is still not known.

The extent of autodoping in the Si/ MgAl_2O_4 system was also examined. Undoped Si films were grown on MgAl_2O_4 at various deposition temperatures (1000 to 1100 C) using a constant amount of SiH_4 and H_2 -He mixture.

As shown in Table 5, films grown in the 1000 to 1050 C range were n-type; at 1075 C and 1100 C they were p-type before annealing. Annealing in O_2 and N_2 caused the films to become more strongly n-type, suggesting the removal of acceptor impurities and/or defects by the annealing process. It thus appears

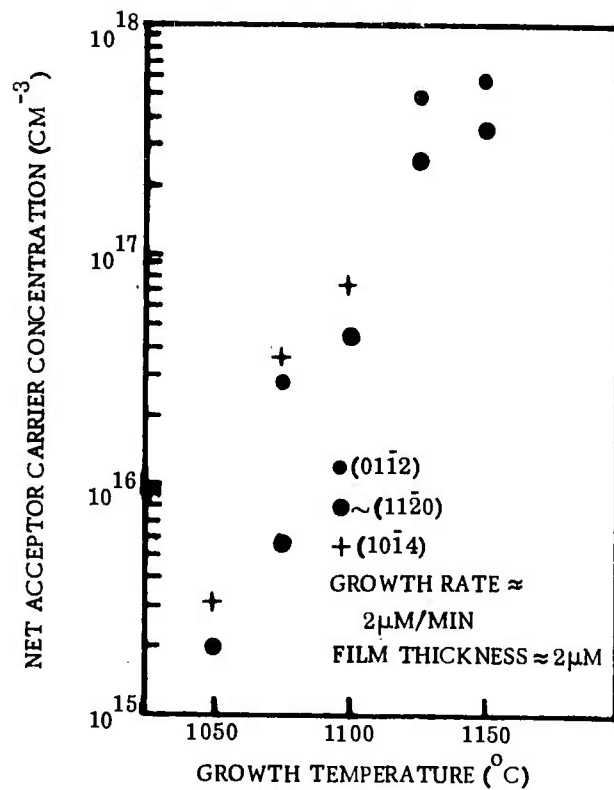


Figure 18. Variation of Net Acceptor Carrier Concentration Due to Al Autodoping as Function of Growth Temperature for Intentionally Undoped Si/Al₂O₃ Films. (Data points are averaged values.)

that the autodoping phenomenon is operative for Si/MgAl₂O₄ in the He-H₂ atmosphere at approximately the same temperatures as for the Si/Al₂O₃ system (Ref 3) but at a considerably lower concentration level.

Table 5. Autodoping in Si/(111) MgAl₂O₄ Using 0.8 Percent H₂-in-He as Carrier Gas

Deposition Temp (C)	Film Thickness (μm)	Growth Rate (μm/min)	Film Resistivity * and Type **	
			Before Anneal (ohm-cm)	After Anneal (ohm-cm)
1000	2.1	3.8	4.2 x 10 ² (n)	1.3 (n)
1025	2.0	3.1	25.4 (n)	0.4 (n)
1050	1.8	2.1	3.2 (n)	0.28(n)
1075	1.8	1.2	4.8 x 10 ² (p)	76. (n)
1100	4.4	0.9	1 x 10 ³ (p)	1. (n)
				(Reflective edge region) 6.6 x 10 ² (p) (Gray central region)

* Four-point-probe measurement

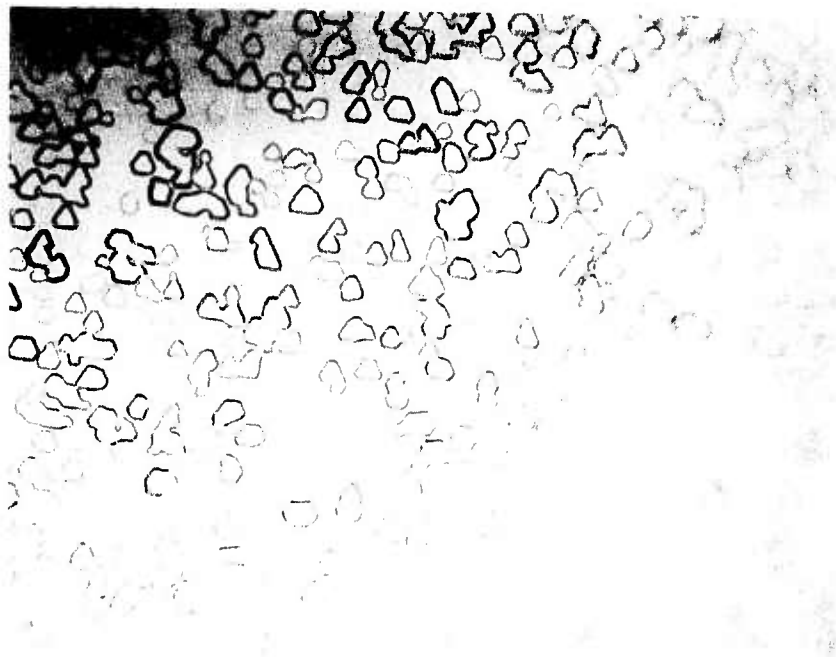
** Thermoelectric probe determination

Two similar and simple experiments were performed, one in H₂, the other in He, to examine the effect of the presence of Al₂O₃ in a system containing Si. An oval Al₂O₃ wafer (13mm x 16mm) was placed on a piece of ~60 ohm-cm HF-cleaned (dipped) mechanically-polished Czochralski-grown Si wafer. The composite was heated in the CVD reactor at a pedestal temperature of 1100C for 1 hour in H₂ and in He atmospheres, with these carrier gases flowing at a rate of 5 lpm.

The results are shown in Figure 19 for the H₂ case. After the Al₂O₃ was removed, a mesa about 1 μm high was in evidence, indicating the exposed Si had been eroded considerably. The eroded Si was highly etched, as shown in Figure 19b; it was p type, as determined with a hot-point probe, near the mesa and on top of the mesa which had been protected by the Al₂O₃ wafer. Angle-



(a)



(b)

25 μm

Figure 19. Evidence of Contamination of Si by Al_2O_3 in H_2 Atmosphere.
a) Overall Appearance (3.7X). b) Etched Region (406X).

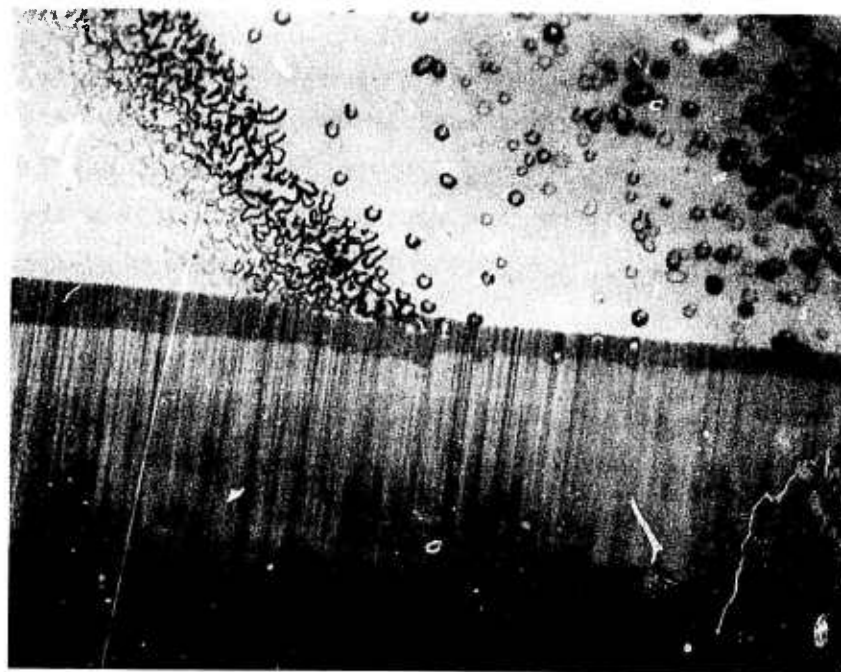
lapping and staining revealed a relatively uniform layer $\sim 2.4 \mu\text{m}$ thick on the mesa and a somewhat irregularly-shaped layer $\sim 1.7 \mu\text{m}$ thick in the etched area near where the wafer was positioned (Figure 20a). A van der Pauw measurement of the mesa, which was cut from the rest of the wafer, gave the following properties: $\rho = 3.5 \text{ ohm-cm}$; $p = \sim 6.3 \times 10^{15} \text{ cm}^{-3}$; $\mu = 284 \text{ cm}^2/\text{V-sec}$.

Some attack was also in evidence when He was used as the carrier gas, but the etching was much less severe; essentially no mesa area was formed. The Si surface below the Al_2O_3 was converted to p type, however, as in the H_2 experiment.

Another piece of Si from the same slice showed no pitting when annealed in H_2 at 1100C for 1 hour in the absence of Al_2O_3 , and it remained n type, as well. The "polished" Si section under the Al_2O_3 from the experiment in H_2 was subsequently annealed. After 1/2 hour in O_2 plus 2 hrs in N_2 , the surface had converted to n type, and angle-lapping and staining revealed an n-type layer $\sim 1 \mu\text{m}$ thick above a p-type layer $\sim 3.8 \mu\text{m}$ thick (as in Figure 20b). The n-type layer had the following properties: $\rho = 0.1 \text{ ohm-cm}$; $n = 6.4 \times 10^{16} \text{ cm}^{-3}$; $\mu = 1013 \text{ cm}^2/\text{V-sec}$. After an additional 18 hours of anneal (1/2 hr O_2 + 17-1/2 hrs N_2) staining revealed a very thin ($\sim 1 \mu\text{m}$ thick) diffuse layer, presumably p-type, at a depth of $\sim 3.5 \mu\text{m}$ from the Si surface. The n-layer above it measured as follows: $\rho = 0.18 \text{ ohm-cm}$; $n = 3.0 \times 10^{16} \text{ cm}^{-3}$; $\mu = 1144 \text{ cm}^2/\text{V-sec}$.

It is difficult to explain the presence of an n-type layer more highly doped than the starting wafer unless the Al_2O_3 introduced an n-type impurity into the Si that would not anneal out in the same fashion as the p-type impurity.

From these results, it can be concluded that even before Si growth begins the Al_2O_3 substrate can be expected to contaminate the gaseous atmosphere with impurities which may attack the growing Si nuclei and leave a highly defective structure at the Si/ Al_2O_3 interface. This effect can presumably be minimized



(a)

45 μ m



(b)

45 μ m

Figure 20. Subsurface Doping in Si Caused by Contamination from Al_2O_3 .
 a) Region below and adjoining Al_2O_3 Wafer (etched area on right.) b) Si Region below Al_2O_3 after Annealing 1/2 hr in O_2 and 2 hr in N_2 .

by the use of an inert atmosphere, lower growth temperatures, and higher growth rates to seal the Al_2O_3 surface as fast as possible.

Etching of the Si in a He atmosphere can probably be explained by the reaction between the Si and the Al_2O_3 wafers, as in Equation (20), or by the presence of traces of H_2 in the He carrier gas, which was not analyzed. The former explanation is the more likely contributor, since a thin Si film can be "volatilized" from a surface of Al_2O_3 leaving the surface etched, at temperatures less than the melting point of Si.

These results are also pertinent to the procedure to be followed and the type of process control needed during annealing of SOS films and islands and formation of complementary-doped islands in CMOS structures, during which bare Al_2O_3 is exposed. It appears that many potential processing problems might be solved by sealing the exposed Si with an oxide layer before additional steps in the device processing are attempted.

5. EFFECTS OF REACTOR CONFIGURATION ON DEPOSITION PROCESS AND FILM PROPERTIES

As part of the study of the effects of various reactor geometries and gas flow patterns on the properties of Si films on Al_2O_3 substrates, experiments were undertaken with a horizontal reactor system of the type commonly used in pilot-line or production facilities and by some other laboratories for the experimental growth of epitaxial Si films. Even though the growth rates used ($\sim 1 \mu\text{m}/\text{min}$) were not exactly the same as those often used in the vertical reactor, and the H_2 carrier-gas flows ($\sim 40 \text{ lpm}$) were increased substantially over those used in the vertical system, the data are considered meaningful. (The vertical system prevents use of such high flow rates due to the turbulence generated in the gas stream. Higher flows are used in the horizontal system to minimize the transfer of Al impurity from one Al_2O_3 substrate to those further downstream.)

The growth temperature was varied from 960 to 1100 C. However, the visual appearance of those films grown at the highest temperatures indicated a deterioration of film quality at temperatures over 1075 C. Only those grown in the range 960 to 1075 C were evaluated electrically. Two different orientations of Al_2O_3 substrates, the $(01\bar{1}2)$ and near the $(11\bar{2}0)$, were compared at most temperatures.

The electrical data on the relatively few films grown, shown in Figure 21, indicate that the electron mobility increases uniformly with decreasing growth temperature (T_g) for the $(01\bar{1}2)$ Al_2O_3 orientation, to a maximum of approximately $600 \text{ cm}^2/\text{V}\text{-sec}$ at 960 C. Carrier concentrations were kept approximately constant at $\sim 2\text{-}6 \times 10^{16} \text{ cm}^{-3}$, and film thicknesses were maintained at $1.0 - 1.4 \mu\text{m}$. For T_g values from 1050 to 1075 C mobilities were about $350 \text{ cm}^2/\text{V}\text{-sec}$.

The mobilities of films grown on $\sim(11\bar{2}0)\text{Al}_2\text{O}_3$, on the other hand, showed a maximum of over $600 \text{ cm}^2/\text{V}\text{-sec}$ at $T_g \sim 1050 \text{ C}$, with a decrease at both higher and lower growth temperatures. These results are in contrast to the data obtained on films grown in the vertical reactor system and emphasize the hazards of comparing data from different laboratories. It is apparent that the determination

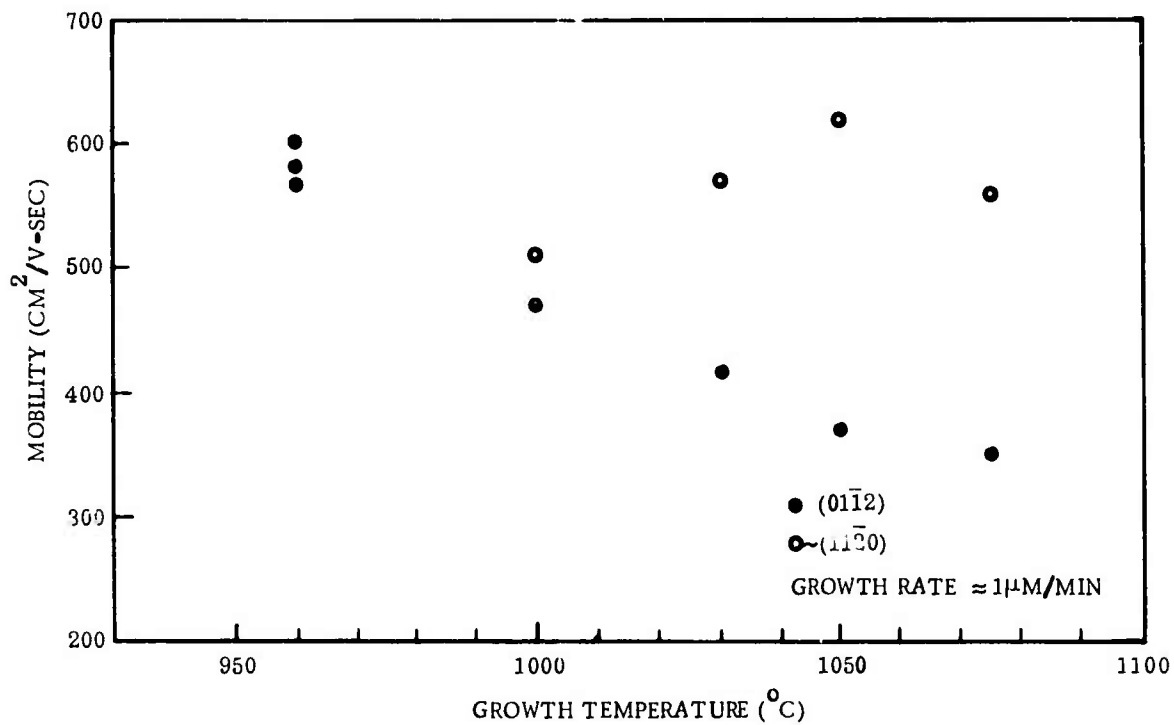


Figure 21. Variation of Hall Mobility with Growth Temperature for N-type Si/Al₂O₃ Films Grown in Horizontal Reactor

of optimum film growth parameters must relate only to the growth apparatus being employed. Ideally, any study designed to produce an optimum heteroepitaxial film must therefore treat the apparatus as an additional growth parameter.

Si growth experiments were also performed in a water-jacketed reactor chamber, to compare the electrical properties of films grown in a water-cooled reactor with those of films grown without cooled walls. The results are given in Table 6 for films grown both with and without water cooling. These results indicate that there is no apparent advantage in the use of a water-jacketed reactor in the vertical reactor system used in these experiments; in fact, the additional handling necessary to detach and attach the reactor from and to the system was found to be a distinct disadvantage.

At low growth rates the amount of deposit on the reactor wall appeared to be less in the case of the cold-wall reactor than for the uncooled reactor. However, because of the additional handling required and in view of the fact that the electrical properties were essentially the same for the two cases, no further studies were carried out with the cold-wall reactor.

Table 6. Properties of Si Films Grown in Jacketed Reactor

Film Orientation	Film Thickness (μm)	Resistivity (ohm-cm)	Carrier Concentration (cm^{-3})	Mobility ($\text{cm}^2/\text{V-sec}$)
	Without Water Cooling			
(100)	1.7	0.71	1.9×10^{16}	460
(111)	1.8	0.78	1.3×10^{16}	630
	With Water Cooling			
(100)	2.0	0.26	5.0×10^{16}	490
(111)	1.9	0.35	2.9×10^{16}	620

During the studies of mobility anisotropy in Si films grown on Al_2O_3 (see Sections 2 and 10) it was found that greater variations in donor concentration over the

area of the film occurred in films grown in the vertical reactor than in those grown in the commercial-type large-pedestal horizontal reactor. This prompted serious consideration of the possibility of major modifications in reactor and/or pedestal (susceptor) design to remove this shortcoming. To determine the magnitude of differences in the carrier concentration as a function of the substrate position on the rf-heated susceptor in the vertical reactor, a wafer of Al_2O_3 1.5 in. in diameter was used as a substrate for Si growth on a susceptor also 1.5 in. in diameter, and a number of Hall bridges were etched in the film after growth. The positioning of the bridges allowed the measurement of carrier concentration as a function of position across the diameter of the wafer. The results of these measurements are shown in Figure 22, where the net donor carrier concentration is plotted as a function of position on the susceptor. Film thickness uniformity was good, but the results indicated a considerable gradient in film electrical properties.

Modifications in susceptor and/or reactor design that would reduce the severity of this nonuniformity were then considered. Susceptors having convex and concave bottom surfaces were tested, and in these cases the outer edges were ~50 and ~100 deg C, respectively, hotter than the center at ~1100 C. Two disks 1-1/2 in dia x 1/8 in thick, one of vitreous carbon and the other of pyrolytic graphite, were placed on a standard 1-1/2 in dia SiC-coated carbon pedestal and heated to growth temperature, but there was no improvement in the temperature profile. A hot spot was observed on the pyrolytic graphite disk, while the vitreous carbon disk showed the same kind of colder center as previously observed on the susceptor itself.

A pedestal which permitted heat-sinking around the outer edge was also fabricated, but with the quartz pedestal holder serving as the heat sink no improvement in temperature control was observed; a 50 deg C differential was found between the center of the pedestal (at 1035 C) and a point near the edge on the top surface.

These difficulties indicated that other approaches should probably be used to resolve the temperature distribution problem. It was determined that by positioning the substrate wafers on the pedestal in regions where the temperature gradients were small and by using the modified multi-armed Hall bridge pattern to help minimize the effects of the nonuniformity in carrier concentrations on electrical measurements, films adequate for the requirements of the program could still be produced in the vertical reactor. This is the course that was pursued.

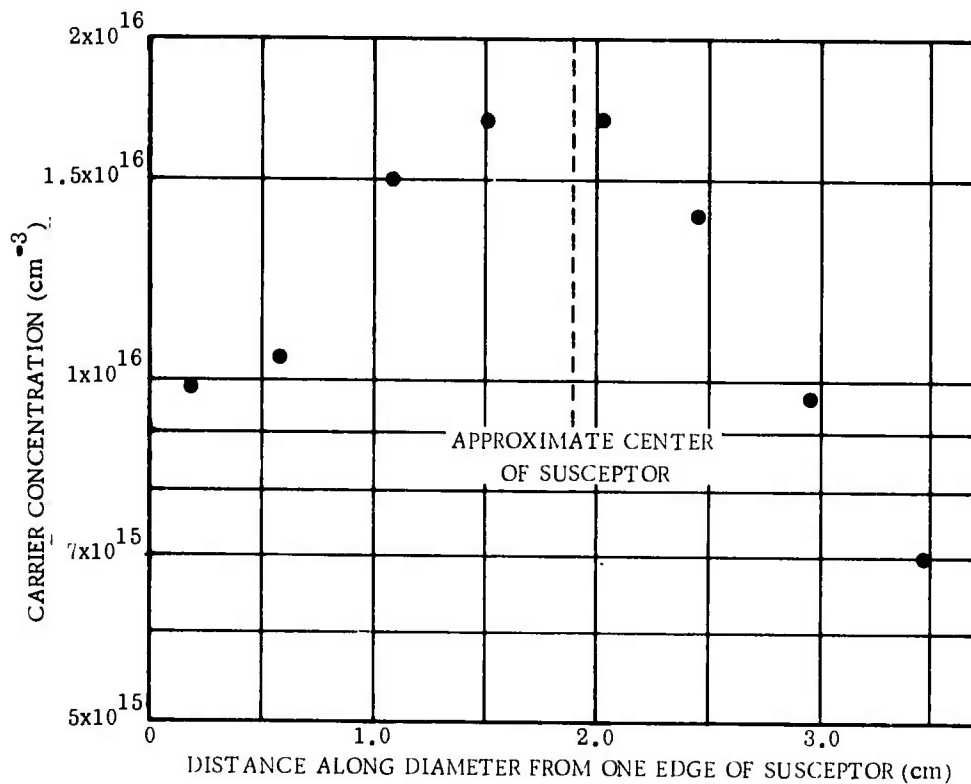


Figure 22. Net Carrier Concentration in Si Film on Al_2O_3 as Function of Position on Susceptor in Vertical Reactor

6. STUDIES OF EARLY-STAGE GROWTH OF Si FILMS ON Al_2O_3

Investigation of the nucleation and early-stage growth of CVD Si films on Al_2O_3 substrates was undertaken in a limited series of experiments. In one study Si nucleation on several etched and unetched pieces from the same substrate slices of (01 $\bar{1}$ 2)-oriented Al_2O_3 was characterized. The etched substrate pieces were gas phase-etched with Freon at 1495C to remove $\sim 8\mu\text{m}$ of material from the surface. Both etched and unetched samples were given the standard H_2 etch at 1300C prior to Si deposition at 1025C for $\sim 1/4$, 1, and 9 sec at a nominal growth rate of $0.7\mu\text{m}/\text{min}$ (116A/sec).

The general appearance of the surfaces was unchanged after the 1/4-sec and the 1-sec nucleation experiments and is shown at low magnification for Freon-etched and unetched substrates in Figure 23. After the Freon etching most areas of the substrate appeared relatively free of scratches; only low-angle grain boundaries and traces of some of the deeper scratches remained (Figure 23b). Some areas showed severe etch-pitting. The slight difference in orientation of the crystal on the two sides of a low-angle grain boundary is readily visible in Figure 23c.

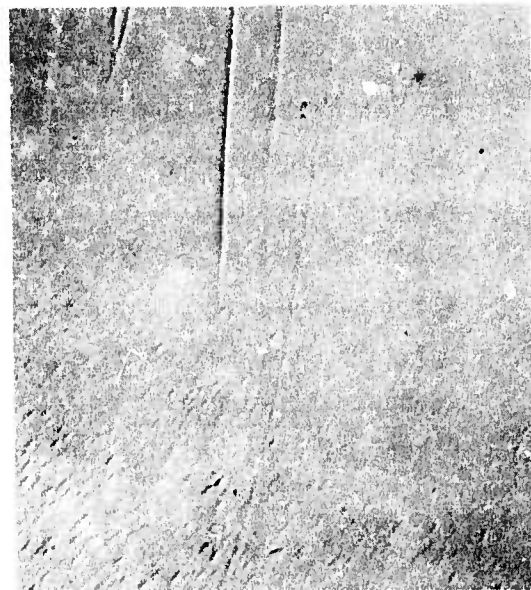
The nuclei resulting from the 1-sec experiment on the etched and unetched surfaces are shown at high magnification in the electron micrographs of Figure 24. Comparison of Figures 24a and 24b with Figures 24c and 24d shows that the size, shape and distribution of the nuclei are the same for both etched and unetched surfaces. There appears to be no preferential nucleation at scratches on either surface in this instance.

The faint trace of a scratch in Figure 24a (going from lower left to upper right) shows the same nuclei distribution as the unscratched regions. Figure 24b is a higher magnification electron micrograph of the same area. Similarly, the crossed scratches of Figure 24c show no preferential nucleation, even at higher magnification in Figure 24d.



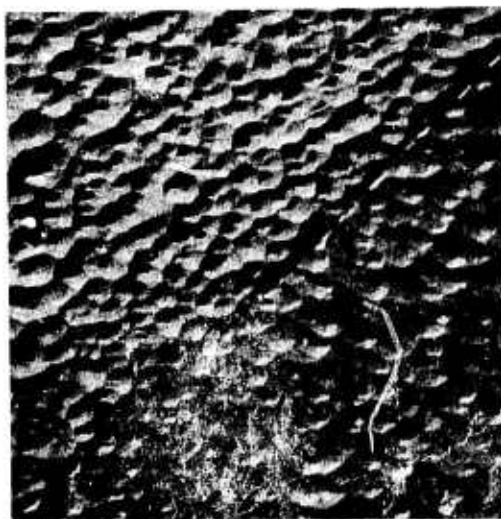
200 μm

(a)



200 μm

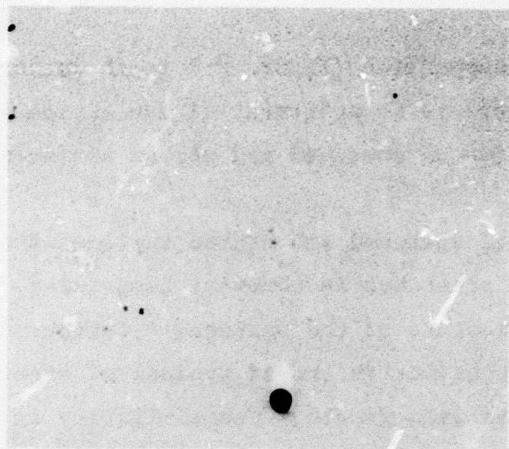
(b)



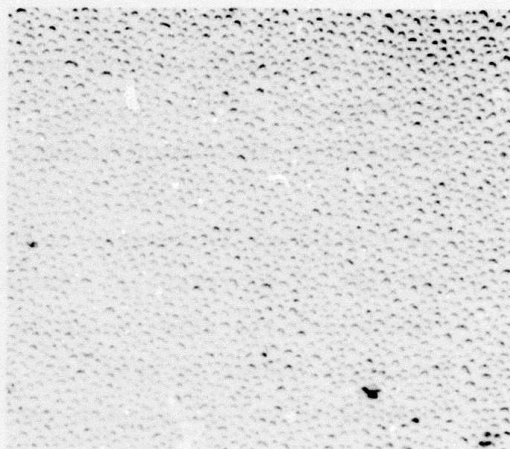
200 μm

(c)

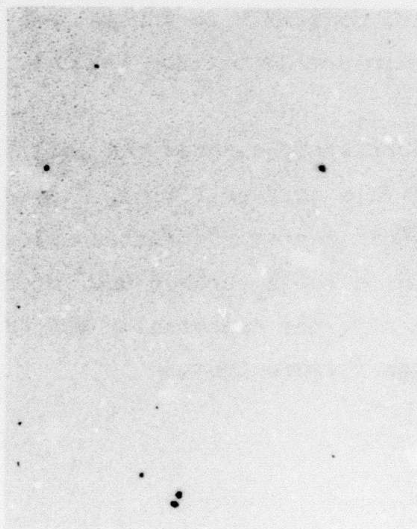
Figure 23. Surfaces of Neighboring Pieces of $(01\bar{1}2)\text{Al}_2\text{O}_3$ after 1 sec Si Nucleation on (a) H_2 -etched Substrate; (b) and (c) Freon-etched Substrate. ((b) and (c) show two regions of the same surface.)



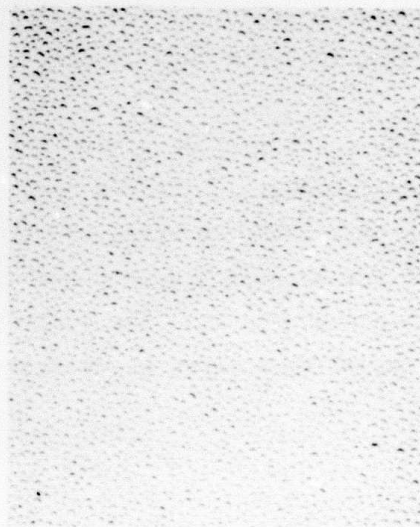
(a) 0.5 μm



(b) 1 μm



(c) 0.5 μm



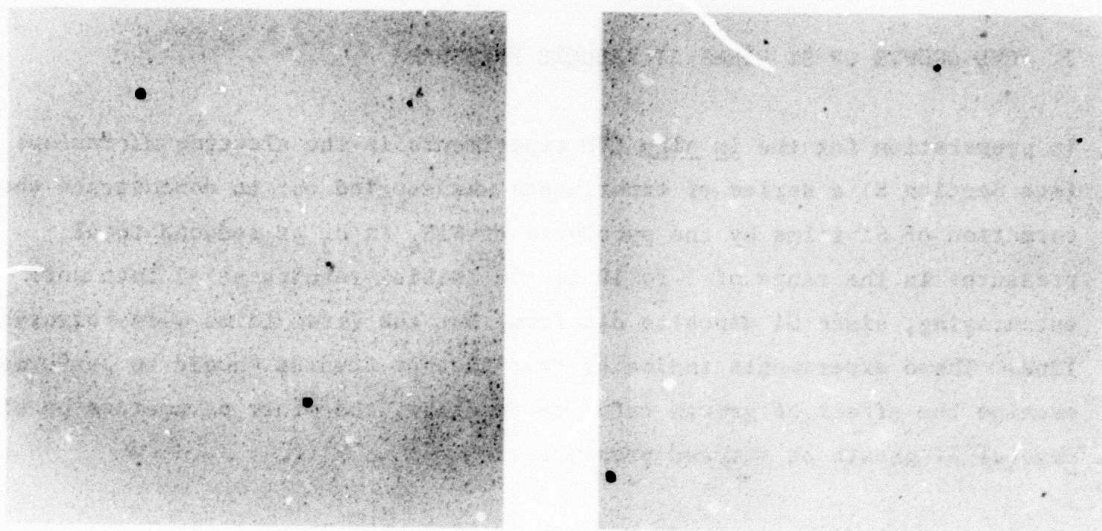
(d) 1 μm

Figure 24. Nature of Si Islands on (a), (b) H_2 and (c), (d) Freon-etched $(01\bar{1}2)\text{Al}_2\text{O}_3$ after 1 sec Si Growth

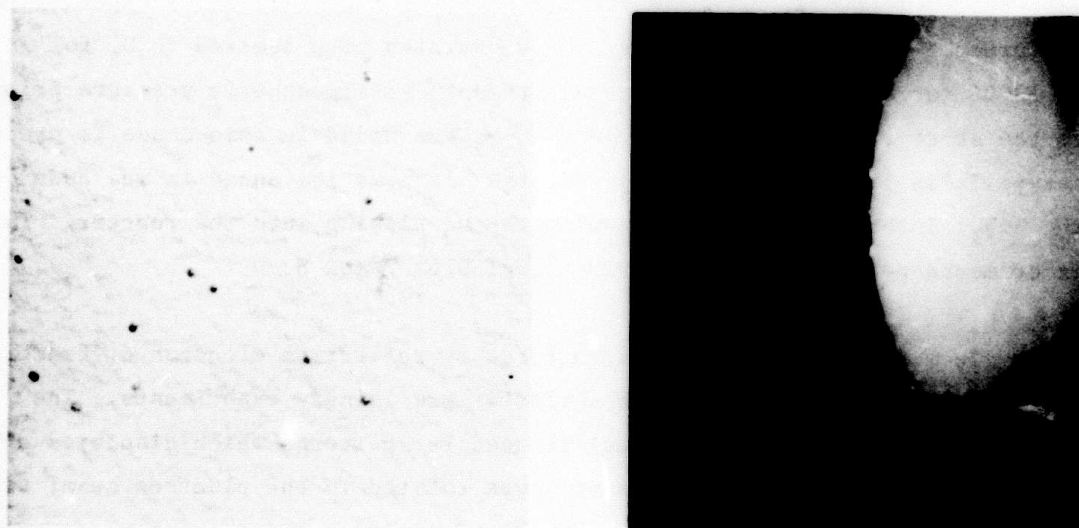
Nucleation resulting from the 1/4-sec deposition (Figure 25) is characterized by fewer and smaller Si nuclei, but there is no preferential nucleation and no apparent difference between nucleation on unetched and etched surfaces.

The similarity in nucleation behavior of unetched and etched surfaces and the lack of preferential nucleation at scratches is somewhat surprising, considering the differences in macrostructure of the surfaces. Further experiments are needed to determine if this behavior is indeed typical of other orientations of Al_2O_3 with respect to Si film growth. The similarity in nucleation behavior may be explained if the etched and unetched surfaces have a similar microstructure (as opposed to the differing macrostructures indicated in Figure 23). On the other hand, because of the high density of nuclei fairly evenly distributed on the surface, earlier growth phenomena at the scratch may have become overshadowed by the subsequent overgrowth. This could suggest that the heteroepitaxial film during growth overcomes some surface defects by virtue of the fact that nuclei possess high surface mobility leading to rapid coalescence. (See discussion in Section 8-2,3.)

It was found that Si growth for 9 sec completely covered the $(01\bar{1}2)\text{Al}_2\text{O}_3$ surface, leaving a rather rough-looking film surface (Figure 26a) at a thickness of $\sim 1400\text{\AA}$, as measured with a Talysurf gauge. Reflection electron diffraction photographs of the Si growth on the H_2 -etched and Freon-etched surfaces showed that the quality of the film was essentially the same and possessed relatively heavy twin structure (Figure 26b).



(a)  (b) 
Figure 25. Nature of Si Islands on (a) H₂-etched and (b) Freon-etched (011̄2)Al₂O₃ after approximately 1/4 sec Si Growth



(a)  (b)
Figure 26. (a) Surface Structure and (b) RED Pattern for 9-sec Si Growth (~1200 Å) on Freon-etched (011̄2)Al₂O₃

7. CVD GROWTH OF Si FILMS AT REDUCED PRESSURES

In preparation for the in situ CVD experiments in the electron microscope (see Section 8) a series of experiments was carried out to demonstrate the formation of Si films by the pyrolysis of SiH_4 in H_2 at reduced total pressures in the range of 1 to 10 torr. Initial results at ~1 torr were encouraging, since Si deposits did form, but the first films were polycrystalline. These experiments indicated that further studies should be performed to examine the effect of growth rate, temperature, and other parameters on single-crystal Si growth at reduced pressures.

The full-scale reactor used for Si deposition work at atmospheric pressure was used for these further experiments, except that a vacuum system connected directly to the outlet of the reactor chamber was used to evacuate the chamber prior to and during the introduction of the H_2 and/or SiH_4 into the apparatus for film growth. The amount of gas flow was controlled by adjustment of the flowmeter settings obtained by bleeding the gas into a low pressure environment until the flowmeter stabilized. The total pressures were read on a thermocouple gauge, adequate for the scope of the qualitative experiments performed. Except for two cases, the substrates were treated in H_2 for 15 min at 1300C (or at 1100C if MgAl_2O_4 was present) at atmospheric pressure prior to the start of the SiH_4 flow. AsH_3 -in- H_2 was added in some cases to produce n-type films for electrical measurements. In some instances it was added to the SiH_4 ; in others it was mixed with the H_2 flowing into the reactor. The experiments performed are summarized in Tables 7 and 8.

The evaluation of film crystal structures by reflection electron diffraction (RED) was made at the end of the series of preliminary experiments. The designating "fibrous" (see tables) is used for patterns which displayed a non-rotating spot pattern when the sample was rotated in the electron beam; single-crystal structure is indicated by "SX," and includes those cases where spot-pattern and Kikuchi-line rotation occurred with sample rotation. The term "poly" indicates that continuous rings were observed in the RED pattern, characteristic of polycrystalline structure.

Table 7. Properties of Si Films Grown on Al_2O_3 by Pyrolysis of SiH_4 at Low Pressures^a

Substrate ^b	Growth Temp (°C)	Flowmeter Settings		Deposition Time (Min)	Film Thickness	Growth Rate	Film Crystal Structure ^c	Remarks**
		SiH_4 *	H_2					
A	885	1.5	Low (see remarks)	68	250 Å	3.7 Å/min	Fibrous	T. P. ~400 μm; gold mirror; NHTH.
B	885	1.5		68	n.d. ^d	n.d.	SX ^e	
A	1045	5.0	None	106	0.89 μm	0.009 μm/min	Poly over SX	Films gray; SiH_4 introduced into evac reactor; gauge press. = 280 μm at start, dropped to 80 μm when SiH_4 passed through reactor.
B	1045	5.0	None	106	n.d.	n.d.	Foly	
A	1100	1.5	Low (see remarks)	60	2500 Å	42 Å/min	Poly	T. P. ~400 μm; gold color; NHTH.
B	1100	1.5	Low (see remarks)	60	n.d.	n.d.	Poly	
A	1105	5.0	Low (see remarks)	60	0.66 μm	0.011 μm/min	Poly	Gray films; T. P. ~420 μm
B	1105	5.0	Low (see remarks)	60	0.75 μm	0.012 μm/min	Poly	
A	1105	5.0	Low (see remarks)	60	0.46 μm	0.008 μm/min	Poly	T. P. ~800 μm; dropped to ~300 μm when $SiH_4 + H_2$ added to evac. reactor.
B	1105	5.0	Low (see remarks)	60	n.d.	n.d.	Poly over SX	

^a Samples grouped together were grown in the same run

^b A = (0112) Al_2O_3 ; B = -(1120) Al_2O_3

^c Determined by reflection electron diffraction

d.n.d. = not determined

^eSX = Single crystals

*Reading of pyrex ball in No. 600 (low-flow) flowmeter (Matheson)

**T. P. = Total pressure

NHTH = No high temperature H_2 treatment of surface

Table 8. Properties of Si Films Grown on Al₂O₃ by Pyrolysis of SiH₄ at Medium Pressures ^a

Substrate ^b	Growth Temp (°C)	Flowmeter Settings			Deposition Time (min)	Film Thickness ^e (μm)	Growth Rate (μm/min)	Film Crystal Structure ^f	Remarks
		SiH ₄ ^c	H ₂ ^d	AsH ₃ -In-H ₂					
A	1000	3.0	7.0	-	60	2.14	0.036	Fibrous on SX ^g	Gray film
B	1000	3.0	-	-	60	n.d.	n.d.	Fibrous and twinned	Gray film
A	1025	3.0	7.0	-	60	2.02	0.034	Fibrous	Gray film
B	1025	3.0	7.0	-	60	2.03	0.034	Fibrous	Gray film
C	1025	3.0	7.0	-	60	n.d.	n.d.	Twinned SX	Gray film
D	1025	3.0	7.0	-	60	n.d.	n.d.	Fibrous	Gray film
A	1030	3.0	7.0	1.0 ^c (Added to H ₂)	105	3.93	0.037	Fibrous on SX	Mirrored; ρ = 0.04 Ω-cm
B	1030	3.0	7.0	"	105	3.62	0.035	SX	Gray;
C	1030	3.0	7.0	"	105	4.07	0.037	Fibrous on SX	Mirrored; ρ = 0.05 Ω-cm
D	1030	3.0	7.0	"	105	3.72	0.036	Fibrous on SX	Gray;
A	1045	3.0	6.0	1.0 ^d (Added to H ₂)	60	1.2	0.020	Fibrous on SX	Gray; ρ = 0.02 Ω-cm
B	1045	3.0	6.0	"	60	0.91	0.015	Fibrous	Mirrored; ρ = 0.04 Ω-cm
A	1050	3.0	7.0	-	60	2.20	0.036	Fibrous on SX	P-type; gray sheen ρ = 1 Ω-cm;
B	1050	3.0	7.0	-	60	1.94	0.032	Fibrous on SX	n _a = 2.1 x 10 ¹⁶ cm ⁻³ , μ = 290 cm ² /V-sec; gray reflective
A	1055	3.0	7.0	1.0 ^c (Added to H ₂)	60	2.86	0.048	Oriented spots	ρ = 0.17 Ω-cm, as deposited
B	1055	3.0	7.0	"	60	2.44	0.040	SX + Kikuchi lines	ρ = 0.13 Ω-cm, as deposited
C	1055	3.0	7.0	"	60	2.47	0.041	SX + Kikuchi lines + spots	ρ = 0.09 Ω-cm, as deposited
D	1055	3.0	7.0	"	60	2.83	0.048	Oriented spots	ρ = 0.10 Ω-cm as deposited
A	1060	3.0	3.0	3.0 ^d (Added to SiH ₄)	120	0.5	0.004	Fibrous on SX	ρ = 0.04 Ω-cm, as deposited
B	1060	3.0	3.0	"	120	0.5	0.004	Poly	ρ = 0.04 Ω-cm, as deposited
A	1070	3.0	7.0	-	60	3.2	0.053	Poly	SiH ₄ + H ₂ into evacuated reactor
B	1070	3.0	7.0	-	60	n.d.	n.d.	Poly	
A	1075	3.0	7.0	1.0 ^c (Added to SiH ₄)	60	2.2	0.037	SX + Kikuchi lines	ρ = 0.13 Ω-cm; n _a = 1.5 x 10 ¹⁷ cm ⁻³ ; μ = 320 cm ² /V-sec
C	1075	3.0	7.0	"	60	2.2	0.037	SX + Kikuchi lines	ρ = 0.12 Ω-cm; n _a = 9.9 x 10 ¹⁶ cm ⁻³ ; μ = 510 cm ² /V-sec
A	1100	3.0	7.0	-	60	2.3	0.038	SX + Kikuchi lines; twins	Gray
B	1100	3.0	7.0	-	60	2.1	0.035	Fibrous on SX	p-type; reflective ρ = 0.11 Ω-cm; n _p = 2.2 x 10 ¹⁷ cm ⁻³ μ = 260 cm ² /V-sec

^a Samples grouped together were grown in same run

^b A = (0112) Al₂O₃; B = (1120) Al₂O₃; C = (111) Czoehralski MgAl₂O₄ (polished by Union Carbide); D = (100) Czoehralski MgAl₂O₄ (polished by Union Carbide).

^c Reading of pyrex ball in No. 600 (low-flow) flowmeter (Matheson)

^d Reading of pyrex ball in No. 607 (high-flow) flowmeter (Matheson)

^e n.d. = Not determined

^f Determined by reflection electron diffraction

^g SX = Single crystal

These preliminary experiments revealed a number of interesting facts. They suggested strongly that single-crystal growth of Si could be obtained over a wide range of temperatures when growth conditions are optimized. The growth of a single-crystal film at low pressures and at the lowest temperature arbitrarily chosen for growth (885C), particularly on $\sim(11\bar{2}0)Al_2O_3$ which in previous CVD growth experiments at atmospheric pressure had not supported epitaxy at low temperatures, was very encouraging. In no previous experiment had such a very thin film grown as a single crystal. Since at 1100C polycrystalline films were obtained in these experiments, it suggested that the differences observed in crystalline structure were caused by the increased growth rate and/or temperature.

At medium pressures (see Table 8), single-crystal films were more readily obtained, particularly when an excess of H_2 was present when the SiH_4 was decomposed. The growth rate of Si was influenced by the H_2 concentration; it was decreased considerably when the H_2 pressure in the reactor was low or pure SiH_4 was decomposed. For a given set of SiH_4 and H_2 flowmeter settings (e.g., $SiH_4 = 3.0$ and $H_2 = 7.0$ (see Table 8)), the Si growth rate was essentially constant ($\sim 0.03-0.05\mu m/min$) over the temperature range studied (1000 to 1100C), but when a relatively high concentration of AsH_3 -in- H_2 (No. 607 flowmeter) was added, the Si growth rate decreased, a phenomenon previously reported by Farrow and Filby (Ref 43) for As-doped Si growth on Si. A low flow of AsH_3 -in- H_2 did not seem to affect the Si growth rate on Al_2O_3 .

It was encouraging to obtain reflective single-crystal growth on $(111)MgAl_2O_4$ as well as on $(01\bar{1}2)Al_2O_3$ and $\sim(11\bar{2}0)Al_2O_3$. In all cases the $(111)Si$ growths appeared to possess better electrical properties than the $(100)Si$ growths. As indicated in Table 8, a Si film $2\mu m$ thick grown on (111) -oriented Czochralski-grown $MgAl_2O_4$ at 1075C exhibited a mobility of $\sim 510 cm^2/V\text{-sec}$ compared with a mobility of $320 cm^2/V\text{-sec}$ measured for $(100)Si$ growth on $(01\bar{1}2)Al_2O_3$, for carrier concentrations $\sim 1 \times 10^{17} cm^{-3}$. The results obtained in these studies suggest that additional experiments using low-pressure growth conditions should be carried out to establish the possibilities of obtaining films of improved properties.

8. GROWTH OF Si BY CVD IN ATMOSPHERES OTHER THAN H₂

Studies were made of the growth of Si films by the pyrolysis of SiH₄ in an all-He atmosphere. In addition to the He being used as a carrier gas, 200 ppm AsH₃-in-He was used as the dopant source, so that the only H₂ in the system would presumably result from the pyrolysis of AsH₃ and SiH₄.

The growth of Si in this atmosphere yielded a great quantity of visible reaction products completely coating the walls of the reactor during the run. The growth rates were found to be considerably less for the same flow rates of SiH₄ than when H₂ was present in the system and were strongly dependent on the total He flow through the reactor. In addition, considerably larger quantities of AsH₃ were required to reach a given doping concentration in the Si.

For example, Si growth rates on Al₂O₃ and MgAl₂O₄ in He were 4-8 times smaller than those obtained in a H₂ atmosphere, and n-type films with carrier concentrations $\sim 10^{16} \text{ cm}^{-3}$ required ~ 35 ccpm of nominally 200 ppm AsH₃-in-He flow but only ~ 0.1 ccpm of 200 ppm AsH₃-in-H₂ flow in a H₂ growth atmosphere.

The most highly reflective films were measured electrically; little difference in properties was found before and after a 1-hr O₂ anneal, presumably due to the minimized autodoping at low growth temperatures. Since many films had carrier concentrations $< 10^{16} \text{ cm}^{-3}$, and hence may exhibit electrical properties strongly influenced by surface-state conduction, it was difficult to draw conclusions from the early data.

The addition of a small amount of H₂ to the reactor chamber, accomplished by switching from AsH₃-in-He to AsH₃-in-H₂ as the dopant, caused a noticeable change in both the amount of wall deposit and the dopant flow rate required to obtain a given donor concentration. Only 0.6 ccpm of AsH₃-in-H₂ as opposed to 35 ccpm of AsH₃-in-He was needed to produce a doping level of $\sim 2 \times 10^{16} \text{ cm}^{-3}$ on (01 $\bar{1}$ 2)Al₂O₃ at 1025C; yet in a H₂ atmosphere both dopant sources appeared to be essentially equivalent.

The initial study of the effect of H₂ additions to He at high SiH₄ concentra-

tions on the Si growth rate is shown in Figure 27. The SiH_4 flow was kept constant at 150 ccpm and the Si growth temperature was 1025C. The data show that essentially a linear increase in growth rate results when H_2 is added to the He carrier gas, at least up to the indicated flow rate of 2000 ccpm. (33 percent of the total carrier gas). Since the growth rate in pure H_2 has been found to be $\sim 15\mu\text{m}/\text{min}$, the dependence on H_2 percentage is not linear throughout the range, leveling off at higher concentrations of H_2 . However, at low H_2 additions to the He (~ 300 ccpm and below), the Si growth rate was essentially constant.

It was also established that for a given He- H_2 ratio the growth rate is very temperature-dependent. This is shown in Figure 28 for a constant SiH_4 flow (nominally 150 ccpm) and 0.8 percent H_2 in He. Over the 100-deg temperature span investigated the growth rate is seen to change by a factor of 4, being lower at the higher temperature.

It is difficult to understand how higher temperatures could cause such a large decrease in the growth rate. The behavior is very different from that observed in a pure H_2 carrier gas atmosphere: distinct mechanisms appear to be operative in the two cases.

Since it was earlier found that the net carrier concentration in As-doped Si films is growth-rate dependent when H_2 is the carrier gas (Figure 19, Ref 3) it was expected that similar effects would be observed in the He- H_2 system. The results obtained in an examination of this question are shown in Table 9. The data indicate that the doping level does not change appreciably with growth rate in He- H_2 atmospheres at 1025C and that good quality n-type films can be grown on $(111)\text{MgAl}_2\text{O}_4$ with carrier mobilities higher than those achieved in the $\text{Si}/\text{Al}_2\text{O}_3$ system. Mobilities as high as $925\text{ cm}^2/\text{V}\text{-sec}$ have been measured in $\sim 2\mu\text{m}$ -thick films, which approaches bulk Si mobilities. The variation of electrical properties with growth conditions for these films is discussed in the following paragraphs.

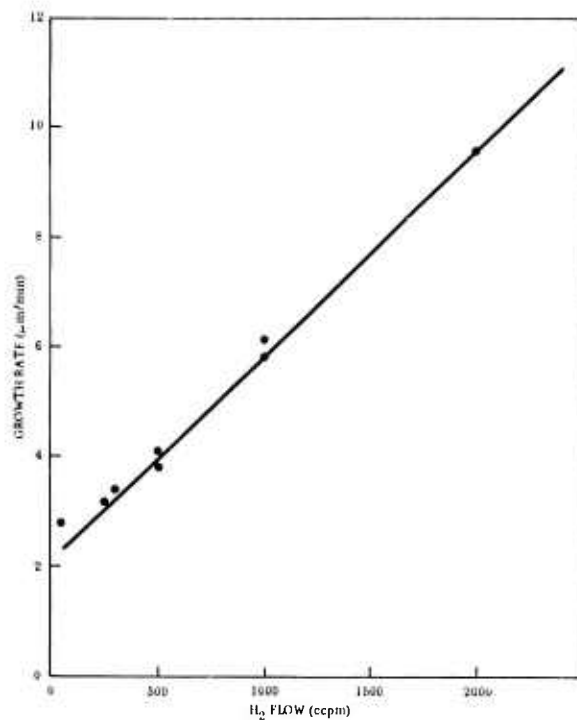


Figure 27. Changes in Si Growth Rate at 1025C Caused by H₂ Additions to He Carrier Gas (SiH₄ flow rate 150 ccpm)

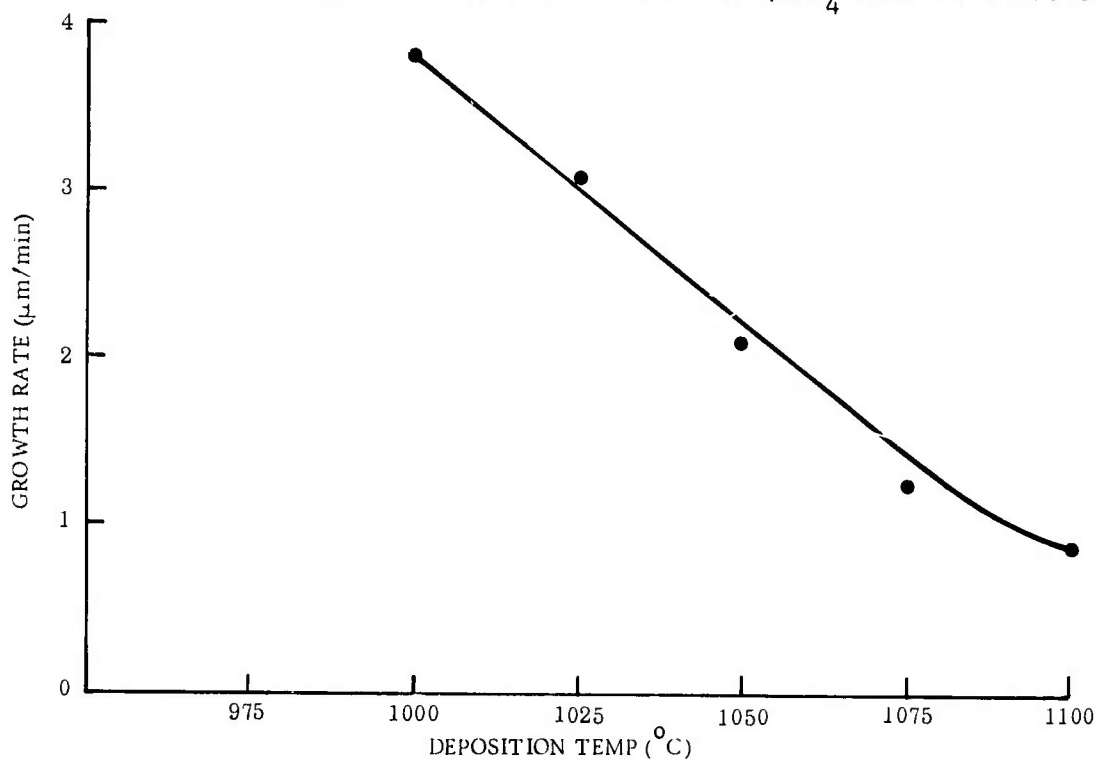


Figure 28. Effect of Growth Temperature on Si Growth Rate for SiH₄ Flow Rate of 150 ccpm and H₂/He = 0.8%

Table 9. Effect of Growth Rate on Doping Level for Si Films Grown on (111)Spinel at 1025C in He-H₂ Atmospheres (constant dopant gas flow rate)

H ₂ in He (%)	Film Thickness (μm)	Growth Rate (μm/min)	Resistivity (ohm-cm)	Carrier Concentration (cm ⁻³)	Mobility (cm ² /V-sec)
0.8	1.90	2.8	0.33	2.6 x 10 ¹⁶	747
4.2	1.87	3.2	0.41	1.9 x 10 ¹⁶	792
8.4	2.05	4.1	0.46	1.5 x 10 ¹⁶	900
16.8	1.85	5.8	0.56	1.6 x 10 ¹⁶	718
33.3	2.10	9.7	0.23	3.0 x 10 ¹⁶	925

Since growth temperature has been shown to be an important parameter in determining film quality, the electrical properties of a group of (111)Si/MgAl₂O₄ samples having net donor concentrations in the 10¹⁶ cm⁻³ range were examined as a function of growth temperature between 950 and 1050C. Low growth rates (<1μm/min) were used for this study, in a mixed 0.8 percent H₂-He atmosphere. Films with mobilities between about 500 and 650 cm²/V-sec were obtained on (111)MgAl₂O₄ over the temperature range, for growth rates between 0.2 and 0.4μm/min and donor concentrations of 2 x 10¹⁶-7 x 10¹⁶ cm⁻³. No optimum growth temperature was suggested by the data.

The variation in electron mobility with growth rate for a growth temperature of 1025C is shown in Figure 29. Growth rates were controlled by changing SiH₄ flows and also by varying the concentration from approximately 0.8 percent to 4 percent H₂ in He. It is apparent from this data that excellent quality Si can be grown at the higher growth rates (>2μm/min).

Additional mobility data are shown in Figure 30, which illustrates a limited amount of data obtained at higher growth rates. This figure also demonstrates the effect of different tanks of SiH₄ on film quality; the open and solid circles are data obtained from samples grown with different sources of SiH₄. The purity of the SiH₄ was evaluated by growing a thick (~100μm) film of Si on p-type Si substrates and measuring the film characteristics. The open

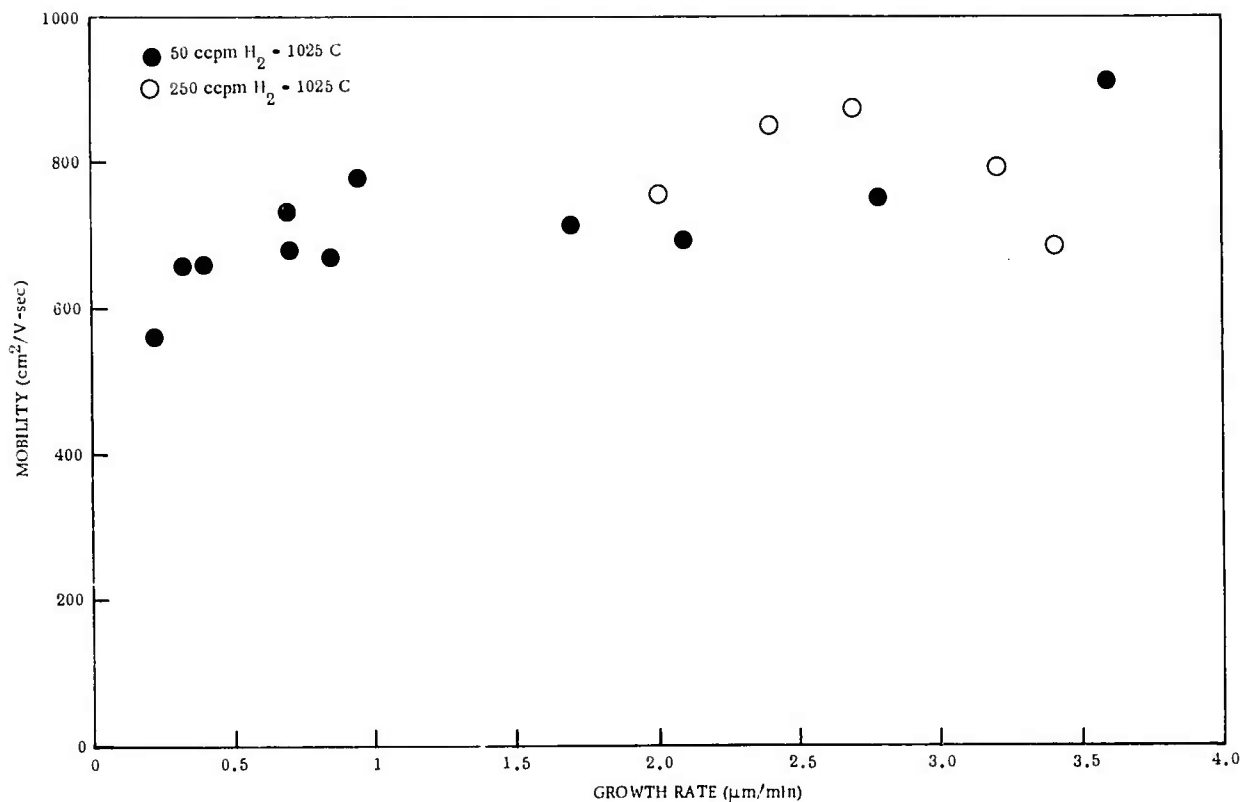


Figure 29. Variation in Hall Mobility with Growth Rate for (111)Si/(111)MgAl₂O₄ (growth temperature 1025C)

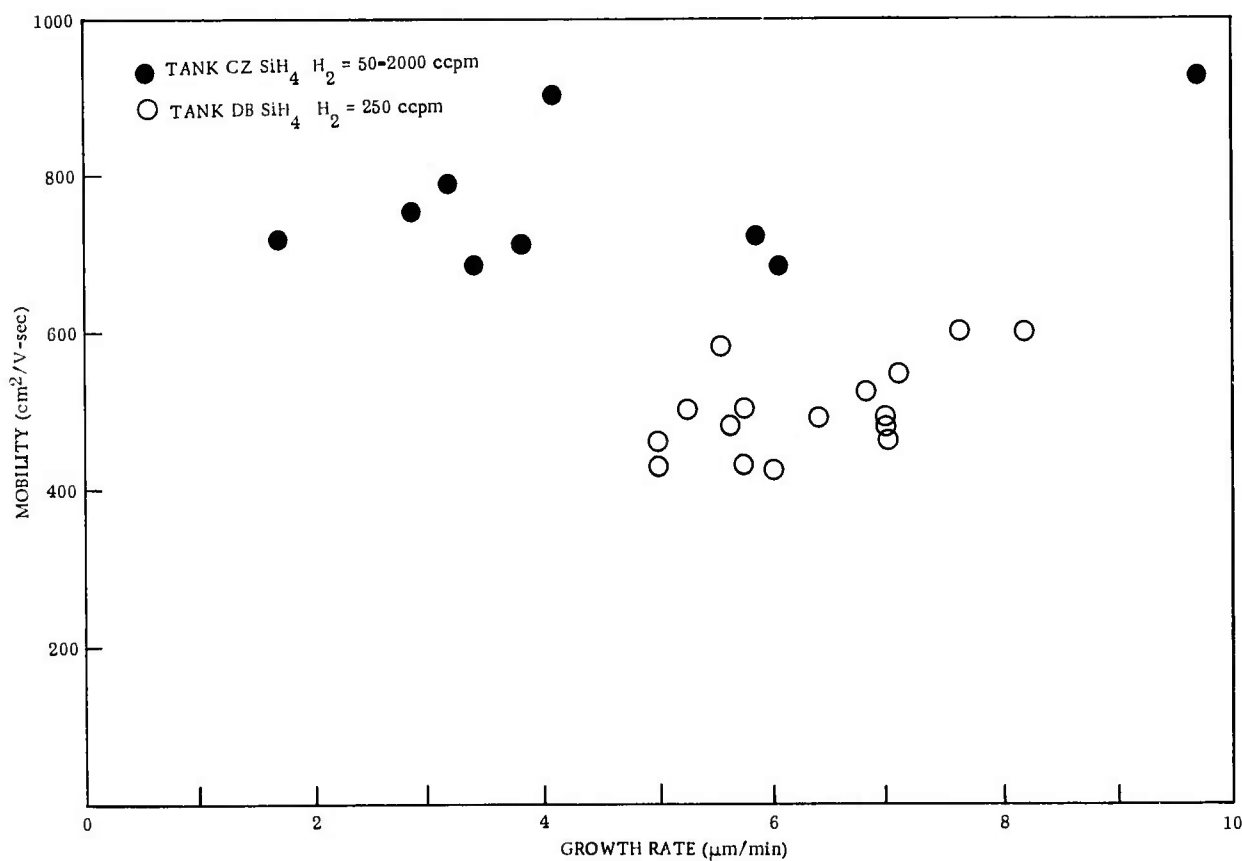


Figure 30. Variation in Hall Mobility with (high) Growth Rate for (111)Si/(111)MgAl₂O₄ (growth temperature 1025C)

circles were grown with a tank of SiH_4 which yielded films having the following characteristics: $\rho = 25 \text{ ohm-cm}$; $n = 2 \times 10^{14} \text{ cm}^{-3}$; and $\mu = 1300 \text{ cm}^2/\text{V-sec}$. The closed circles were grown with SiH_4 which produced films with $\rho = 47 \text{ ohm-cm}$, $n = 1.0 \times 10^{14} \text{ cm}^{-3}$, and $\mu = 1300 \text{ cm}^2/\text{V-sec}$. The purity of the two tanks thus appears to be equivalent based on Si growth on Si, but the quality of Si films produced on MgAl_2O_4 was markedly different. (See Section 4 for further discussion of the purity of the CVD reactants used in these studies.)

Not only did the electrical properties change with changes in source tanks of SiH_4 but the Si growth rates in the He- H_2 mixtures also were affected. The general shape of the curve in Figure 27 was reproduced but the curve was shifted to reflect the fact that not until the H_2 addition reached $\sim 1000 \text{ ccpm}$ ($\sim 20\%$ in He) did the Si growth rate show a major increase. The growth rate then became linear, but the slope of the curve was not as great as shown in Figure 27. These differences may be explained if the concentrations of SiH_4 and impurity H_2 in the source tanks change with time and with the supplier, and the SiH_4 flowmeter reading is not that of pure SiH_4 .

Of the four different concentrations of H_2 in He that were examined most often (5, 10, 25 and 50%), the 10 and 25% values seemed to give the best results. At 5 and 50% the films produced were cloudy in appearance and had high resistivity, inconsistent with the amount of dopant that was present. While good "mirrored" Si films could be obtained with 10% H_2 concentration at 1000, 1025 and 1050C, those films grown at 1000 and 1025C possessed the better electrical properties. At 1050C high-resistivity films were obtained for the same dopant concentration used for films grown at 1025C. Although only a few films were prepared in the 25% H_2 atmosphere they appeared to be equivalent to those grown with 10% H_2 concentration.

A visual observation of the quality of Si film growth indicated that greater care in surface preparation is required for (111) MgAl_2O_4 than for Al_2O_3 substrates. Various cleaning procedures were tried, and even when one particular procedure seemed to be sufficient the results were not always reproducible.

The edges of the sample were almost always gray in appearance, but the film portion in the center of the substrate was reflective in many cases; electrical measurements were made on those samples.

Considerable subsurface work damage was found in (111)MgAl₂O₄ processed into polished substrates by various vendors and at Rockwell. This damage was revealed by etching the polished surface in hot HF or hot HBF₄ for ~45 to 90 min. A high temperature (~1500C) anneal in air seemed to reconstruct the MgAl₂O₄ surface and to minimize or remove scratches, but the electrical properties of films grown on these surfaces did not appear to be any better than those measured in films grown on mechanically polished substrates.

A few experiments were performed to determine the effect of heating (111)MgAl₂O₄ in H₂ at 1100C prior to film growth at 1025C in He-H₂. The electrical properties of Si films grown on these surfaces and on surfaces not treated in H₂ were not considered significantly different.

A (01 $\bar{1}$ 2)-oriented Al₂O₃ substrate was included in several of the early Si/MgAl₂O₄ growth experiments in order to compare the quality of the resulting films in different H₂-He atmospheres. The data obtained are recorded in Table 10 for two growth temperatures and growth rates. At 1025C the growth on (111)MgAl₂O₄ was consistently superior to that on (01 $\bar{1}$ 2)Al₂O₃; however, the lower mobilities on Al₂O₃ are consistent with those found previously in the H₂ system at 1025C. At 1050C, where the growth on (01 $\bar{1}$ 2)Al₂O₃ appeared to improve somewhat in the H₂ system, the films were comparable in quality.

These results led to a comparison of the properties of ~2 μ m thick films grown at ~1060C with the same source of SiH₄ on the three Al₂O₃ orientations - (11 $\bar{2}$ 0), (10 $\bar{1}$ 4), (01 $\bar{1}$ 2) - in 100% H₂ and in 10%-90% H₂-He atmospheres. The electrical properties were measured, using the van der Pauw technique, after several O₂-N₂ annealing sequences.

Table 10. Comparison of Properties of Si/Al₂O₃ and Si/MgAl₂O₄

Grown at Two Different Temperatures

Growth Temp (C)	% H ₂ in He	Growth Rate (μm/min)	Thickness (μm)	Resistivity (ohm-cm)	Net Donor Carrier Concn. (cm ⁻³)	Mobility (cm ² /V-sec)	Substrate
1025	0.8	0.40	1.95	0.20	7.6 x 10 ¹⁶	410	(01 $\bar{1}$ 2)Al ₂ O ₃
		0.41	1.93	0.25	3.8 x 10 ¹⁶	660	(111)MgAl ₂ O ₄
1025	4.2	2.2	1.6	1.2	1.3 x 10 ¹⁶	411	(01 $\bar{1}$ 2)Al ₂ O ₃
		2.4	1.8	0.77	1.1 x 10 ¹⁶	744	(111)MgAl ₂ O ₄
	4.2	2.9	2.2	0.10	1.4 x 10 ¹⁷	440	(01 $\bar{1}$ 2)Al ₂ O ₃
		3.1	2.3	0.11	9.4 x 10 ¹⁶	598	(111)MgAl ₂ O ₄
1050	0.8	0.27	1.60	0.35	2.7 x 10 ¹⁶	650	(01 $\bar{1}$ 2)Al ₂ O ₃
		0.33	1.96	0.43	2.3 x 10 ¹⁶	630	(111)MgAl ₂ O ₄

The resulting data are compiled in Table 11. Since only a few samples were grown in this study and since, except in the case of Si grown on (10 $\bar{1}$ 4)Al₂O₃, the carrier concentrations of the films differed by as much as a factor of 2, it was difficult to conclude which atmosphere is preferred for film growth on (01 $\bar{1}$ 2) and \sim (11 $\bar{2}$ 0)Al₂O₃. For (10 $\bar{1}$ 4)Al₂O₃, the results suggested the He-H₂ mixture is preferred; for the other Al₂O₃ orientations the He-H₂ atmosphere does not appear to be detrimental and could be beneficial. Further studies in this area are required to clarify some of these questions.

Most of the studies of Si growth on MgAl₂O₄ on this program were directed to the use of (111)MgAl₂O₄, since this orientation has produced higher mobility films than have been reported previously in the literature for either (100) or (110)MgAl₂O₄. However, it was hoped that the process used for Si deposition in this work would provide better film growth on the (110) and (100) orientations; unfortunately, the number of experiments involving these orientations was limited.

Table 11. Effect of Growth Atmosphere on the Properties of 2 μ m-thick Si Films on Al₂O₃

Al ₂ O ₃ Substrate Orientation	Si Film Orientation	Growth Atmosphere	Electrical Properties*			No. of Anneals [†]
			Resistivity (ohm-cm)	Carrier Conc. (cm ⁻³)	Mobility (cm ² /V-sec)	
(10 $\bar{1}$ 4)	(111)	10% H ₂ in He	0.57	2.0 x 10 ¹⁶	560	1
			0.49	2.1 x 10 ¹⁶	596	2
		100% H ₂	0.73	2.3 x 10 ¹⁶	366	1
			0.69	2.3 x 10 ¹⁶	390	2
(01 $\bar{1}$ 2)	(100)	10% H ₂ in He	0.73	2.1 x 10 ¹⁶	400	1
			0.62	2.6 x 10 ¹⁶	395	2
		100% H ₂	0.32	4.4 x 10 ¹⁶	447	1
			0.30	4.5 x 10 ¹⁶	462	2
~(11 $\bar{2}$ 0)	~(111)	10% H ₂ in He	0.61	1.9 x 10 ¹⁶	549	1
			0.49	2.1 x 10 ¹⁶	618	2
		100% H ₂	0.35	3.6 x 10 ¹⁶	500	1
			0.33	3.5 x 10 ¹⁶	545	2

* Obtained by van der Pauw technique measurements

† Each anneal consisted of 1/2 hr in O₂ + 2 hrs in N₂.

The Si films grown on (100)MgAl₂O₄ were only partially reflective at growth temperatures of 1025C and were slightly inferior electrically to (111)Si films grown simultaneously on (111)MgAl₂O₄ substrates. For example, a 2μm-thick (100) film had the following properties: resistivity = 0.53 ohm-cm; carrier concentration = 3.5x10¹⁶ cm⁻³; carrier mobility = 470 cm²/V-sec. The properties of the companion (111)Si film were ρ = 0.70 ohm-cm, n = 1.4x10¹⁶ cm⁻³, μ = 630 cm²/V-sec. At 1050C essentially similar results were obtained, with the (111) film being better than the (100) film.

Film growth on (110)MgAl₂O₄ appeared to improve with deposition temperature, for where only gray films were formed at growth temperatures of 1025 and 1050C under growth conditions satisfactory for (111) substrates, somewhat reflective films were obtained at 1075C and 1100C. The differences in quality may be thickness-dependent rather than growth temperature-dependent, for epitaxial film quality is normally expected to improve with thickness.

Work with MgAl₂O₄ substrates on another parallel program at Rockwell led to the interesting result that (100)Si epitaxial growth also occurs on (110) MgAl₂O₄ substrates, in addition to the (110)Si growth previously observed. The orientation relationships observed are

$$(100)Si // (110)MgAl_2O_4 \text{ and } [\bar{1}10]Si // [0\bar{1}\bar{1}]MgAl_2O_4 .$$

Thus, (110)MgAl₂O₄ is found to bring about the epitaxial growth of (100)Si just as it has been shown previously to produce (100)GaAs epitaxy. This phenomenon is of sufficient interest and importance to the understanding of the mechanisms of epitaxial growth that it should be investigated further, with correlations made with surface finish, substrate composition and accuracy of orientation, and other deposition parameters.

With respect to the MgAl₂O₄ substrate surface and its effect on film quality, the following conclusions can be reached based on the results of electrical measurements on Si/MgAl₂O₄ samples:

1. When the MgAl_2O_4 substrate is properly processed (i.e., polished and cleaned) Si films grown on good quality MgAl_2O_4 from two different vendors are essentially equivalent.
2. Substrates with high-density subsurface damage but which have not been etched to remove the work-damaged surface layer can still support the growth of Si films with acceptable electrical properties.
3. Even heavily-etched scratched surfaces can permit the growth of films with good electrical properties.
4. Thicker films ($\sim 5\mu\text{m}$) exhibit higher carrier mobilities than thinner ones ($\leq 2\mu\text{m}$).
5. The electrical properties of $2\mu\text{m}$ -thick films of (111)Si on MgAl_2O_4 are at least as good as those of (111)Si on Al_2O_3 , and quite often better than those of (100)Si on Al_2O_3 .
6. Although annealing has been found to change the MgAl_2O_4 surface in some manner, the electrical properties of Si films grown on annealed surfaces do not appear to be better than those measured in films grown on unannealed surfaces.

9. EFFECT OF ANNEALING DURING GROWTH ON Si FILM PROPERTIES

To examine the effects of annealing thin Si films ($\sim 0.5\mu\text{m}$ thick) at early stages of growth a group of Si/ Al_2O_3 samples was prepared with the deposition process interrupted at various stages to permit a 20-minute annealing period in H_2 followed by resumption of growth to the desired final thickness. Electrical measurements were then made on the Si films after the usual $\text{O}_2\text{-N}_2$ annealing sequence to evaluate the results of the H_2 annealing process. Preliminary studies indicated this treatment was not detrimental to a 2000Å-thick film, but its effect on $\sim 1000\text{Å}$ -thick films was not known.

The data obtained are presented in Table 12, in which it can be seen that a $0.67\mu\text{m}$ -thick (111)Si film annealed at 800C exhibited a carrier mobility of $490\text{ cm}^2/\text{V-sec}$, considerably better than the mobility of $190\text{ cm}^2/\text{V-sec}$ measured for another film which was annealed at 1100C. The data, although sparse, indicated that the 800C/1100C combination is better than the 800C/1050C combination for (111)Si on $\sim(11\bar{2}0)\text{Al}_2\text{O}_3$.

Further studies of the effects of annealing in H_2 at intermediate stages during the growth of Si films on Al_2O_3 involved the growth and anneal of $\sim 2000\text{Å}$ of Si at a growth rate of $\sim 4\mu\text{m}/\text{min}$ followed by further growth at the same rate. The results, shown in Table 13, confirmed that the annealing of very thin Si films on Al_2O_3 followed by additional film growth does not impair the ultimate mobilities of films so grown. The best films in this series of depositions, annealed in H_2 or unannealed, were grown on $\sim(11\bar{2}0)$ -oriented Al_2O_3 substrates; mobilities $>400\text{ cm}^2/\text{V-sec}$ were obtained in films only $0.6\text{-}0.7\mu\text{m}$ thick.

However, the annealing studies did not demonstrate a significant improvement in the overall quality of Si films grown by this deposit-anneal-deposit technique relative to those prepared by the conventional single-deposition method.

The effects on film properties of various annealing sequences after the Si/ Al_2O_3 composite was completed were also investigated. The results of anneal-

Table 12. Electrical Properties of Si Films Annealed in H₂ for 20 min after Growth of ~1000Å Thickness on Al₂O₃ Substrates (growth rate ~2µm/min)

Growth Temperature (C)	Film Orientation	Annealing Temperature (C) *	Measured		Resistivity (ohm-cm) **	Carrier Conc. (cm ⁻³) **	Mobility (cm ² /V-sec) **
			Final Thickness† of Film (µm) *	Final Thickness† of Film (µm) *			
1050	(100)	800	0.55	0.55	1.01	2.9x10 ¹⁶	210
1050	(111)	800	0.61	0.61	>10 ⁴	-	-
1050	(100)	1050	0.53	0.53	0.41	4.0x10 ¹⁶	380
1050	(111)	1050	0.48	0.48	2.58	1.4x10 ¹⁶	180
1100	(100)	800	0.64	0.64	0.87	3.3x10 ¹⁶	220
1100	(111)	800	0.67	0.67	0.55	2.3x10 ¹⁶	490
1100	(100)	1100	0.50	0.50	0.59	3.2x10 ¹⁶	330
1100	(111)	1100	0.55	0.55	1.49	2.2x10 ¹⁶	190

† Thickness measured at two locations on main segment of Hall bridge.

* Growth of final portion of film to thickness given carried out after annealing first ~1000Å at specified temperature.

**Numbers represent single determination of electrical parameter by standard techniques, after 1 hr O₂ anneal at 1100C.

Table 13. Electrical Properties of Si Films Annealed in H₂ for 20 min after Growth of ~2000Å Thickness on Al₂O₃ Substrates (Growth rate ~4µm/min)

Growth Temperature (C)	Substrate Orientation	Annealing Temperature (C)	Measured Final Thickness of Film (µm)	Resistivity (ohm-cm)*	Carrier Con. (cm ⁻³)*	Mobility (cm ² /V-sec)*
1100	(01 $\bar{1}$ 2)	750	0.56	0.71	3.3x10 ¹⁶	270
1100	(10 $\bar{1}$ 4)	750	0.56	0.76	4.2x10 ¹⁶	200
1100	~(11 $\bar{2}$ 0)	750	0.61	0.52	2.9x10 ¹⁶	420
1100	(01 $\bar{1}$ 2)	850	0.53	0.64	3.4x10 ¹⁶	285
1100	(10 $\bar{1}$ 4)	850	0.58	1.0	3.0x10 ¹⁶	200
1100	~(11 $\bar{2}$ 0)	850	0.59	0.76	2.3x10 ¹⁶	360
1100	(01 $\bar{1}$ 2)	940	0.59	0.57	3.9x10 ¹⁶	280
1100	(10 $\bar{1}$ 4)	940	0.61	0.98	3.1x10 ¹⁶	207
1100	~(11 $\bar{2}$ 0)	940	0.68	0.58	2.8x10 ¹⁶	390
1100**	(01 $\bar{1}$ 2)	-	0.60	0.43	4.7x10 ¹⁶	311
1100**	(10 $\bar{1}$ 4)	-	0.62	0.96	3.5x10 ¹⁶	187
1100**	~(11 $\bar{2}$ 0)	-	0.68	0.31	4.2x10 ¹⁶	478

*Numbers represent single determination of electrical parameter by standard techniques, after O₂-N₂ annealing steps.
 **No intermediate annealing step used.

ing a group of samples in an inert gas after previous extended O₂ anneals are given in Table 14. The data indicate the relative stability of the Si properties to both O₂ and N₂ anneals following an initial anneal in O₂ for a total of 2 hr.

Table 14. Effects of Extended O₂ and N₂ Anneals on Electrical Properties of Three As-doped, ~2μm-thick Si/Al₂O₃ Films (growth temperature 1100C)

Orientation of Al ₂ O ₃ Substrate	Annealing Treatment	Si Film Resistivity (ohm-cm)	Carrier Concentration (cm ⁻³)	Mobility (cm ² /V-sec)
(10 $\bar{1}$ 4)	1100C O ₂ (1 hr)	0.45	2.7 x 10 ¹⁶	520
	+1100C O ₂ (1 hr)	0.35	3.2 x 10 ¹⁶	560
	+1100C O ₂ (1 hr)	0.32	3.3 x 10 ¹⁶	590
	+1100C O ₂ (30 min)+			
	1100C N ₂ (4 hr)	0.33	3.1 x 10 ¹⁶	610
~(11 $\bar{2}$ 0)	1100C O ₂ (1 hr)	0.61	1.9 x 10 ¹⁶	550
	+1100C O ₂ (1 hr)	0.44	2.6 x 10 ¹⁶	560
	+1100C O ₂ (1 hr)	0.35	2.9 x 10 ¹⁶	610
	+1100C O ₂ (30 min)+			
	1100C N ₂ (4 hr)	0.37	2.8 x 10 ¹⁶	620
(01 $\bar{1}$ 2)	1100C O ₂ (1 hr)	0.46	3.5 x 10 ¹⁶	390
	+1100C O ₂ (1 hr)	0.30	5.1 x 10 ¹⁶	410
	+1100C O ₂ (1 hr)	0.29	5.8 x 10 ¹⁶	370
	+1100C O ₂ (30 min)+			
	1100C N ₂ (4 hr)	0.31	4.9 x 10 ¹⁶	410

In order to determine if a N₂ anneal is as effective as an O₂ anneal for the deactivation of electrically-active Al, several As-doped Si films were subjected to a N₂ anneal followed by an O₂ anneal. Identical control samples were annealed only in O₂. The resistivity was measured after each step with a 4-point probe, and the conductivity type was determined with a thermoelectric probe. The

results are shown in Table 15, and strongly suggest that the mechanism of Al deactivation is not primarily oxide gettering.

Table 15. Effects on Film Properties of Order of Sequential Annealing Steps in O₂ and N₂ for ~2 μ m-thick As-doped Si Films Grown at Various Temperatures on ~(11 $\bar{2}$ 0)Al₂O₃ at Rate of ~2 μ m/min

Growth Temp (C)	Substrate Designation	Annealing Treatment	Resistivity (ohm-cm)	Conductivity Type
1150	LM-27A	As grown	0.095	P
		1100C N ₂ (2 hr)	3.1	P
		+1100C N ₂ (2 hr)	3.4	N
		+1100C O ₂ (1 hr)	3.2	N
1150	LM-27B (control)	As grown	0.095	P
		1100C O ₂ (1 hr)	1.0	N
1125	LM-33A	As grown	0.26	P
		1100C N ₂ (2 hr)	6.0	N
		+1100C N ₂ (2 hr)	~10 (est.)	N
		+1100C O ₂ (1 hr)	~10 (est.)	N
1125	LM-33B (control)	As grown	0.41	P
		1100C O ₂ (1 hr)	0.74	N
1100	LM-32A	As grown	0.52	P
		1100C N ₂ (2 hr)	2.1	N
		+1100C N ₂ (2 hr)	1.7	N
		+1100C O ₂ (1 hr)	1.3	N
1100	LM-32B (control)	As grown	0.73	P
		1100C O ₂ (1 hr)	0.53	N

A significant fraction of Al was found to become electrically inactive after extended N_2 anneals. This suggested that most of the Al remains in the film and probably complexes with defects and/or other impurities to form neutral centers. Subsequent O_2 anneals had little additional effect on film properties. If the film was initially treated with O_2 prior to the N_2 anneal a lower resistivity n-type film resulted, indicating that O_2 is slightly more effective in reducing the effect of Al. These data imply that oxide gettering plays a significant but lesser role in reducing the active Al content.

Most of the Si films grown on Al_2O_3 and $MgAl_2O_4$ substrates in the He- H_2 atmosphere during this contract were subjected to a series of anneals at 1100C. The Si films were oxidized for 1/2 hr in dry O_2 , then annealed in dry N_2 for either 2 or 4 hrs. The oxide was then removed and the electrical properties were measured by the van der Pauw or Hall techniques. This process of annealing and measuring was then repeated sequentially until the electrical properties appeared to stabilize, with mobility used as the indicator for stabilization. The electrical properties of 2 μ m-thick films appeared essentially stable after 4 hrs of annealing time. This time period is slightly greater than that previously thought to be sufficient for Si deposits of this thickness. For 5 μ m-thick Si films on both Al_2O_3 and $MgAl_2O_4$ substrates much longer anneal times, from 6 to 10 hrs, were found necessary for comparable stabilization.

The effects of N_2 anneals on the electrical properties of as-grown intentionally-undoped p-type films were also examined. In most cases, a reduction in net acceptor concentration by approximately a factor of two was found after a 2-hour anneal at 1100C. An additional 2-hour anneal usually produced little additional change in acceptor concentration, with but slight decreases in Hall mobility. A subsequent O_2 anneal produced little additional change, just as in the case of the As-doped films.

A technique has been suggested in the literature (Ref 44) to improve the lifetime and carrier mobilities of Si/ Al_2O_3 films. The technique involves annealing the films in a HCl- O_2 mixture, which supposedly results in removal of many of those impurities which deleteriously affect the carrier lifetime.

Preliminary experiments in this program to determine the effects upon film mobility proved negative, i.e., no improvement in film quality was achieved.

A number of experiments were also performed with relatively thin Si films to determine the effects on film properties of annealing in H_2 in the reactor just after film growth. The data are summarized in Table 16 for the various annealing conditions used.

The results indicate that 60-min anneals in H_2 at 1100C deteriorated the quality of Si films 0.25-0.5 μ m thick, presumably by introducing additional defects and/or Al as an impurity. A 20-min anneal did not improve the electrical properties of a ~0.5 μ m-thick film but may have affected a film 0.3 μ m thick. In all cases reflection electron diffraction (RED) showed the films to be single crystal, even though the long anneals resulted in partially gray-looking overgrowths for the (111)Si films.

Table 16. Properties of Si Films Grown at 1100C at a Nominal Growth Rate of 2 μ m/min (annealed and unannealed samples)

Film Orientation	Total Thickness (μ m)	Resistivity ^{**} (ohm-cm)	Carrier Concentration ^{**} (cm^{-3})	Mobility ^{**} ($\text{cm}^2/\text{V-sec}$)	Remarks
100	0.33	0.19	1.3×10^{17}	265	No H ₂ anneal
111	0.38	0.61	3.5×10^{16}	300	
100	0.29	0.40	5.7×10^{16}	275	Anneal in H ₂ at 1100C for 20 min after growth
111	0.29	1.3	3.6×10^{16}	140	
100	0.25	~90.	$\sim 5.8 \times 10^{14}$	~60*	Anneal in H ₂ at 1100C for 60 min after growth
111	0.24	1.5	$\sim 3.9 \times 10^{16}$	110	
100	0.62	0.45	3.9×10^{16}	360	No H ₂ anneal
111	0.56	0.84	2.3×10^{16}	330	
100	0.53	0.35	5.4×10^{16}	330	Anneal in H ₂ at 1100C for 20 min after growth
111	0.51	0.60	2.5×10^{16}	370	

*Probably dominated by surface conduction

**Measurements made after O₂-N₂ annealing sequence at 1100C

10. GaAs GROWTH STUDIES

The main effort during this program was concerned with Si growth on Al_2O_3 and MgAl_2O_4 ; however, consideration was also given to problems associated with the growth of GaAs using the metalorganic process, i.e., deposition of GaAs by the pyrolysis of trimethylgallium (TMG) and arsine (AsH_3), a process developed at Rockwell in 1968 (Ref 45). The studies took mainly two avenues: (1) evaluation of new sources and batches of the reactants by the "use-test," i.e., growth of GaAs on (0001) Al_2O_3 and film electrical evaluation; and (2) GaAs growth on Cr-doped high-resistivity GaAs using some of the materials evaluated in (1).

In previous studies (Ref 46) at Rockwell it had been demonstrated that there are differences in the quality of the TMG and AsH_3 -in-gas mixtures, and in-line purification procedures were found necessary to help improve the quality of the reactants. Experience indicates that a "use test" is probably sufficient for reactant evaluation, with (0001) Al_2O_3 as the substrate for GaAs growth. During this contract program several combinations of reactants were used in GaAs film growth.

The results are recorded in Table 17. The electrical properties appear to be consistent with data obtained on other TMG- AsH_3 combinations; the results suggest that there has been a considerable improvement in the consistency of the quality of reactants now available as compared with material available a few years ago. The GaAs films on Al_2O_3 with low carrier concentrations were found to have low mobilities, as was previously observed (see Figure 7 of Ref 46).

A comparison of source tank combinations (see Table 17) BR-AT, CE-AT, and CK-AT indicates a large donor impurity concentration in tank BR; the electrical properties indicate, however, that good quality films can be produced with BR and AT at concentrations not below $\sim 2 \times 10^{16} \text{ cm}^{-3}$. Additions of a donor to the CK-AT combination led to good quality GaAs films on Al_2O_3 , for a doping level of $\sim 2 \times 10^{16} \text{ cm}^{-3}$. Actually, when precautions were taken to

Table 17. Evaluation of Source Materials by GaAs Growth on (0001)Al₂O₃

TMG		AsH ₃ (10%)		Film Properties			
Tank Identification	Source	Tank Identification	Source	Thickness (μm)	Resistivity (ohm-cm)	Carrier Conc. (cm ⁻³)	Mobility (cm ² /V-sec)
CK	Texas Alkyls	CR	Phoenix Research	28.3	1.06	2.0 x 10 ¹⁵	3030
CK	Texas Alkyls	CD	Matheson	23.5	7.5	5.0 x 10 ¹⁴	1700
BR	Ventron	AT	AIRCO	32.2	0.05	1.9 x 10 ¹⁶	6400
CE	Texas Alkyls	AT	AIRCO	36.3	3.7	6.8 x 10 ¹⁴	2500
CK	Texas Alkyls	AT	AIRCO	36.2	8.5	3.9 x 10 ¹⁴	1900
CA	Texas Alkyls	BY	AIRCO	25.4	11.3	3.6 x 10 ¹⁴	1500
DF	Texas Alkyls	DN	Three H Corp.	28.	19.7	3.0 x 10 ¹⁴	1045

remove moisture from the gas stream, all the AsH_3 tanks listed in Table 17 were useful for GaAs film growth. Tank DN, from Three H Corporation, was found to be the driest of those evaluated.

Several of the films grown with those reactant gases which produced low carrier concentrations were angle-lapped and stained to determine the thickness of the interface high-resistivity p-type layer. Layers 8-12 μm thick were found for undoped films with carrier concentrations in the range $4-8 \times 10^{14} \text{ cm}^{-3}$. The behavior of these p-type layers was identical to that previously observed in the GaAs/ Al_2O_3 system (Ref 46), where the thickness of the p-layer was found to depend upon the donor concentration in the gas sources. If the films in this case were also dominated by acceptor centers from the same source, then the donor impurity concentration in these source gases must have been the order of 10^{13} cm^{-3} or less. An alternative explanation for the cause of the p-type conductivity could be the presence of a deep-level acceptor impurity (e.g., Cr or Fe) in the source gases; this could also lead to an automatic compensation. Earlier data on films grown with other combinations of AsH_3 and TMG tended to rule out this possibility, however.

GaAs films were also grown on GaAs substrates in order to examine the properties of thick and thin films and compare homoepitaxial film properties with heteroepitaxial film properties. The DF-DN source tank combination was used in this study. These experiments were also planned to produce films that would subsequently be useful for FET fabrication.

Surprisingly, the results of film growth on GaAs substrates were consistent with those found for growth on $(0001)\text{Al}_2\text{O}_3$. Very thin undoped films ($\sim 1\mu\text{m}$ thick or less) were found to be inhomogeneous in their electrical properties when grown on (100) and (111)GaAs substrates. When dopant was added to the film during growth, a 28 μm -thick film on (111)GaAs possessed the following properties: $\rho = 0.035 \text{ ohm-cm}$; $n = 4.0 \times 10^{16} \text{ cm}^{-3}$; and $\mu = 4530 \text{ cm}^2/\text{V-sec}$. These properties are not very different from those obtained on $(0001)\text{Al}_2\text{O}_3$.

A 1 μm -thick film grown directly on GaAs and doped to $2.2 \times 10^{16} \text{ cm}^{-3}$ had a

mobility of only $1620 \text{ cm}^2/\text{V-sec}$. However, when layers $1\mu\text{m}$ thick were grown on $3\mu\text{m}$ high-resistivity layers of GaAs grown initially on (111)GaAs substrates, mobilities of $3500\text{-}3900 \text{ cm}^2/\text{V-sec}$ were realized for $n \sim 5 \times 10^{16} \text{ cm}^{-3}$. Simultaneous double-layer growth on Al_2O_3 led to a mobility value of $\sim 3300 \text{ cm}^2/\text{V-sec}$ for $n = 3.4 \times 10^{16} \text{ cm}^{-3}$. These results indicated that there were important interface problems to be solved before high quality $1\mu\text{m}$ -thick homoepitaxial layers and heteroepitaxial layers could be grown directly on an etched/cleaned substrate.

11. CONCLUSIONS

It was during the analysis of the Si films grown in these studies that two major contributions to the understanding of Si heteroepitaxial film systems were made: 1) It was demonstrated that the charge carrier mobilities typically obtained for n-type Si heteroepitaxial films up to $\sim 2\mu\text{m}$ thick are in error when the carrier concentrations are below 10^{16}cm^{-3} , i.e., surface-state conduction is an important factor in such films; and 2) a mobility anisotropy exists in Si films on Al_2O_3 that is a function of current direction in the plane of the film and is dependent upon the orientation of the substrate and of the film. For (100)Si on $(01\bar{1}2)\text{Al}_2\text{O}_3$, an average anisotropy in mobility of $\sim 9\%$ was obtained; even greater average anisotropies were measured in (111)Si films on $(10\bar{1}4)$ ($\sim 30\%$) and $\sim (11\bar{2}0)\text{Al}_2\text{O}_3$ ($\sim 16\%$) when the films were grown in a H_2 atmosphere.

The existence of the mobility anisotropy helps to explain the variation in electrical properties of films grown in various laboratories that might otherwise have placed in doubt much of the data accumulated under this program prior to the determination of the magnitude of mobility anisotropy. Most of the data for films grown on the three Al_2O_3 orientations $(10\bar{1}4)$, $\sim (11\bar{2}0)$, and $(01\bar{1}2)$ was obtained on oval substrates, each set cut from a single boule of Al_2O_3 ; the original square-type Hall-effect pattern was, for reasons of processing convenience, placed in approximately the same position on all films evaluated. Thus the data on any one orientation are considered directly comparable, and differences in electrical properties can probably be related to the parameter changes that were made.

Since anisotropy for (100)Si is less than that for (111)Si, and measurements on the square-type bridge were made with the current flow in a direction other than that displaying a mobility maximum, the data support even more the contention that (111)Si films on $\sim (11\bar{2}0)\text{Al}_2\text{O}_3$ are superior to (100)Si films on $(01\bar{1}2)\text{Al}_2\text{O}_3$. Since the electrical measurements on the square bridge on $(10\bar{1}4)\text{Al}_2\text{O}_3$ were made ~ 20 deg from the direction of maximum mobility, any suggestion of equivalence in the electrical properties of (111)Si grown on $(10\bar{1}4)\text{Al}_2\text{O}_3$ and (100)Si on $(01\bar{1}2)\text{Al}_2\text{O}_3$ at growth temperatures $< 1050\text{C}$

is in error; the (111)Si would be expected to be electrically superior to the (100)Si films when measured in the direction of maximum mobility.

As previously indicated, the deposition studies during this program were directed toward identifying the 1) preferred substrate, 2) optimum growth temperatures, 3) preferred film orientations, 4) preferred growth atmosphere, 5) preferred substrate orientations, and 6) optimized overall growth process. These identifications must be made on the basis of several criteria, including the electrical properties of the films grown on the substrates being compared, but the true test of the conclusions will be when these film-substrate combinations are made into devices and used in the intended applications.

The electrical data point to Czochralski MgAl_2O_4 as the preferred substrate for Si growth, since mobilities as high as $925 \text{ cm}^2/\text{V-sec}$ were measured in (111)Si films grown on mechanically polished surfaces, mobility anisotropy is nil, and autodoping is less for MgAl_2O_4 as compared with Al_2O_3 as the substrate. However, further effort must be expended in learning how to work with MgAl_2O_4 , for MgAl_2O_4 appears to be very sensitive in its reaction to H_2 at high temperatures ($>1100\text{C}$), to materials used in cleaning the surface, to impurities in the SiH_4 , and to device processing steps. On the other hand, Al_2O_3 is hardier to the problems that seem to plague MgAl_2O_4 ; for those devices which do not depend upon the highest achievable and the most uniform mobility, Al_2O_3 should be considered as the preferred substrate.

The optimum growth temperature is a function of the substrate and orientation chosen. For (111) MgAl_2O_4 a growth temperature of $\sim 1025\text{C}$ is recommended when the film is grown in a He or He- H_2 atmosphere. Growth on $(10\bar{1}4)\text{Al}_2\text{O}_3$ and $\sim(11\bar{2}0)\text{Al}_2\text{O}_3$ appears to be best in the temperature range $1075\text{-}1100\text{C}$, while the best Si on $(01\bar{1}2)\text{Al}_2\text{O}_3$ was found in the range $1050\text{-}1075\text{C}$, in either H_2 or He- H_2 atmospheres.

Of those studied, the preferred film orientation is (111)Si, although some high mobilities were obtained in (221)Si films grown on $(11\bar{2}2)\text{Al}_2\text{O}_3$. (100)-oriented Si growth (on $(01\bar{1}2)\text{Al}_2\text{O}_3$) under "optimum" growth conditions

invariably had poorer electrical properties than (111)Si films grown under "optimum" conditions on $\sim(11\bar{2}0)Al_2O_3$. On $MgAl_2O_4$, (111)Si was also superior to (100)Si.

The atmosphere preferred for the growth of Si might be He were it not for the fact that the reaction to form Si is very inefficient in a He atmosphere, and the wall deposits of the intermediate silicon hydrides are very heavy. The addition of H_2 to the He solves these problems, and good Si growth is achieved on (111) $MgAl_2O_4$ and on most orientations of Al_2O_3 . Unfortunately, the Si growth rate has not been always controllable in the mixed atmosphere, presumably due to the fact that the growth rate is influenced by small temperature changes when mixed-gas compositions are used. In the mixed-gas system, particularly, a thickness monitoring device is beneficial to help determine when a film of a particular thickness has been grown. Better growth rate control is achieved when growth is performed in a H_2 atmosphere; except for Si growth on (111) $MgAl_2O_4$ and perhaps $(10\bar{1}4)Al_2O_3$, a H_2 atmosphere appears adequate and at least as good as He- H_2 atmospheres for Si growth on other orientations of Al_2O_3 studied under this program.

Autodoping was not studied to any major extent in the He- H_2 atmospheres, but it was demonstrated that in a H_2 atmosphere a significant amount of H_2 and Al_2O_3 reaction product is introduced into the gas phase at $\sim 1100C$, and would be present when film growth is initiated at or near that temperature. Growth in H_2 at low temperatures would help minimize this problem, and the use of a minimum amount of H_2 in the atmosphere would also help. These considerations must be made consistent with the other optimum growth parameters for the substrate and orientation of interest.

Electrical data point to $\sim(11\bar{2}0)$ -oriented Al_2O_3 and (111) $MgAl_2O_4$ as being the preferred substrate orientations for Si growth, both influencing (111)Si growth. However, the industry has chosen (100)Si/(01 $\bar{1}$ 2) Al_2O_3 as the primary film-substrate combination for the fabrication of MOS devices. The criterion for this selection appears to be that in bulk Si the (100) plane has a lower

surface-state density (SSD) than does the (111) plane; however, the differences in SSD between (100) and (111)Si films grown on insulators are not known. It may be that other properties of the heteroepitaxial films overshadow the SSD contribution, and superior devices may still be possible in (111)Si.

All of the above can be combined into an optimized overall growth process, but the process must be related to the ultimate requirements of the film. If the highest mobilities are desired, then Si films should be grown at $\sim 1025\text{C}$ on (111)-oriented MgAl_2O_4 or at $\sim 1075\text{C}$ on $\sim(11\bar{2}0)$ -oriented Al_2O_3 in He- H_2 mixtures. When the best (100)Si films are desired, they can be grown on $(01\bar{1}2)\text{Al}_2\text{O}_3$ at $1050\text{-}1075\text{C}$ in atmospheres of H_2 or He- H_2 mixtures. For most orientations, growth rates from $\sim 2\mu\text{m}/\text{min}$ to $\sim 4\mu\text{m}/\text{min}$ appear to be sufficient, although good growth has also been achieved on $(01\bar{1}2)\text{Al}_2\text{O}_3$ at lower rates.

Finally, because the growth conditions are dependent upon reactor geometry and should be optimized for the particular film thickness desired, the above recommendations are limited to the growth system used in these investigations and to films $\sim 2\mu\text{m}$ thick. However, the results that have been obtained can be used as guides for studying film growth in other types of reactors.

SECTION 4

ANALYSIS AND PURIFICATION OF CVD REACTANTS

It had become clear even before the start of this contract program that the probable impurity content of the various reactants used for CVD of Si and GaAs heteroepitaxial films probably provided the real limitation on the achievable impurity levels in the films themselves. To explore this a study was undertaken to attempt to identify the impurities present in the reactants and to establish the concentrations of the principal impurities that might influence the properties of the films if they were to become incorporated into the films during growth.

During the first year, techniques of gas chromatography were developed for analysis of the reactants used for Si and GaAs heteroepitaxy by CVD. A general-purpose gas-handling system was constructed for the highly volatile and reactive gases studied, with silicone oil and polymer columns used for the chromatography. Several extraneous impurity peaks were observed in the chromatograms of SiH_4 samples; diborane (B_2H_6) was tentatively identified as a significant impurity (~10 ppm), although not confirmed by mass spectrometer techniques. Small quantities of purified SiH_4 , free of diborane, were prepared by successive injections in the chromatograph. The quantities were too small, however, for use in laboratory CVD experiments.

Beginning in the second year of the program samples of SiH_4 and of trimethylgallium (TMG) used for Si and GaAs CVD experiments were analyzed for impurity content by sensitive mass spectrometric techniques. Disilane and trimethylsilane, together with several other impurities of less concern, were found in the SiH_4 samples. The analyses of TMG left some uncertainties regarding the correct impurity levels, although these were largely resolved by later analyses carried out in the final half of the second year.

Significant impurity concentrations in some of the reactants (especially SiH_4) severely limited the accuracy of the study of the effects of deposition param-

eters on Si film properties on several occasions during the early part of the contract work. Cooperative efforts with vendors for preparation of improved-purity reactants continued throughout the program, as did analyses of reactants by mass spectrometer techniques.*

1. REACTANT ANALYSIS BY GAS CHROMATOGRAPHY**

Studies were initiated early in the program to analyze SiH_4 and trimethylgallium (TMG) first and then AsH_3 , using techniques of gas chromatography and mass spectrometry. Among the various techniques available in analytical chemistry, this combination was selected as the most convenient method to analyze volatile inorganic compounds, as such components are expected to be present at the sub-ppm concentration level in the reactants of interest here.

Gas chromatography (GC) by itself is not an absolute method to identify the components of a sample. The general procedure used in qualitative GC is to compare experimental retention data with those obtained with reference samples. The results then have to be confirmed by an analytical method, preferably employing direct coupling from the detector of a gas chromatograph to the inlet of a mass spectrometer. Special adapters are needed to eliminate large excesses of carrier gas from the main flow. However, in these experiments the direct coupling was not available; the sample from the effluent of the gas chromatograph was collected in a special trap and then injected into a mass spectrometer.

Monosilane, SiH_4 , was studied primarily. It was assumed that the contaminants originated in the SiCl_4 used to prepare SiH_4 . Boron compounds, which may be present in SiCl_4 , can be reduced to volatile hydrides such as diborane (B_2H_6). The relatively close boiling points of the pair SiH_4 - B_2H_6 do not allow effi-

* These analyses were carried out by West Coast Technical Service, Inc., San Gabriel, CA.

**This work was done by Marie Dixmier and R. L. Pecsok of the Chemistry Department of the University of California at Los Angeles.

cient elimination of the latter by typical industrial fractional condensation processes. But the difference of 30C in their boiling points is sufficient to separate these two compounds by analytical GC, if the right column packing is selected.

All of the reactant materials used in semiconductor heteroepitaxial studies by CVD are highly volatile and reactive gases. Special care was taken in this work to prevent hazardous contact of these gases with air and moisture.

The general function of the gas handling system used in this study (Figure 31) was to introduce the sample under vacuum through a three-way valve, and to dispose of the sample by purging with He (at a high flow rate) to the burning port. A 500-ml stainless-steel trapping cylinder was used to temporarily condense the sample fraction before injection. Connections and fittings were made of 316 stainless steel, as were the shut-off and metering valves. The injection valve was a three-way mini-volume valve (Carle No. 5521) with interchangeable loops of different volumes.

After extensive testing and some modification this system was shown to be explosion-proof, but for routine use even minor leaks must be avoided. The injection valve was found to be less dependable than the other parts of the system. A bellows valve or a purge-model valve with a closed housing would be preferable for systems such as this.

In the first experiments, classical gas-liquid chromatography was used. Non-polar stationary phases such as silicone oil are known to separate silanes (Refs 47, 48) or light boranes (Refs 49, 50, 51). The first packing used was Dow-Corning silicone DC-200, 20% by weight on Chromosorb P, acid-washed and silanized. A Loenco gas chromatograph (Model 160), equipped with a 4.2m x 6mm o.d. stainless-steel column and a thermal conductivity detector, was used for the investigations. Isothermal elution at 40C was obtained with a He flow rate of 50 ml/min. The sample volume, measured in a 2.5-ml loop under 2.5 psi of SiH_4 , was calculated to be about 4 ml at STP.

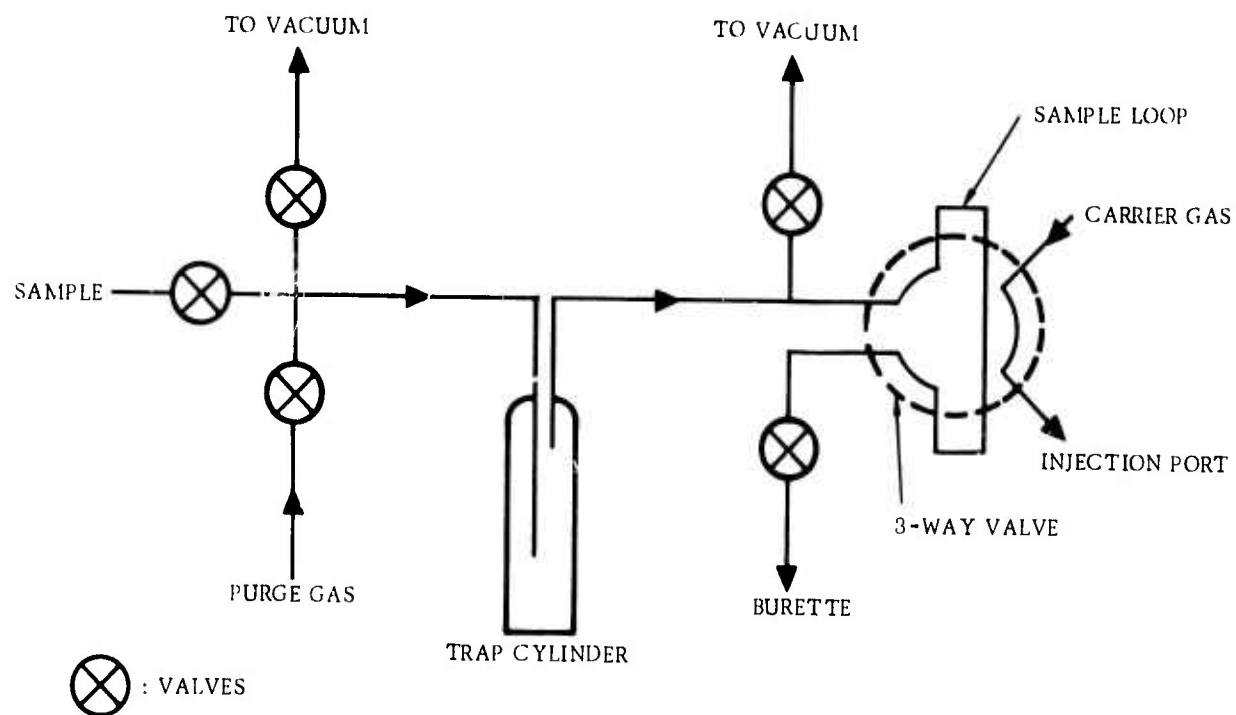


Figure 31. Schematic of Gas Sample Handling System for GC

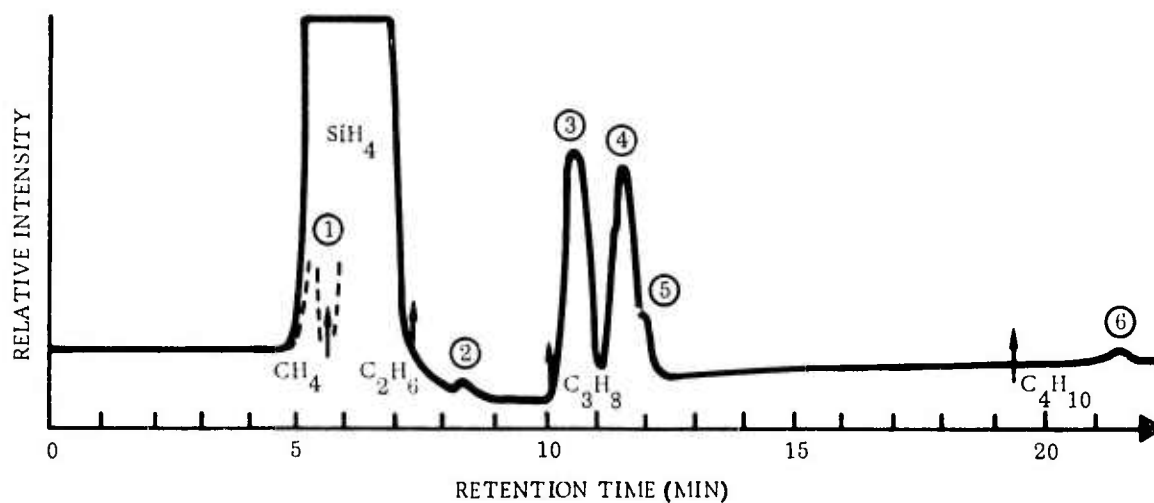


Figure 32. SiH₄ Chromatogram on DC-200 Silicone Column Packing

Samples of semiconductor-grade SiH_4 from four different supply cylinders gave the same basic chromatogram (Figure 32), with at least six impurities detected by the thermal conductivity detector. Retention indices versus n-paraffin homologs and concentrations in ppm calculated by the area method are given in Table 18. Identification of one of these impurities as B_2H_6 was attempted by comparison with a known B_2H_6 reference sample.

It should be pointed out that in analytical GC, characterization of a given solute is given by a unique specific retention time. But in semipreparative GC, when large amounts of solute are injected, large variations of retention times can be expected because of overloading effects. Under these conditions, equilibrium distribution of the sample between the phases is not maintained, and the excess sample will travel at a higher speed through the column (Ref 52). For large samples of both B_2H_6 and SiH_4 there was a decrease in retention times from the analytical data. Retention times were evaluated from experimental data with a 3 percent range of variation. With the DC-200 column, the B_2H_6 noncorrected retention time was 12% greater than for SiH_4 . This small difference in retention times was not sufficient to separate these two compounds on a preparative scale, or even to detect B_2H_6 completely hidden in the main peak of SiH_4 .

The experimental results confirmed the general behavior of a silicone column toward nonpolar solutes; i.e., retention times were in order of the boiling points. As the chemical reactivities of SiH_4 and B_2H_6 are similar, it could not be expected that a polar stationary phase would enhance the separation by specific selectivity. Thus, in order to increase the ratio of the retention times a solid packing having a large specific area was used. A second column was prepared with Chromosorb 102 (Johns Manville) as packing for gas-solid chromatography. This is a cross-linked copolymer of divinyl benzene-styrene which exhibits a surface area 100 times greater than the Chromosorb P used previously. This column was 5.4m x 6mm o.d., packed with 60 to 80 mesh Chromosorb 102. The column was first maintained at ambient temperature, with a He flow rate of 40 ml/min.

Table 18. Retention Index and Concentration
of Impurities in SiH₄ Sample

<u>Impurity</u>	<u>Concentration (ppm)</u>	<u>Retention Index</u>
(1) H ₂ + air	7000	-
(2)	<10	250
(3)	260	305
(4)	415	323
(5)	10	-
(6)	<10	>400

A typical chromatogram of a SiH₄ sample on the Chromosorb 102 column is shown in Figure 33. Four impurity peaks are evident before the main SiH₄ peak. By comparison with reference samples these peaks appear to correspond to (1) H₂, (2) N₂+O₂ (air), (3) CH₄, and (4) CO₂.

No impurities were detected after the SiH₄ peak. Unfortunately, with the available chromatographic equipment, it was not possible to expect a large improvement in detection. However, the difference of retention times of SiH₄ and CH₄ was about three times larger with Chromosorb 102 than with the DC-200 column.

In order to reduce the retention times of solutes eluted after the SiH₄ peak, an isothermal chromatogram at 60C was obtained with a reference mixture of SiH₄ and B₂H₆ and is shown in Figure 34. Retention data are expressed here in corrected retention distance

$$d'_R = d_R - d_M, \quad (21)$$

where d_M is related to hydrogen and $d_R = t_R \times$ (chart speed), with t_R the retention time in minutes and the recorder chart speed 1 in/min in this case.

It is interesting to compare the experimental retention data with the boiling

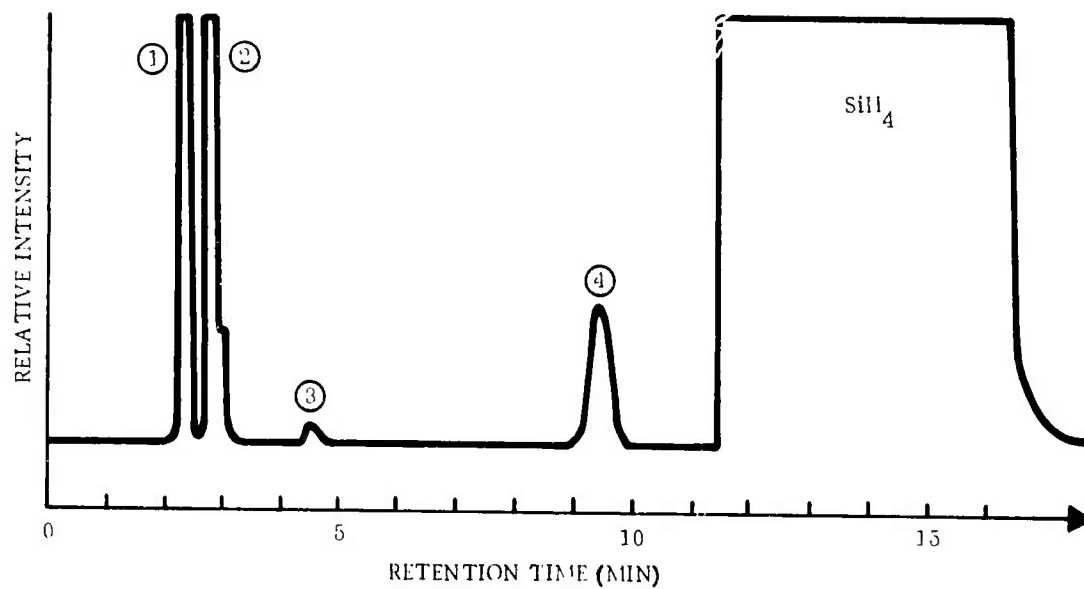


Figure 33. Chromatogram for SiH_4 and other Compounds on Chromosorb 102 Column at Ambient Temperature

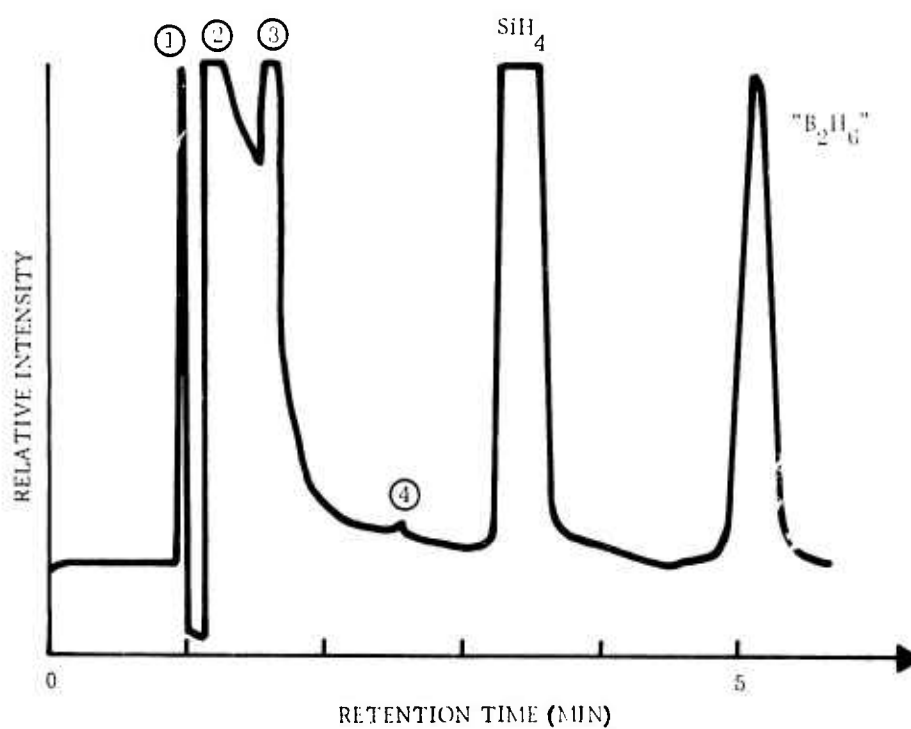


Figure 34. Chromatogram of Mixture of SiH_4 and B_2H_6 on Chromosorb 102 Column at 60C.

points of the different compounds which might be present in the SiH_4 sample. This was done by the use of a thermodynamic relation derived from the Clausius-Clapeyron equation. This simplified relation is

$$\log d'_R \propto \text{BP} . \quad (22)$$

A classical calculation related d'_R to the vapor pressure of a given solute, and the vaporization enthalpy of the pure solute to its boiling point. Although this relation applies strictly to compounds of an homologous series, it was interesting to verify the behavior of C, Si, and boron hydrides on Chromosorb 102. Results are given in Table 19.

The experimental values verify the relation of Equation (22) and confirm that, as in gas-liquid chromatography on a silicone oil, these solutes were eluted in the order of their boiling points. However, an important improvement was obtained with Chromosorb 102, specifically, the large increase of B_2H_6 retention versus that of SiH_4 - 80% compared with the 12% on the silicone DC-200 column. Even with large overloading of the Chromosorb 102 column with preparative injections of SiH_4 , a good separation of the couple SiH_4 - B_2H_6 could be expected, sufficient to detect the latter at the sub-ppm level.

In order to confirm and identify the nature of the solutes, several collected effluents were injected into the CEC Model 21-620 mass spectrometer. In a 50 ml glass flask previously evacuated, the effluent stream of solute and carrier gas was trapped in totality. The time of collection was roughly one minute, selected near the maximum of the detector signal. As will be shown later, this technique gives good yields of recovery for preparative collection of purified samples, but for mass spectrometry the results were very poor. The main reason appeared to be that the sample was too dilute for the injection system of the mass spectrometer; the sample was diluted by a factor of 10^3 from the injection volume.

Attempts to identify peak 3 in the sample represented in Figure 32 and even B_2H_6 in the sample of Figure 33 failed. Only one impurity present in both the

SiH₄ sample (Figure 32) and the B₂H₆ reference mixture was identified and that was CH₄. Results from two collected samples compared with the theoretically expected relative intensities for the mass spectrometric analyses are given in Table 20.

Table 19. Comparison of Retention Data and Boiling Points of Solutes Eluted According to Figure 33

	<u>CH₄</u>	<u>SiH₄</u>	<u>B₂H₆</u>
d' _R (mm)	28	115	207
log d' _R	1.45	2.06	2.32
BP (C)	-161.5	-112	-92.5

Table 20. Mass Spectrometric Data for CH₄

m/e	Relative Intensity (70V)		
	<u>1st Sample</u>	<u>2nd Sample</u>	<u>Theory</u>
16	100	100	100
15	81.7	83.6	85.9
14	(33.4)	11.2	16.1

More informative results were obtained in collection experiments in some semi-preparative GC. Three series of successive GC collections of purified SiH₄ were obtained, with four, seven and 10 runs, respectively. In each run, the amount of SiH₄ collected was calculated to be 5 mg, corresponding to the injection volume of 4 ml. The recovered material was tested for purity by recycling the sample through the Chromosorb 102 column for the first two series and through both the DC-200 and Chromosorb 102 columns for the last series. Elimination of impurities 2 through 6 (see Figure 32 and Table 18)

was demonstrated by elution of successive equal volumes of purified and crude SiH_4 on the DC-200 column.

In the Chromosorb 102 column, impurities 3 and 4 (see Figure 33) were completely removed, but traces of air still remained. B_2H_6 was not detected in the SiH_4 sample with the Chromosorb 102 column because of the poor sensitivity of the thermal conductivity detector.

It was thus not possible to certify the dependability either of the particular gas chromatographic techniques used or of the collection apparatus. However, the retention time of B_2H_6 on Chromosorb 102, almost two times larger than that of SiH_4 , shows that GC can be a promising and efficient method to detect and even to separate B_2H_6 from SiH_4 . Therefore, a compromise would have to be made between the reliability of preparative-scale GC and its limited production capability for industrial purposes.

2. REACTANT ANALYSIS BY ROUTINE MASS SPECTROMETRY

Analyses of the reactants used in the CVD experiments were also made routinely by sensitive mass spectrometric techniques with the assistance of external analytical service laboratories. Numerous samples of SiH_4 and of trimethylgallium (TMG) used for Si and GaAs CVD experiments were analyzed for impurity content.

During the course of the program, eight different tanks of "pure" SiH_4 were used in the studies of Si deposition. These were all analyzed for impurity content by an analytical service laboratory* using mass spectrometric techniques. One of the tanks was also reanalyzed after the pressure had dropped in use to 35 psi from an original value of 85 psi.

These data are given in Table 21, together with an independent analysis performed by another laboratory** and supplied with one of the SiH_4 tanks by the vendor. First, the discrepancies in the data of the two analyses obtained for the tank CP of SiH_4 supplied by Vendor D are significant. The analytical procedures used in the supplied analysis apparently were not able to detect, for example, less than 3000 ppm of O_2 , an impurity of importance in SiH_4 which could lead to the formation of SiO_2 (and resulting pinholes) in deposited Si films. The other differences in the analytical data for this tank indicated insufficient sensitivity in the mass spectrometer methods used in the analysis to properly establish the concentrations of those impurities which could be detrimental to high-purity Si growth.

Note the relatively high concentrations of H_2 and disilane in some of the tanks. The effects of these impurities on Si growth seem to be minimal in a growth system using H_2 as the carrier gas. However, if He is the carrier it is difficult to predict how these impurities might affect the film nucleation

*West Coast Technical Service, Inc., San Gabriel, CA.

**Gollob Analytical Service, Berkeley Heights, NJ

Table 21. Mass Spectrometric Analyses of SiH₄

Constituent	Tank CL ^{††}		Tank CP ^{††}		Tank CZ ^{††}		Tank BZ ^{††}
	Cyl. RR32277 (Vendor A) ppm	ppm	Cyl. 15-1796 (Vendor D) ppm	ppm	(At 85 psi) ppm	(At 35 psi) ppm	
Hydrogen	115		ND 1x10 ³		38	18	<5*
Water	1		NR	2	4	<1*	<1*
Argon	26		ND 10	97	68	46	<1*
Hydrocarbons as butane	1		NR	1	<1*	<1*	<1*
Disilane	195		70	28	10	8	9
Boron compounds	<1*		NR	<1*	<1*	<1*	NR
Carbon dioxide	<1*		ND 10	39	<1*	2	<1*
Monochlorosilane	<1*		NR	<1*	<1*	<1*	<1*
Oxygen	<5*		ND 3x10 ³	<5*	<5*	<1*	<5*
Helium	<2*		ND 20	<5*	<5*	<1*	<2*
Siloxane	<5*		ND 10	<5*	<5*	<1*	<5*
Trimethylsilane	NR		NR	NR	NR	NR	23
Silane (SiH ₄)	Balance		Balance	Balance	Balance	Balance	Balance

*Limits of detector

ND = None detected, so less than ...

NR = Not reported

† Analyses performed by West Coast Technical Service, Inc., unless otherwise noted.
 †† Laboratory designation of SiH₄ tank.

⊙ Analysis supplied with tank, done by Gollob Analytical Service

Vendors: A: Will Ross, Inc., Matheson Gas Products Div., Cucamonga, CA
 D: Scientific Gas Products, Inc., Edison, NJ
 C: Synthatron Corp., Edgewater, NJ

mechanism. Another source of concern is the CO_2 content in tank CP from Vendor D. This impurity also could lead to SiO_2 formation in a H_2 atmosphere by a "water-gas" reaction,



the water then reacting with SiH_4 to form SiO_2 .

The remeasurement of the impurity levels in the SiH_4 from Vendor C was prompted by a sudden inability to control Si film growth rates within reasonable limits (~10 percent) with either He or H_2 carrier gases. The second analysis, however, did not provide an indication of the cause of this difficulty. A change in SiH_4 tanks apparently solved the problem of growth-rate control, although the electrical properties of the films grown on MgAl_2O_4 with the first tank of SiH_4 (tank CZ) were quite good; mobilities were between 700 and 925 $\text{cm}^2/\text{V-sec}$ for films with carrier concentrations of 10^{16} - $10^{17}/\text{cm}^3$.

The change to another tank of SiH_4 (supplied by a fifth vendor* for evaluation) was coincident with the growth of films with reduced mobilities - lower than 700 $\text{cm}^2/\text{V-sec}$. With the change of SiH_4 tanks growth and dopant control had to be reestablished; Si films were grown on (111) MgAl_2O_4 with mobilities similar to those obtained on (0112) Al_2O_3 (~400-500 $\text{cm}^2/\text{V-sec}$) but inferior to those obtained previously on (111) MgAl_2O_4 (700-925 $\text{cm}^2/\text{V-sec}$).

To explore the situation further, the condensable component of the reactant was trapped in the SiH_4 line at -78C and transferred to a specially prepared sampling cylinder for mass spectrometer analysis. The presence of H_2O and tetrahydrofuran (THF) in this sample was established and was consistent with the fact (determined subsequently) that the manufacturer used THF as a solvent in the preparation of the SiH_4 . The low mobilities, however, were not consistent with the fact that a 100 μm -thick film of Si grown on p-type Si had reasonable electrical properties ($\rho=24.8$ ohm-cm, $n=1.98 \times 10^{14} \text{ cm}^{-3}$, and $\mu = 1270 \text{ cm}^2/\text{V-sec}$). It appears that something in the SiH_4 was affecting the

*Liquid Carbonic Corporation

growth quality on insulating substrates. The results also suggested that SiH_4 and H_2O can coexist in a closed container but that their reaction is catalyzed by exposure to air.

This impurity problem has prevented an accurate evaluation of the effects of deposition parameters on Si film properties. It would be necessary to perform such studies with sufficient quantities of starting materials to complete the entire investigation, with the hope that the gas purity would not be affected by changes in total tank pressure. In view of this, 200 gm of SiH_4 were obtained from Synthatron Corporation for further studies of Si growth on MgAl_2O_4 . However, this tank (DC) was returned to the vendor for replacement after high concentrations of H_2 , H_2O , and Ar were found. As noted in Table 22, its replacement (tank DM) was of considerably higher purity.

Both tanks DI and DM were also evaluated by means of Si growth on p-type Si substrates. A 100 μm -thick film of Si grown using tank DI had the following electrical properties: $\rho = 9.3 \text{ ohm-cm}$; $n = 4.8 \times 10^{14} \text{ cm}^{-3}$; and $\mu = 1390 \text{ cm}^2/\text{V-sec}$. A film grown using tank DM had the following properties: $\rho = 57 \text{ ohm-cm}$; $n = 6 \times 10^{13} \text{ cm}^{-3}$; and $\mu = 1750 \text{ cm}^2/\text{V-sec}$. In both cases, the electrical characteristics are indicative of very good film quality and thus of good SiH_4 having relatively little content of impurities damaging to the properties of the Si films.

Analyses were also made of the AsH_3 used in the deposition of GaAs. A tank of AsH_3 -in-He (nominally 10% AsH_3) was obtained from Airco for GaAs growth studies. In evaluating it by means of GaAs growth on Al_2O_3 , using a good source of trimethylgallium, it was found that considerable condensate was obtained at -45C . The tank was returned to the vendor, and it was analyzed by West Coast Technical Service, Inc. The gas was found to contain the following:

AsH_3	12.2 mole percent	Argon	17 ppm
Water	15 ppm	CO_2	4 ppm
N_2	56 ppm	H_2S	4 ppm
Oxygen	15 ppm	He	balance

Table 22. Mass Spectrometer Analyses of SiH₄

Constituent	Tank DE Cyl. RR41849 (Vendor A) ppm	Tank DI Cyl. G170 (Vendor B) ppm	Tank DC Cyl. C-1016 (Vendor C) ppm	Tank DI Cyl. 6-967 (Vendor C) ppm
Hydrogen	75	10	2.49 (mole %)	305
Water	<1*	<1*	690	1
Argon	250	63	220	30
Hydrocarbons	<1	<1*	<1	<1
Disilane	6	92	24	10
Boron compounds	<1*	<1*	<1*	<1*
Carbon dioxide	2	<1	<1	NR
Monochlorosilane	<1*	<1*	<1*	<1*
Oxygen	<1*	<1*	<1*	<1*
Helium	<1*	<1*	<1*	<1*
Siloxanes	<1*	<1*	<1*	<1*
Silane (SiH ₄)	balance	balance	balance	balance

* Limits of detection NR = Not reported

† Analyses performed by West Coast Technical Service, Inc. Vendors: A: Will Ross, Inc., Matheson Gas Products Div., Cucamonga, CA

‡ Laboratory designation of SiH₄ tank B: Union Carbide Corp., Linde Div., Los Angeles, CA

C: Synthatron Corp., Edgewater, NJ

The high concentration of water, O_2 , CO_2 , and H_2S could be expected to affect the quality of the GaAs films. The mass spectrometric analysis of the replacement tank (DP) is shown in Table 23 together with results obtained for a tank (DN) of AsH_3 -in- H_2 obtained from Three-H Corporation and for tank CR, 10 percent AsH_3 -in- H_2 , obtained from Phoenix Research Corporation. Based on attempts to condense H_2O from the gases in tank DN, it was concluded that the mixture was quite dry. GaAs films grown using tank DN were found to have a doping level ($3 \times 10^{14} \text{ cm}^{-3}$) as low as that obtained with the best gases that had been evaluated prior to that time.

Another tank of 10 percent AsH_3 -in- H_2 (tank CR), obtained as a research sample from Phoenix Research Corporation for similar evaluation by GaAs deposition, was described in the vendor's analytical report as containing no impurity greater than 1 ppm. No condensate was obtained at $-45C$, and thick undoped GaAs films were found to be p-type; this indicated a low donor impurity content in the reactant. Several GaAs films were grown at various AsH_3 -TMG ratios, with H_2Se added as dopant. This tank was found to be relatively good for GaAs growth on Al_2O_3 ; a doped $20\mu\text{m}$ -thick film on (0001) Al_2O_3 had the following electrical properties: $\rho = 0.07 \text{ ohm-cm}$; $n = 1.7 \times 10^{16} \text{ cm}^{-3}$ and $\mu = 5470 \text{ cm}^2/\text{V-sec}$. At higher doping levels ($n = 5.5 \times 10^{17} \text{ cm}^{-3}$) a $31\mu\text{m}$ -thick GaAs film had a mobility of $\sim 3900 \text{ cm}^2/\text{V-sec}$, also a reasonable value for a film with that doping level. Unfortunately, the material was depleted before it could be analyzed by mass spectrometer methods locally.

The analysis of TMG was limited to that of the residual gases in the TMG bubbler. The data indicated 25 ppm dimethylchlorogallium, 0.14 mole percent of a material with a mass spectrum peak suggesting it to be hexamethyldigallium, and ~ 2 ppm of unidentified boron-containing compounds. No Al, Si, P, Zn, As, or Cd compounds were detected (limit of detection < 2 ppm).

It is clear from the analyses of reactant impurities described above that significant differences are found in the purity of these materials. Not only do they vary from supplier to supplier but also different tanks of the same material from the same supplier are not consistent in purity. Another matter

Table 23. Mass Spectrometric Analyses of AsH_3 in Carrier Gas from Three Vendors

Constituent	Tank DP ^a AsH_3 -in-He Cyl. RSG-80-1889	Tank DN ^b AsH_3 -in- H_2 Cyl. 2264	Tank CR ^c AsH_3 -in- H_2 Cyl. 35-90038
Hydrogen	<5 ppm*	90+ (mole %) ^d	Balance
Methane	<1 ppm*	<1 ppm*	<1 ppm
Oxygen	<1 ppm*	ND 0.001*	<1 ppm
Argon	<1 ppm*	ND 0.001*	NR
Hydrocarbons	<1 ppm*	<1 ppm*	NR
Carbon dioxide	<1 ppm*	ND 0.001*	<1 ppm
Water	1 ppm	<1 ppm*	NR
Nitrogen	2 ppm	9 ppm	<1 ppm
Arsine	11.72 (mole %)	10.1 (mole %)	10.1 (mole %)
Helium	balance	NR	NR

* Limits of detection ND = None detected, so less than ... NR = Not reported

[†] Laboratory designation of AsH_3 tank.

^a Analyzed by West Coast Technical Service, Inc., San Gabriel, CA; supplier - Air Reduction Co., Inc., Airco Industrial Gases Div., Vernon, CA

^b Supplier - Three-h Corporation, Manamassa, NJ

^c Analysis submitted by Phoenix Research Corporation, Edison, NJ; supplier - same.

^d Analyzed by Gollob Analytical Service, Berkeley Heights, NJ

^e Analyzed by West Coast Technical Service, Inc., San Gabriel, CA

for concern is the lack of agreement in the analyses supplied by two different analytical laboratories for the same tank of reactant and the apparent differences in detection limits for the same element or compound that different laboratories possess. It is therefore difficult to determine which results are the most reliable and which supplier of the gases is best. A "use test" appears to be a reasonable way of evaluation of the materials for the intended application, but this method is time-consuming.

Although it is expected that some of the impurities found, such as O_2 , CO_2 , H_2O and methylsilane, should influence the quality of Si grown from SiH_4 , it seems curious that these materials which have been identified as being present in the source tanks in various concentrations do not appear visibly to adversely influence Si growth on Si or Al_2O_3 . These impurities probably will behave differently in H_2 , He, and/or He- H_2 atmospheres, however, and may be the cause of the difficulties in obtaining reproducible growth on $MgAl_2O_4$ surfaces, which appear to be quite sensitive to different source tanks of SiH_4 .

It is also probable that the impurity concentrations in the gases will change with tank pressure; i.e., as the major component is used, the impurities of low vapor pressure will contribute a larger percentage to the total pressure within the tank, particularly when the tank pressure is relatively low. Thus, at lower tank pressures changes in the quality of the films might result.

The analyses demonstrate the ultimate lack in understanding of the role of impurities in epitaxial film growth and the minimum requirements for the analytical methods that should be used in detecting these impurities. A collaborative study in this area involving the reactant supplier, the analytical laboratory, and the ultimate user is evidently needed.

SECTION 5

CHEMISTRY AND REACTION KINETICS OF CVD PROCESSES*

Because of the obviously important role played by the chemical reactions involved in CVD processes in determining substrate surface conditions, film growth kinetics, and ultimate film properties, it was considered essential to examine some of the fundamentals of the chemistry and reaction kinetics of these processes.

In particular, the processes used in this contract program for growing hetero-epitaxial films of Si and GaAs were of special interest. Consequently, investigations of the basic chemistry involved in the formation of Si by SiH_4 pyrolysis and of GaAs by the trimethylgallium (TMG)- AsH_3 reaction were undertaken. The initial plan was to study the influence of the Al_2O_3 surface on the mechanism of decomposition of SiH_4 as a function of temperature, and to examine the decomposition modes and reaction products of TMG and AsH_3 as functions of temperature, concentration ratio, and H_2 partial pressure to attempt to determine the requirements for formation of optimum-quality GaAs.

It was anticipated that significant contributions could thereby be made to the fundamental knowledge sought in the contract program and at the same time generate potential improvements in the manner of application of these chemical reactions to the practical growth of semiconductor thin films for various device applications. One question of continuing interest that might be answered by these studies related to whether the release of Si by the pyrolysis of SiH_4 occurs in the gas phase near a substrate surface or on the substrate surface itself. This point was of considerable importance to the planned in situ CVD experiments with Si in the electron microscope (Section 8).

*These investigations were conducted by M. A. Ring, M. Sefcik, H. Schlyer, R. Jenkins and A. Vanderwielen of the Department of Chemistry, California State University, San Diego, CA.

1. PYROLYSIS OF SiH₄

The pyrolysis of SiH₄ over Al₂O₃ was investigated in the initial studies. The Al₂O₃ was preheated to various temperatures (400 to 1200C) prior to each pyrolysis to determine the effects due to heat treatment.

The reactions were carried out in flow systems with low-temperature traps which removed the heavier less stable products from the stream. This allowed for the determination of the effect of pyrolysis temperature on the yield of Si₂H₆ in the pyrolysis of SiH₄:



SiH₄ pyrolyses over single crystal Al₂O₃ beads were carried out in two sets of experiments. In the first series, the decompositions were carried out so that the Al₂O₃ beads would be covered with one or more monolayers of Si during most of the decomposition. In the second series, the decompositions were examined only while one monolayer was being deposited.

In the first series, the pyrolysis of SiH₄ was carried out in a flow system containing a Hg Toepler pump and two low-temperature traps maintained at -160C and positioned beyond the heated zone. The quartz-walled heated zone (6.2 cm³ volume) had a surface-to-volume ratio of 42.8 when packed with 3/32-in Al₂O₃ beads and 2.84 without the beads. The Al₂O₃ beads were washed in a 9:2 mixture of HNO₃:HF and then rinsed with water, trichloroethylene, deionized water, and methanol, prior to use. It is estimated that fewer than six monolayers of Si were deposited in each experiment. The -160C cold traps maintained the SiH₄ pressure at 12 torr.

After a 30-min flow pyrolysis, the test surface was recleaned and a second decomposition was carried out under the same conditions. At that point, Si

was deposited from a 400C SiH_4 decomposition. The initial experiments were repeated over the Si-coated test surface to compare the decomposition rate over the test surface versus that over amorphous Si. The results over Al_2O_3 , SiO_2 and Pyrex glass are reported in Table 24.

The results from experiments 3, 4, 8, 9, 12 and 13 demonstrate that the rate of SiH_4 decomposition over Si deposited from SiH_4 decompositions at 400C is not dependent on the surface-to-volume ratio. Thus, these decompositions appear to be homogeneous. Similarly, the results from experiments 1, 2, 5, 6, 10 and 11 demonstrate that this same decomposition is not affected by SiO_2 , Pyrex glass or Al_2O_3 when these surfaces are coated with a few (or possibly less than one) monolayers of Si.

To circumvent the difficulty of rapid coverage of the test surface by the depositing Si a static pyrolysis unit was constructed which consisted of a Si-mirrored pyrolysis chamber, containing cleaned Al_2O_3 beads, connected by a "U" trap to a combination Toepler pump-McLeod gauge. With this apparatus it was possible to detect H_2 produced from the SiH_4 pyrolysis well before one monolayer of Si was deposited on the Al_2O_3 beads.

In this second series of experiments, the Al_2O_3 beads were cleaned as previously described. The beads were placed in a side arm of the vessel which was evacuated to 10^{-5} torr. A Si mirror was deposited inside the vessel from a 400C SiH_4 decomposition. After the remaining SiH_4 and H_2 were distilled off, the beads were dropped into position and preheated under dynamic vacuum for 2 hours or more. The temperature was changed to the run temperature and SiH_4 (10 cc, gas phase) was condensed into the vessel and allowed to expand into the heated zone.

All experiments listed in Table 25 were carried out with the same quantity of SiH_4 . After each run, the H_2 - SiH_4 mixture was pumped through a U trap containing glass beads and cooled to -196C . The Toepler pump was always operated five times. The H_2 being pumped was retained in the McLeod gage by a valve. The H_2 was then distilled off. Since some SiH_4 passes a -196C bath,

Table 24. SiH₄ Pyrolysis Experiments

Expt. No.	Pyrolysis Temp. (C)	Test Surface Exposed to Pyrolysis	SiH ₄ Consumed (mmol)	Si ₂ H ₆ Produced (mmol)	H ₂ Produced (mmol)
surface/volume = 2.84					
1	521	SiO ₂ (quartz)	0.09	0.03	0.17
2	521	SiO ₂ (quartz)	0.07	0.03	0.17
3	521	Si	0.07	0.03	0.20
4	521	Si	0.09	0.05	0.22

surface/volume = 11.9					
5	522	Pyrex	0.09	<0.01	0.29
6	522	Pyrex	0.11	<0.01	0.30
7	522	pyrex	0.13	<0.01	0.29
8	522	Si	0.09	<0.01	0.26
9	522	Si	0.08	<0.01	0.24

surface/volume = 42.8					
10	525	Al ₂ O ₃	0.17	0.03	0.48
11	526	Al ₂ O ₃	0.19	0.03	0.51
12	524	Si	0.16	<0.01	0.50
13	524	Si	0.17	0.01	0.49

Table 25. Decompositions of 10 cc of SiH_4 over Al_2O_3

Preheat Temp. (C)	Time (min)	SiH_4 Decomp. Temp. (C)	mmoles of H_2 ($\times 10^4$)
Uncoated Beads			
400	2	260	0.032
	30	254	1.06
	30	254	0.55
Coated with Si			
	30	255	0.14
	30	256	0.06

Uncoated Beads			
100	2	256	0.11
	2	252	0.04
	30	254	0.43

Uncoated Beads			
1000	30	246	1.22
	30	242	0.14
	30	244	0.03
Coated with Si			
	30	244	0.02
	30	242	0.01

Uncoated Beads			
1200	30	248	0.20
	30	245	0.10
Coated with Si			
	30	248	0.01
	30	250	0.01

a SiH_4 background was required for each experiment. The Toepler pump again was operated five times with the SiH_4 condensed in the -196°C trap. The quantity of SiH_4 pumped into the McLeod gauge was subtracted from the H_2 determination for that run. The SiH_4 background was almost constant and was about 10% of the largest quantities of H_2 obtained. After two or three runs a Si mirror was in evidence, and the above experiments were repeated to determine the homogeneous contribution to these experiments.

Results over cleaned Al_2O_3 beads are listed in Table 25. The beads were not cleaned between successive experiments, so that these were consecutive or cumulative experiments. The results from Table 25 clearly demonstrate that single-crystal Al_2O_3 does catalyze the thermal decomposition of SiH_4 . The decomposition rate as measured by the yield of H_2 per unit time was between 10 and 100 times greater over a cleaned Al_2O_3 surface than over the beads coated with amorphous Si. The decomposition over amorphous Si is homogeneous, as demonstrated by the data in Table 24.

Preheating the cleaned Al_2O_3 to 1000 and 1200C prior to SiH_4 decomposition did not appear to change the rate of decomposition. That is, no effect on the catalysis due to the preheating of the Al_2O_3 beads could be detected.

2. REACTION OF TMG AND AsH_3

The metalorganic-hydride reaction between trimethylgallium (TMG) and AsH_3 was also examined, to determine the conditions required to obtain pure GaAs.

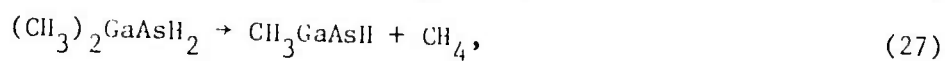
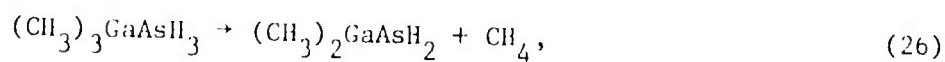
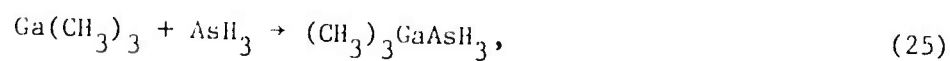
The experiments can be divided into three groups. The first series examined the reaction to determine what volatile products were obtained, and how the ratio of these products varied with temperature. The second series of experiments was designed to prepare GaAs over various surfaces. The third set of experiments attempted to determine what radicals could be present in the reaction system.

The first reactions between TMG and AsH₃ were carried out over GaAs in a flow system containing an all-Pyrex gas pump, a short thermal zone and a U trap. In these first experiments, equimolar TMG-AsH₃ mixtures at 50 torr were cycled through the system for periods of 4 hours. Methane (CH₄) and H₂ were both formed. The CH₄/H₂ ratio was about 2.2 from reactions at temperatures from 190 to 280C; this ratio was 4.2 for a 153C pyrolysis. The ratio of CH₄ produced to TMG consumed was about 1.2. Similar results were obtained when these experiments were carried out with the U trap cooled to -23C.

The reaction was also examined with equimolar TMG-AsH₃ mixtures in a static reaction vessel over Pyrex or GaAs surfaces. When these reactions were carried out between 85 and 110C the CH₄/H₂ ratio was greater than 10. This ratio was 4.0 at 170C and 2.9 at 220C. The other data from these experiments were not consistent enough for useful interpretation.

The results from the above experiments demonstrate that both CH₄ and H₂ can be produced in the reaction. The ratio CH₄/H₂ increased as the temperature was decreased so that the CH₄-forming steps evidently have a lower activation energy than the H₂-forming steps. This fact would suggest that these products were produced in unrelated reactions.

The probable sequence of reactions involved in these experiments is as follows:



Data to support the reaction of Equation (29) will be presented later. Since the ratio CH₄-produced/TMG-consumed was usually between 1 and 2 for reactions

carried out below 110C only reactions (25), (26) and (27) were operative under these conditions.

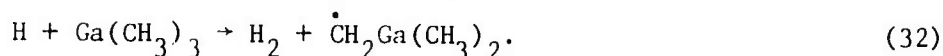
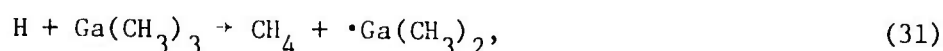
The experiments designed to obtain GaAs were carried out in an 80 cc Pyrex vessel with a 50 cc side arm connected by a Teflon valve. In two experiments the vessel was coated with an As mirror formed by the decomposition of AsH_3 at about 250C. The reaction vessel was heated to 175C and a measured quantity of AsH_3 (~35 cc) was condensed into the side arm at -196C. The valve was then closed and the AsH_3 allowed to warm to ambient temperature. Approximately 7.5 cc of TMG was expanded into the main vessel (into a calibrated volume) and its pressure measured. The stopcock was closed and the valve to the side arm opened to allow the AsH_3 to expand into the main portion of the reaction vessel.

After 1-1/2 hours, the products were distilled through -78C and -196C cold traps. The products passing the -196C trap were Toepler-pumped into a calibrated volume for quantitative measurement. Mass spectra of these mixtures were obtained to determine the CH_4/H_2 ratio. The fraction condensed at -196C was AsH_3 , while that condensed at -78C was TMG. (The quantities of these reactants were determined by pressure-volume measurements.) The reaction vessel was then closed off and heated to 450C for at least four hours. The products (H_2 and CH_4) were analyzed in the same manner.

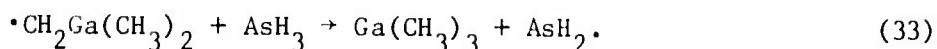
The results from these reactions are given in Table 26. For the three experiments listed the ratio CH_4 -produced/TMG-consumed was 3.05, 2.92 and 2.88, respectively, with an average value of 2.95. For these three experiments the CH_4 produced during the 1-1/2-hr 175C pyrolyses averaged 87% of the total produced; the balance was obtained after heating the solid product at 450C. Similarly, most of the hydrogen was obtained in the 1-1/2-hr period. These data demonstrate that the final solid product was undoubtedly GaAs and a mixture of As and AsH polymer. In experiment 3 it appears that all of the AsH polymer had been decomposed to As metal. It is thus concluded that GaAs can in fact be obtained from the reaction of TMG with AsH_3 , and that an excess of AsH_3 should be used in any application of the process.

AsH₂C₄H₉. The products and the induced polymerization of 1,4-C₄H₆ are consistent with the presence of H atoms and AsH₂ radicals.

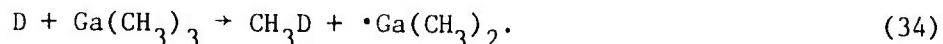
There, it appears that AsH₃ does decompose to yield H atoms and AsH₂ radicals. However, the results from Table 26 indicate that these species do not react with TMG in competition with excess AsH₃. The most likely interaction between H atoms or AsH₂ radicals with TMG would be the following:



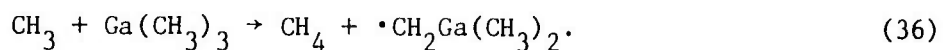
Data which suggest that reaction (31) does not occur can be cited. If reaction (32) occurred, the radical produced would abstract an H atom from AsH₃ forming TMG:



To examine the possibility of reaction between H atoms and TMG, experiments with the flow pyrolysis of SnD₄ were carried out with TMG at 85C, without a cold bath on the trap. The methane produced was a mixture of CH₃D and CH₄ in a ratio of about 1:10. If the D atoms did abstract a CH₃ group from TMG essentially all CH₃D should have been obtained:



The small quantity of CH₃D formed probably came from a reaction of CH₃ radicals and SnD₄. (CH₃)₄Sn and (CH₃)₃SnH were obtained; thus, TMG methylated SnD₄. The alkylstannanes probably decomposed producing CH₃ radicals which could abstract D atoms from SnD₄ or H atoms from TMG:



Thus, it appears that the small quantity of CH_3D formed in the SnD_4 -TMG reaction probably did not occur via reaction (34).

Finally, the thermal stability of TMG was examined over a Si mirror and over GaAs. No decomposition of TMG was observed when TMG was pyrolyzed statically for 2 hr at a pressure of 78 torr at 175C over a Si mirror or at a pressure of 96 torr at 180C over GaAs.

The static pyrolysis of TMG at a pressure of 99 torr (11 cc) at 235C for 2 hr over a Si mirror yielded 3 cc of a mixture of $\text{Si}_2(\text{CH}_3)_6$, $\text{Si}(\text{CH}_3)_4$ and $\text{HSi}(\text{CH}_3)_3$. Methane and ethane were not obtained and almost all of the TMG was consumed. When this experiment was repeated at 340C the same products were observed, along with considerable quantities of CH_4 . These results suggest that TMG reacts molecularly with Si above 235C. At 340C, TMG decomposes to yield CH_3 radicals which react with TMG to form CH_4 . The absence of CH_4 (or C_2H_6) from the reaction at 235C suggests that free methyl radicals were not produced at that temperature.

The results with the TMG- AsH_3 system can be summarized as follows:

1. The reaction between TMG and AsH_3 can be described by reactions (25)-(30) below 235C.
2. Reactions (26)-(28) can be followed by examining the ratio of the CH_4 produced to the TMG consumed.
3. Reaction (28) is slow compared with reactions (25)-(27).
4. Reaction (25) proceeds faster with excess AsH_3 when the quantity of TMG remains constant.
5. Reaction (28) appears to go to completion under the conditions of these experiments only above 400C.
6. Under these reaction conditions TMG begins to decompose at 340C.

The last two results suggest that further studies should be made of the reaction of TMG with AsH_3 at high temperatures, where GaAs is formed on the surfaces of interest. This reaction should then be compared with the decomposition of TMG at these temperatures over these same surfaces and over GaAs.

Three different Al_2O_3 orientations were successfully thinned by this method - (0001), $(10\bar{1}4)$, and $(01\bar{1}2)$. Considerable study of properties of the resulting thinned substrates was carried out, and improvements in the ion-thinning process for preparation of substrates for the in situ experiments were realized during the final year of the program.

Mechanical lapping and polishing methods that produce good quality surfaces suitable for use as substrates for epitaxy were developed for several orientations of Al_2O_3 - (0001), $(01\bar{1}2)$, $(10\bar{1}4)$, $(11\bar{2}0)$, ~6 deg off $(11\bar{2}0)$ and $(11\bar{2}2)$. By means of etch-rate techniques developed for this material it was possible to determine the apparent depth of damage in Al_2O_3 substrate wafers at various stages of preparation, and considerable information of this type was obtained.

In addition, the routine characterization of substrate surfaces at various stages of preparation has continued throughout the program, utilizing various standard techniques of x-ray and electron diffraction analysis and optical and electron (including scanning) microscopy.

1. PREPARATION OF INSULATOR SUBSTRATE SURFACES FOR USE IN HETEROEPITAXY EXPERIMENTS

For a period of several years it has been known to investigators involved in various types of epitaxial growth of metals or semiconductors on the surfaces of substrate wafers (whether crystalline or noncrystalline) that a surface of a certain minimum quality is required for the deposited film to have the desired properties. This is especially true in the semiconductor/insulator systems, where optimized properties of the semiconductor are usually required, indicating that single-crystal film growth is essential (or at least highly desirable). This in turn dictates a single-crystal substrate wafer, but experience has shown that more than just a highly perfect crystal lattice is required for the epitaxial growth to be of optimized quality. That is, the structure and the condition of the surface itself are dominant characteristics that must meet certain minimum requirements.

A considerable amount of effort was expended on this program to develop new methods and improve on old methods for preparing substrate surfaces adequate for use in heteroepitaxy studies. The substrate materials of special interest were primarily Al_2O_3 - used for most of the experimental epitaxial growth investigations on this contract - and secondarily MgAl_2O_4 - a substrate material that has experienced several changes in recent years in its status as a substrate for semiconductor epitaxial film growth for device use. In both cases the main interest was in the epitaxial growth of Si by CVD on the prepared substrate surface; the growth of GaAs films on these materials was also of interest, although it did not receive the same program emphasis as did Si growth.

Two techniques for producing polished high-quality surfaces on Al_2O_3 (or MgAl_2O_4) wafers for use in semiconductor heteroepitaxy are discussed below. Both methods were examined extensively during the course of this contract. The mechanical polishing process, of course, is the traditional method for producing a smooth and relatively flat surface on crystal wafers of various types; this is the process used by most commercial suppliers of "polished" substrate wafers of almost any of the readily available materials. The gas-phase etching process, on the other hand, is relatively new and untested for the materials involved here but appears to offer considerable promise for use in obtaining good epitaxial surfaces on certain orientations of Al_2O_3 .

a. Mechanical Polishing Methods for Al_2O_3 and MgAl_2O_4

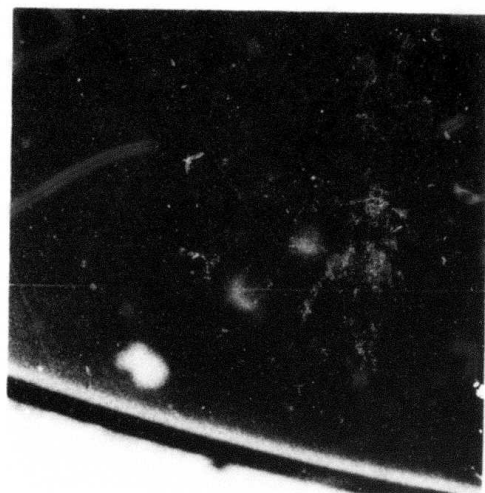
Considerable improvement in mechanical polishing procedures for insulating substrates - especially Al_2O_3 - was achieved with good reproducibility as the result of work done on this contract. Al_2O_3 substrates of six different orientations - (0001), (01 $\bar{1}$ 2), (10 $\bar{1}$ 4), (11 $\bar{2}$ 2), (11 $\bar{2}$ 0) and near-(11 $\bar{2}$ 0) - were successfully polished to "epitaxy finishes" in this work.

An indication of the magnitude of the problem of achieving relatively scratch-free surfaces on Al_2O_3 wafers was given by the demonstration in the first year of the program that Al_2O_3 surfaces prepared by customary mechanical polishing

techniques and used routinely for semiconductor heteroepitaxy typically exhibited a severe surface and subsurface damage, with many scratches often several microns deep and often rendered invisible to close inspection by amorphous or fine-grained debris embedded in the scratches in the final polishing stages. Such defects and impurities would obviously be influencing factors in film nucleation processes and contribute to defects in the resulting films.

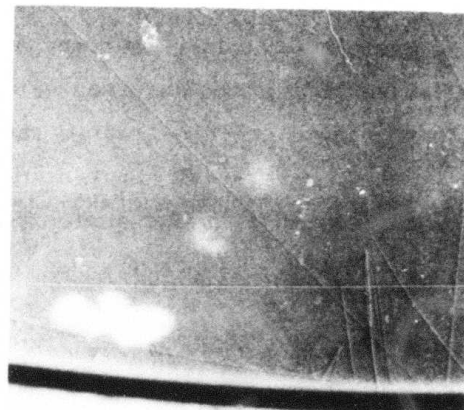
For example, most groups of $(10\bar{1}4)$ -oriented Al_2O_3 substrates as received from the vendors were found to exhibit unacceptably deep surface scratches. Similar scratches were also found in the surfaces of $(10\bar{1}4)Al_2O_3$ substrates prepared in Rockwell laboratories with $1\mu m$ diamond as the final abrasive, although the surface finish obtained by this method was better than that on the vendor-polished substrates. Good epitaxial growth of Si had been achieved previously on Al_2O_3 substrates of this orientation prepared in the same way at Rockwell, but systematic examination of the surfaces of these substrates revealed defects of sufficient magnitude to affect adversely the nucleation process, thus raising doubts as to the film quality ultimately achievable.

The $(10\bar{1}4)Al_2O_3$ orientation was found to be particularly difficult to polish properly for semiconductor epitaxy; subsequent in-house mechanical polishing of vendor-polished $(10\bar{1}4)Al_2O_3$ substrates with finer abrasives and modified polishing techniques usually revealed pre-existing surface and subsurface damage. An example of this is shown in Figure 35, in which the surface of such a substrate is shown in the as-received condition from the vendor (Figure 35a) and after two additional polishing steps in Rockwell laboratories (Figures 35b and c). All photomicrographs show exactly the same portion of the substrate surface; the scratches revealed in Figure 35a are shown in an accentuated condition in the other photographs. Also seen are what appear to be "new" scratches but are actually previously existing scratches uncovered by the fine polishing procedure through removal of debris packed into the scratches in one of the final preparation steps carried out by the vendor. Detailed investigation of such examples at all stages showed beyond doubt that the "new" scratches appearing in the later stages were not introduced by the fine



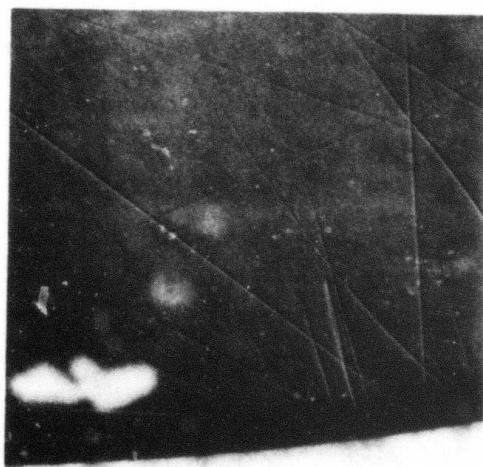
a

190 μm



b

190 μm



c

190 μm

Figure 35. Photomicrographs of Same Region of Surface of $(10\bar{1}4)\text{Al}_2\text{O}_3$ Substrate at Various Stages of Polishing; (a) as Received from Vendor; (b) after ~ 2 min Polishing with Cab-O-Sil ($0.05\mu\text{m SiO}_2$) on Nylon Cloth; (c) after Additional 5 min Polishing

polishing but were present originally. For example, gas-phase etching methods to be described in the next section readily revealed the nature of the extensive surface damage found in these polished substrates and established the existence of severe scratches in the surfaces.

The scanning electron microscope (SEM) was also used in the evaluation of polished surfaces of $(01\bar{1}2)$, (0001) , and $(10\bar{1}4)Al_2O_3$ substrate wafers.* Because of the insulator characteristics of the samples it was necessary to coat the wafers with a very thin metal conducting film to avoid charging effects on the electron beam. A technique was developed for returning to the same point on the surface of a wafer for further examination at a subsequent time. This technique involved specially designed SEM sample mounting pedestals which permitted relocation of a substrate accurately in its previous position on the pedestal by means of a set of "cross hairs" or XY axes scribed both on the top of the pedestal and on the back side of the substrate wafer. Once accurate alignment of these two sets of "cross hairs" was achieved (with the aid of an optical microscope) it became possible to return to a given point on the wafer by means of the calibrated XYZ micrometer motions of the SEM. Each "quadrant" of the sample, as defined by the XY axes, was arbitrarily divided into four working areas for detailed examination. As a result, a sample was examined in 16 reference areas which covered a majority (although not all) of the surface of the wafer.

A series of three typical photomicrographs made in the same region of a substrate of $(10\bar{1}4)Al_2O_3$ at three different magnifications is shown in Figure 36. The low magnification (200X) photograph of Figure 36a shows a surface scratch which is relatively difficult to see clearly. As the magnification is increased, however, the nature of the scratch marked by the arrows in Figure 36a becomes quite clear. This type of scratch is introduced early in the substrate polishing process, and usually survives the later steps in the polishing to become a "permanent" blemish, unless the wafer is relapped.

*The SEM analyses were done at the Rockwell International Science Center in Thousand Oaks, CA, by L. H. Hackett, Jr.

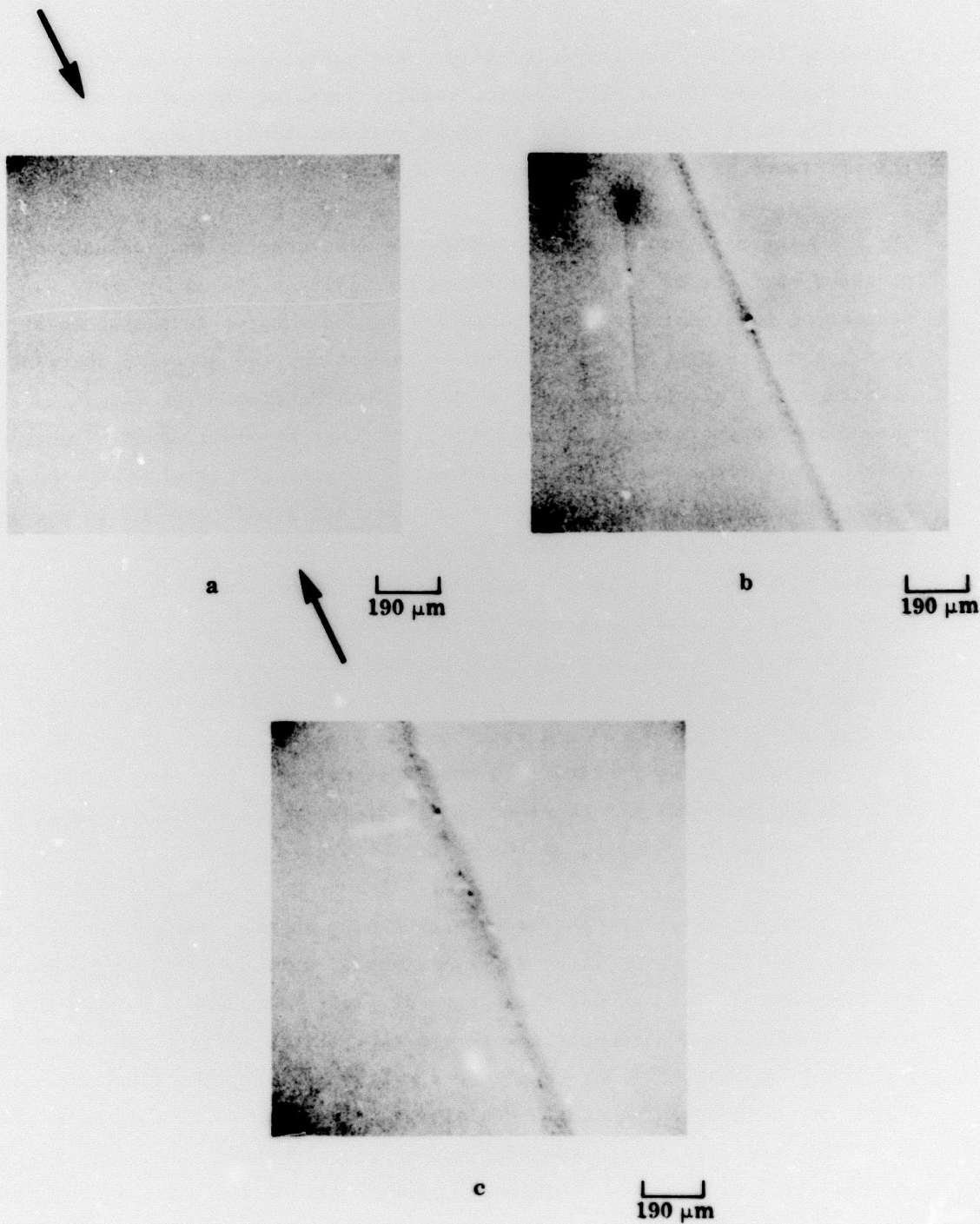


Figure 36. Scanning Electron Micrographs of Surface of $(10\bar{1}4)Al_2O_3$ Substrate, Showing Detail of Polishing Scratch (Arrows) at a) 200X, b) 10,000X c) 20,000X

Further study showed that pre-existing surface damage was common to all of the crystallographic orientations of Al_2O_3 obtained from vendors. The amorphous or fine-grained material packed into the scratches is probably powdered Al_2O_3 remaining from the polishing process. (Details of vendor polishing procedures are generally not available, for proprietary reasons.)

In general, it appears that it is important to start with Al_2O_3 slices the order of 50 mils thick. Attempts to improve the surface finish on vendor-polished substrates by subsequent polishing at Rockwell have been only partially successful because, typically, these polished wafers are in the thickness range below 20 mils, and considerable material removal is required to eliminate deep damage and to generate an acceptable new surface; extensive wafer breakage often results in these cases.

The problem of producing scratch-free Al_2O_3 surfaces of epitaxial quality by mechanical polishing still remains to be completely solved. The main difficulty arises due to the rate of material removal achieved during the final polishing steps ($3\mu\text{m}$, $1\mu\text{m}$, and $0.25\mu\text{m}$ diamond) with the methods developed to date. Observations indicate that at these stages the Al_2O_3 wafers (mounted on a flat block) and also the lapping or polishing plate (charged with diamond abrasive) change in flatness due to the excessive time required to remove scratches caused by the preceding step ($6\mu\text{m}$ diamond). As "perfect" contact between the wafers and the lap is lost, new scratches begin to appear; some of the largest previously-existing scratches ($3\text{-}6\mu\text{m}$) begin to enlarge. Usually at that time it is best to start over at the $6\mu\text{m}$ step.

A method is needed which removes sufficient material in the final steps of the polishing cycle, yet still maintains adequate contact (flatness) between the parts being polished and the lap charged with the abrasive. This requirement has not yet been fully met and, as a result, some of the polishing problems associated with Al_2O_3 are not yet totally solved. It must be remembered, however, that the surface quality required for epitaxial growth of semiconductors is considerably beyond that normally associated with the term "polished surface." As a result, special procedures had to be devised.

The basic techniques used for mechanically polishing Al_2O_3 wafers on this contract were developed in the first year of the program. In addition, the $(10\bar{1}4)$ orientation of Al_2O_3 required considerably more attention to develop a reproducible polishing procedure, and MgAl_2O_3 substrates were polished by procedures developed on other programs not related to this contract. The basic procedures developed and used for all of these surfaces are described below.

(1) $(10\bar{1}4)\text{Al}_2\text{O}_3$

After considerable work with wafers of this orientation, which had been the most difficult of the Al_2O_3 orientations on which to obtain a relatively scratch-free epitaxial finish, it was determined that each wafer to be lapped and polished required that its edge be beveled at the point of intersection with each face of the wafer, so that no sharp edges remained after mounting to serve as starting points for chipping or more extensive breakage. Earlier observations had indicated that this type of edge breakage during lapping and polishing operations was probably responsible for much of the damage produced on the wafer surface. The edge beveling greatly reduced this problem.

Al_2O_3 wafers of this orientation were typically mounted, after beveling, in groups of four or five on a single holder. The samples were then lapped using three specially designed cast-iron laps in sequence. The laps were charged with slurries of synthetic diamond abrasive of particle size 5, 3, and $1\mu\text{m}$, respectively. A typical surface of $(10\bar{1}4)\text{Al}_2\text{O}_3$ after the $1\mu\text{m}$ lapping step is shown in Figure 37; numerous scratches are readily visible.

Following the $1\mu\text{m}$ step, another specially designed lap (in this case brass) was charged with $0.5\mu\text{m}$ synthetic diamond abrasive and used in a last polishing process on the optical polisher, prior to transferring the mounted samples (on the holder) to a vibratory polisher for final polishing. The surface of a $(10\bar{1}4)\text{Al}_2\text{O}_3$ wafer after the brass-lap polishing step with $0.5\mu\text{m}$ diamond is shown in Figure 38a.

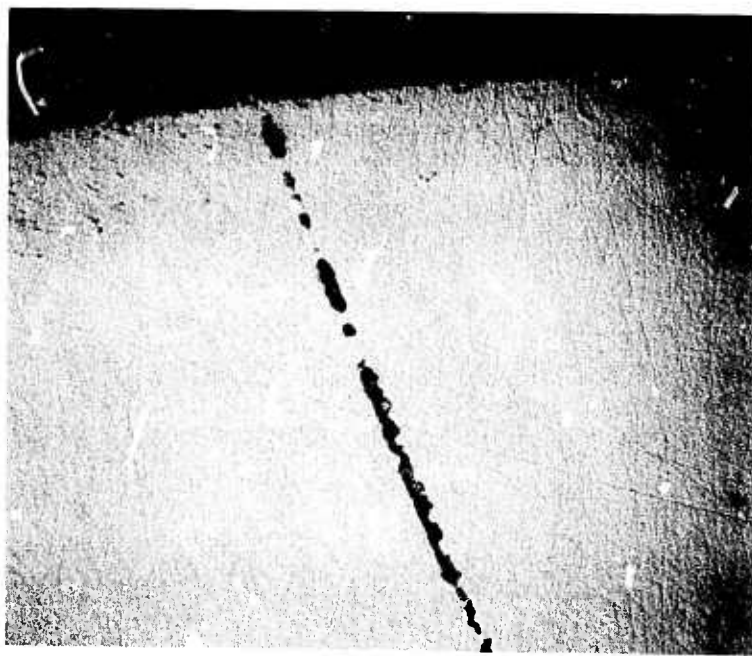
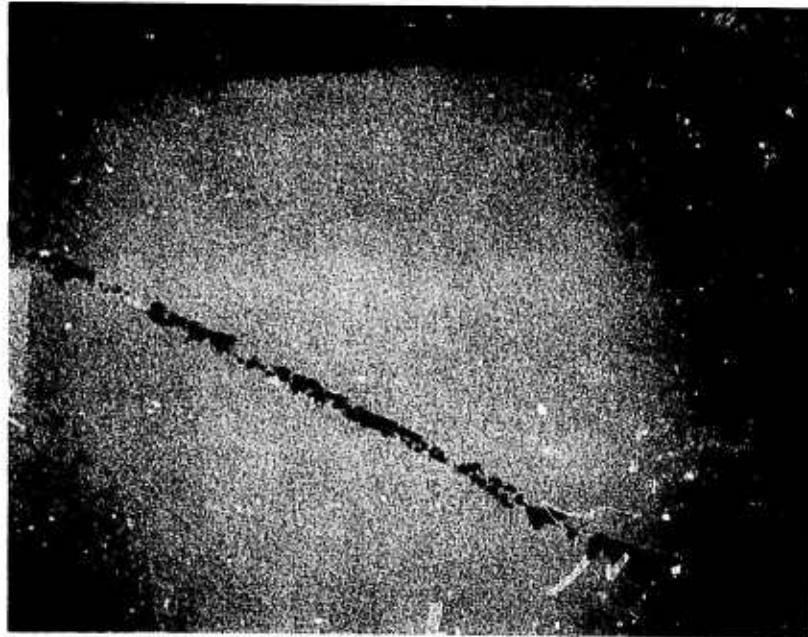


Figure 37. Typical Surface Finish Obtained on $(10\bar{1}4)Al_2O_3$ Substrate with Special Cast Iron Laps with Slurry of $1\mu m$ Synthetic Diamond on Optical Polisher (94X).

Figure 38b shows the same region of the Al_2O_3 wafer shown in Figure 38a, but after the next step - 66 hr of polishing time on the vibratory polisher, with nylon cloth providing the polishing surface and the carrier for a slurry of synthetic diamond abrasive of $0.25\mu m$ particle size. Following completion of that step, the wafers were then final-polished with $0.25\mu m$ "top" diamond* using a perforated Pellon cloth.

This method of processing constitutes the most successful technique developed to date for this particular orientation of Al_2O_3 ; it provides a surface acceptable for heteroepitaxy experiments and was adopted as the "standard"

*This designation is given a particular "cut" of synthetic diamond abrasive by Fletcher Engineering, Inc., Westminster, CA. It consists primarily of $0.1\mu m$ synthetic diamond particles, processed by deionization and subsequent stabilization in solution.



(a)



(b)

Figure 38. a) Surface Finish on $(10\bar{1}4)Al_2O_3$ Substrate after Using Special Brass Lap with Slurry of $0.5\mu m$ Synthetic Diamond on Optical Polisher. b) Same Area after 66 hr Polishing on Vibratory Polisher Using $0.25\mu m$ Synthetic Diamond on Nylon Cloth (94X)

mechanical polishing procedure for this orientation of Al_2O_3 .

(2) $(0001)\text{Al}_2\text{O}_3$

Basal-plane Al_2O_3 was perhaps the easiest of the six orientations on which to obtain a good-quality epitaxy finish. The procedure used for polishing these substrates was as follows: The as-sawed wafers were first lapped on both sides using 400-mesh boron carbide. The substrates were then rough-polished on three cast-iron laps in sequence, using diamond slurries of 5, 3, and $1\mu\text{m}$ particle size. A brass lap with $0.5\mu\text{m}$ diamond slurry was then used for the final rough polishing on the optical polisher. The wafers were then polished with a Linde "A" ($0.3\mu\text{m}$ Al_2O_3) mixture on the optical polisher using a perforated Pellon cloth. Final polishing was completed on the vibratory polisher using a Linde "B" ($0.05\mu\text{m}$ Al_2O_3) mixture.

This procedure routinely produced surfaces of (0001)-oriented Al_2O_3 suitable for epitaxy experiments.

(3) $(01\bar{1}2)\text{Al}_2\text{O}_3$

The polishing procedure developed for the $(01\bar{1}2)$ plane of Al_2O_3 was essentially identical to that used for basal-plane wafers. The two orientations were approximately equivalent in their polishing characteristics.

(4) $(11\bar{2}2)\text{Al}_2\text{O}_3$, $(11\bar{2}0)\text{Al}_2\text{O}_3$, and 6 deg off $(11\bar{2}0)\text{Al}_2\text{O}_3$

These orientations all were polished with the same procedure as was developed for the $(10\bar{1}4)$ orientation, except that the duration of the final polishing step was extended 10 to 25% beyond that typical of the $(10\bar{1}4)$ procedure.

(5) MgAl_2O_4

Polishing methods developed on a separately-funded program* for a variety of

*Subcontract from Crystal Technology, Inc., Mountain View, CA, as part of AFML Contract No. F33615-70-C-1544.

crystallographic orientations of stoichiometric spinel (MgAl_2O_4) were applied to some of the substrates used for Si heteroepitaxy experiments in this contract program.

The procedure used for preparing (111) and (110) MgAl_2O_4 substrate wafers for epitaxial growth was as follows. As-cut MgAl_2O_4 slices were mounted on appropriate polishing jigs with wax, using standard techniques. The wafers were lapped on a vibratory polisher, first with $12\mu\text{m}$ and then with $5\mu\text{m}$ SiC abrasive, to remove surface damage caused by the sawing operation and to provide a smooth flat surface for subsequent processing. The lapped wafers were then pre-polished with a slurry of Linde "A" ($0.3\mu\text{m}$ Al_2O_3) on nylon cloth in the vibratory polisher. Typical time for this step was ~26 hr, with at least two changes of the abrasive slurry required. Observation of the substrate surface following this step, using the Nomarski interference-contrast objective on the microscope, showed that very shallow scratches remained in the surface.

To remove the Linde "A" scratches an additional polishing step using a slurry of Linde "B" ($0.05\mu\text{m}$ Al_2O_3) on nylon cloth was employed, resulting in moderate overall improvement of the surface finish, with much finer scratches still present. Although other polishing cloths were occasionally used in the Linde "B" step, the best results were obtained with nylon.

Use of these substrates for Si growth clearly demonstrated that, just as for mechanically polished Al_2O_3 , the appearance of the surface can be very misleading. Some surfaces that looked scratch-free really contained scratches that were filled in by polishing powder and debris. This condition was revealed during attempts to clean MgAl_2O_4 surfaces for Si growth; it was found that after about 10 to 30 min in hot HF, most of the "fill-in" material was removed. Figure 39 shows adjacent regions of the surface of a broken slice of (111) MgAl_2O_4 ; the right side was "etched" for 30 min in hot HF. The defects shown were apparent in MgAl_2O_4 polished by either of the two principal vendors* as well as by Rockwell laboratories.

*Union Carbide Corp. and Crystal Technology, Inc.

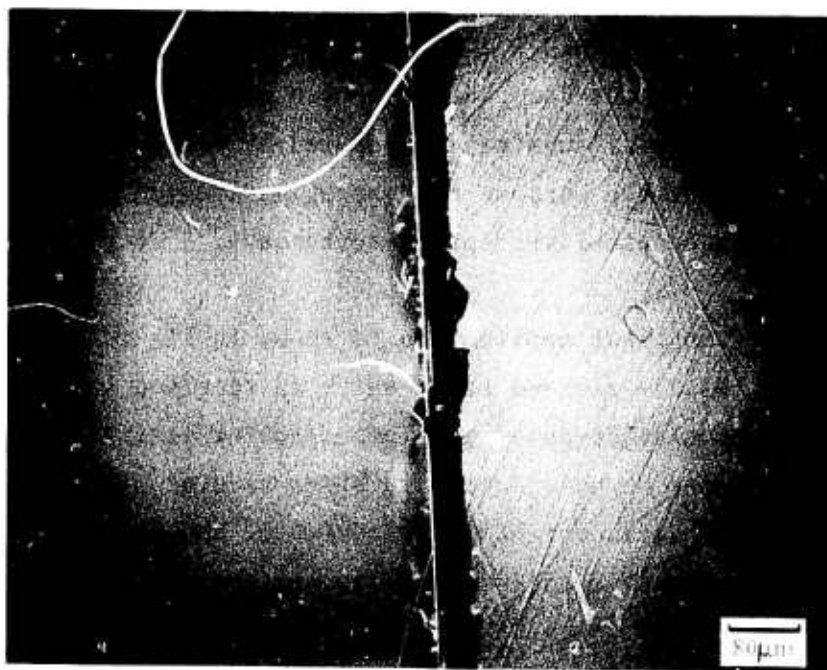


Figure 39. (111) Czochralski MgAl_2O_4 (a) before Etching;
(b) after Etching in Hot HF for 30 min

Just as was the case for some Al_2O_3 substrate surfaces, it was not evident from the quality of Si films grown on these polished but defective substrates that the surfaces were as poor as later scrutiny showed them to be. The explanation for the high quality of Si films that could occasionally be grown on relatively poor substrate surfaces, both for Al_2O_3 and for MgAl_2O_4 , is yet to be found.

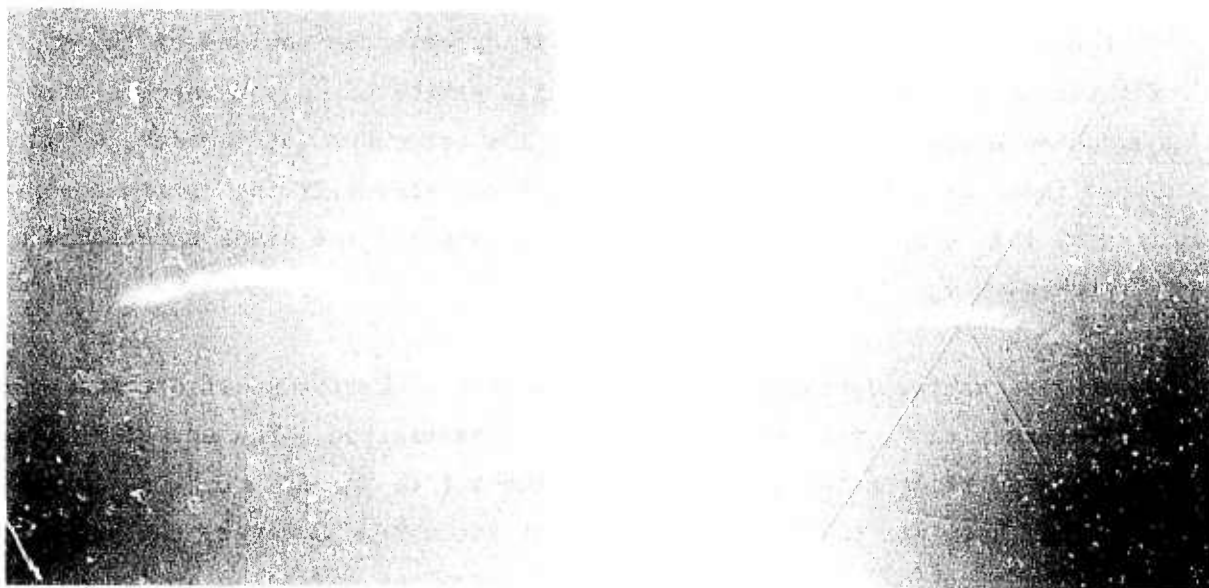
b. Gas-phase Etching/Polishing Techniques

In addition to the attention given to the problems of mechanical polishing, considerable effort was devoted to the use of gas-phase etching to reveal the surface quality of substrates prepared by vendors and by Rockwell personnel, and for the purpose of developing etching/polishing techniques for improving mechanically-prepared surfaces.

An example of the first application is shown in Figure 40, in which the surface of a (01 $\bar{1}$ 2)-oriented Al₂O₃ wafer as received and the same region after two successive steps of gas-phase etching is illustrated. No mechanical polishing was done on this substrate after receipt from the vendor. Note that a considerable amount of material (~8 μ m) had been removed in Figure 40c. Study had showed that such pre-existing surface damage was common to all of the crystallographic orientations of Al₂O₃ obtained from vendors, as indicated above, and that the amorphous or fine-grained material packed into the scratches was probably powdered Al₂O₃ remaining from the polishing process.

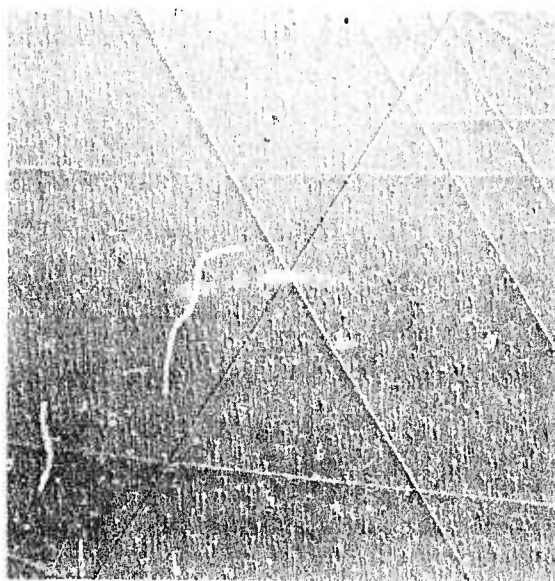
That proper polishing techniques could minimize the occurrence of this effect was shown by a particular instance in which a pair of basal-plane ((0001) orientation) Al₂O₃ substrates were compared; one was vendor-polished and the other was polished in Rockwell laboratories. The latter had a much superior finish, with very few scratches visible at 115X with the Nomarski interference objective. Replica electron micrographs of both samples at 10,000X showed that the one with superior finish still appeared practically free of scratches, while the vendor-polished surface appeared (at this magnification) almost entirely covered with a variety of scratches.

After gas-phase etching at 1400C in Freon, which removed ~0.4 μ m of material from the surface, replica electron micrographs showed no indication of scratches on the Rockwell-polished surface, although numerous shallow etch pits and some low-angle grain boundaries were evident on perhaps 10% of the area observed. Numerous other surface features, appearing to be vertical steps, were detected



a 

b 



c 

Figure 40. Photomicrograph of Surface of $(01\bar{1}2)Al_2O_3$ Substrate
 a) as Received from Vendor; b) after Gas-phase Etching in Freon at 1450C
 for 5 min ($\sim 3\mu m$ of material removed); c) after 15 min (total) Etching
 ($\sim 8\mu m$ of material removed)

at these defects and, in fewer number, in defect-free regions of the surface. The vendor-polished sample, however, still exhibited many scratches after the gas-phase etching. This indicated that the scratches (or the damaged regions below them) were probably deeper than $0.4\mu\text{m}$. Virtually the entire observed area of this sample was covered with etch pits and the steps associated with scratches.

As an alternative approach to the achievement of better substrate surfaces for heteroepitaxy, gas-phase etching was investigated. The use of SF_6 (Ref 53) and various fluorinated halocarbons (Freons) (Ref 54) for removing layers of Al_2O_3 had been previously demonstrated at Rockwell. However, the use of this technique requires careful control to optimize the polishing action and to minimize the etching of defects at the Al_2O_3 surface.

To this end, gas-phase etching/polishing studies were begun with the Al_2O_3 orientations of greatest interest - $(01\bar{1}2)$, $(10\bar{1}4)$, and near- $(11\bar{2}0)$. Based on the previous work (Ref 54), it was decided to concentrate the effort on etching with Freons.

Etch-rate data for Al_2O_3 as a function of the flow rate of Freon gas are recorded in Figures 41-43 for pedestal temperatures of 1400, 1450, and 1500C. These data indicate that $(01\bar{1}2)\text{Al}_2\text{O}_3$ etches at a greater rate than $(10\bar{1}4)\text{Al}_2\text{O}_3$, the rate ratio being ~4:1 at 1400 and 1450C but ~2:1 at 1500C. The spread in the data points is mostly due to the fact that the etch rate was calculated from the weight loss of the slice, and 0.1 mg error can represent a considerable error in the etch rate, particularly when the measured weight loss was normally less than 2 mg. (No correction was made for the weight loss from the sides of the substrate or from the outer edge of the underside of the wafer, which normally is reached by the gas stream.)

Etch temperature, substrate orientation, and etch rate were found to have an effect on surface quality, particularly on $(01\bar{1}2)\text{Al}_2\text{O}_3$. From Figure 44, it appears that 1500C is preferred to the other two temperatures for etch polishing $(01\bar{1}2)\text{Al}_2\text{O}_3$ at Freon flows of ~13 ml/min, even though the etch rate is approxi-

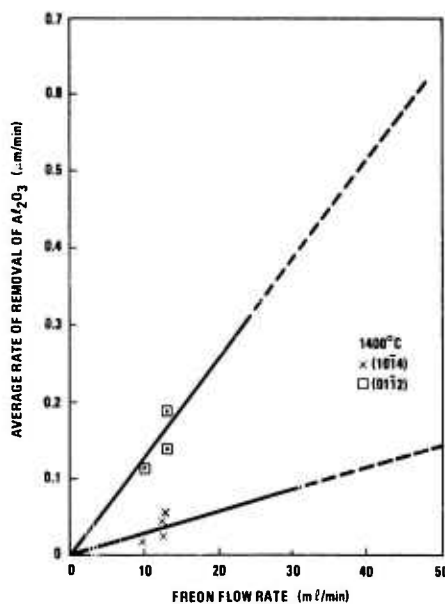


Figure 41. Rate of Etching of Al_2O_3 by Freon at 1400C

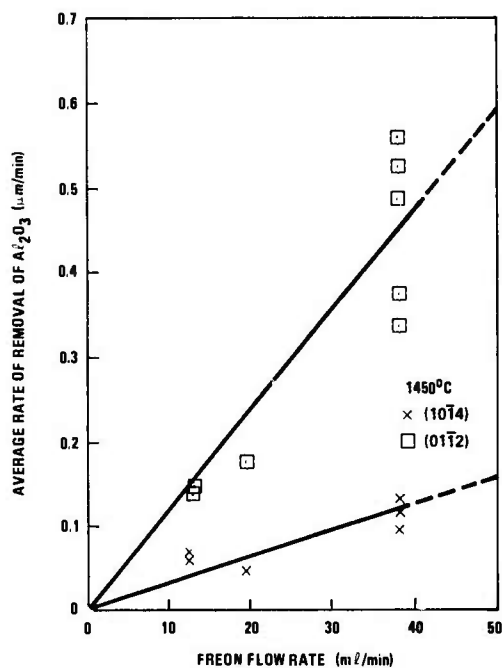


Figure 42. Rate of Etching of Al_2O_3 by Freon at 1450C

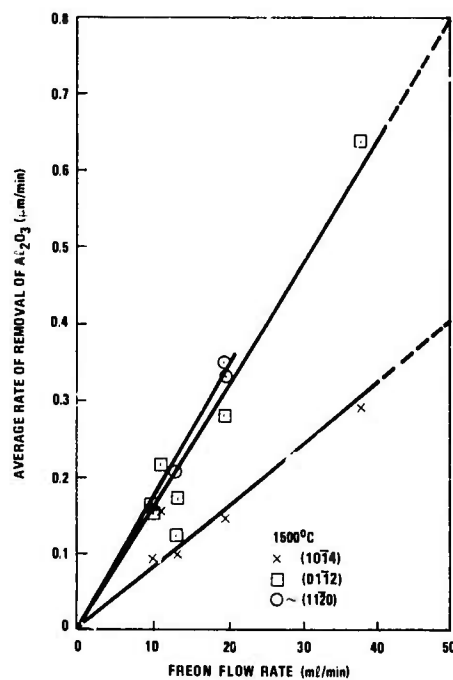
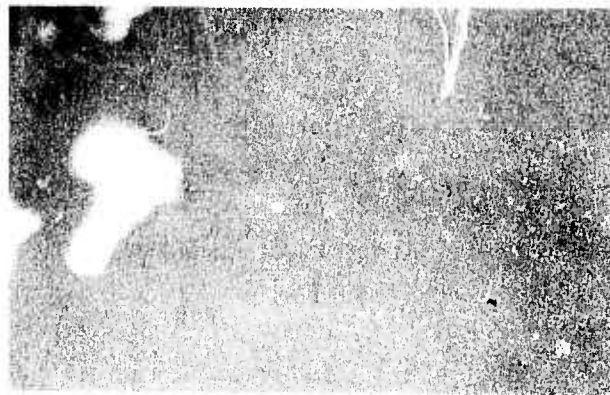


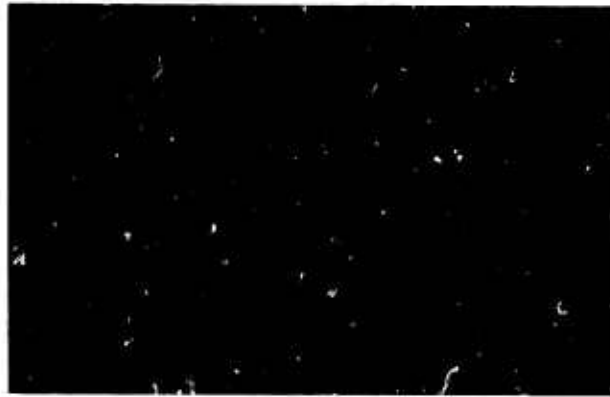
Figure 43. Rate of Etching of Al_2O_3 by Freon at 1500C



a
1400C



b
1450C



c
1500C

Figure 44. $(01\bar{1}2)Al_2O_3$ Surface after Etch-polishing with Freon at Flow Rate of 13 ml/min at Three Temperatures. (Approximately 5 μ m of surface removed from each substrate)

mately the same for the three temperatures. Structural defects started to appear on the sample etched at 1400C and were evident on the 1450C sample, but only faint scratches could be seen on the substrate etched at ~1500C. Greater Freon flows, such as 20 ml/min and 40 ml/min, appeared to etch rather than to polish the $(01\bar{1}2)$ -oriented surface.

Another portion of the sample shown in Figure 44c was photographed at different stages of etching, using the same polishing conditions (13 ml/min at 1500C). Figure 45a represents the as-received vendor-polished surface. The "0" seen in the photographs was scribed on the back of the sample and was readily visible at the magnification employed (53X); this was used to provide reference points for returning to the same part of the substrate for examination at a future time. Few scratches are visible in Figure 45a. After the removal of $\sim 5\mu\text{m}$ of surface (Figure 45b), the original scratches seemed to have disappeared; however, grain boundaries and new scratches were then exposed. In Figure 45c the grain boundaries and some scratches appear more pronounced, even though $9\mu\text{m}$ of surface (on the average) had been removed. It is evident the gas-phase polishing is effective in removing work damage from $(01\bar{1}2)\text{Al}_2\text{O}_3$. Whether it would provide a film with better electrical properties has not been determined.

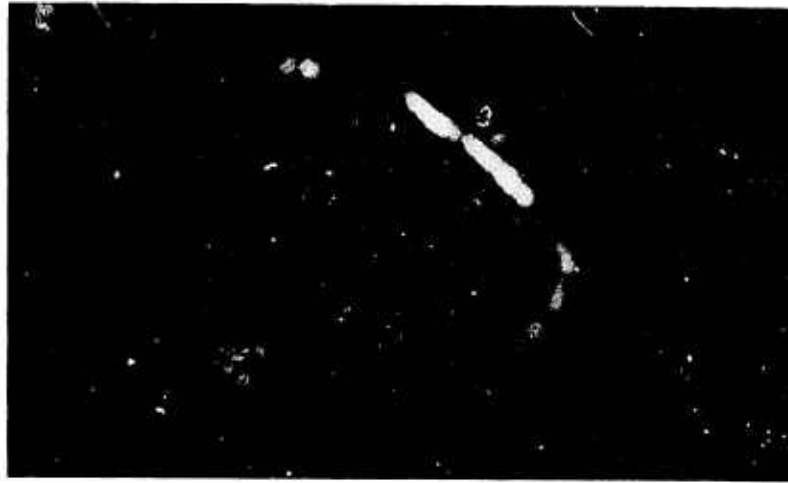
No set of parameters has yet been found sufficient for gas-phase etch-polishing of $(10\bar{1}4)\text{Al}_2\text{O}_3$. Figures 46 and 47 indicate that the subsurface regions of $(10\bar{1}4)$ -oriented substrates are typically extremely poor. The substrate as received from the vendor appeared to be essentially featureless, but after removal of $\sim 2\mu\text{m}$ of material the scratch density was revealed. A majority of these scratches could be removed; light scratches were removable, but major ones were either propagated or were so deep originally as to require removal of major amounts of the substrate surface. This, in turn, usually caused pitting of the surfaces.

Czochralski-grown Al_2O_3 oriented near $(11\bar{2}0)$ seemed to polish well with Freon except when the work damage in the slices was very deep. In some cases, the removal of $\sim 5\mu\text{m}$ of surface seemed sufficient; for other substrates, the removal



190 μm

a



190 μm

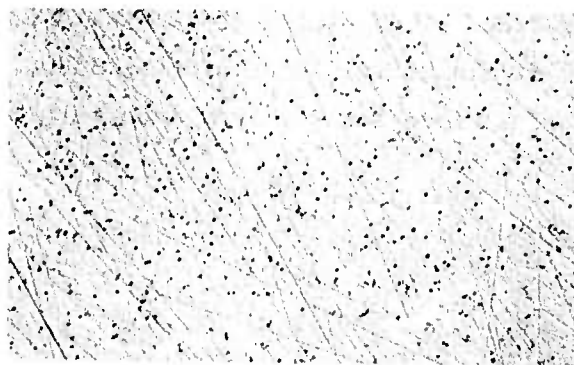
b



190 μm

c

Figure 45. Effect of Progressive Etching of (0112)Al₂O₃ at 1500C with Freon Flow Rate of 13 ml/min. Surface (a) as Received, (b) after 5 μm of Surface Removed, (c) after 9 μm of Surface Removed.



190 μm

a
1400C



190 μm

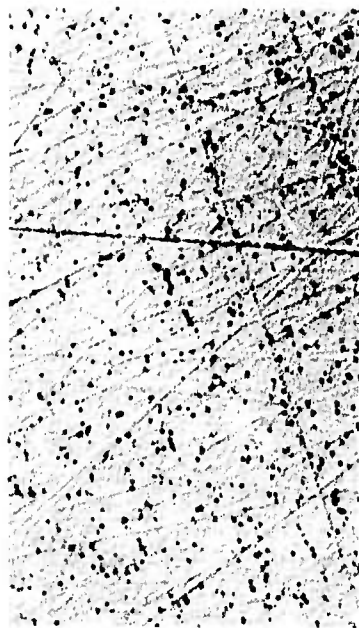
b
1450C



190 μm

c
1500C

Figure 46. $(10\bar{1}4)\text{Al}_2\text{O}_3$ Surface after Etch-polish with Freon at Flow Rate of 13 ml/min at Various Temperatures. (Approximately $3\mu\text{m}$ of surface removed from each substrate.)



190 μm

a
1450C



190 μm

b
1500C

Figure 47. $(10\bar{1}4)\text{Al}_2\text{O}_3$ Surface after Etch-polishing with Freon at Flow Rate of 60 ml/min at (a) 1450C and (b) 1500C. (approximately $2\mu\text{m}$ of surface removed from each substrate.)

of at least $12\mu\text{m}$ was still insufficient to remove obvious work damage. These results suggest that close control of the sawing and mechanical polishing processes used in earlier stages of Al_2O_3 substrate preparation is necessary in order to standardize on a gas-phase polishing process for removal of work damage.

Gas-phase etching with Freon was also used for several other purposes: (1) as a means for thinning Al_2O_3 substrates; (2) for slow but prolonged etching on $\sim(11\bar{2}0)$, $(01\bar{1}2)$ and $(0001)\text{Al}_2\text{O}_3$; and (3) to assess the subsurface damage, if any, caused by various polishing procedures, specifically that for $(10\bar{1}4)\text{Al}_2\text{O}_3$. The first application will be described in Section 6-3. The other two will be discussed below.

(1) Prolonged Gas-phase Etching

Al_2O_3 substrates oriented in the $\sim(11\bar{2}0)$, $(01\bar{1}2)$, and (0001) planes were treated with Freon for 25 min periods using etch-polishing conditions which had been previously identified as less orientation dependent. The results are depicted in the accompanying photomicrographs, which were obtained with a Nomarski interference contrast attachment on a metallurgical microscope.

Figure 48 shows that gas-phase etching of Czochralski-grown $(01\bar{1}2)\text{Al}_2\text{O}_3$ can produce considerable etching of the crystal planes, but the structure changes in character with etching time, with the surface apparently becoming smoother as a stable surface is found by the etching action. Etching of good quality Al_2O_3 oriented to $\sim(11\bar{2}0)$ (Figure 49) seemed to reveal only the work damage due to polishing the substrate; however, some areas of Verneuil-grown substrates did possess a relatively high density of diamond-shaped etch pits (not shown in the figure).

The same set of etch-polish conditions proved to be helpful in preparing smooth surfaces on $(0001)\text{Al}_2\text{O}_3$, shown in Figure 50. After 25 min of etching, scratches were still visible. After 50 min the scratches were essentially gone, and the surface remained smooth after 75 and 100 min of etching. However, a number of

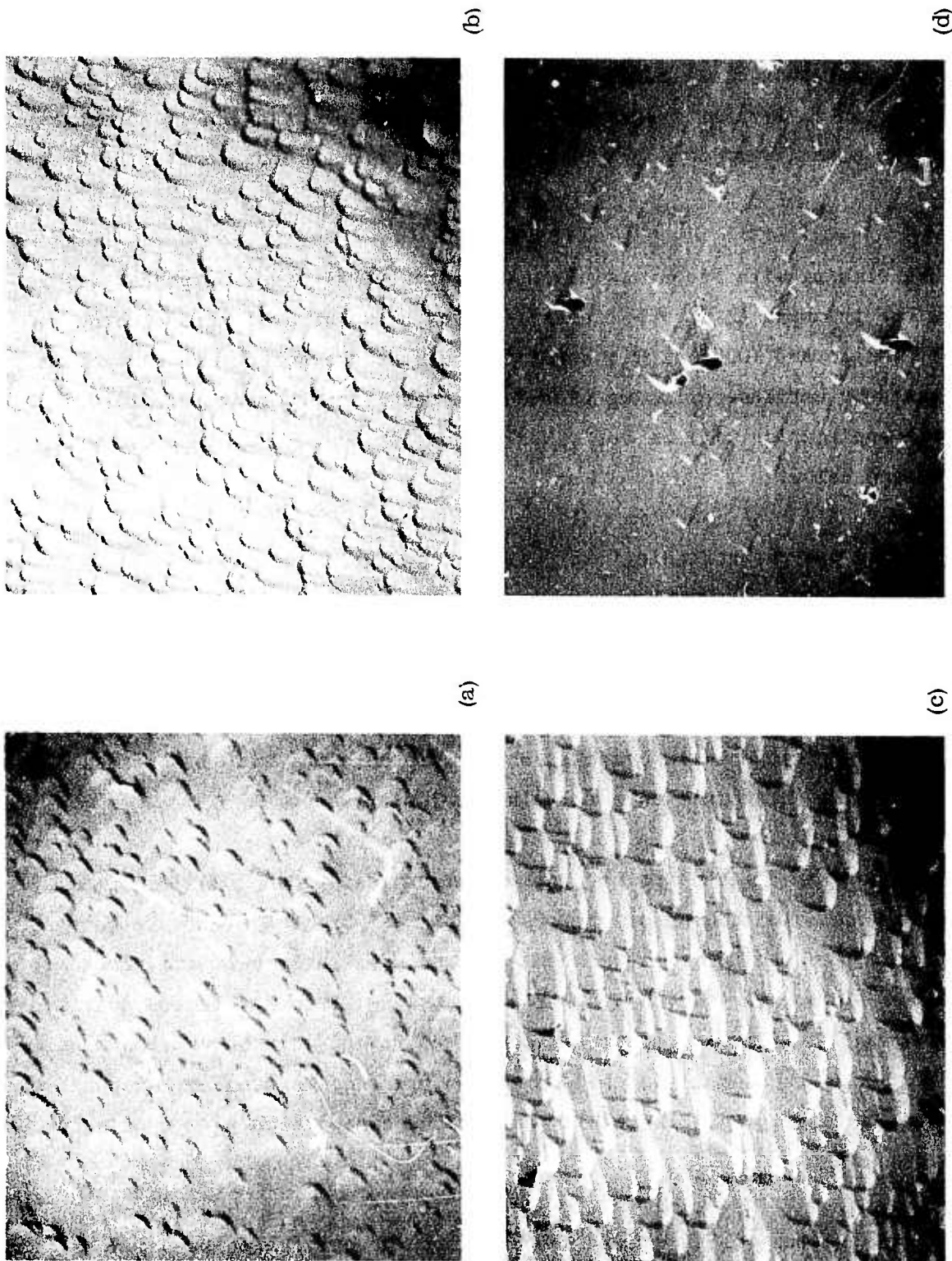
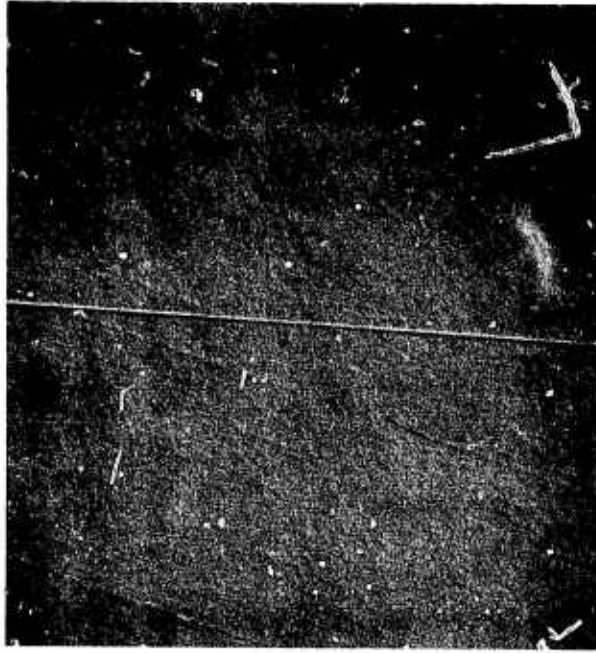


Figure 48. Surface of Czochralski-grown $(01\bar{1}2)Al_2O_3$ after Etching at 1500C with Freon at Flow Rate of 13 ccpm for (a) 25 min, (b) 50 min, (c) 75 min, and (d) 100 min. (All 110X)



(a)



(b)



(c)



(d)

Figure 49. Surfaces of Different Substrates of Verneuil-grown $(11\bar{2}0)Al_2O_3$ after Etching at 1500C with Freon at Flow Rate of 13 ccpm for (a) 25 min, (b) 50 min, (c) 75 min, (d) 100 min.

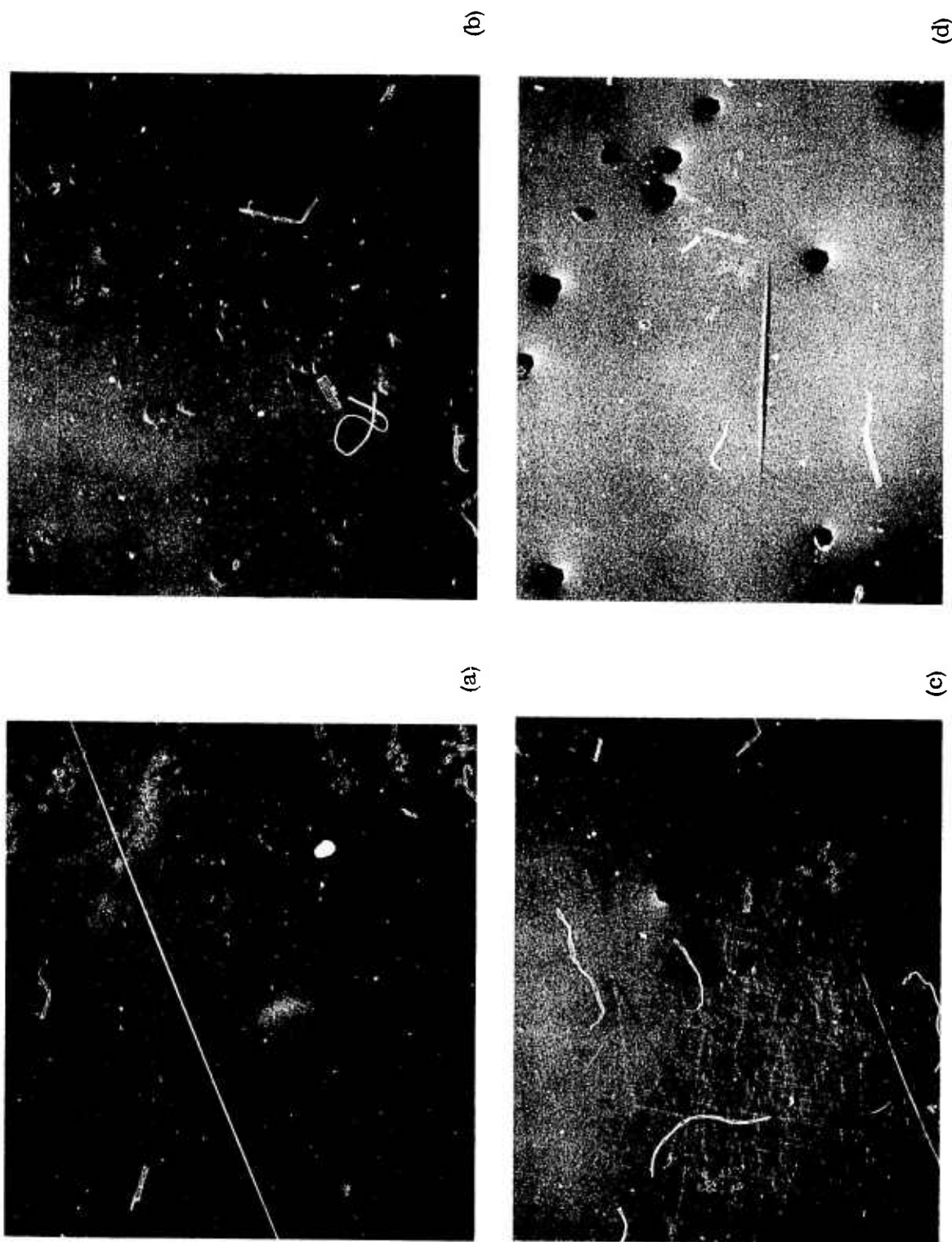


Figure 50. Surface of $(0001)Al_2O_3$ after Etching at 1500C with Freon at Flow Rate of 13 ccpm for (a) 25 min, (b) 50 min, (c) 75 min, and (d) 100 min

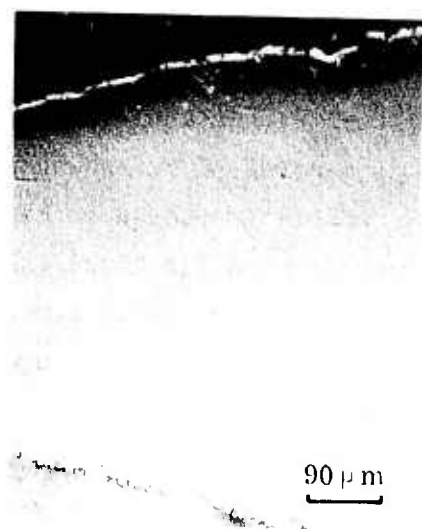
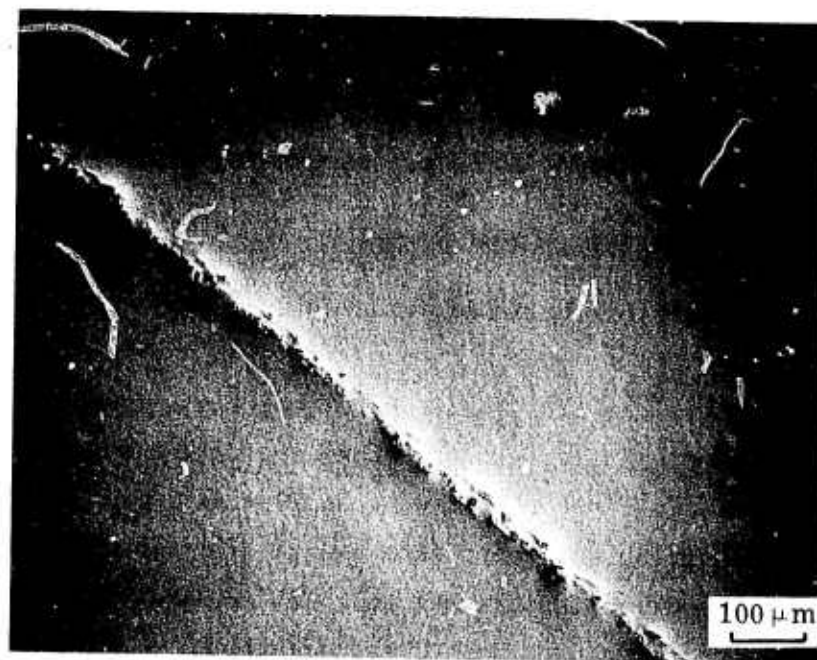
hexagonal etch pits were evident; these may be characteristic of the substrate or caused by reaction of impurities in the etchant and etching atmosphere with the substrate. Figure 50 is included to show the sensitivity of the gas-phase etching process to certain types of defect structure present in these substrates cut from Verneuil-grown Al_2O_3 .

(2) Evaluation of Mechanical Polishing Procedures

As previously indicated, the $(10\bar{1}4)\text{Al}_2\text{O}_3$ orientation has been found to be particularly difficult to polish properly for semiconductor epitaxy; subsequent mechanical polishing at Rockwell of vendor-polished material has always brought out greater surface and subsurface damage than has been acceptable. Light polishing of vendor-polished substrates at Rockwell apparently removes polishing debris which, when packed into the scratches, gives the impression that the surface is of high quality when this is simply not the case.

Such surfaces after a light gas-phase etch showed even more indication of the damage introduced during the mechanical polishing, and the technique of gas-phase etching for such evaluation was employed. Figure 51 represents the surface of a $(10\bar{1}4)\text{Al}_2\text{O}_3$ substrate wafer after being polished in Rockwell laboratories by the method described in preceding sections. The major defect shown was deliberately introduced to act as a point of reference for examination during the polishing and etching process. Before gas-phase etching but after mechanical polishing the surface was very smooth and displayed essentially no character (Figure 51a), but after 10 min ($\sim 0.2\mu\text{m}$ material removed) and 30 min of etching ($\sim 0.6\mu\text{m}$ removed) some subsurface damage was revealed (Figures 51b and c). However, the amount of damage was only a fraction of that found in vendor-polished material; the data offered evidence that considerable progress had been made in polishing $(10\bar{1}4)\text{Al}_2\text{O}_3$, a significant achievement.

The studies of gas-phase etching consistently revealed such surface and subsurface work damage on Al_2O_3 , caused by the mechanical processing of the substrate in preparing a surface conducive to epitaxy. Yet it is striking



(b)



(c)

Figure 51. Surface of $(10\bar{1}4)Al_2O_3$ (a) after Mechanical Polishing; (b) after 10-min Etch with Freon at 1400C; (c) after 30-min Etch with Freon at 1400C ($\sim 0.6\mu m$ removed.)

that such damaged surfaces have been long used in the industry for the epitaxial growth of Si and other semiconductors. Some experimental results obtained with substrates of this type may provide an indication of why this has been possible. Further experiments were carried out with the various substrate surfaces shown in Figures 48 and 49. Si films were grown and their electrical properties were measured. The data are shown in Table 27 and are somewhat surprising. Essentially identical carrier mobilities were found for films grown on unetched substrates and for those on substrates etched for as long as 100 min (~20 μ m of thickness removed), for both Czochralski- and Verneuil-grown Al_2O_3 .

This was taken to indicate that (1) the work damage is even greater than 20 μ m deep in these substrates (which were prepared by commercial vendors), or (2) the Si overgrowth is able to "overcome" much of the substrate surface imperfection during its growth, with the actual mobility-limiting factor being the stress-producing thermal contraction (see Section 2-5) and/or lattice mismatch between the two materials, or (3) there is a third species present on the substrate surface in this CVD reaction and it provides the real growth-influencing sites. The question remains unanswered; further experiments are needed to examine this matter in more detail.

Table 27. Effect of Gas-phase Etching of (0112)Al₂O₃ on Si Film Properties*

Film Growth Temperature (C)	Etching Time (min)	Final Film Thickness (μm)	Resistivity (ohm-cm)	Carrier Concentration (cm ⁻³)	Mobility (cm ² /V-sec)
1075**	0	2.13	0.45	2.7 x 10 ¹⁶	510
	25	2.28	0.32	3.6 x 10 ¹⁶	540
	50	2.13	0.46	2.8 x 10 ¹⁶	490
	100	2.05	0.57	2.1 x 10 ¹⁶	530
1075***	0	2.25	0.31	4.4 x 10 ¹⁶	460
	25	2.28	0.28	4.7 x 10 ¹⁶	470
	50	2.20	0.31	4.2 x 10 ¹⁶	480
	75	2.23	0.31	4.4 x 10 ¹⁶	460
	100	2.23	0.28	4.7 x 10 ¹⁶	490

*Nominal growth rates ~5μm/min

**Good quality Verneuil-grown Al₂O₃ substrates

***Czochralski-grown Al₂O₃ substrates

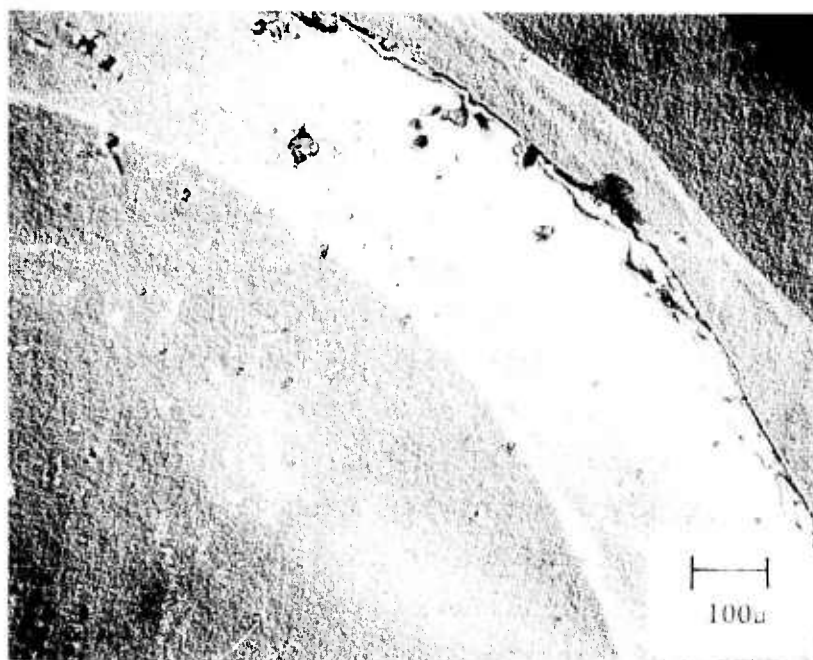
c. Ion-beam Etching/Sputtering

The first test of the ion-beam sputtering apparatus used for preparing thinned Al_2O_3 substrates for the in situ CVD experiments (see Section 8) was to use it to ion-etch the surface of a mechanically polished $(10\bar{1}4)$ -oriented Al_2O_3 wafer. Evidence of scratches originally present on the polished surface remained after removing more than $9\mu\text{m}$ of material. The results after successive removal of a total of less than 0.1 and $9.6\mu\text{m}$ of Al_2O_3 are shown in Figure 52. In the photomicrographs the irregular line at the extreme top right is the edge of the sample; the area immediately next to it was untouched by the ion beam during the etching process and represents the original condition of the Al_2O_3 surface. Only the area in the lower left portion of each photomicrograph represents the region of the crystal which had been fully etched by the ion beam; the remaining intermediate areas were partially etched.

Comparison of the etched and unetched regions of the sample as shown in Figure 52a reveals that the light ion-etching ($<0.1\mu\text{m}$) enhanced the visibility of the original scratches. This effect, similar to that noted with Freon etching, was attributed to the removal of polishing debris which had filled-in the scratches. Further ion-etching, sufficient to remove 2.7 and $7\mu\text{m}$, began to produce a smoother surface, although the original scratches remained clearly visible.

After removal of $9.6\mu\text{m}$ of Al_2O_3 (Figure 52b) the surface appeared significantly improved, yet traces of the original scratches were still present. Although the scratches themselves were not $9.6\mu\text{m}$ deep prior to the start of the ion-etching process, it does appear that the damaged regions below the scratches may have extended at least this deep into the original polished crystal surface, causing a preferential etching effect until the damaged regions were completely removed.

Thus, the results obtained with ion etching appeared to be quite similar to those found for gas-phase etching. Neither technique was pursued sufficiently, however, for it to become a regularly used procedure in the preparation of Al_2O_3 substrates for the heteroepitaxy studies.



(a)



(b)

Figure 52. $(10\bar{1}4)Al_2O_3$ Wafer Ion-beam Etched at Low Angle to Remove (a) $<0.1\mu m$, (b) $9.6\mu m$.

2. DETERMINATION OF DEPTH OF DAMAGE IN Al_2O_3 SUBSTRATES

The investigations described in Section 6-1 clearly demonstrated the prevalence and the significant depth of the work damage that is characteristic of mechanically prepared surfaces of Al_2O_3 , MgAl_2O_4 , and similar materials of interest as substrates for semiconductor heteroepitaxy.

To attempt to determine quantitatively the depth of this damaged region caused by the mechanical sawing, lapping, and polishing processes used on Al_2O_3 to produce epitaxy substrates, a series of etching experiments was undertaken. These experiments used the "constancy-of-etch-rate" technique (Ref 55), which is based on the observation that the highly strained crystal surfaces produced by localized heating and by the pressure of a saw blade and/or abrasive particles etch more rapidly than those with less strain. Therefore, as the crystal surface is etched, decreasing amounts of strain are encountered and the etch rate decreases accordingly until a constant value is reached.

The procedure used was to observe the etching rate as a function of the amount of surface material removed (based on weight-loss determination), with the appearance of a constant etch rate taken as indication that the main part of the damaged region had then been removed. The chemical etchant used in these measurements was a 1:1 (volume ratio) mixture of H_3PO_4 and H_2SO_4 (Ref 56), with a temperature of -200C and continuous agitation of the etchant required. Although there may be some uncertainty about the exact structural significance of the etch rate reaching a constant value, the technique has been found useful with other substrate materials (e.g., BeO) for indicating depths of severe damage and variations in this depth as a function of mechanical treatment and of crystallographic orientation.

Approximately circular Al_2O_3 substrate wafer blanks in the as-sawed condition and 0.020-0.030 in thick were used for these measurements. The orientations used were (0001), (01 $\bar{1}$ 2), (10 $\bar{1}$ 4), (11 $\bar{2}$ 0), and ~ 6 deg off of (11 $\bar{2}$ 0). The samples

were evaluated in the as-sawed condition and then uniformly processed on both sides with a given lapping or polishing compound and evaluated again by the etching process. Surface areas were determined from micrometer measurements of dimensions. The samples were carefully cleaned and weighed on a microbalance before and after etching for 10-20 min intervals. The weight loss for a given time interval was calculated on a $\text{mgm/cm}^2\text{-min}$ basis, then converted to $\mu\text{m/min}$ by introducing the density of Al_2O_3 (3.98 gm/cm^3). This weighing, etching, reweighing and calculating procedure was repeated until the etch rate became constant. The etch rate data were then plotted as a function of total etching time.

Since the etch rate for each time increment is an average value, the data points are placed in the center of the time increment. The exact time at which the etch rate is considered to become constant is open to some question; to allow for this uncertainty, the range of values reported in Table 28 show the maximum variation. In order to minimize experimental errors further, two samples of each surface preparation and orientation were examined. The curves in Figures 53, 54, 55 and 56 reflect the average rates of each sample set.

The saw-cut wafers (Figure 53) show the largest amount of damage, as would be expected. The slices were cut on a tensioned-membrane inside-diameter (ID) saw using a blade impregnated with 340-mesh synthetic diamond abrasive. The etch rates after the initial damage was removed were slightly higher, due to the larger surface area created by the large number of faceted etch pits. To check this, the acid temperature was raised to 300C where chemical polishing occurs. The facets were thus removed, and the etch rate was then measured again at 200C; it then equaled the rates measured on flat, non-faceted surfaces.

The depth of damage curves for the rough-lapped (400-mesh boron carbide) surfaces are shown in Figure 54. In this case there was a very small variation in the etch rates between the hardest - $(10\bar{1}4)$ - and softest - (0001) - orientations. Therefore, the etch rates for the $(11\bar{2}0)$, 6 deg off $(11\bar{2}0)$, and $(01\bar{1}2)$ surfaces are plotted as a single line. It is not clear at this time why the difference in etch rates is so small at this stage of processing.

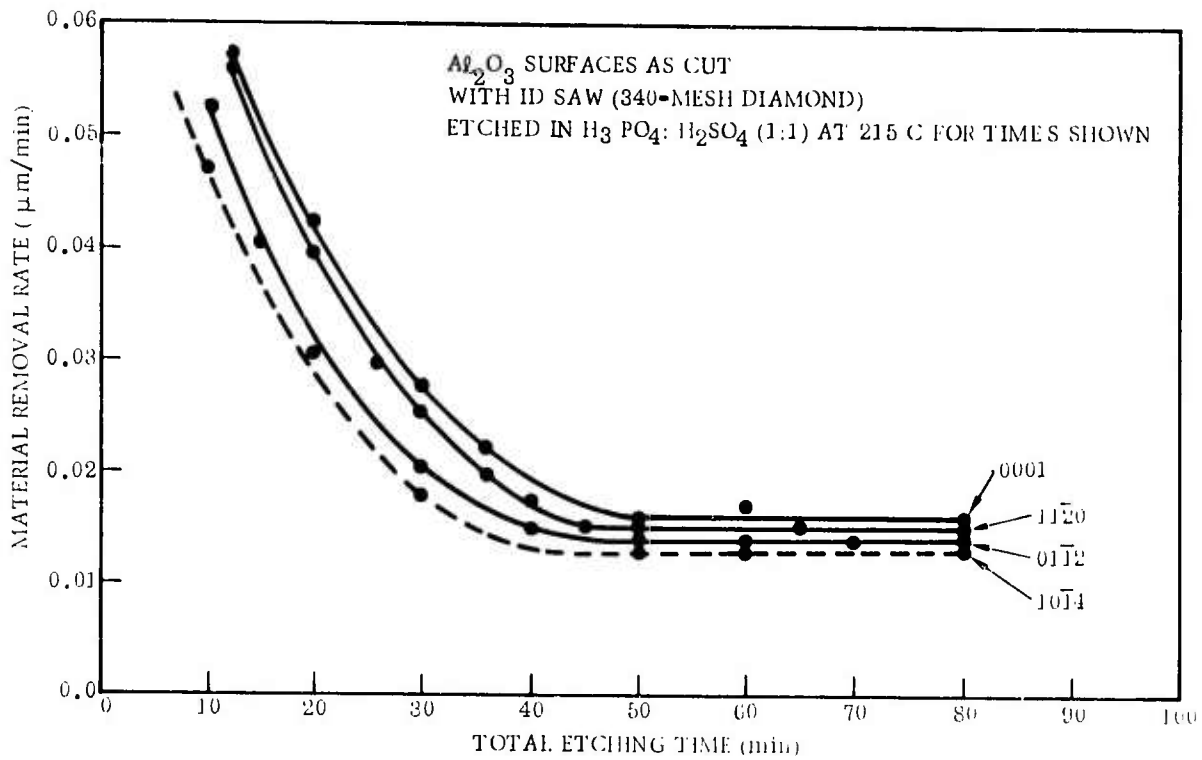


Figure 53. Variation in Al_2O_3 Etching Rate with Depth into Wafer for As-sawed Surfaces of Several Orientations

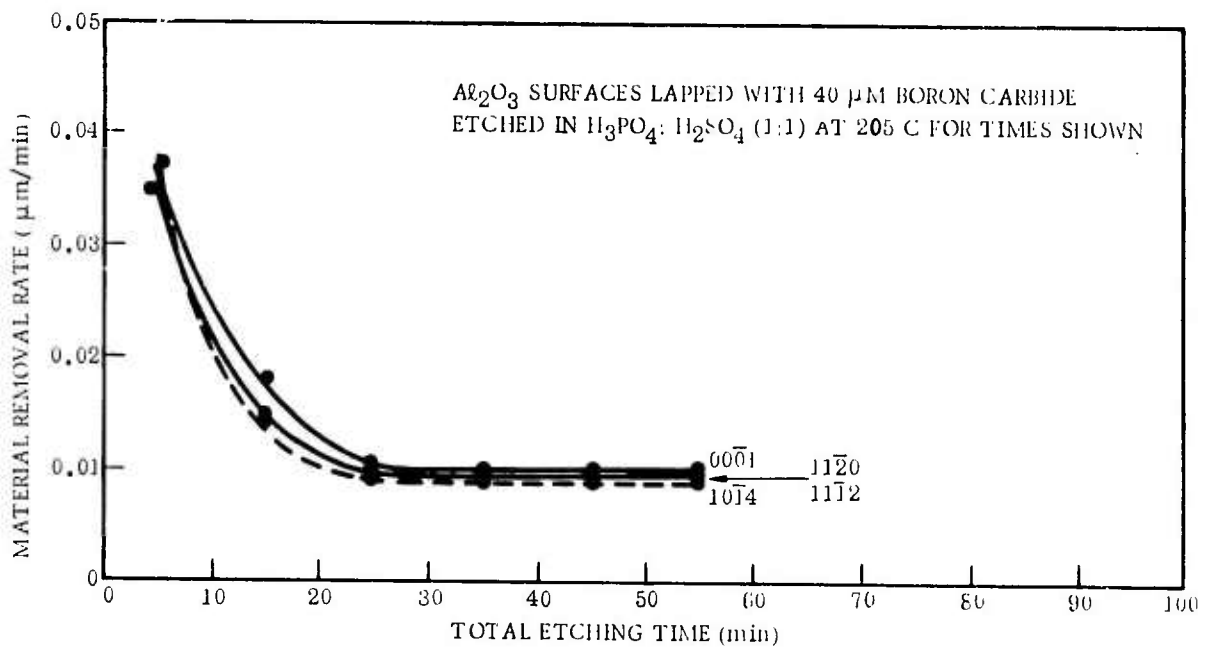


Figure 54. Variation in Al_2O_3 Etching Rate with Depth into Wafer for Surfaces of Several Orientations Lapped with 40 μm Boron Carbide

The etch rates for the 12 μ m SiC fine lapped surface (Figure 55) and the final-polished 0.25 μ m "top" diamond* surface (Figure 56) are low - characteristic of the surface preparation, with distinct termination of the damaged layers.

The depths of damage calculated from these data are shown in Table 28. The times (min) required to remove the damaged layer under the etching conditions described above are also listed. The depths of damage determined for the epitaxial polish are approaching the experimental limits of the technique. They can be considered valid, however, since they are self consistent and two samples of each orientation were run independently and are in excellent agreement.

The etch rates found in these studies are approximately 30% lower than those reported by Reisman et al (Ref 56) at the equivalent temperature. This discrepancy would be accounted for if those investigators had determined only an average etch rate over the first hour of etching - that is, if the damaged layer at the surface had not been removed prior to determining the etch rate. The results of both studies are in excellent qualitative agreement with respect to the orientation dependence of etch rates.

The significance of the very shallow (<0.1 μ m) depth of damage in final-polished Al₂O₃ surfaces, irrespective of crystallographic orientation, is yet to be fully evaluated. Perhaps the main point to be emphasized is that, although very effective mechanical polishing procedures (Section 6-1-a) have been developed on this program for the Al₂O₃ orientations cited here, there still is a damaged region of detectable depth at the surface, and it is the microscopic features of the surface (such as this thin damaged layer) that ultimately influence the film nucleation and early-stage growth mechanisms. Thus, although a high-quality final polish may be a necessary surface condition for good heteroepitaxial semiconductor growth it is evidently not a sufficient condition.

*See Section 6-1-a for description of this polishing material.

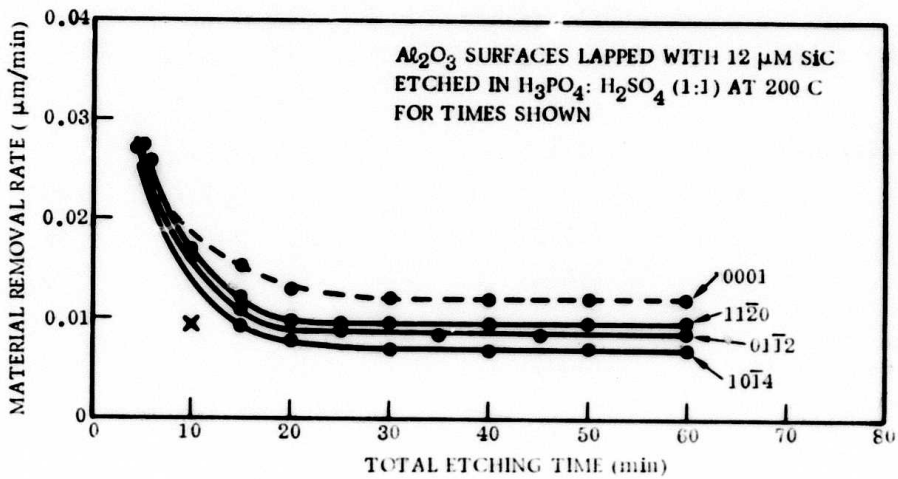


Figure 55. Variation in Al₂O₃ Etching Rate with Depth into Wafer for Surfaces of Several Orientations Lapped with 12 μm Silicon Carbide

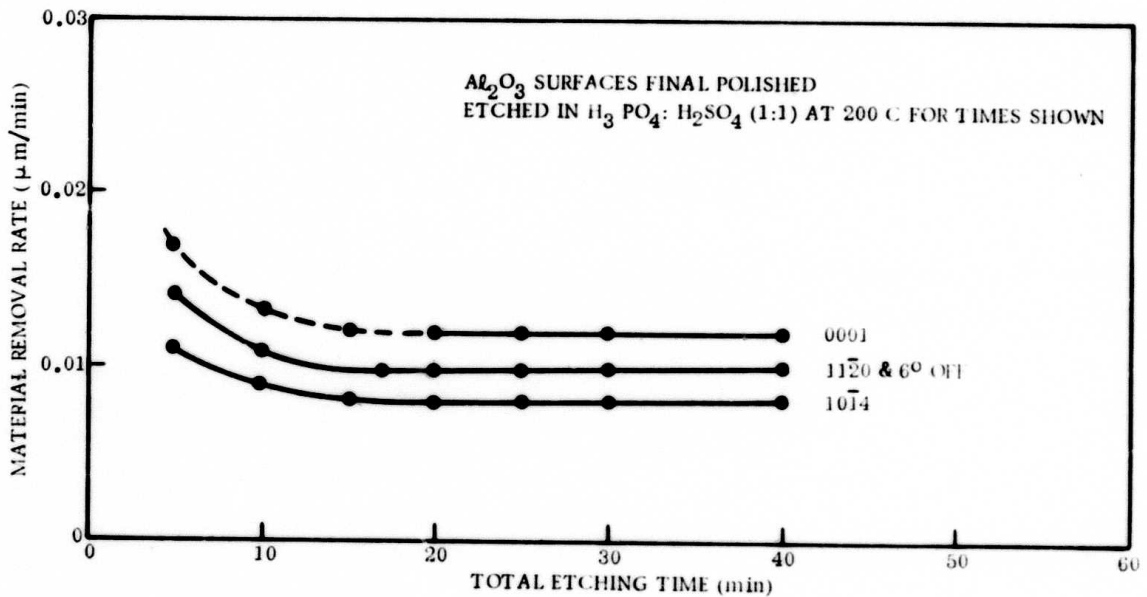


Figure 56. Variation in Al₂O₃ Etching Rate with Depth into Wafer for Surfaces of Several Orientations Polished with 0.25 μm "Top" Diamond

Table 28. Depth of Surface Damage in Al₂O₃ Wafers by Etch-rate Method

<u>Surface Preparation</u>	<u>Crystallographic Orientation of Surface</u>	<u>Depth of Damage (μm)</u>	<u>Removal Time (min)</u>
ID saw cut (340-mesh diamond)	(0001)	1.8 ± 0.1	50
	(01 $\bar{1}$ 2)	1.6 ± 0.1	48
	6 deg off (11 $\bar{2}$ 0)	1.2 ± 0.2	46
	(11 $\bar{2}$ 0)	1.2 ± 0.2	46
	(10 $\bar{1}$ 4)	1.0 ± 0.1	42
400-mesh boron carbide rough lap (40μm particle size)	(0001)	0.65 + 0.03 - 0.02	27
	(01 $\bar{1}$ 2)	0.64 ± 0.01	27
	6 deg off (11 $\bar{2}$ 0)	0.63 ± 0.01	26
	(11 $\bar{2}$ 0)	0.63 ± 0.01	26
	(10 $\bar{1}$ 4)	0.62 + 0.01 - 0.02	25
12μm SiC fine lap	(0001)	0.22 ± 0.02	23
	(01 $\bar{1}$ 2)	0.21 ± 0.02	22
	6 deg off (11 $\bar{2}$ 0)	0.20 ± 0.02	22
	(11 $\bar{2}$ 0)	0.20 ± 0.01	21
	(10 $\bar{1}$ 4)	0.18 ± 0.02	20
Epitaxial final polish (0.25μm "top" diamond)	(0001)	0.08 ± 0.01	15
	(01 $\bar{1}$ 2)	*	*
	6 deg off (11 $\bar{2}$ 0)	0.07 ± 0.01	15
	(11 $\bar{2}$ 0)	0.07 ± 0.01	15
	(10 $\bar{1}$ 4)	0.07 ± 0.01	15

*Data not yet available

3. PREPARATION OF ULTRATHIN ELECTRON-TRANSPARENT Al_2O_3 SUBSTRATES

The in situ Si CVD experiments in the electron microscope (Section 8) required Al_2O_3 substrates which were transparent to 100KV electrons, i.e., with thicknesses of 200-500Å (0.02-0.05 μm) or less. The best available mechanical polishing procedures were found suitable for reduction only to 25 to 50 μm in thickness. Three other methods were attempted for the final thickness reduction: ion-beam sputtering (ion thinning), chemical etching, and gas-phase etching at elevated temperatures. Ion-beam sputtering was by far the most successful, being the only method actually to produce samples 200-500Å thick. However, it was found to be a slow process, with removal rates varying from a low of 0.1 $\mu\text{m/hr}$ to the normal rate of 0.5 $\mu\text{m/hr}$. After modifications, the operation of the ion-beam machining apparatus was refined into a relatively routine, albeit time-consuming procedure, requiring 2 to 5 working days of operating time per sample.

The work with these techniques is described in the following sections.

a. Mechanical Lapping/Polishing Techniques

Whether as a preliminary step to further wafer thinning by other techniques or as a single method for attempting to achieve the required 25 μm thickness for use in ion-beam sputtering, the first step in preparing Al_2O_3 wafers for eventual electron transparency is mechanical polishing to as small a thickness as practicable. The mechanical lapping and polishing procedures used in these investigations typically started with Al_2O_3 wafers 250 μm thick, with both sides commercially polished. The wafers were attached to a polishing jig with a low-melting-point wax and lapped on a vibratory polishing machine to ~125 μm thick, using 400-mesh boron carbide abrasive. The jig and mounted wafers were then transferred to an optical polishing machine and polished with successively finer diamond abrasives, beginning with 3 μm particle size. Below a thickness of 75 to 125 μm the samples often fractured during polishing or upon removal from the polishing jig, because of the large residual stresses present.

The following parameters were changed in various ways in attempts to produce the 25 μ m thickness required: shape, mounting arrangement, and edge condition of wafers; size and number of wafers (hence surface area and polishing pressure); size of abrasive and wafer thickness at which the abrasive was first applied; type of slurry; size and surface configuration of lapping plate; and type of polishing motion.

With this general lapping and polishing method, only one group of wafers (which had been lightly chemically etched in $H_3PO_4:H_2SO_4(1:1)$ solution before lapping) was successfully polished on both sides to a thickness of $\sim 40\mu$ m. This group was then successfully cut into about 0.75mm-dia disks for subsequent ion-beam thinning. Attempts to reproduce the polishing were unsuccessful. A second group of wafers, without the chemical etching, was polished to 60 μ m and subsequently cut into 0.75mm-dia disks. Only one side of the latter group was polished; the other side was lapped only and quite rough. These samples were totally unsatisfactory because of the rough surface remaining after ion thinning.

Despite considerable effort on this contract program to develop a satisfactory mechanical polishing/thinning method the thinnest sample produced was $\sim 40\mu$ m thick. Later in the program, a commercial source (Insaco Inc, Quakertown, PA) was able to supply mechanically-polished Al_2O_3 wafers less than 25 μ m thick, with occasional samples $\sim 12\mu$ m thick. These thinner wafers were used for most of the ion-beam sputtering that was done near the end of the contract.

b. Gas-phase Etching and Chemical Etching Methods

The high-temperature Freon etching already described (Section 6-1) was sufficiently promising in its main characteristics to warrant its investigation as a method for thinning thick (125 μ m) Al_2O_3 wafers to the electron transparency required for the in situ studies.

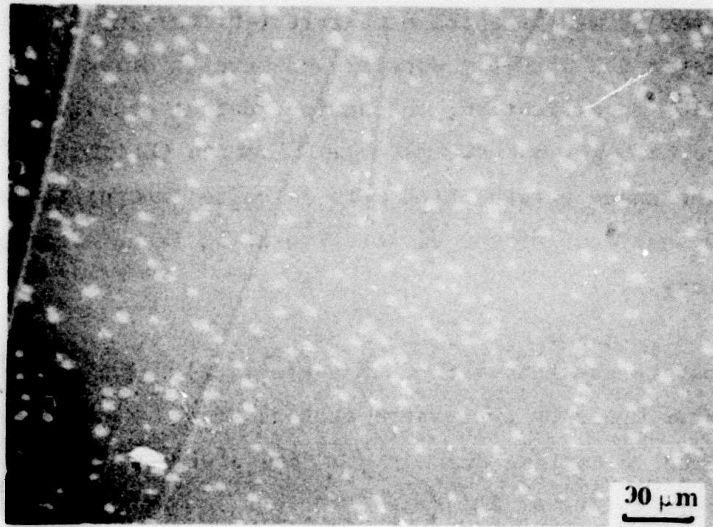
A (10 $\bar{1}4$)-oriented mechanically-polished substrate, initially treated with

Freon at 1550C for 60 min at a low etch rate ($\sim 0.1\mu\text{m}/\text{min}$) to remove $\sim 7\mu\text{m}$ of material, displayed the etch-pit density and scratch structure shown in Figure 57. At 110X magnification, the surface defect density as shown in Figure 57a is quite high, but at 450X magnification (Figure 57b) it can be observed that the space between etch pits is quite smooth; it can be assumed that these Al_2O_3 surfaces of low dislocation after Freon etching would be usable for epitaxy.

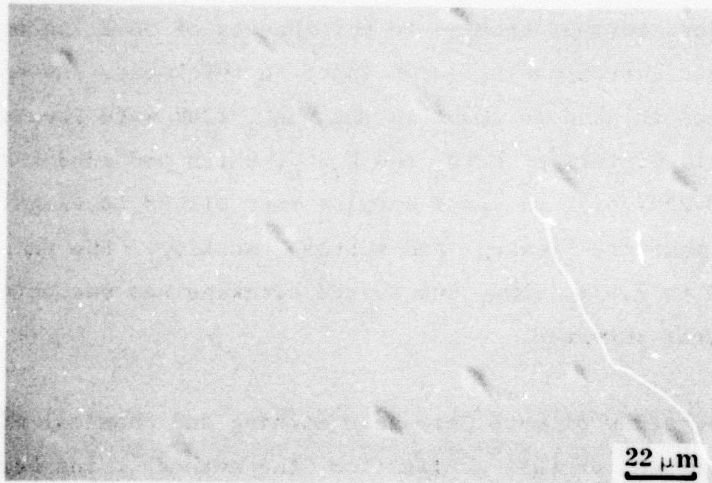
However, in order to use this method as a practical thinning technique, greater etch rates would be necessary; etching at a nominal rate of $0.6\mu\text{m}/\text{min}$ for 3 hr resulted in extreme deepening of the dislocation etch pits and a general severe faceting of the entire surface, as shown in Figure 58. Thus, Freon etching at high rates did not appear satisfactory for thinning and producing smooth surfaces on $(10\bar{1}4)$ -oriented Al_2O_3 , so no further thinning was attempted by this means.

Chemical etching of Al_2O_3 in KMnO_4 flux at 700 to 1000C was also attempted as a possible means of thinning substrates. $(01\bar{1}2)$ -oriented wafers originally $250\mu\text{m}$ thick were readily reduced to $\sim 100\mu\text{m}$ with a relatively flat and uniform surface. However, further etching to thicknesses of $50\mu\text{m}$ led to rapid edge dissolution and a corresponding large taper in thickness. As an alternate approach, samples thinned to $100\mu\text{m}$ in the KMnO_4 flux were then etched further at $\sim 225\text{C}$ in a 1:1 mixture of H_3PO_4 and H_2SO_4 , which provided a much slower etching rate ($0.25\mu\text{m}/\text{hr}$). Several samples were etched to slightly less than $50\mu\text{m}$ with only moderate breakage and surface faceting. One sample was further thinned to 7.5 to $25\mu\text{m}$, but severe breakage was encountered and only a few small pieces survived.

Although further study of both gas-phase etching and chemical etching could have been undertaken for this application, the method of ion-beam sputtering appeared so much more promising that all effort was concentrated on it.



a



b

Figure 57. Surface Structure of $(10\bar{1}4)Al_2O_3$ after Removal of $\sim 7\mu m$ of Al_2O_3 by Freon Etch at 1550C (Etch rate $\sim 0.1\mu m/min$)



Figure 58. Surface of Verneuil-grown $(10\bar{1}4)Al_2O_3$ after Etching with Freon at 1500C for ~3 hr at Nominal Rate of $0.6\mu\text{m}/\text{min}$.³ (Several deep large etch pits (as in center) were randomly distributed on surface.)

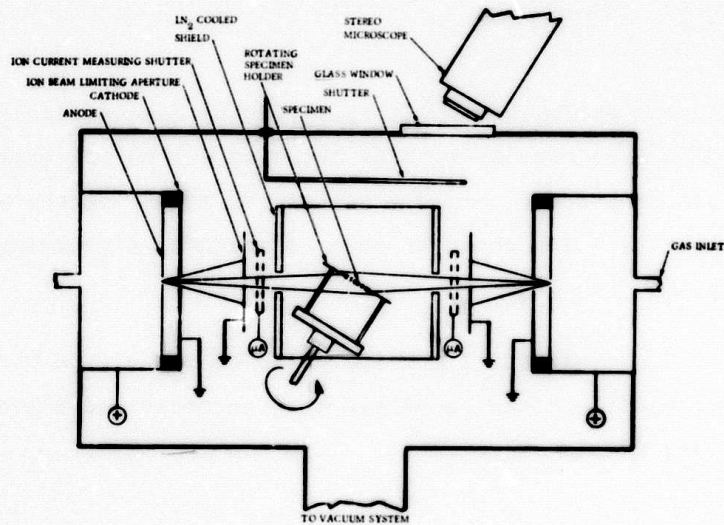


Figure 59. Configuration of IBMA Working Chamber (Not to scale)

c. Ion-beam Sputtering Techniques

Ion-beam sputtering (also called ion thinning or ion-beam machining) is a technique whereby material is removed by controlled sputtering caused by a directed ion beam. The ion-beam sputtering done on this program was performed in an Edwards ion-beam machining apparatus (IBMA). It consists of a conventional high-vacuum system containing two opposed ion guns and appropriate feedthroughs in the working chamber.

The sample is held as shown in the schematic diagram of Figure 59, so that each side is struck by an ion beam at a glancing angle of 5 to 30 deg. Argon ions are used, with energies typically 5-10KV. The sample is usually rotated in its own plane at 15 rpm to improve uniformity of material removal. Appropriate shutters are used to measure the ion-beam current, which varies from 0 to 200 $\mu\text{a}/\text{cm}^2$, typically 70 $\mu\text{a}/\text{cm}^2$.

The IBMA used for this work was extensively modified to overcome certain operational difficulties and to improve the operating convenience. A new sample holder was built to hold specimens up to 0.75 in in diameter and to permit tilting the sample for a beam angle down to 5 deg instead of the standard 10 deg.

A new gas metering system was built by replacing the original-equipment leak valves with more precise vernier metering valves for control of the low gas flow ranges required. Vacuum-tight on-off toggle valves were also installed so the gas flow could be shut off without disturbing the vernier valve setting.

A new viewing flange was built and installed on top of the working chamber. This and other modifications permitted more accurate and convenient operation in the following ways:

1. A larger recessed window permitted viewing the sample with a stereo microscope during ion bombardment, even at large sample tilt angles.

Considerable time was saved as the flange no longer had to be removed periodically for sample examination during an extended thinning operation.

2. A shield protected the ion-current measuring shutters from all but the central portion of the beam. Only the current actually used for ion-beam thinning was measured, not the total current.
3. A movable shutter prevented the window from being coated with material sputtered from the sample and its holder.
4. A larger liquid-nitrogen shield was installed, increasing the shielding efficiency.

(1) Operating Procedures

After a wafer was mechanically lapped and polished to be as thin as possible, as described earlier, the next step was to cut the thinned slices into disks, a process in which additional samples usually fractured. This was done, while the thinned wafers were still mounted on the polishing jig, by a high-speed thin-walled brass tube "biscuit-cutter" operating in a slurry of a diamond cutting compound. The thinner samples were more prone to fracturing during this operation. Initially, samples 3mm in diameter were produced. As more experience was obtained, the size was reduced to ~0.75mm for the substrates eventually used in the in situ CVD studies.

The larger disks used in the preliminary studies were installed in the IBMA sample holder, sandwiched between two metal grids having 75 mesh openings per inch. The 17.5 μ m-thick grid protected the Al_2O_3 below the grid bars from being sputtered, so the Al_2O_3 sample had a "waffled" surface after thinning; the resulting ridges provided mechanical strength. The grid served a second purpose by providing a number of individual thinned areas

rather than one large thinned region, thus increasing the yield of usable thin areas by a factor of 4-50. Thinning normally proceeded until a small perforation was noted in one area; the sample was then examined in the transmission electron microscope for possible use as a substrate.

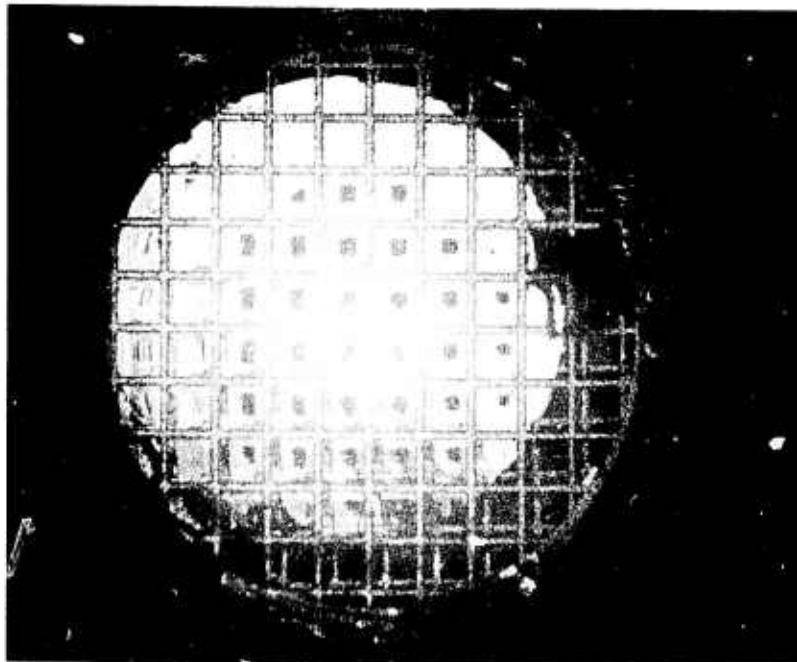
The appearance of a sample thinned beyond the customary stopping point is shown in Fig 60, photographed with monochromatic light to show thickness contours by means of interference fringes. Since this particular sample was only 5.5 μ m thick initially, perforation occurred before the shielding grid was completely sputtered away.

The 0.75mm-dia samples thinned for the in situ studies were mounted onto a 50 μ m-thick Ta sheet containing a 0.50mm-dia hole. Several samples were mounted on the same holder, each held down with a small amount of soft wax applied around the rim. Thinning then proceeded from both sides until a perforation occurred. The area around the perforation was wedge-shaped in thickness but suitably thin for substrate use over an area \sim 5 μ m wide.

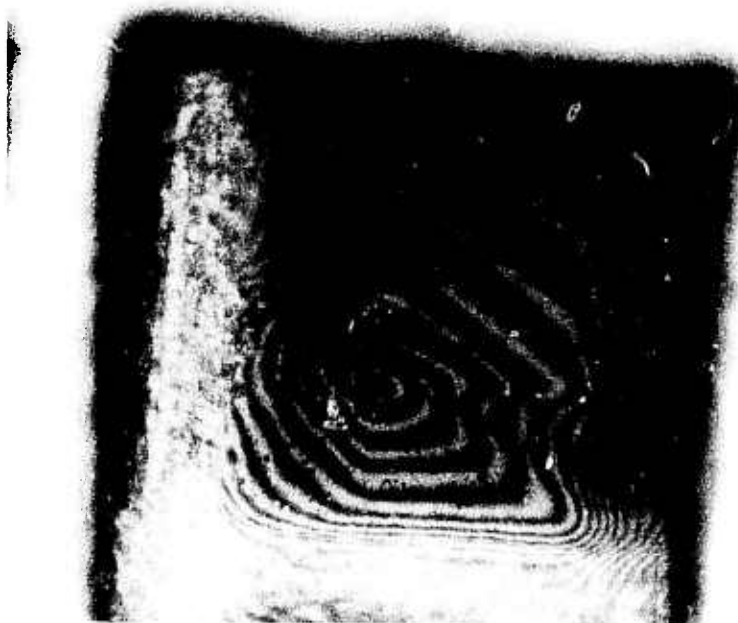
Figure 61 shows a sample 0.75mm in dia just prior to perforation. Illumination with monochromatic light reveals the thickness contours (interference fringes). As a result of the fracture through one edge, the internal stresses caused a wrinkling of the thinnest portion of the crystal. In general, the thin areas were surprisingly robust, so that the overall fabrication yield (excluding the cutting into 0.75mm disks but including ion thinning and the handling involved in loading into the heating mesh of the microchamber) was nearly 10%.

(2) Effects of Various Experimental Parameters

Operating variables affecting the material removal rate and final sample appearance include ion-beam current density, incidence angle of beam with respect to sample, ion-beam energy, crystallographic orientation of sample, axial alignment of beam and sample, and stability of the ion beam. Only the first two were found to be of major importance.



a



b

Figure 60. Optical Micrograph of Ion-thinned $(0001)\text{Al}_2\text{O}_3$ Substrate
(a) 25X, (b) 450X

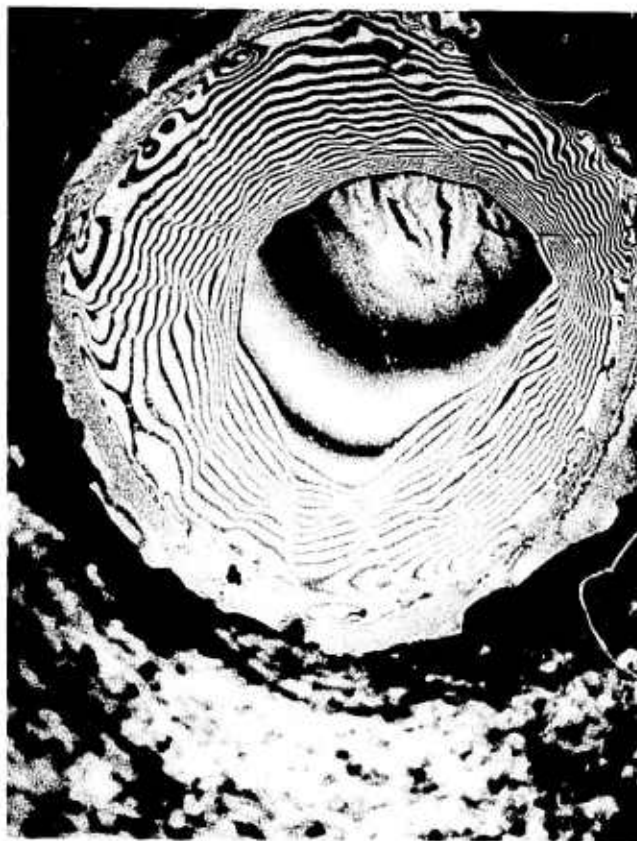


Figure 61. Ion-thinned Al₂O₃ (0.030 in dia) prior to Perforation (110X)

The removal rate was linearly proportional to the ion-beam current density. Thus, it was proper to measure the removal rate in terms of an integrated current, e.g., thickness of material removed per $\mu\text{a-hr}$. A removal rate expressed as $\mu\text{m/hr}$, while useful for time estimates, requires a statement of current density to allow prediction of the breakthrough point.

Al_2O_3 is a high-melting-point material with a large energy required to form point defects; hence, from a radiation damage standpoint, there was no limit to the usable ion-beam current. In contrast, metals typically form defect clusters indicative of radiation damage at current densities much above $100 \mu\text{a/cm}^2$. No defect clusters were observed in any Al_2O_3 samples, even those thinned at $200 \mu\text{a/cm}^2$. There was a practical upper limit to the current density, however, because the high Ar flow rate caused the ion guns to become unstable, frequently causing automatic shutoff of the apparatus. The optimum current density was found to be $70\text{-}100 \mu\text{a/cm}^2$.

The incidence angle of the ion beam with respect to the sample surface controlled both the thinning rate and the final surface topography of the sample. At a glancing angle of 30 deg (the maximum permitted by the apparatus geometry) the thinning rate was typically $100 \text{ to } 160 \text{ \AA}/\mu\text{a-hr}$, approximately twice that observed at 10 deg . However, at 30 deg the sample surface was more likely to be irregular and covered with protuberances; to minimize the presence of protuberances, a smaller incidence angle was found necessary, but this had the practical disadvantage of increasing the required processing time. All in situ samples were ion-thinned at 30 deg because of the shadowing effect of the holder on the small samples.

The energy of the Ar ion beam was found to be relatively unimportant within the range $6 \text{ to } 10 \text{ KV}$. Neither the thinning rate nor the sample surface morphology was greatly affected. Higher energies, especially 10 KV , had the disadvantage of being more likely to cause electrical arcing within the ion guns and consequent automatic shutdown. Since there were no compensating advantages, the energy was standardized at 6 KV for all samples.

No variation in removal rate was observed as a function of crystallographic orientation for the (0001), (10 $\bar{1}$ 4), and (01 $\bar{1}$ 2) orientations of Al₂O₃ investigated. The fluctuations in removal rate from sample to sample from unidentified causes were greater than any variation in etching rate. However, there did appear to be variations in the final surface morphology, as discussed subsequently.

From a general operational standpoint, beam stability was an important factor for it determined the degree to which the machine would run unattended. As thinning proceeds, sputtering occurs not only from the sample but also from the holder, beam shields, and cathode as well, and the sputtered material is deposited elsewhere in the system. In particular, material from the cathode may deposit between the anode and cathode, causing a short circuit and automatic shutoff of the apparatus. When this occurs during attended operation the machine can be turned on again and will operate for 5 to 120 min before again arcing, but during unattended operation this operating time is lost. Arcing can be prevented by thoroughly cleaning the ion gun, but since this requires ~1 hr of down-time for every 20 to 50 operating hours, an economical operating "duty-cycle" must be selected.

Sputtering of the cathode occasionally produced a more serious problem. The original cylindrical beam-exit canal normally becomes conical in operation due to the erosion by the beam, but it may also become skewed. In this case the most intense portion of the ion beam does not strike the sample and the thinning rate is reduced. The reduced thinning rate of some samples is partially the result of this effect. The cathode canal normally increases in size until the cathode must be replaced (typically after 100 to 200 hr of operation), but replacement may be required earlier if the canal becomes skewed.

(3) Sample Surface Morphology

Many preliminary samples, and to a lesser extent the samples eventually used in the in situ CVD experiments, had a rough and irregular surface morphology,

ranging from an essentially flat surface with numerous but isolated hemispherical protuberances (rare) to an undulating surface completely covered with such features (common). These features were undesirable because large numbers made it virtually impossible to find an adequately large thin area to use as the substrate for the in situ experiments.

The protuberances identified on both optical and electron micrographs of Al_2O_3 ion-thinned samples were conclusively identified as an artifact of the ion etching technique. These approximately hemispherical bumps are visible in the optical photomicrographs of Figures 60, 61, and 62 and the electron micrograph of Figure 67. These features ranged from 50 to fractions of a micron in diameter and typically about one fourth that in height. They were evidently caused by some form of contamination shielding the sample surface from the ion beam, thus preventing sputtering in that location.

Figure 62 clearly shows that one source of such contamination was the wire grid used during thinning. Protuberances formed even if a grid was not used, however, for the sample holder was an unavoidable source of contamination. The incidence of these surface features could be reduced, but not entirely eliminated, by thorough cleaning, appropriate shields, and use of a small beam-incidence angle. The small protuberances visible in a linear arrangement in Figure 61 strongly suggest residual contamination from improper cleaning of the surface. (It should be emphasized that the "objects" visible in Figure 66 are not protuberances but intersections of extinction contours.)

Another causative factor in the formation of an irregular final surface on ion-thinned Al_2O_3 was an initially rough surface. This was demonstrated by the ion-thinning of samples $\sim 5\mu\text{m}$ thick which were polished and smooth on one surface and lapped and quite rough on the other. The polished side remained smooth as a result of the sputtering action of the ion beam, with the exception of the normal formation of a few protuberances. The lapped side was made smoother by the sputtering but was still relatively rough, even when some region of the crystal first reached zero thickness. At this juncture the surface was found to consist of numerous approximately hemispherical

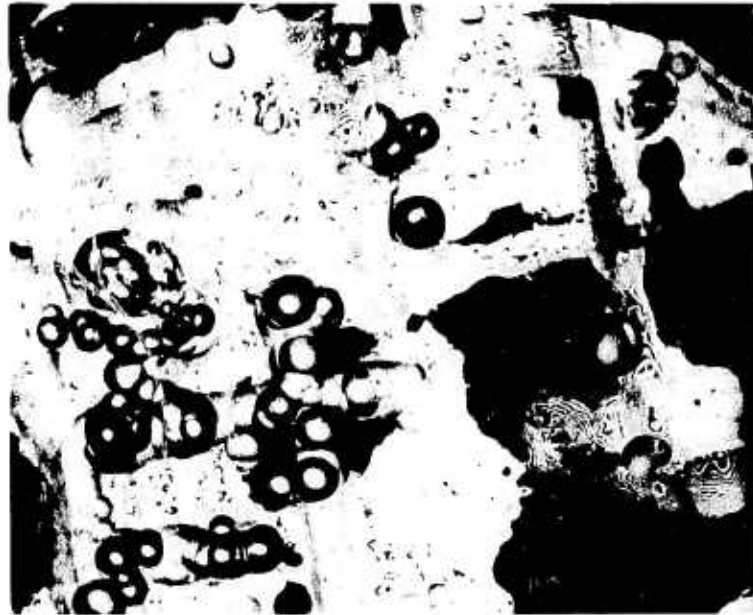


Figure 62. Optical Photomicrograph of Thinned $(10\bar{1}4)\text{Al}_2\text{O}_3$
Substrate (110X)

mounds 20 to 40 μ m in dia. At the edges and intersections of the mounds there were numerous electron-transparent regions which had an extremely large thickness gradient and a correspondingly narrow thin area. This behavior was observed for beam incidence angles of 10 and 30 deg. It was concluded that an initially smooth surface was a necessary condition for the formation of large ion-thinned regions.

(4) Sample Thickness Variations

Another problem encountered in the ion thinning of Al_2O_3 for electron microscope examination was the large thickness gradient that invariably resulted, so that suitably thin (electron transparent) regions were very limited in extent. Large areas of relatively uniform thickness in the range 200-500 \AA were seldom found. This in turn made alignment of the samples in the CVD microchamber of the electron microscope very tedious and time consuming. Causative or potentially causative factors in the thickness non-uniformity included (1) shadowing of the sample by the grid or holder during thinning, (2) formation of protuberances (see above), (3) starting thickness of the ion-thinned Al_2O_3 wafer, and (4) the nature of the thinning process itself. The first factor was controllable by selection of the proper system geometry, but the remaining factors were only indirectly controllable.

The magnitude of the thickness gradient represented in Figure 60b was analyzed by optical interferometry using monochromatic sodium light. The asymmetrical shape is the result of the bottom grid being slightly misaligned with respect to the top grid during thinning, as shown in Figure 60a. The thickness variation in this case had a slope of 1:50, which generally appeared to persist down to the thinnest regions, typified in Figures 66, 67 and 68. The thickness was found to vary from zero to 200 \AA over a transverse distance of $\sim 1\mu$ m. In practice, the thinnest regions (0 to 50 \AA) near a hole would break off during handling.

One source of excessive thickness gradient is obvious from Figures 60 and 61. The grid in Figure 60 and the holder in Figure 61 partially shielded some areas

of the sample, the exact area being determined by the incidence angle and the thickness of the grid or holder. If a hole became enlarged and the region examined was in the shadowed area, the thickness gradient was naturally greater. This problem was avoided simply by limiting electron microscopic examination to the unshadowed center of the grid square.

The area of a sample always exposed to the ion beam within a grid square of the 75-mesh grid during the thinning process was calculated. The grid had a repeat spacing of $338\mu\text{m}$, with open areas $268\mu\text{m}$ wide not covered by the grid bars. The height of the grid ($18\mu\text{m}$) caused some of the sample to be shadowed a portion of the time. At a beam angle of 30 deg, the area never in shadow was 59% of the open area. At a beam angle of 10 deg the corresponding figure was 5%. If for some reason the grid was not in contact against the sample but was instead raised another $7\mu\text{m}$, for example, there would be no region within a grid square that would be exposed at all times to a beam incident at 10 deg. The data for other angles are listed in Table 29.

The later samples thinned by this technique and intended for use in the in situ CVD experiments had less severe thickness gradients in the central region of the thinned area because they were thinned without use of a grid. Analysis of photomicrographs of the type shown in Figure 61 indicated the gradient to be typically 1:1000 or 1:500 for the central region. Although thickness gradients could not be measured with the transmission electron microscope, this gradient appeared to persist even in the thinnest regions of the sample. The outer region, partially shadowed by the holder during thinning, had a gradient typically of 1:25. If ion thinning was not stopped at precisely the moment a perforation first appeared, the central region was rapidly eroded away and the edge of the hole assumed the more severe gradient of the outer region.

One group of flux-grown (0001)-oriented Al_2O_3 crystal platelets*, initially $\sim 5\mu\text{m}$ in thickness, were ion-thinned and exhibited thickness irregularities that were less frequent and less severe. The factor most likely responsible for the improved result was the small initial thickness, but another possi-

*Kindly supplied by Prof. E. White, Imperial College, University of London.

Table 29. Size of Completely Unshadowed Area for Various Beam Incidence Angles in IBMA

Grid Height (μm)	Incidence Angle (deg)	Length of Grid Shadow (μm)	Portion of Total Grid Square Length Unshadowed (%)	Portion of Total Grid Square Area Unshadowed (%)
18	90	0	100	100
18	30	31	77	59
18	25	39	71	50
18	20	50	63	40
18	15	67	50	25
18	10	102	23	5
18	5	207	0	0
25	30	43	68	46
25	25	54	60	36
25	20	69	49	24
25	15	93	30	9
25	10	142	0	0
25	5	288	0	0

bility was the relatively smooth starting surface of the crystal. Thus, improvement in thickness uniformity and the consequent enlargement of the thinned area was a strong impetus for producing starting (pre-ion-thinning) Al_2O_3 wafers less than $25\mu\text{m}$ thick. Another impetus, of course, was reduction of the ion-beam thinning time required.

It is possible that a limiting thickness gradient is imposed on all samples by the nature of the ion-beam sputtering process itself. Thin areas, i.e., where sample thickness approximately equals ion penetration depth, are more

rapidly eroded than thick areas, and this fact alone may set a lower limit to the gradient attainable. Although the importance of this effect was never determined, it is unlikely to be the limiting factor for all samples, especially since adequately thinned regions were indeed obtained.

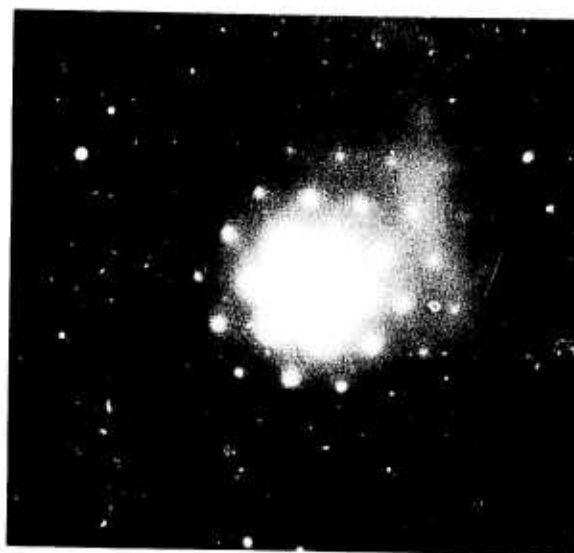
A final factor influencing the uniformity of thickness of samples is the cross-sectional profile of the ion beam. The profile was determined experimentally by thinning a large Al_2O_3 wafer. The beam has conical symmetry, with the most intense region along the axis of the ion gun. The 1.3-cm dia sample used for the evaluation had a saucer-shaped surface after thinning, with a 3.5-mm dia region $49\mu\text{m}$ deep approximately in the center, tapering to $10\mu\text{m}$ deep near the edges. In the deepest region the removal rate was unusually high, $1.4\mu\text{m/hr}$, while at the edges the rate was $0.3\mu\text{m/hr}$.

The deepest region was located $\sim 1\text{mm}$ from the geometric center of the sample, indicating a misalignment by this amount of the center of rotation of the sample and the axis of the ion beam. For most samples this misalignment is unimportant; however, for samples smaller than 1mm dia it means the sample will be out of the most intense portion of the ion beam for a fraction of the time during rotation, making the effective thinning rate lower than normal.

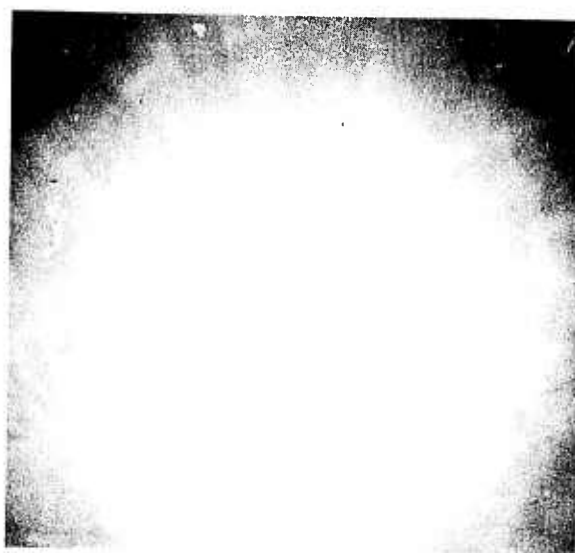
(5) Characteristics of Thinned Samples Used for In Situ CVD Experiments

Three different orientations of Al_2O_3 were successfully thinned by ion beam sputtering - (0001), $(10\bar{1}4)$, and $(01\bar{1}2)$. Reflection electron diffraction spot patterns and Kikuchi patterns obtained from samples in these three orientations are shown in Figures 63, 64 and 65. The spot patterns are from thin regions ($\sim 500\text{\AA}$) and the Kikuchi patterns are from thicker regions ($\sim 10,000\text{\AA}$). These are believed to be the first such patterns obtained from single-crystal Al_2O_3 by transmission electron microscopy.

These three orientations were selected for ion thinning for the following reasons. The $(01\bar{1}2)$ orientation is widely used in the semiconductor industry and permits the largest range of temperature and deposition conditions



(a)



(b)

Figure 63. Electron Diffraction (a) Spot and (b) Kikuchi Pattern from $(0001)\text{Al}_2\text{O}_3$ Substrate.

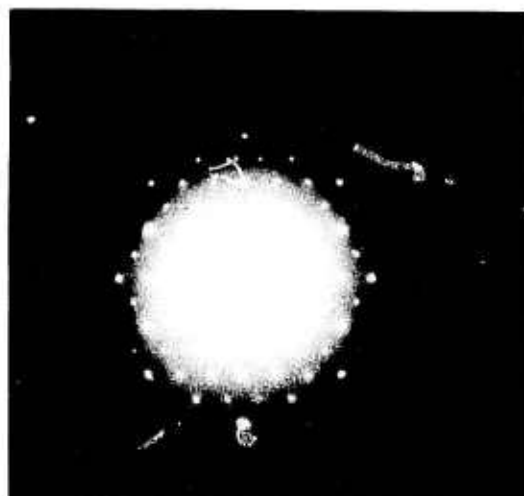


Figure 64. Electron Diffraction Spot and Kikuchi Pattern from $(10\bar{1}4)Al_2O_3$ Substrate



(a)



(b)

Figure 65. Electron Diffraction (a) Spot and (b) Kikuchi Pattern from $(01\bar{1}2)Al_2O_3$ Substrate.

for single-crystal epitaxial Si growth. All in situ experiments were conducted on material of this orientation. The basal-plane orientation was selected because initially this was the only orientation available in samples sufficiently thin to serve as starting wafers for the ion-beam sputtering; these were flux grown crystals 5 μ m in thickness. The (10 $\bar{1}$ 4) orientation was selected because excellent (111)Si growth can be obtained on this plane of Al₂O₃. However, this is a difficult orientation to polish, as indicated previously; since production of 50 μ m-thick starting samples for ion thinning proved too time consuming, work on this orientation was stopped.

Representative electron micrographs made on thinned Al₂O₃ substrates are shown in Figures 66 through 72. The substrates used for in situ depositions (see Section 8) are also typical of the ion thinning results.

The samples were all of relatively high quality single-crystal Al₂O₃, so no internal defect structure is visible in the micrographs. The ideal uniformly-thinned crystal would appear featureless on an electron micrograph. However, three characteristics are clearly visible in these figures - extinction contours, surface structures, and a thickness gradient; the significance of the latter two factors has already been discussed. The combination of these factors is least noticeable in Figures 69 and 71; accordingly, the samples involved in those micrographs were the most desirable substrates for in situ CVD. The other samples would be less suitable as substrates.

Many regions in the prepared samples had a thickness gradient that was larger than desirable; these samples were less suitable as substrates, for that reason. Thin regions with suitable large areas were seldom observed in more than one location per sample. The thickness gradient always limited the usable thin region to <5 μ m in width, and frequently to <1 μ m. As previously discussed, the thinnest crystals prior to ion-beam sputtering (the 5 μ m (0001) platelets) were more uniform in thickness and had less severe gradients after ion thinning, emphasizing the importance of obtaining thin and uniform pre-ion-thinning samples.



Figure 66. Electron Micrograph of (0001) Al_2O_3 Substrate

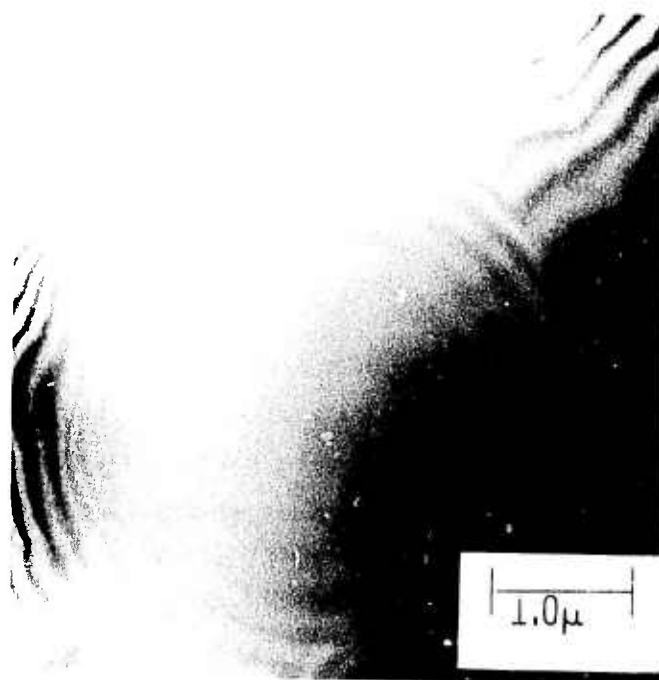


Figure 67. Electron Micrograph of (0001) Al_2O_3 Substrate

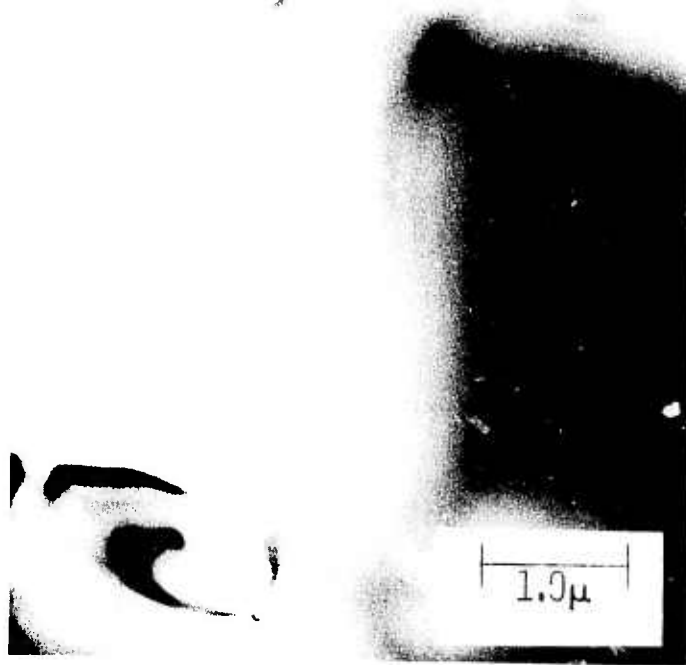


Figure 68. Electron Micrograph of $(10\bar{1}4)Al_2O_3$ Substrate.

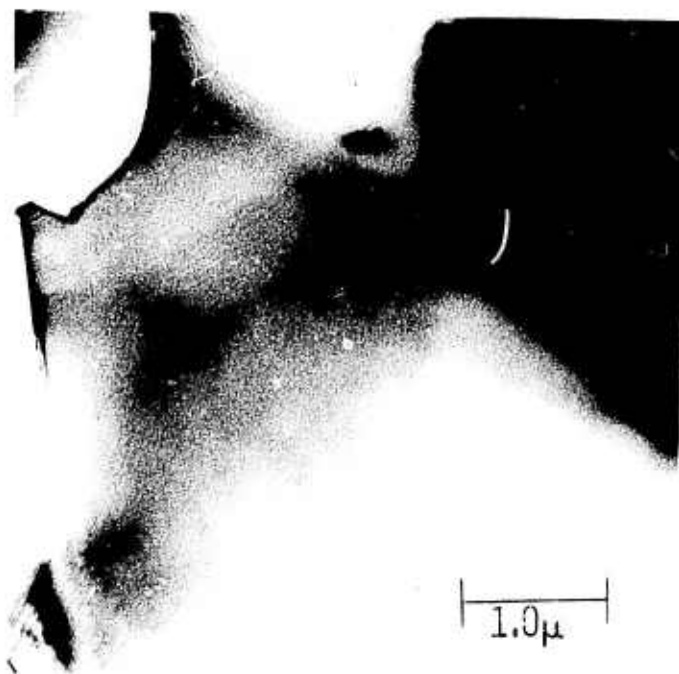


Figure 69. Electron Micrograph of (10\bar{1}4)Al₂O₃ Substrate



Figure 70. Electron Micrograph of (10\bar{1}4)Al₂O₃ Substrate



Figure 71. Electron Micrograph of $(01\bar{1}2)Al_2O_3$ Substrate.



Figure 72. Electron Micrograph of $(01\bar{1}2)Al_2O_3$ Substrate

The extinction contours, observable in all of the micrographs, but especially pronounced in Figures 66, 67 and 72, are the result of constructive and destructive interference of the electron waves passing through the crystal. Extinction contours in electron microscopy are analogous to interference fringes in optical microscopy, but unlike the latter their spacing is not simply related to the thickness of the crystal. Slight tilts of the crystal dramatically change the contour spacing. Extinction contours are quite sensitive to crystal orientation and thus reflect minor amounts of strain or buckling in the crystal. When those characteristics are absent, as in Figure 67, the extinction contours give a qualitative indication of local thickness variations.

The combination of a thickness gradient and local strains and buckling can result in rather interesting combinations, as shown in Figures 66 and 72. It is emphasized that the circular semisymmetrical patterns in these figures are not objects in the crystal but rather intersections of the extinction contours. This can be readily demonstrated by tilting the sample slightly during examination; the circular intersections then move about the crystal. The obscuring presence of extinction contours is generally best eliminated by producing uniformly thin, strain-free, unbuckled crystals by the ion-beam sputtering process.

An interesting feature was observed in the electron micrograph of Figure 70. The large oblong particle and two smaller particles shown were inclusions originally present in the Al_2O_3 as a second phase. That they were inclusions and not particulate matter resting on the surface was determined by examining the extinction contours in the Al_2O_3 around the inclusion; at higher magnifications the strain brought about by their presence was revealed. No other inclusions or suggestions of a second phase were ever detected on any other sample. Indeed, no internal structure of any type, including dislocations, was observed on any other sample. This is not to imply that such structure was totally absent, because dislocations in particular were known to be present. Rather, it was the result of the low statistical probability of observing a limited number of defects in a small field of view.

Certain samples exhibited a microscopic surface structure after thinning; this is particularly noticeable in Figures 69 and 72. This semiregular, wavy or terraced structure was noticed a small percentage of the time on $(10\bar{1}4)$, somewhat less on $(01\bar{1}2)$ orientations, but not at all on (0001) samples, which suggests crystallographic origin. However, the direction of the features in Figure 69 does not appear to be crystallographic, and the structure did not appear on all samples or in all thin areas of the same sample. The surface structure was more pronounced in areas where the thickness gradient was least, suggesting a complex interaction between the crystalline sample and the ion-sputtering mechanism. The structure did not appear to be simply related to ion-beam energy or incidence angle, and its origin is currently unknown. No samples with the morphology of Figures 69 or 72 were used as in situ substrates.

SECTION 7

Al_2O_3 CHARACTERIZATION BY CARRIER INJECTION AND TRANSPORT MEASUREMENTS*

A technique utilizing the photoelectric process in a metal-insulator-semiconductor (MIS) structure has been used by a number of workers (Refs 57-59) to study the interface between a semiconductor and an insulator. In this method a thin insulating layer (~2000 Å) is grown on a polished semiconductor wafer and a semitransparent metal film is deposited on top of the insulator layer to form the MIS structure. A monochromatic beam of light is directed onto the semitransparent electrode and is partially absorbed in the metal layer. The remainder of the incident light is absorbed in the semiconductor material close to the semiconductor-insulator interface, since the insulator is transparent to light for the photon energies used.

Electrons are excited in both the metal layer and the semiconductor by the absorbed photons. If a bias voltage is applied across the MIS structure with the metal layer (electrode) positive with respect to the semiconductor, then electrons excited in the semiconductor near the interface will flow through the insulator and into the metal electrode, provided the electrons have sufficient energy to overcome the interface barrier. The photoelectric current is measured by a meter in the external circuit, as shown in Figure 73. When the metal electrode is biased negatively with respect to the semiconductor, a current due to photoelectric emission of electrons from the metal electrode flows through the insulator to the semiconductor.

By studying the photoelectric yield as a function of photon energy, it is possible to obtain information on the interface barrier height (location of the conduction band of the insulator at its two interfaces), the electron affinity of the insulator, the amount of band bending in the semiconductor, and the effect of mobile ions in the insulator. The photoelectrons emitted

* These studies were carried out at the University of California at Los Angeles in the Electrical Sciences and Engineering Department by C. R. Viswanathan and R. Y. Loo.

from the region of the semiconductor adjoining the insulator provide a type of electric "probe" which helps to characterize the interfacial region of the semiconductor.

When a substrate of Al_2O_3 serves as the insulator and a Si or GaAs film is grown on one surface of the wafer and a semitransparent Al film is deposited on the other face of the wafer, data of the type described in Section 11-3 can be obtained. In addition to yielding information on the interface barrier height and the amount of band bending in the semiconductor near the interface, such experiments demonstrated that electrons excited either in the semiconductor film or in the metal layer can be transported through single-crystal Al_2O_3 substrates whose thickness is the order of several mils - a result totally unexpected from the work of others (Ref 60). The fact that photoelectrons excited on one side of the transparent substrate flow completely through the thick substrate is a very significant result, and its discovery early in this program (Ref 61) led to further studies of related phenomena associated with the Al_2O_3 substrates (Refs 62, 63).

In particular, the injection and transport of carriers in thick single-crystal Al_2O_3 substrates was studied in detail. In this investigation, Al_2O_3 substrates were obtained from vendors with both sides polished. The substrates were etched in boiling H_3PO_4 for an hour and were thoroughly washed in acetone and distilled water and then dried in a N_2 stream. Semitransparent Al films of a few hundred angstroms thickness were deposited on both sides of the Al_2O_3 substrates to produce a MIM sandwich structure. A bias voltage from a battery supply was applied across the MIM sandwich, and the current through the sample was measured by a picoammeter (APR Model No. 135).

A monochromatic beam of light was incident on the semitransparent metal electrode, as in Figure 73. While electrons were excited in both the electrodes, electron injection into the insulator occurred (resulting in a photocurrent in the external circuit) from that electrode which was biased negative with

respect to the other. Thus, electron injection was possible from either of the two electrodes by a suitable choice of the polarity of the bias voltage.

Extensive studies of the transport mechanisms of photoinjected electrons in Al_2O_3 crystal wafers were carried out using this experimental arrangement, and the results are described here.

1. THEORY OF TRANSPORT OF ELECTRONS IN INSULATORS

When electrons are injected at one face of an insulating substrate the electrons will travel in the insulator toward the opposite face under the action of a suitable electric field in the insulator. It might be supposed that the electrons would eventually reach the other face and be collected by the metal electrode thereon. This would be possible, however, only in a perfect crystal free of electron traps. Usually the electrons will travel some distance and become trapped at a defect or impurity center.

In zero applied field the electrons will execute some type of Brownian motion before they are trapped. During this motion in the crystal the electrons are considered as being in the conduction band, and when they are trapped they are localized in the crystal, occupying an energy state with its level in the band gap of the insulator. Electrons can also be transported across an insulating layer by a quantum mechanical tunneling process; however, such a tunneling process is observable only in very thin insulating layers.

The average distance (mean range) a photoelectron travels before it is trapped when a weak electric field is present is called the "Schubweg." If it is assumed that an electron has a probability $\frac{1}{T}$ per unit time of being captured by a trap, then the average time that an electron spends in the conduction band before it is trapped is equal to T and the mean range W is equal to

$$W = \mu \mathcal{E} T, \quad (37)$$

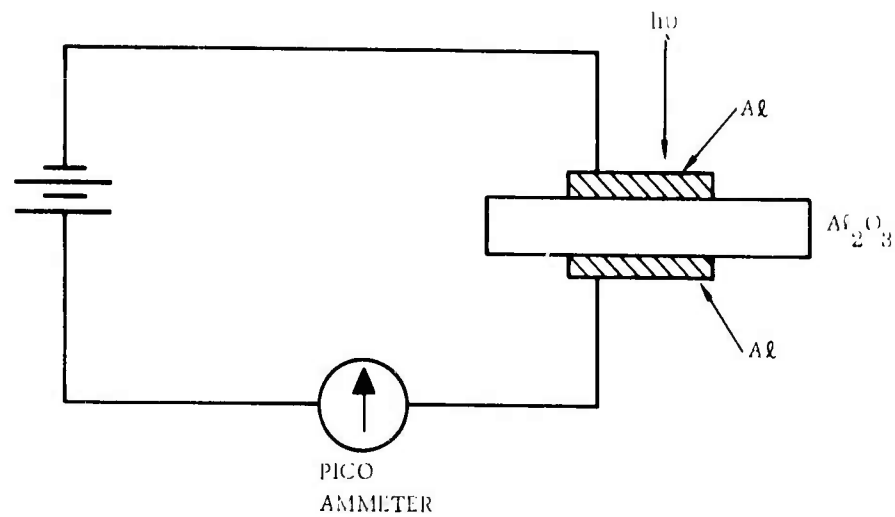


Figure 73. Schematic of Experimental Arrangement for Measuring Properties of Photoinjected Carriers in Al_2O_3

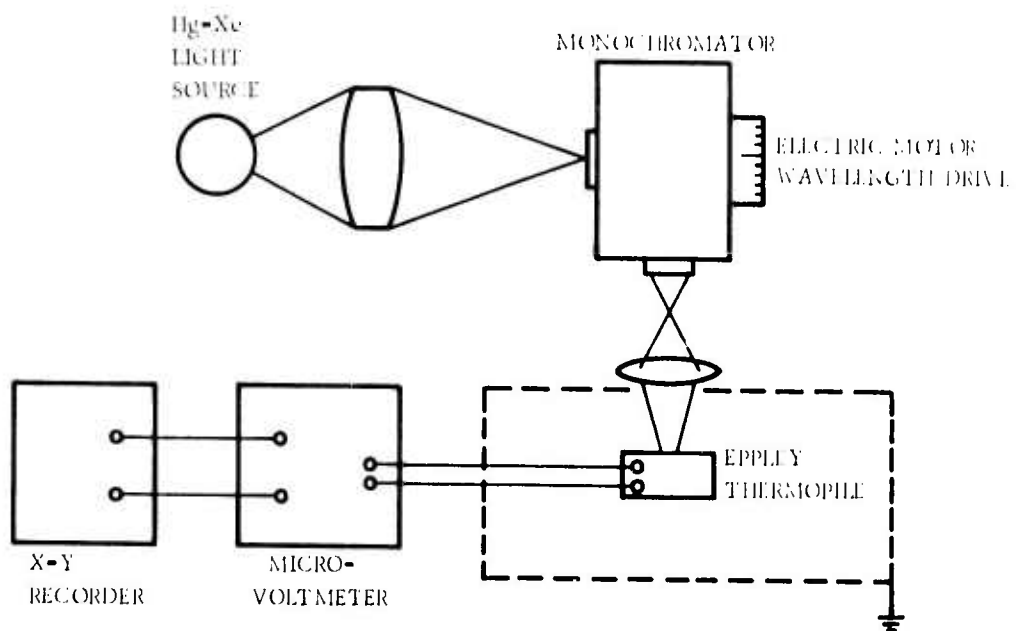


Figure 74. Schematic Diagram of Experimental Setup for Calibrating Light Source.

where μ is the mobility of the conduction band electron in the insulator and ξ is the electric field.

It is now possible to derive a theoretical expression for the current-voltage relationship. If there are n electrons present at time t , then in a time interval dt the number of electrons captured will be equal to

$$dn = -n(t) \frac{dt}{T}. \quad (38)$$

This on integration yields

$$n(t) = n_0 e^{-t/T}, \quad (39)$$

where n_0 is the number of electrons injected at time $t=0$. If electrons are injected at one end of the insulating layer, say at $x=0$, then in a time interval t they would have traveled a distance

$$x = \mu \xi t. \quad (40)$$

Therefore

$$n(t) = n_0 e^{-x/\mu \xi T} = n_0 e^{-x/W}. \quad (41)$$

The number of electrons captured in a distance between x and $x+dx$ is equal to

$$dn = - \frac{n_0 e^{-x/W} dx}{W}. \quad (42)$$

If d is the thickness of the insulating layer, the number of electrons reaching the electrode on the opposite face is equal to

$$n(d) = n_0 e^{-d/W}. \quad (43)$$

The average distance that the electron traverses is calculated using both the electrons that reach the other end of the crystal and those that get trapped on the way. Therefore, the average distance \bar{x} is equal to

$$\bar{x} = \frac{\int_0^d x dt + n_0 d e^{-d/W}}{n_0} = W(1 - e^{-d/W}) . \quad (44)$$

The current in the external circuit I for an injection of N_0 electrons per second at one end of the crystal is equal to

$$I = \frac{n_0 q \bar{x}}{d} = \frac{q n_0 W}{d} (1 - e^{-d/W}) . \quad (45)$$

From Equation (37) $W = \frac{\mu VT}{d}$, so

$$I = q n_0 \frac{\mu TV}{d^2} (1 - e^{-d^2/\mu VT}) . \quad (46)$$

Defining $V_0 = \frac{d^2}{\mu T}$, it follows that

$$I = q n_0 \frac{V}{V_0} (1 - e^{-V_0/V}) . \quad (47)$$

It must be pointed out that the above derivation is valid only for the initial value of the current and under the condition that there are no space-charge effects.

Another model that describes the voltage dependence of photoelectric current due to injection of photoelectrons in an insulator is due to Berglund and Powell (Ref 64); this model considers the scattering of photoinjected electrons in the potential barrier resulting from a combination of the image potential and that due to the externally applied electric field. Assume that the interface at which photoelectrons are injected is located at $x=0$ and that the interface potential at $x=0$ is ϕ_1 . Then the potential at any point in the insulator is given by

$$\phi(x) = \phi_1 + \int_0^x \xi(x) dx - \frac{q}{16\pi K_I \epsilon_0 x}, \quad (48)$$

where K_I is the optical dielectric constant of the insulator. The second term in Equation (48) is due to electric field while the third term is due to image force. Neglecting any localized charge in the insulator, it is possible to show that the potential reaches a maximum at a distance x_0 given by

$$x_0 = \left[\frac{q}{16\pi K_I \epsilon_0 \xi(x_0)} \right]^{1/2} \quad (49)$$

and the maximum value of the potential is given by

$$\phi_{\max} = \phi_1 + \int_0^{x_0} \xi(x) dx - \frac{q}{16\pi K_I \epsilon_0 x_0}. \quad (50)$$

The voltage dependence of photoinjected current can be expressed in the form

$$I = A(\hbar\omega) (\hbar\omega - q\phi_{b0} + kv^{1/2})^p e^{-\sqrt{V_0/V}}, \quad (51)$$

where ϕ_{b0} = interface potential barrier, $\hbar\omega$ = photon energy, $V_0 = \frac{qd}{16\pi K_I \epsilon_0 l^2}$, l = mean free path for scattering in the insulator, and p = a parameter that depends on the electron energy distribution and typically varies between 1 and 3.

Equation (51) can be rewritten as

$$I = I_0 e^{-\sqrt{V_0/V}}, \quad (52)$$

where I_0 is the current that would flow in the absence of scattering and the exponential factor gives the attenuation in the photocurrent due to scattering in the insulator. I_0 can be considered practically independent of voltage if the photon energy $\hbar\omega$ is chosen to be much larger than the interface barrier potential ϕ_{b0} .

In the above derivation it has also been assumed that the scattering probability is the same throughout the insulator, independent of position in the insulator. This expression is strictly applicable only if the injected electrons are not trapped. In the presence of trapping, an additional process has to be considered to explain the transport of photoinjected electrons. This is particularly necessary if the insulator thickness is large (several microns thick), as in these studies.

In a thick insulating layer there will be bulk effects which will determine the transport process. As was shown earlier, the injected electrons will travel a certain distance and become trapped. An applied electric field will promote the excitation of this trapped electron into the conduction band of the insulator, and this excited electron will be transported in the crystal until it is again trapped or reaches the other electrode. This type of transport mechanism is called the Poole-Frenkel model.

In this model the current flow increases exponentially with the square root of the applied voltage. The trap is assumed to be located at an energy level E_a below the conduction band. When an electric field is applied the potential barrier is reduced in the direction of electron flow under the action of the electric field, and the potential barrier is increased in the opposite direction. The barrier attenuation in the direction of the current flow is

$$\Delta\phi_{PF} = \beta_p \xi^{1/2}, \quad (53)$$

where

$$\beta_p = 2 \left[\frac{q^3}{4\pi K_I \epsilon_0} \right]^{1/2}. \quad (54)$$

The current density in the Poole-Frenkel model as modified by Ieda et al (Ref 65) is given at high fields by

$$J = BT^2 \left[(\beta_p \xi^{1/2} / 2kT) - 1 \right] e^{-(E_a - \beta_p \xi^{1/2}) / kT}, \quad (55)$$

where B is a constant. At lower fields, the behavior is ohmic and the conductivity follows Ohm's law.

All the different processes can be combined to account for the photoelectric current measured using the MIM structure. A detailed theoretical program is required to correlate theory and experiment. However, it can be assumed that the voltage dependence in the injection process is negligible since the photocurrent is limited by the Poole-Frenkel mechanism; in this case the photocurrent can be expressed in a simplified form as

$$I = AT^2 \xi e^{-\frac{(E_a - \beta \xi^{1/2})}{kT}} \quad (56)$$

$$= AT^2 \frac{V}{d} e^{-\frac{(E_a - \beta \xi^{1/2})}{kT}}, \quad (57)$$

where A is a constant.

2. MEASUREMENT OF QUANTUM EFFICIENCY OF PHOTOINJECTION

In order to understand the photoinjection process and the subsequent carrier transport mechanism it was necessary to determine the quantum efficiency of the photoelectric process. The quantum efficiency is defined as the number of photoelectrons giving rise to the photocurrent per incident photon for a given photon energy and bias voltage across the MIM structure; this is usually measured for the steady-state photocurrent. If F is the incident photon flux and I is the photoelectric current, then the quantum efficiency η is given as

$$\eta = \frac{I}{qF}. \quad (58)$$

In order to determine the quantum efficiency, the photon flux F had to be determined. The Hg-Xe 1000w light source used in the photoelectric measurement was calibrated using an Eppley thermopile in the experimental arrangement

shown schematically in Figure 74. The light beam from the light source operating at the usual power level was focused on the entrance slit of the monochromator. The light from the output slit was focused on the thermopile, the output voltage from which was read by a millimicrovoltmeter (Keithley Model 149) whose output in turn was fed to an X-Y recorder (Hewlett-Packard 7004B). The output voltage divided by the calibration factor for the thermopile gave the photon flux. The monochromator was electrically driven and the output voltage was recorded as a function of the photon energy.

The MIM structure samples were prepared with different values of Al electrode film thickness varying from 400 to 4000Å (Ref 66). Several (0001)Al₂O₃ substrates of thickness 0.010 and 0.015 in were used in these quantum efficiency measurements.

The quantum efficiency η is plotted as a function of photon energy for various bias voltages in Figure 75 for a sample having a 400Å-thick Al electrode. The plot of quantum efficiency as a function of bias voltage at different photon energies is given in Figure 76 for the same sample. It can be seen that typical values of quantum efficiency lie in the range of 2×10^{-5} electrons per incident photon. The variation of quantum efficiency η with the thickness of the Al electrode is plotted in Figure 77 for an incident photon energy of 4.8 eV, in Figure 78 for an incident photon energy of 5.2 eV, and in Figure 79 for an incident photon energy of 5.5 eV.

It can be inferred from these results that the quantum efficiency rises initially with Al film thickness and then decreases after reaching a peak. It is apparent that the thickness of the Al film at which the maximum value of quantum efficiency occurs decreases with increasing photon energy. The initial rise in the photoelectric yield with increasing thickness is due to the increase in the number of photons absorbed. The peak represents the absorption of all incident photons. Subsequent decay represents a fall in photoelectric current, since the number of electrons that can reach the conduction band of the insulator falls off exponentially with Al film thickness as

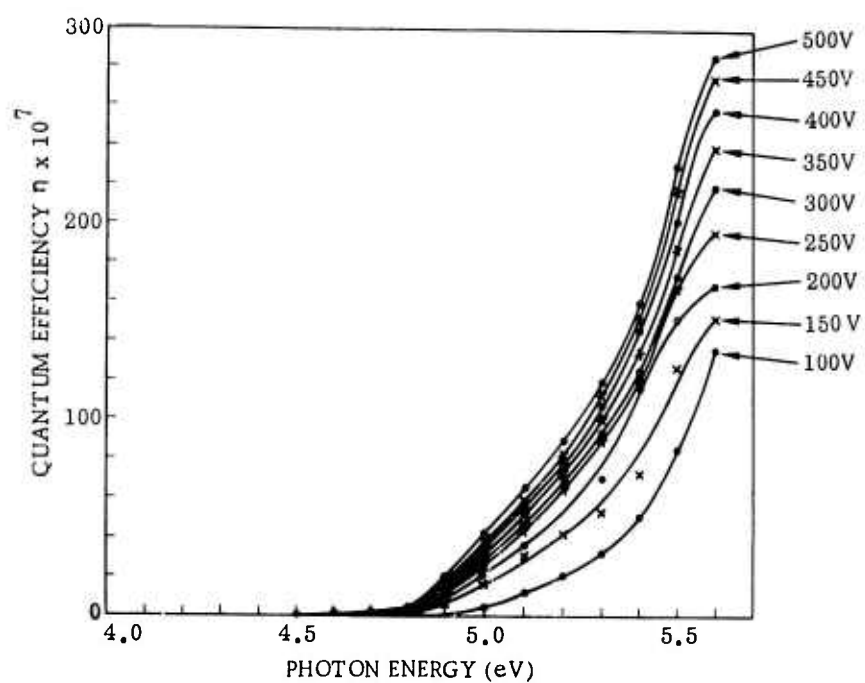


Figure 75. Quantum Efficiency as Function of Photon Energy for Various Bias Voltages for Carrier Photoinjection into Al_2O_3 from Al Film 400Å Thick.

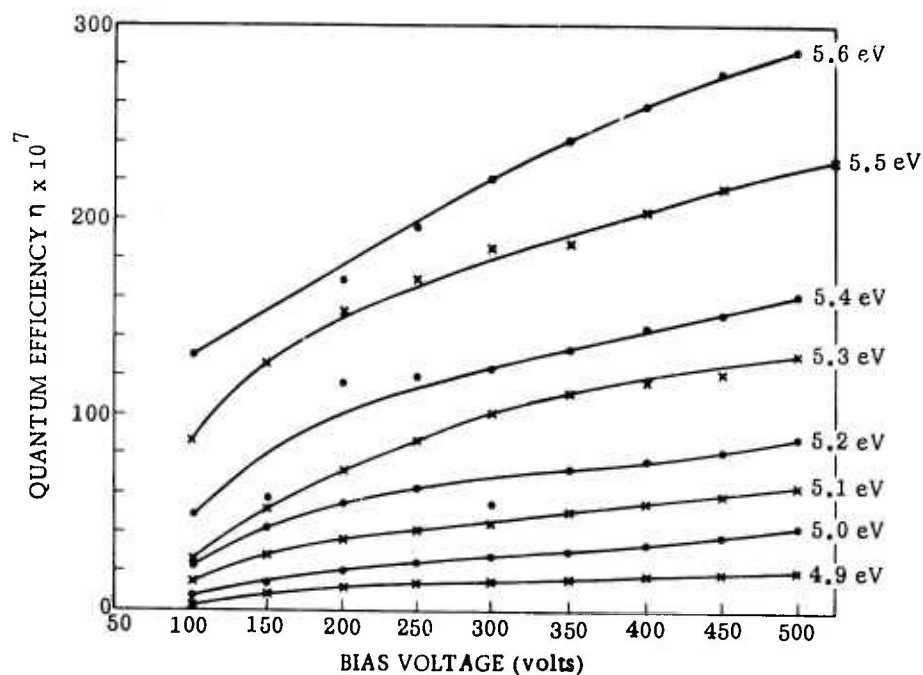


Figure 76. Quantum Efficiency of Carrier Photoinjection into Al_2O_3 from 400Å Al Film as Function of Bias Voltage, for Various Photon Energies

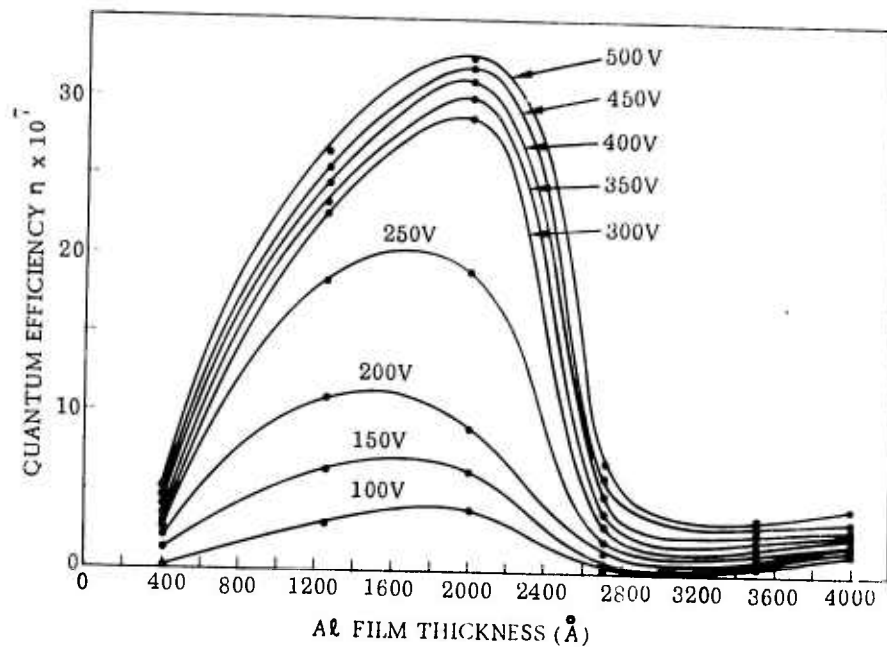


Figure 77. Quantum Efficiency of Carrier Photoinjection into Al_2O_3 as Function of Al Electrode Thickness for 4.8 eV Photon, for Various Bias Voltages.

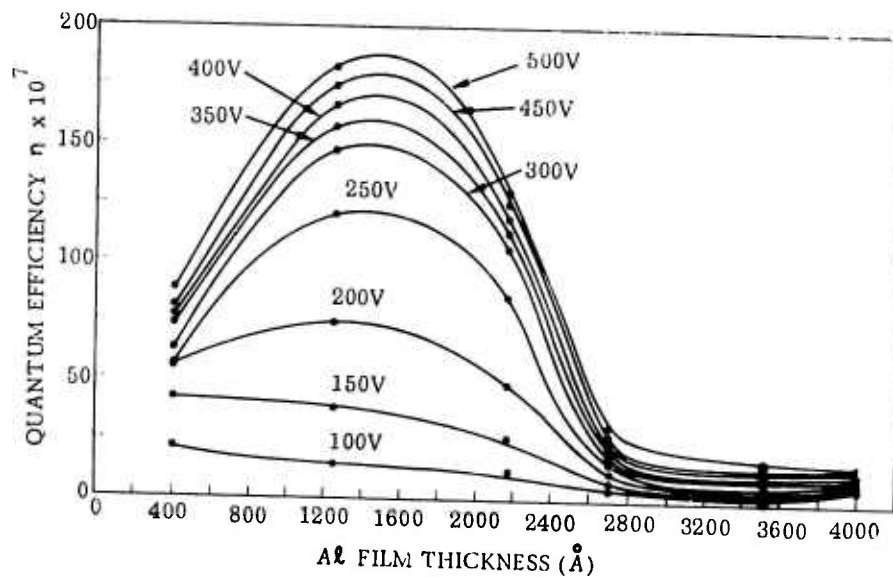


Figure 78. Quantum Efficiency of Carrier Photoinjection into Al_2O_3 as Function of Al Electrode Thickness for 5.2 eV Photon, for Various Bias Voltages.

$$I = I_0 e^{-x/L}, \quad (59)$$

where L is called the escape length.

In order to determine L , some of the experimental points of Figure 78 were plotted in terms of photocurrent and were connected by a smooth curve as shown in Figure 80, and the decay portions were fitted with an exponentially decaying behavior by a suitable choice of the parameter L . This procedure yielded a value of 350\AA for the escape length L in Al for an incident photon energy of 5.2 eV. The reported (Ref 67) values of escape length for electrons in other metals are 740\AA for Au, 400\AA for Ag, 170\AA for Pd, and between 50 and 200\AA for Cu. Thus, the value of 350\AA for Al films as found in these experiments appears to be the right order of magnitude.

3. PHOTOCURRENT VARIATION WITH SAMPLE TEMPERATURE

In order to understand the transport mechanism of the photoinjected electrons in Al_2O_3 the photoelectric current at various sample temperatures was measured. For this purpose, a substrate of (11 $\bar{2}$ 0) Al_2O_3 0.037 in thick was polished on both sides and used to fabricate a MIM structure. Al electrodes were deposited on both faces of the substrate. As indicated previously, the photocurrent increases to a peak on illumination with light and then starts to decay as a function of time and ultimately reaches a steady-state value. The steady-state values of photocurrent were measured for different bias voltages at four different temperatures, with an incident photon energy of 5.0 eV. The resulting values of photocurrent are plotted as a function of V on a semilog plot in Figure 81. The experimental data points are connected by smooth curves.

If the voltage dependence of the current is assumed to be given by Equation (57), it is possible to obtain a fit to the experimental data. The parameter β_p (see Equation (54)) was calculated to be 3.57×10^{-24} joules/ $V^{\frac{1}{2}}$ meter $^{-\frac{1}{2}}$. When this value of β_p is used in Equation (57) the agreement is not evident. The value of β_p required to give a good fit was found to be approximately four times the theoretical value. The values of β_p/kT for several temperatures,

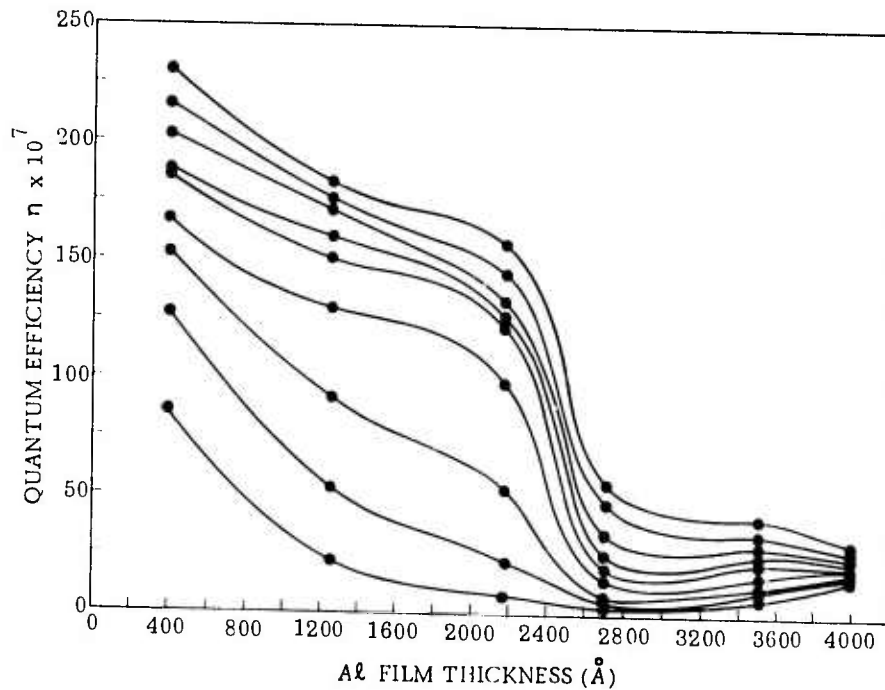


Figure 79. Quantum Efficiency of Carrier Photoinjection into Al_2O_3 as Function of Al Electrode Thickness for 5.5 eV Photon, for Various Bias Voltages.

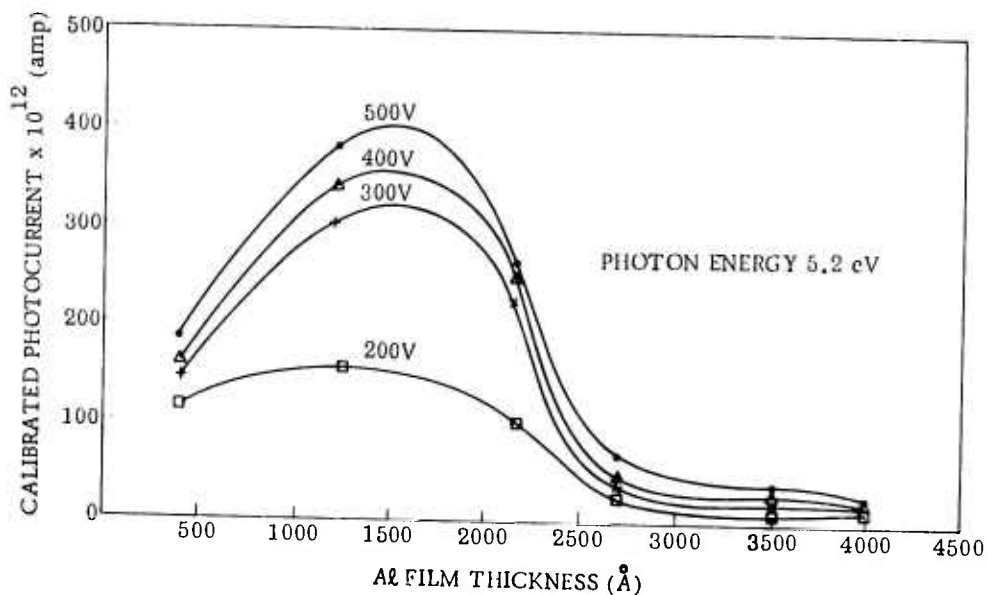


Figure 80. Calibrated Photocurrent in Al_2O_3 as Function of Al Electrode Thickness for 5.2 eV Photon Energy, at Several Bias Voltages.

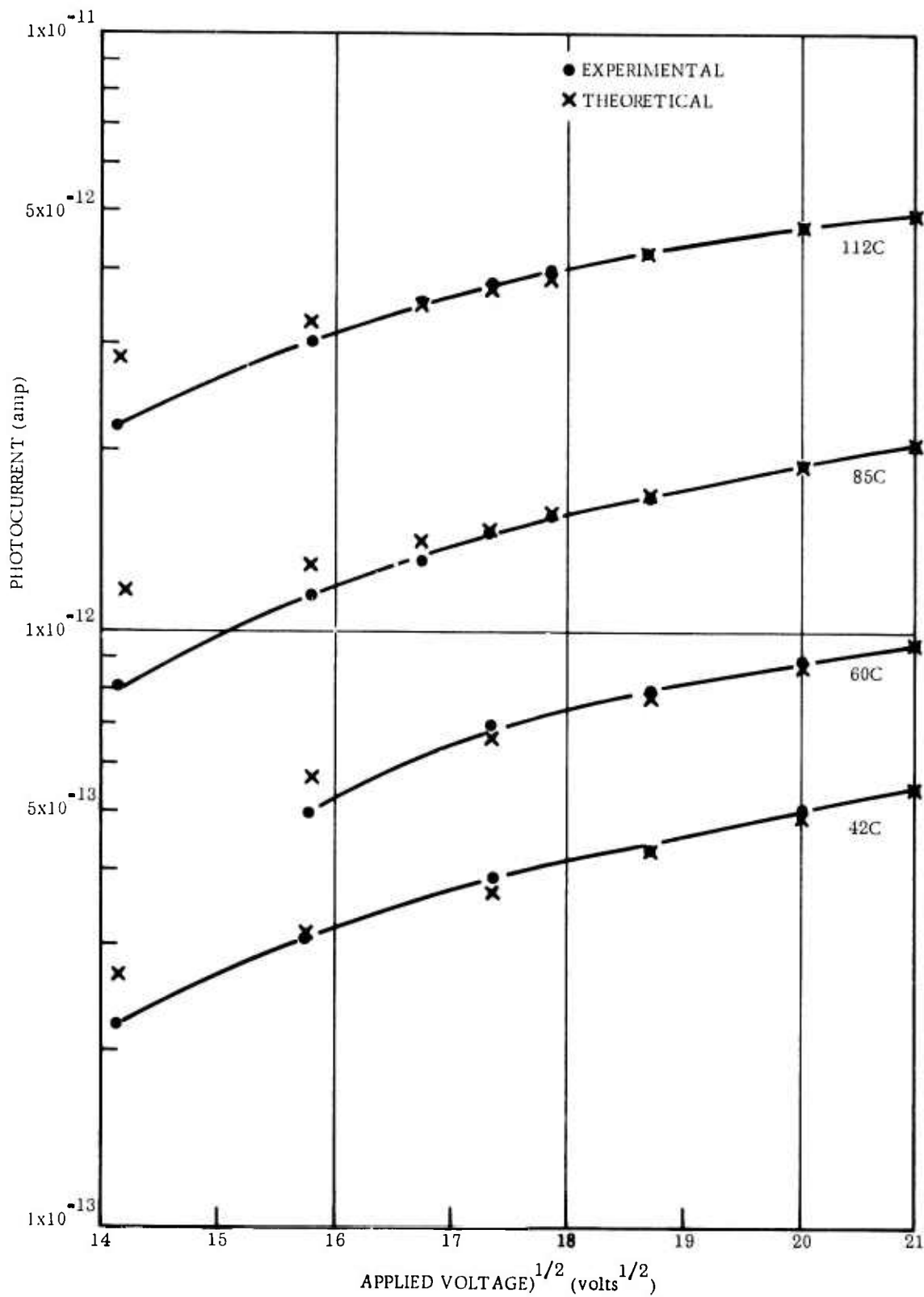


Figure 81. Photoinjected Current in Al_2O_3 as Function of Bias Voltage at Various Temperatures, for 5.0 eV Photon Energy.

both theoretical and adjusted to fit the experimental data, are given in Table 30.

Table 30. Values of β_p for Al_2O_3 at Several Temperatures*

Temperature (K)	$(\beta_p/kT) \times 10^3$	
	Theoretical	Adjusted Value
315	0.57	2.3
333	0.39	1.5
358	0.36	1.4
385	0.34	1.3

* β_p is coefficient of $\xi^{1/2}$ in Equation (53).

At large values of the electric field the exponential factor in Equation (57) is the dominant one. Using the appropriate values of β_p/kT given in the table the theoretical values shown by crosses in Figure 81 were obtained; it can be seen that there is very good agreement with experimental results, particularly for the higher field values. The discrepancy between the theoretical values of β_p and the adjusted values has been noticed by other workers also, but there is not a good explanation for it at this time.

If $\log(1/T^2)$ is plotted as a function of $1/T$, a straight line whose slope is equal to $(E_a - \beta_p \xi^{1/2})/k$ should result, according to Equation (57). Figure 82 shows such a plot, but in view of the limited number of temperatures at which measurements were made it is not possible to draw a straight line with good accuracy through the experimental points. However, the same slope does appear to exist for the four different bias voltages, and this slope corresponds to an activation energy of 0.17 eV. It is assumed that correction due to the electric field is not possible here because of the paucity of experimental points. It is concluded from these data that the trap levels in Al_2O_3 are 0.17 to 0.18 eV below the conduction band.

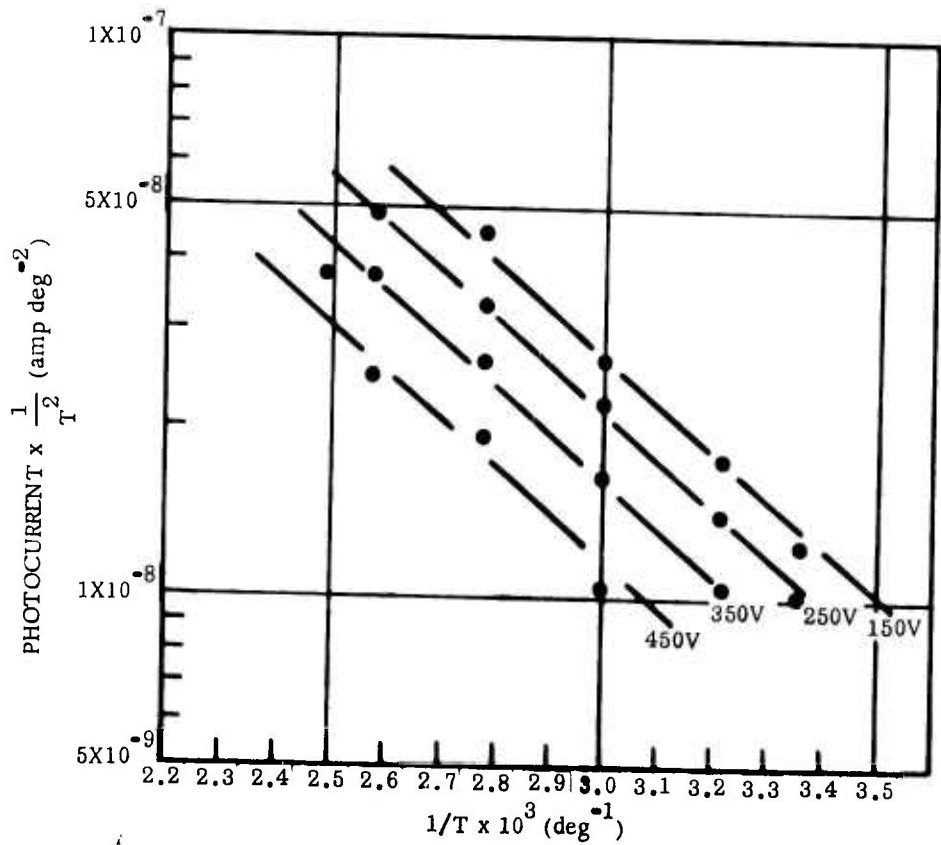


Figure 82. Plot of $\text{Log}(I/T^2)$ as Function of $1/T$ to Test Equation (57), for Various Bias Voltages

This investigation thus established that (1) the Al_2O_3 used for substrates for growth of heteroepitaxial semiconductor films has trap levels approximately 0.18 eV below the conduction band; (2) the transport of photoinjected electrons occurs through the Poole-Frenkel conduction mechanism; and (3) the quantum efficiency for the photoelectric process appears to be about 10^{-5} . Such a low value for the quantum efficiency arises from several contributions, but the main attenuation is due to the term $e^{-E_a/kT}$ in the Poole-Frenkel model (Equation (57)), which accounts for a factor of $\sim 10^{-3}$.

Due to the long time needed to obtain each experimental point, it was not possible to study other Al_2O_3 orientations. It also was not possible to study the photocurrent at very high temperature because the Al_2O_3 appeared to become leaky due to prolonged maintenance at elevated temperature. Study of the transport of photoinjected carriers in single-crystal Al_2O_3 substrates should be continued not only to understand better the transport process in single-crystal insulators but also to characterize further the nature of Al_2O_3 substrates as they are used for semiconductor heteroepitaxy.

REFERENCES

1. R. P. Ruth, "Fundamental Studies of Semiconductor Heteroepitaxy," First Semiannual Report, 28 January 1971, ARPA Order No. 1585, Contract No. DAAH01-70-C-1311. Prepared by North American Rockwell, Autonetics Division, Anaheim, CA, for USAMICOM, Redstone Arsenal, AL.
2. R. P. Ruth, "Fundamental Studies of Semiconductor Heteroepitaxy," Second Semiannual Report, July 1971, ARPA Order No. 1585, Contract No. DAAH01-70-C-1311. Prepared by North American Rockwell, Autonetics Division, Anaheim, CA, for USAMICOM, Redstone Arsenal, AL.
3. R. P. Ruth, "Fundamental Studies of Semiconductor Heteroepitaxy," Third Semiannual Report, January 1972, ARPA Order No. 1585, Contract No. DAAH01-70-C-1311. Prepared by North American Rockwell Electronics Group, Research and Technology Division, Anaheim, CA, for USAMICOM, Redstone Arsenal, AL.
4. R. P. Ruth, A. J. Hughes, J. L. Kenty, H. M. Manasevit, and A. C. Thorsen, "Fundamental Studies of Semiconductor Heteroepitaxy," Fourth Semiannual Report, July 1972, ARPA Order No. 1585, Contract No. DAAH01-70-C-1311. Prepared by North American Rockwell Electronics Group, Research and Technology Division, Anaheim, CA, for USAMICOM, Redstone Arsenal, AL.
5. R. P. Ruth, A. J. Hughes, J. L. Kenty, H. M. Manasevit, A. C. Thorsen, C. R. Viswanathan, and M. A. Ring, "Fundamental Studies of Semiconductor Heteroepitaxy," Fifth Semiannual Report, January 1973, ARPA Order No. 1585, Contract No. DAAH01-70-C-1311. Prepared by North American Rockwell Electronics Group, Research and Technology Division, Anaheim, CA, for USAMICOM, Redstone Arsenal, AL.
6. H. Reiss, J. Appl. Phys. 39, 5045 (1968).
7. E. Hückel, Z. Physik 70, 204 (1931); 72, 310 (1931); 76, 628 (1932).
8. a. H. Kuhn, Helv. Chim. Acta 31, 1441 (1948); 34, 1308 (1951);
J. Chem. Phys. 17, 1198 (1949).
b. K. Rudenberg and C. W. Scherr, J. Chem. Phys. 21, 1565 (1953).
9. E. W. Montroll, J. Math. Phys. 11, 635 (1970); with R. G. J. Mills, 2525 (1970).
10. P. K. Rawlings and H. Reiss, Surface Sci. 36, 580 (1973).

11. See, e.g., Appendix A in "GaAs on Beryllia Substrates for Application to Microwave Generation," Second Quarterly Report, 8 September 1970, Contract No. N00019-70-C-0080. Prepared by Autonetics, Anaheim, CA, for Naval Air Systems Command, Washington, D.C.
12. B. Lewis, *Thin Solid Films* 7, 179 (1971).
13. H. Sato and S. Shinozaki, *Surface Sci.* 22, 229 (1970).
14. M. Bettman, in *Single Crystal Films*, ed. by M. H. Francombe and H. Sato (Pergamon Press, Oxford, 1964), p. 177.
15. D. W. Pashley, *Advan. Phys.* 14, 327 (1965).
16. J. W. Matthews, in *Physics of Thin Films*, Vol. 4, ed. by G. Hass and R. E. Thun (Academic Press, New York, 1967), p. 137.
17. J. H. van der Merwe, in *Single Crystal Films*, ed. by M. H. Francombe and H. Sato (Pergamon Press, Oxford, 1964), p. 137.
18. J. H. van der Merwe, *J. Appl. Phys.* 34, 117, 123 (1967); 41, 4725 (1970).
19. N. H. Fletcher, *J. Appl. Phys.* 35, 234 (1964); *Phil. Mag.* 16, 159 (1967).
20. N. H. Fletcher and P. L. Adamson, *Phil. Mag.* 14, 99 (1966).
21. C. C. Chang, *J. Vac. Sci. and Tech.* 8, 500 (1971); *J. Appl. Phys.* 39, 5570 (1968).
22. J. Callaway and A. J. Hughes, *Phys. Rev.* 156, 860 (1967); 164, 1043 (1967).
23. M. D. Feit and H. B. Huntington, *Phys. Rev.* 172, 580 (1968).
24. R. A. Johnson, *Phys. Rev.* 145, 423 (1966).
25. P. Wynblatt, *Phys. Stat. Sol.* 36, 797 (1969).
26. P. A. Tick and A. F. Witt, *Surface Sci.* 26, 165 (1971).
27. R. A. Swalin, *J. Phys. Chem. Solids* 18, 290 (1961).
28. A. Scholz and A. Seegar, *Phys. Stat. Sol.* 3, 1480 (1963).
29. E. B. Moore, Jr. and C. M. Carlson, *Solid State Commun.* 4, 47 (1966); A. J. Bennett, B. McCarroll and R. P. Messmer, *Surface Sci.* 24, 191 (1971); G. D. Watkins, R. P. Messmer, C. Weigal, D. Peak and J. W. Corbett, *Phys. Rev. Lett.* 27, 1573 (1971).

30. B. McCarroll and R. P. Messmer, *Surface Sci.* 27, 451 (1971).
31. J. H. Gieske and G. R. Barsch, *Phys. Stat. Sol.* 29, 121 (1968).
32. O. L. Anderson, in *Physical Acoustics*, ed. by W. P. Mason, Vol. III, Part B (Academic Press, Inc., New York, 1965), p. 43.
33. D. J. Dumin, *J. Appl. Phys.* 36, 2700 (1965); A. C. Ipri and J. N. Zemel, *J. Appl. Phys.* 44, 744 (1973).
34. J. B. Austin, *J. Am. Ceram. Soc.* 14, 795 (1931).
35. A. J. Hughes and A. C. Thorsen, *J. Appl. Phys.* 44, 2304 (1973).
36. A. C. Thorsen and A. J. Hughes, *Appl. Phys. Lett.* 21, 579 (1972).
37. A. J. Hughes, to be published.
38. H. M. Manasevit, R. L. Nolder, and L. A. Moudy, *Trans. TMS-AIME* 242, 465 (1968).
39. D. J. Dumin and P. H. Robinson, *J. Appl. Phys.* 39, 2759 (1968).
40. W. E. Ham, *Appl. Phys. Lett.* 21, 440 (1972).
41. L. J. van der Pauw, *Philips Res. Repts.* 13, 1 (1958).
42. D. J. Dumin and E. C. Ross, *J. Appl. Phys.* 41, 3139 (1970).
43. R. F. C. Farrow and J. D. Filby, *J. Electrochem. Soc.* 118, 149 (1971).
44. D. J. Dumin, *Solid State Electron.* 13, 415 (1970).
45. H. M. Manasevit and W. I. Simpson, *J. Electrochem. Soc.* 116, 1725 (1969).
46. A. C. Thorsen and H. M. Manasevit, *J. Appl. Phys.* 42, 2519 (1971).
47. K. Borer and C. S. G. Phillips, *Proc. Chem. Soc.* 1959, 189.
48. G. S. G. Phillips and P. L. Timms, *Anal. Chem.* 35, 505 (1963).
49. G. R. Seely, J. P. Oliver and D. M. Ritter, *Anal. Chem.* 31, 1993 (1959).
50. K. Borer, A. B. Littlewood and C. S. G. Phillips, *J. Inorg. Nucl. Chem.* 15, 316 (1960).

51. H. W. Myers and R. F. Putnam, *Anal. Chem.* 34, 664 (1962).
52. A. B. Littlewood, *Gas Chromatography* (Academic Press, New York, 1970), p. 225.
53. H. M. Manasevit and F. L. Morrirtz, *J. Electrochem. Soc.* 114, 204 (1967).
54. H. M. Manasevit, *J. Electrochem. Soc.* 115, 434 (1968).
55. J. W. Faust, Jr., *Electrochem. Tech.* 2, 339 (1964).
56. A. Reisman, M. Berkenblit, J. Cuomo, and S. A. Chan, *J. Electrochem. Soc.* 118, 1653 (1971).
57. R. Williams, *Phys. Rev.* 140A, 569 (1965).
58. A. M. Goodman, *Phys. Rev.* 144, 588 (1966).
59. C. R. Viswanathan and S. Ogura, *Proc. IEEE* 57, 1552 (1969).
60. W. Pong, *J. Appl. Phys.* 40, 1733 (1969).
61. C. R. Viswanathan, R. Loo and S. Ogura, *J. Vac. Sci. Technol.* 9, 230 (1971).
62. C. R. Viswanathan and R. Y. Loo, *Appl. Phys. Lett.* 21, 370 (1972).
63. C. R. Viswanathan and R. Y. Loo, *Thin Solid Films* 13, 87 (1972).
64. C. N. Berglund and R. J. Powell, *J. Appl. Phys.* 42, 573 (1971).
65. M. Ieda, G. Sawa, and S. Kato, *J. Appl. Phys.* 42, 3737 (1971).
66. W. S. Wong, M. S. Thesis, UCLA (1973).
67. C. R. Crowell, W. G. Spitzer, L. E. Howarth, and E. E. Bate, *Phys. Rev.* 127, 2006 (1962).